4-4-2019 11:15 AM

Improving Material Mapping in Glenohumeral Finite Element Models: A Multi-Level Evaluation

Nikolas K. Knowles, *The University of Western Ontario*

Supervisor: Ferreira, Louis, *The University of Western Ontario*

A thesis submitted in partial fulfillment of the requirements for the Doctor of Philosophy degree in Biomedical Engineering

Abstract

An improved understanding of glenohumeral bone mechanics can be elucidated using computational models derived from computed tomography data. Although computational tools, such as finite element analysis, provide a powerful quantitative technique to evaluate and answer a variety of biomechanical and clinical questions, glenohumeral finite element models (FEMs) have not kept pace with improvements in modeling techniques or model validation methods seen in other anatomic locations. The present work describes the use of multi-level computational modeling to compare, develop and validate FEMs of the glenohumeral joint.

Common density-modulus relationships within the literature were evaluated using a multi-level comparative testing methodology to determine if relationships from alternate anatomic locations can accurately replicate the apparent-level properties of glenoid trabecular bone. Two different relationships were able to replicate the micro-level loading to within 1.4%, compared to microFEMs when accounting for homogeneous or heterogeneous tissue moduli.

The multi-level comparative methodology was then used to develop a glenoid-specific trabecular density-modulus relationship. This allowed for controlled and consistent development of the relationship that was adapted for use in whole-bone scapular FEMs. The density-modulus relationship developed was able to simulate micro-level apparent loading to within 1.3%, using a QCT-density specific relationship.

Micro-level FEM characteristics were then compared to determine the optimal parameters for microFEMs and the effect of down-sampled images as FEM input. This was accomplished by creating glenoid trabecular microFEMs from microCT images at 32 micron, 64 micron or down-sampled 64 micron, spatial resolution. It was found that microFEMs accounting for material heterogeneity at the highest spatial resolution were the most accurate. MicroFEMs generated from down-sampled images at 64 microns were found to differ from those generated from scanned 64 micron images, indicating that caution should be used with down-sampled images as input for microFEMs.

The optimal QCT-FEM parameters and material mapping strategies (elemental or nodal) were then explored using the same multi-level computational methodology. Little difference was found when comparing elemental or nodal material mapping strategies for all element types; however, QCT-FEMs generated with hexahedral elements and mapped with elemental material mapping, most accurately replicated micro-level apparent loading. Comparisons by material mapping strategy are also presented for linear and quadratic tetrahedral elements.

Experimental validation of whole-bone scapular models was then explored by loading cadaveric scapulae within a microCT and using digital volume correlation (DVC) and a 6-degree of freedom load cell to compare full-field displacements and reaction loads to whole-bone scapular QCT-FEMs generated with different material mapping strategies and density-modulus relationships from the literature. It was found that elemental and nodal material mapping strategies were able to accurately replicate experimental DVC displacement field results. There was only minimal variation between elemental or nodal material mapping, and although percentage errors in reaction forces varied from -46% to 965%, QCT-FEMs mapped with density-modulus relationships from the literature were able to replicate experimental reaction loads to within 3%.

Finally, morphometric parameters and apparent modulus between non-pathologic normal and end-stage osteoarthritic humeral trabecular bone was compared. It was found that morphometric differences compared to normal bone only occurred in the most medial aspects of end-stage OA bone, within the subchondral region. Moving distally from the articular surface showed near identical morphometric parameters. The end-stage OA group also exhibited a more linear bone-volume-modulus relationship compared to non-pathologic normal bone. The largest differences were seen at bone volume fractions greater than 0.25. This indicates that if high bone volume OA bone is being modeled, then a linear bone-volume-fraction-modulus (or density-modulus) relationship may more accurately replicate bone loading; however, if the high bone-volume-fraction bone is removed (such as with humeral joint replacement surgery), a power-law relationship similar to normal non-pathologic bone may accurately replicate bone loading.

Keywords

Glenohumeral Joint, Trabecular Bone, Digital Volume Correlation, Quantitative CT, Micro CT, Finite Element Analysis

Co-Authorship Statement

Chapter 1:	NK Knowles – sole author
Chapter 2:	NK Knowles – study design, data collection, statistical analysis, wrote manuscript
	GDG Langohr – study design, model generation, edited manuscript
	M Faieghi – developed hexahedral mesh code, edited manuscript
	A Nelson – microCT imaging parameters, edited manuscript
	LM Ferreira – study design, edited manuscript
Chapter 3:	NK Knowles – study design, data collection, statistical analysis, wrote manuscript
	GDG Langohr – study design, model generation, edited manuscript
	M Faieghi – developed hexahedral mesh code, edited manuscript
	A Nelson – microCT imaging parameters, edited manuscript
	LM Ferreira – study design, edited manuscript
Chapter 4:	NK Knowles – study design, data collection, statistical analysis, wrote manuscript
	K Ip – study design, model generation
	LM Ferreira – study design, edited manuscript
Chapter 5:	NK Knowles – study design, data collection, statistical analysis, wrote manuscript
	J Kusins – model generation, edited manuscript
	AM Pucchio – data collection, edited manuscript
	LM Ferreira – study design, edited manuscript
Chapter 6:	NK Knowles – study design, data collection, statistical analysis, wrote manuscript

J Kusins – model generation, edited manuscript

M Faieghi – developed hexahedral mesh code and data extraction code, edited manuscript

M Ryan – digital volume correlation data collection

E Dall'Ara – digital volume correlation data collection, edited manuscript

LM Ferreira – study design, edited manuscript

Chapter 7: NK Knowles – study design, data collection, statistical analysis, wrote manuscript

J Kusins – model generation, edited manuscript

GS Athwal – patient selection

LM Ferreira – study design, edited manuscript

Chapter 8: NK Knowles – sole author

Dedication

To Kellan and Kieran

Acknowledgements

To my family – whose support through this has made it all possible. Your love and support provided an often much needed distraction from the at times all consuming research.

To Dr. Ferreira, your support throughout this process, both with regards to my sometimes-unconventional research interests and for the support that allowed me to raise and support two children throughout this process – I am eternally grateful. To Dr. Ferreira and Dr. Athwal, your ambition and knowledge and the opportunities provided have allowed me to grow tremendously as a researcher. The foundation provided during my time at the HULC will inevitability be a tremendous benefit to my career. To Dr. Nelson, your guidance, training and assistance during microCT scanning helped in such an incredible manner – thank you.

To my lab-mates at the HULC. You have all contributed greatly to the success of my research. Jon, if not for your contribution to the DVC chapter and associated discussions, this chapter would not be what it is. Reza, your patience, guidance, and assistance in writing code for this research is much appreciated. To all the co-op students who have assisted me with data collection, I am so grateful for your help. Shruthi and Aoife, if not for your assistance, the research included in this thesis would not have been possible. To the HULC Surgical Fellows that I have worked with during these four years - your knowledge and guidance have provided invaluable advancement in my views and understanding of the glenohumeral joint.

Finally, I would like to thank my funding sources, without whom this research would not have been possible. The Natural Sciences and Engineering Research Council of Canada, the Ontario Graduate Scholarship program, the Lawson Health Research Institute Pilot Grant Program, the Collaborative Musculoskeletal Training program at the University of Western Ontario, and Western's Bone and Joint Institute.

Table of Contents

List of Tables

List of Figures

List of Appendices

Nomenclature

ρ	Density
μ	Micro
F	Force
k	Stiffness
Δ	Change
ε	Strain
σ	Stress
g	Grams
A	Area
BV/TV	Bone Volume Fraction
Tb.Th	3D Trabecular Thickness
Tb.Sp	3D Trabecular Separation
Tb.N	3D Trabecular Number
SMI	Structural Model Index
kVp	Peak Voltage
SED	Strain Energy Density
app	Apparent
BMD	Bone Mineral Density
vBMD	Volumetric Bone Mineral Density
2D	Two-Dimensional
3D	Three-Dimensional
FE	Finite Element

FEM	Finite Element Model
CT	Computed Tomography
mm	Millimetre
µm	Micrometre
MPa	Megapascal
RoM	Range of Motion
HU	Hounsfield Units
K_2HPO_4	Dipotassium Phosphate
HA	Hydroxyapatite
OA	Osteoarthritis
SD	Standard Deviation
SE	Standard Error
E	Elastic (Young's) Modulus
QCT	Quantitative Computed Tomography

CHAPTER 1 – INTRODUCTION

OVERVIEW: *Computational models in biomechanics allow for a cost effective and repeatable method of evaluation of a variety of basic science and clinically-motivated questions. Development of accurate computational models rely on model validation and characterization. Although much work has been done to validate and characterize the accuracy of computational models of many anatomic locations, the glenohumeral joint has not gained similar attention. Furthermore, variations due to pathology are often overlooked in model development. This chapter describes shoulder anatomy, the structure and function of bone, including mechanical properties, variations that occur due to osteoarthritis, and the generation of computational finite element models from x-ray computed tomography data. A brief summary of the experimental techniques used to validate these models and studies reporting the use of quantitative imaging data as input, are also provided.*[1]

[1]A version of this work has been published: Knowles NK, Reeves RM, Ferreira LM. Quantitative Computed Tomography (QCT) Derived Bone Mineral Density (BMD) in Finite Element Studies: A Review of the Literature. Journal of Experimental Orthopaedics. 2016; 3:36

1.1 FUNCTIONAL ANATOMY:

1.1.1 The Glenohumeral Joint

The glenohumeral joint (GHJ) consists of two bones – the humerus and the scapula (Figure 1.1) – that allow the upper limb the greatest range of motion (RoM) of any joint in the human body. The joint is held in place by a complex system of ligaments and tendons which provide stability and strength. Although the rotational range of motion of the GHJ is large, there are also small translations of the proximal humerus within the articular socket of the scapular, known as the glenoid fossa, throughout the RoM. These translations occur due to the unconstrained nature of the GHJ, with the 'ball' of the proximal humerus having a smaller radius of curvature than the shallow and flat 'socket' of the glenoid. Although the osseous structures of each bone differ, the surfaces are covered in articular cartilage, that support the joint by distributing loads and decreasing friction throughout arm movement. The structure and function of bone and articular cartilage are discussed in section 1.1.2. When the muscles, ligaments and tendons surrounding the GHJ alter joint motion and associated loading as the result of injury or pathology, the bone and articular cartilage may become compromised and undergo adaptive changes. These localized adaptive changes to the bone and cartilage is known as osteoarthritis and will be discussed in section 1.2.

1.1.2 Bone and Articular Cartilage

Bone is a connective tissue that is composed of a complex heterogeneous system of marrow, blood vessels and nerves that collectively supply blood and store nutrients within the body. Bone is composed of hydroxyapatite, collagen and water and can be classified into two main structural organization – cortical and trabecular bone – characterized primary by the degree of porosity (Figure 1.2). Trabecular bone has a porosity of 40-90%, while cortical bone has a porosity of 5-15%. Bone provides structural support to the body, protects internal organs, and maintains hemostasis of the body's vascular system (Ethier and Simmons, 2007). Bone responds to mechanical stimuli at the cellular-level in a process known as bone remodeling (Nordin and Frankel, 2001). This process, termed Wolff's law, was first described by Julius Wolff (Wolff, 1892), in which he observed that bone

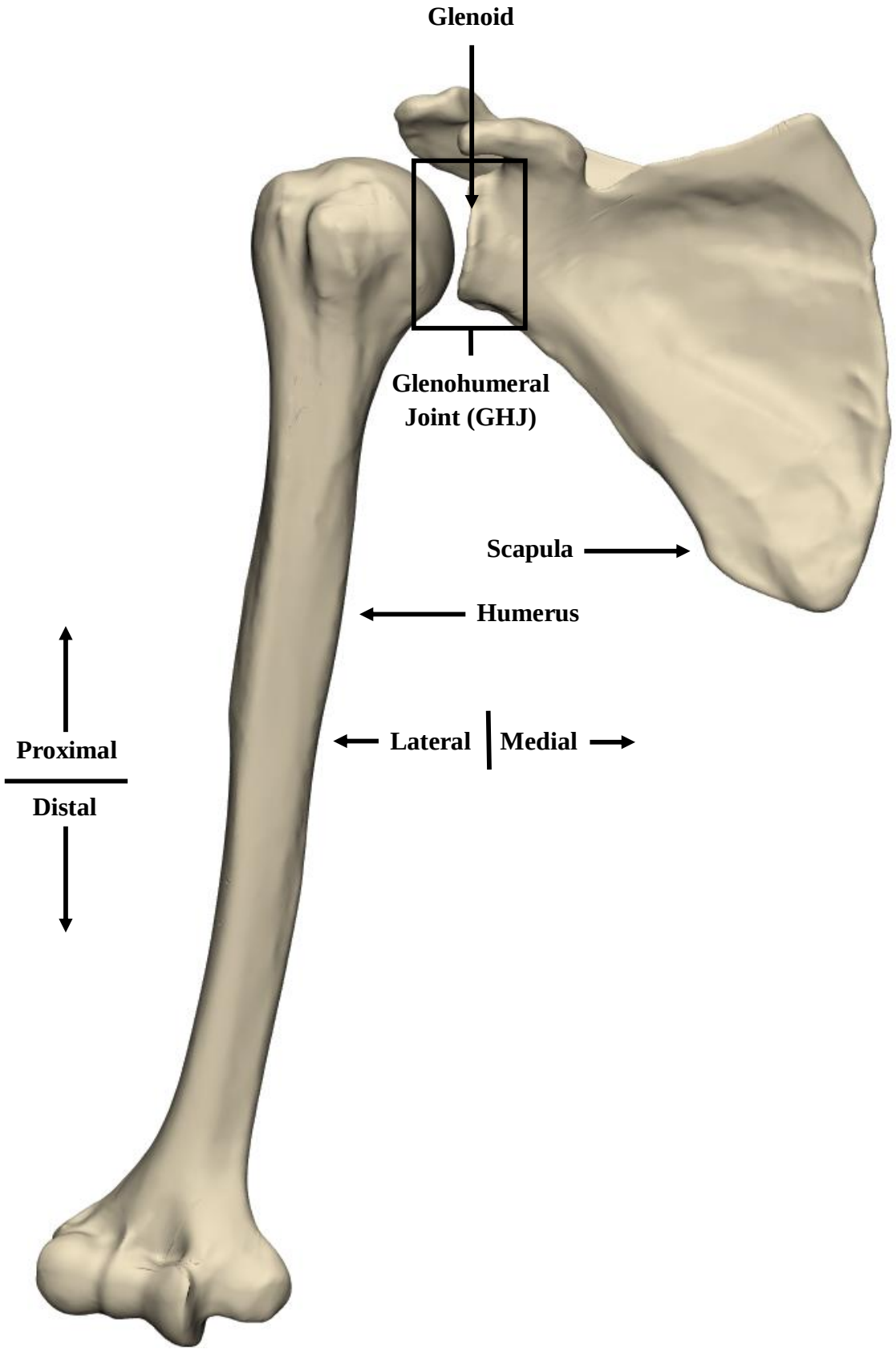

Figure 1.1: The glenohumeral joint (GHJ), comprised of the humerus and scapula

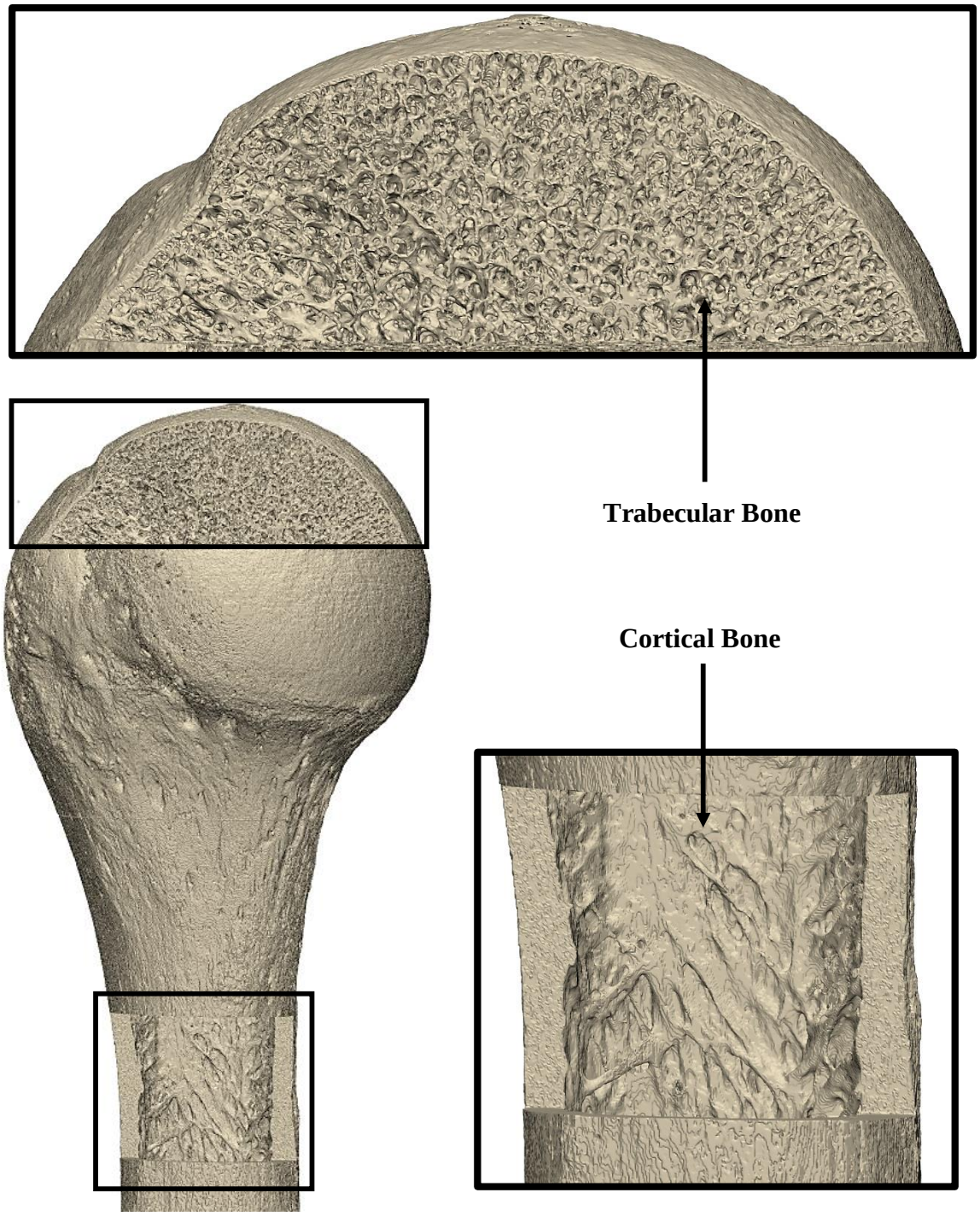

Figure 1.2: Trabecular and cortical bone within the humerus

density was directly a function of the applied stresses and strains, with increased bone density in areas of high stress and low bone density in areas of low stress. This bone adaptation is important in the natural life cycle to allow bone to adapt to variations in mechanical stimuli or repair due to injury, but also has drastic effects when joint loads are altered due to joint replacement components and/or pathology. Whether healthy or pathologic, bone has unique structural organization that can now be visualized using modern tomography techniques (Figure 1.3). These will be further discussed in section 1.3.1.

Bones articulate with each other at synovial joints, with motion provided through complex interconnected systems of muscles, ligaments and tendons. The body's nervous system regulates these motions. Articular (hyaline) cartilage covers the articular surfaces of the connections of two bones at joints. This dense connective tissue provides a low-friction bearing surface, improves shock absorption, and improves the conformity of the two articular surfaces. The dense matrix is composed of approximately 1-5% chondrocytes, 65-80% water, 10-20% collagen and 4-7% proteoglycans. Chondrocytes are the functional cells of cartilage, while proteoglycans are structural proteins whose movement within the matrix is resisted by loosely arranged collagen fibers to resist tensile and shear forces (Fox et al., 2009). Collagen fiber orientation varies by region within the matrix to provide support for various loads. The fibers are aligned parallel on the superficial surface, randomly orientated in the middle and perpendicular, adjacent to the subchondral bone in the deep surface. The large water content is responsible for much of the shock absorption properties of cartilage. Cartilage is avascular and as such has a limited ability to self-repair. In osteoarthritic joints, this causes pain and associated loss of function as cartilage begins to erode. The associated bone and cartilage adaptive changes and apparent mechanical property variations that occur as the result of the osteoarthritic process are discussed in section 1.2.

1.1.2.1 Bone Densitometric Measures

1.1.2.1.1 Tissue Density

The tissue (material) density (ρ_{tissue}) is the fraction of bone mass/bone volume given by the equation:

$$\rho_{tissue} = \frac{M_w}{BV} \qquad \text{(Equation 1.1)}$$

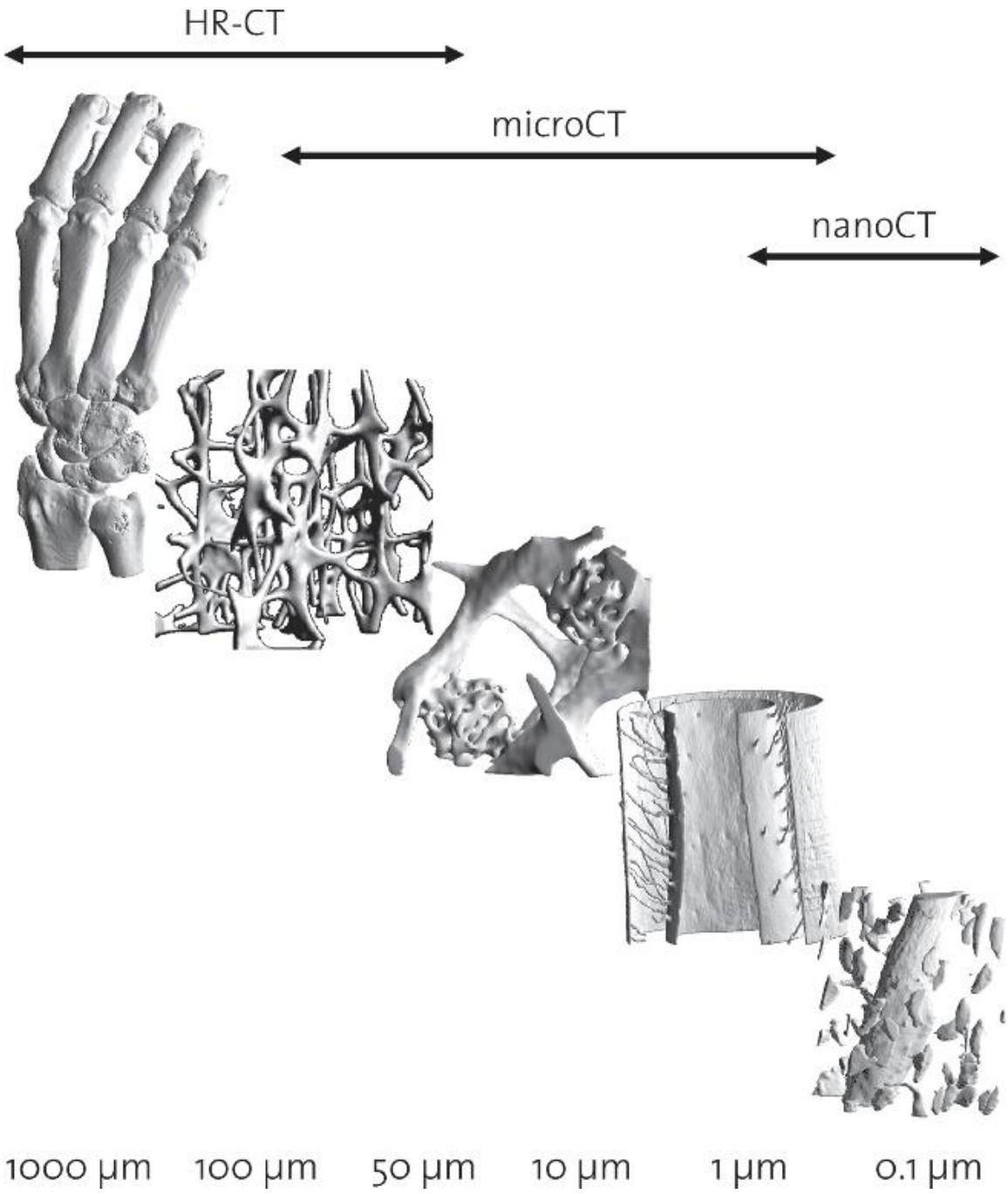

Figure 1.3: Visualization of bone at multiple hierarchical levels

Reproduced with permission from (Stauber and Müller, 2006)

where M_w is the wet mass of the sample and BV is the bone volume, excluding pores (Galante et al., 1970). To determine the volume of bone tissue, the difference between the wet and submerged mass is used by means of Archimedes principle. Volumetric measurements may also use more recent imaging techniques, such as micro-CT to accurately quantify the BV of each sample.

1.1.2.1.2 Ash Density

Ash density (ρ_{ash}) is a physical density measure and is calculated as:

$$\rho_{ash} = \frac{M_a}{TV} \quad \text{(Equation 1.2)}$$

where M_a is the ash mass and TV is the bulk or total sample volume. In the method described by Les et al. (1994), physical measurements were taken on cylindrical bone samples to determine the total sample volume. The sample was ashed in a muffle furnace at 800°C for 24 hours and weighed to determine the ash mass. A similar study tested the effect of ashing temperature on sample mass. Öhman et al. (2007) found that ashing their samples at a temperature of 650°C for 24h in a muffle furnace, produced little variation in measured ash mass, compared to increased furnace temperatures. Although the original method described by Les et al. (1994) is still most commonly used, more accurate methods of initial volume measurement, such as micro-CT, may also be employed.

1.1.2.1.3 Apparent Density

Apparent density (ρ_{app}) is also a physical density measure and is calculated as:

$$\rho_{app} = \frac{M_w}{TV} \quad \text{(Equation 1.3)}$$

where M_w is the wet mass of the sample and TV is the bulk or total sample volume. To determine wet mass, Galante et al. (1970) first washed samples to remove marrow, immersed samples in distilled water, and degassed under vacuum. Samples were then removed from water, centrifuged for 15 min at 8000 g, and then suspended from an analytical balance for submerged mass. Samples were removed and blotted dry and weighed in air for wet mass. Similarly, Keyak et al. (1994) measured bone cubes by first defatting samples in an ethyl alcohol bath. Samples dried for 24 hours at room temperature and were weighed for dry mass. The cubes were rehydrated under vacuum in water for 24 hours, centrifuged at 750 g for 15 minutes, and weighed for hydrated mass. Sample

apparent density was then calculated with the known cube volume. This measure is equivalent to the tissue density multiplied by the bone volume fraction of a sample, and thereby is influenced by changes in bone volume fraction or tissue density.

1.1.2.1.4 Radiological Density

Radiological, or mineral equivalent (K_2HPO_4 or HA) density (ρ_{K2HPO4}, ρ_{HA} , or ρ_{QCT}) is calculated by sampling the average CT number (HU) value of all voxels within a region of interest of a calibration phantom with sample rods of known densities. The radiographic density of the rods can be estimated using the calibration parameters supplied by the phantom manufacturer and simple linear regression calculations (Les et al., 1994; Schileo et al., 2008). This quantitative CT (QCT) calibration can be made on an entire volume, or by individual CT image. This non-invasive method provides a measure of volumetric bone mineral density (vBMD). With clinical-resolution scanners, vBMD provides a density measure similar to apparent density, with the density of each voxel incorporating both mineralized tissue and other constituents (i.e., muscle, marrow, fat, etc.). It has been suggested that vBMD is approximately equal to half of the apparent density (Keyak et al., 1994b); however, various relationships within the literature have shown variations from this value. These will be further discussed in sections 1.3.1.1 & 1.4.6.

1.1.2.2 Trabecular Bone Morphometry

As discussed, trabecular bone is a highly porous structure, with interconnected rods and plates. Bone morphometric parameters were first examined using 2D sections with stereologic methods (Danielsson, 1980), indirectly-derived using a rod- or plate-like structure (Parfitt et al., 1987). The underlying assumptions using 2D methods of trabecular bone morphometry may lead to errors in measurements, and as such, 3D volumetric model-independent methods are now recommended to quantify bone microarchitecture (Bouxsein et al., 2010; Hildebrand et al., 1999; Laib et al., 1997). The specific algorithms in measuring each of these parameters are summarized in the guideline article by Bouxsein et al. (2010), and only the parameters used within this thesis are presented here.

Bone volume fraction (BV/TV) is used to quantify the amount of bone volume (BV) within a specified region (TV) and is determined as the ratio of these two measures (Figure

1.4). Three common morphometric parameters are used to quantify trabecular architecture – mean trabecular thickness (Tb.Th), mean trabecular separation (Tb.Sp), and trabecular number (Tb.N). Trabecular thickness and trabecular separation are calculated using a sphere fitting method, in which the largest possible sphere is fit to the trabeculae or enclosed space, respectively (Hildebrand and Rüegsegger, 1997). The average diameter of these spheres is used to determine each parameter. The mean trabecular number is calculated using the distance transformation method, as the inverse of the mean distance between the mid-axis of the structure (Danielsson, 1980). The final morphometric measure described in this thesis is the structure model index (SMI). This measure quantifies the amount of rod- and plate-like structures that exist within a trabecular region. A value of 0 is achieved for perfect plates, 3 for perfect rods, and 4 for perfect spheres. Although this metric is still commonly reported, it has been suggested that SMI is not an accurate method of determining the amount of rods and plates in a structure, and more direct measures that quantify the actual number of rods and plates should be used (Bouxsein et al., 2010; Stauber and Müller, 2006). Using the densitometric Equations 1.1 and 1.3 defined in section 1.1.2.1, the BV/TV can be related to apparent and tissue density using the relationship:

$$\frac{BV}{TV} = \frac{\rho_{app}}{\rho_{tissue}} \qquad \text{(Equation 1.4)}$$

If tissue density is considered to be uniform throughout a sample (Kabel et al., 1999; Mueller et al., 1966), then the apparent density and bone volume fraction can be used interchangeably (scaled by tissue density).

1.1.2.3 Mechanical Properties

1.1.2.3.1 Trabecular Bone

Trabecular bone, also known as cancellous or spongy bone, has mechanical properties partially dependent on the micro-architecture at the tissue-level. Determination of properties at this level can be performed on individual trabeculae or on trabecular cores used to determine apparent mechanical properties that are translated to the whole-bone

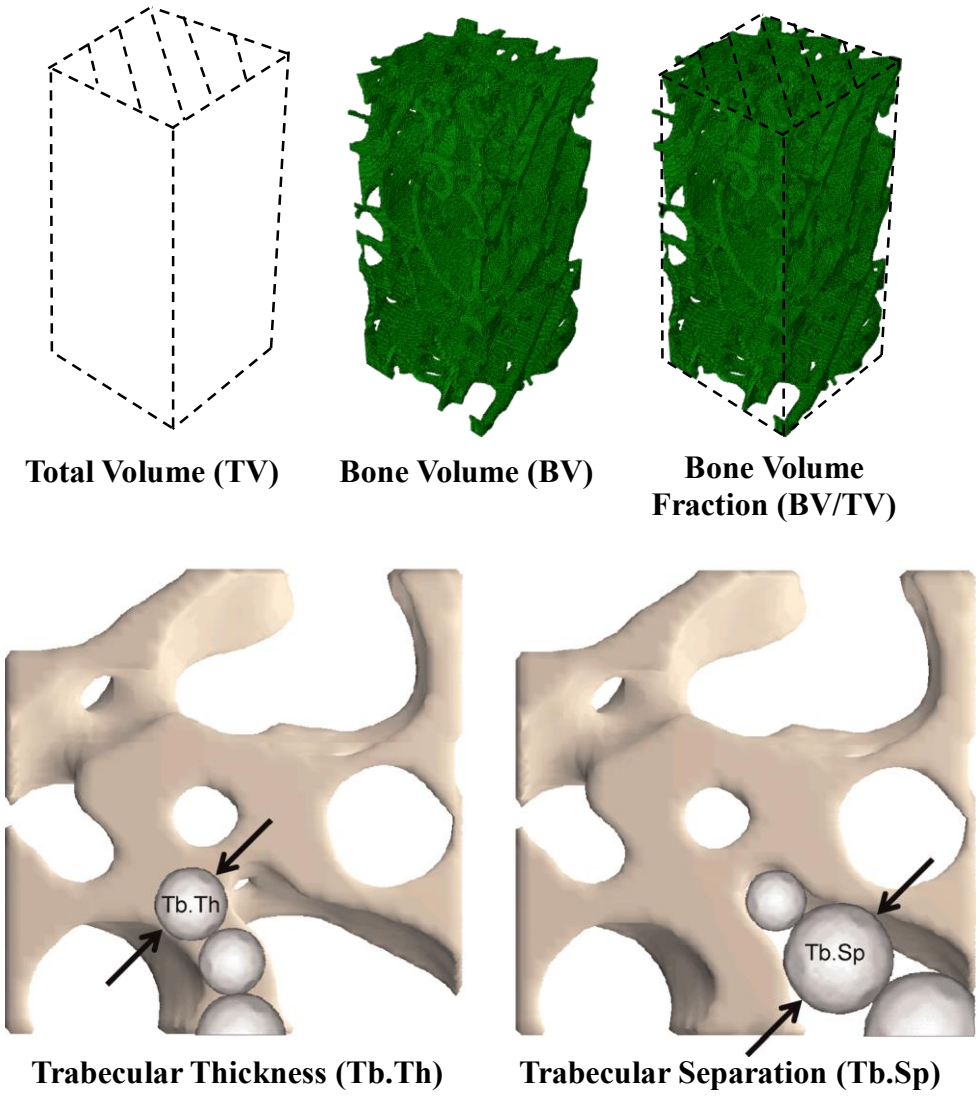

Figure 1.4: Representations of bone volume fraction (BV/TV) trabecular thickness (Tb.Th) and trabecular separation (Tb.Sp)

Reproduced with permission from (Bouxsein et al., 2010)

level. Trabecular bone is comprised of a series of rods and plates, with mineralization, architecture and collagen fiber orientation dictating the mechanical response under load. The structural organization results in a primarily bending dominated structure under compressive loading. The trabecular tissue-level properties of individual trabeculae differ from the those of the apparent properties of organized trabecular regions, used to determine apparent mechanical properties. The elastic modulus of individual trabeculae can be measured using buckling (Townsend et al., 1975), bending (Choi et al., 1990; Choi and Goldstein, 1992), tension (Rho et al., 1993), or compression tests (Bini et al., 2002), as well as ultrasonic methods (Rho et al., 1993), or nanoindentation (Rho et al., 1997). Difficulty arises when testing individual trabeculae in accounting for variations in cross-sectional area, material heterogeneity, and boundary conditions, resulting in elastic modulus values that range from 1.0 – 20.0 GPa (Wu et al., 2018). Bone remodeling occurs on the periphery of trabeculae, leading to decreased mineralization and tissue density (Oftadeh et al., 2015), which reduces individual trabeculae stiffness; in particular, the bending stiffness since this superficial reduction occurs furthest from the neutral bending axis.

To determine the mechanical properties of structurally organized trabecular cores, indentation (Aitken et al., 1985; Harada et al., 1988), tensile or compressive tests are often employed (Helgason et al., 2008a). It is recommended that tensile and compressive tests be performed using end-caps on the specimens to eliminate end-artifacts during mechanical testing, with extensometers attached directly to the end-caps or to the centre of the specimen (Helgason et al., 2008a; Keaveny et al., 1994; Morgan and Keaveny, 2001). This testing method will be further discussed in section 1.4.3. Specimens should have a height-to-diameter (or height-to-edge length for rectangular specimens) aspect ratio of 2:1, with a core diameter of at least 5 mm to ensure a sufficient number of trabeculae exist in the cross-sectional area being tested (Helgason et al., 2008a). Side-artifact, due to coring damage and the loss of load-carrying capacity of outer trabeculae, can also be accounted for (Ün et al., 2006). More recent studies have suggested that the 2:1 aspect ratio is not necessary as long as specimen length is greater or equal to 10 mm (Lievers et al., 2010b), and cores with diameters of 8.3 mm or greater are not affected by side-artifacts (Lievers et al., 2010a).

Trabecular bone is an anisotropic material, which affects its measured elastic modulus (Ciarelli et al., 1991). Although anisotropic, it has been suggested that up to 90% of

trabecular bone's mechanical properties can be explained by its volume fraction or apparent density (Carter and Hayes, 1977; Maquer et al., 2015). Therefore, variations in density by anatomic site, pathology, or age can have a significant effect on the mechanical properties of trabecular bone. The elastic modulus can vary by up to 100-fold (Goldstein et al., 1983); however, structurally organized human trabecular bone generally has an (apparent) elastic modulus between 10 and 3,000 MPa (Morgan et al., 2018). Due to the strong relationship between elastic modulus and apparent density, (apparent) density-(apparent) modulus relationships are often used to model bone as a continuum of mechanical properties in computational simulations. For anatomic locations that span a relatively large density range, these relationships generally follow a power-law relationship between apparent density (or bone volume fraction) and apparent modulus (Carter and Hayes, 1977), with an exponent between 2 and 3 (Equation 1.5 & 1.6) (Hodgskinson and Currey, 1993; Zysset et al., 1994). However, it has been suggested within lower density ranges, this relationship may exhibit more linearity (Morgan et al., 2018).

$$E_{apparent} = \alpha\left(\rho_{apparent}\right)^{\beta} \qquad \text{(Equation 1.5)}$$

$$E_{apparent} = \alpha\left(\frac{BV}{TV}\right)^{\beta} \qquad \text{(Equation 1.6)}$$

Experimental loading of trabecular cores can also be combined with computational models to back-calculate tissue-level mechanical properties (van Rietbergen et al., 1995). Generation of a linear-isotropic micro-finite element model (FEM) is performed for the specimens undergoing mechanical testing using direct conversion of the CT voxels into hexahedral finite elements. The generation of finite element models using hexahedral elements will be discussed in section 1.3.3. An arbitrary tissue modulus of 1 GPa is applied to all elements within the micro-FEM and the experimental setup is replicated computationally. This method has determined trabecular tissue modulus values ranging from 5.0 to 20.0 GPa (Wu et al., 2018). The most recent studies utilizing this method account for the variations in boundary conditions that may occur experimentally (Chen et al., 2017), by modeling the end displacements driven by digital volume correlation (DVC) measurements (Costa et al., 2017). This method indicates that back-calculated tissue-modulus is on the lower end at 4.6 GPa. Digital volume correlation is further explained in section 1.4.5.

The high level of porosity in trabecular bone influences its mechanical properties. Despite not having a clearly defined linear region in stress-strain curves, trabecular bone is often modeled as a linear-isotropic material. The strength varies in both compression and tension, and although localized compressive yield strains are generally around 0.7%, load-carrying capacity can be maintained up to strains of 50%. Due to its viscoelastic behaviour, among other factors, trabecular bone can withstand cumulative damage over time, maintaining much of its strength (Morgan et al., 2018). *In-vivo*, this may be compensated by normal bone remodeling processes, or may lead to clinically-relevant fractures. When testing bone *in-vitro*, this damage accumulation may alter the measured mechanical properties.

1.1.2.3.2 Cortical Bone

Similar to trabecular bone, cortical (or compact) bone's mechanical properties are anisotropic, with elastic moduli of approximately 18 GPa along the longitudinal direction (Mirzaali et al., 2016; Reilly and Burstein, 1975) – double that of the transverse directions. The tensile stress-strain curve is bi-linear with failure strain of less than 3%. The compressive stress-strain curve exhibits increased strength compared to the tensile properties, but failure occurs abruptly at approximately 1.5% strain (Morgan et al., 2018). Cortical bone is also viscoelastic, but only modest changes in elastic modulus are observed with increasing strain rate (McElhaney, 1966). As with trabecular bone, cortical bone is influenced by damage accumulation (Zioupos et al., 2008), which also alters mechanical properties, but this micro damage is a normal consequence of physiologic loading (Fondrk et al., 1999; Frost, 1960).

1.1.2.3.3 Whole Bones

The mechanical properties at the whole-bone level are a combination of trabecular and cortical bone properties and distributions, as well as geometrical factors. Difficulties in mechanical property evaluation at the whole-bone level arise from the difficulty in replicating physiologically relevant boundary conditions. The tensile and compressive properties of whole bones are dependent on cross-sectional area, while bending and torsional stiffness depend on local distributions of trabecular and cortical bone throughout the structure. These spatially variable distributions of material lend well to CT analysis, which is able to capture local variations in apparent density (Morgan et al., 2018). The

strong dependence of strength and elastic modulus on apparent density allows for whole-bone computational models to be generated with a continuum of materials accounting for each bone type and geometrical organization. A separate density-modulus relationship can be applied to each of trabecular bone and cortical bone (Equations 1.5 & 1.6). The transition between the two types of bone has been suggested to occur at an apparent density of 1.0 g/cm^3 (Gray et al., 2008), or bone can be separated into distinct regions of trabecular and cortical bone using image processing techniques. The former has shown excellent correlations with experimental data (Dahan et al., 2016), while the latter has been explored in a more robust and systematic manner, but only in the femur (Enns-Bray et al., 2018, 2016; Helgason et al., 2016). These variations in trabecular and cortical piecewise material mapping will be explored in Chapter 6.

1.2 OSTEOARTHRITIC GLENOHUMERAL JOINTS:

1.2.1 Disease Characteristics

Osteoarthritis (OA) is characterized by joint morphological pathology and/or biomechanical changes (Arden and Nevitt, 2006). The symptomatic biomechanical changes lead to loss of joint range of motion and stiffness, causing pain and functional loss. These are directly related to the morphological variations that occur within the joint, including loss of articular cartilage, subchondral bone sclerosis, subchondral cyst formation, abnormal bone formation, leading to osteophyte formation and synovial inflammation (Brandt et al., 2008). These pathologic characteristics are visible in CT scans of OA glenohumeral joints and contribute to their bone's altered biomechanical properties (Figures 1.5 & 1.6).

1.2.2 Etiopathogenesis

There are disagreements in the literature as to the exact etiopathogenesis of OA and whether structural changes in the cartilage lead to structural changes in the underlying subchondral bone, or if subchondral changes lead to the progression of cartilage degradation. In theories predicated on cartilage structural changes, chondrocytes are destroyed, the extra-cellular matrix is altered, and proteoglycans are depleted as the result

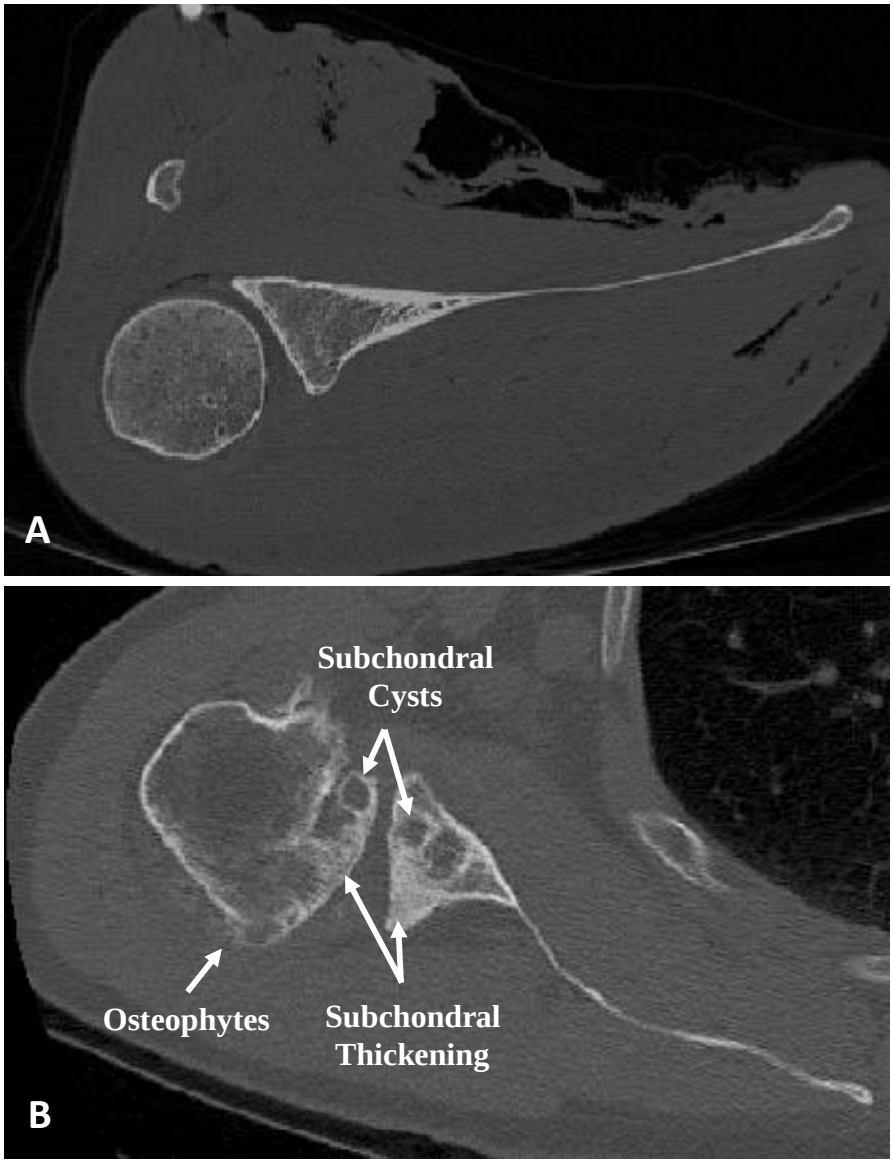

Figure 1.5: Axial clinical-CT images of a normal (A) and OA (B) glenohumeral joint

Evidence of subchondral cysts, thickening and osteophytes are indicated.

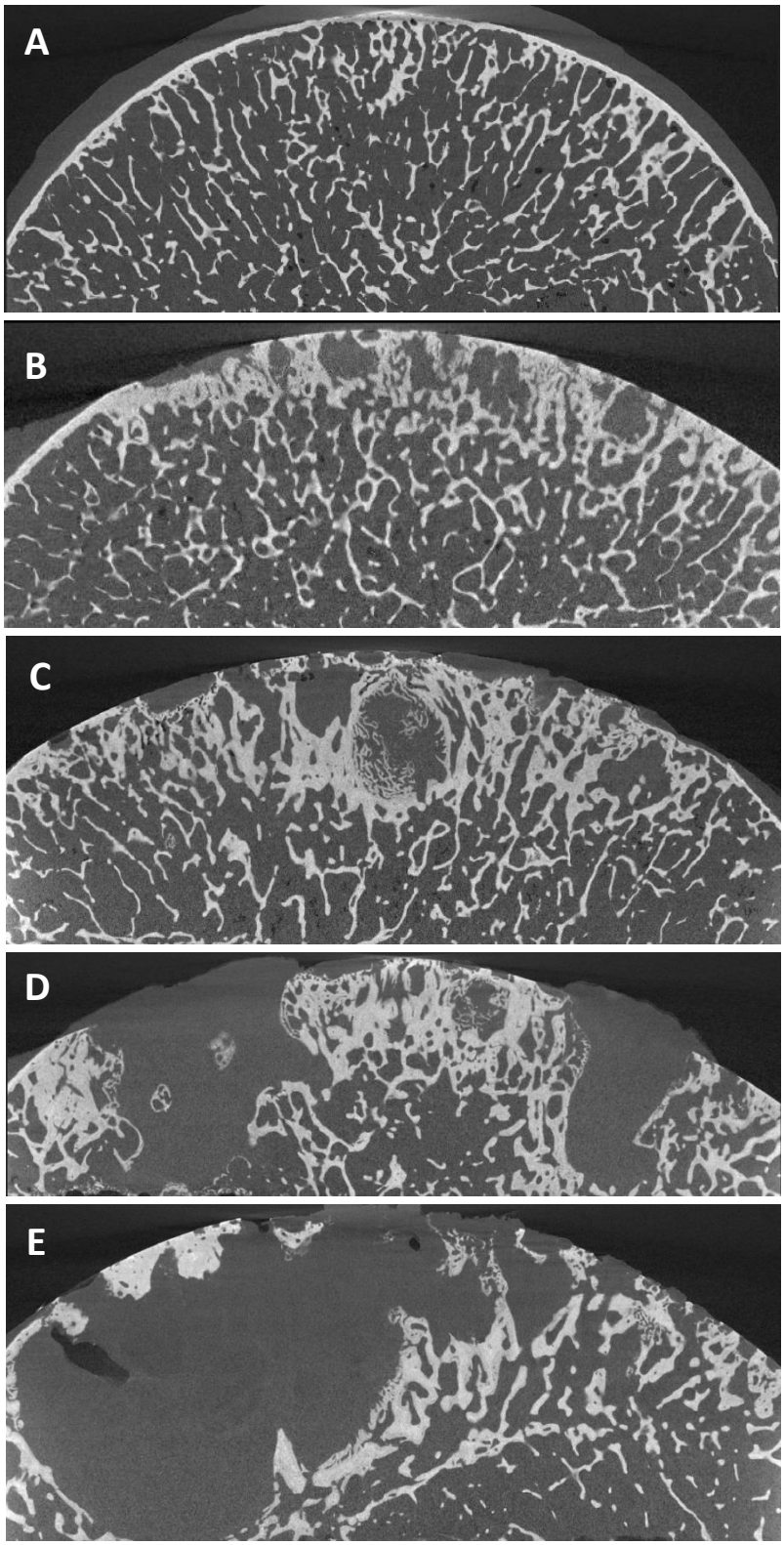

Figure 1.6: Coronal micro-CT images of a normal humeral head (A) and humeral heads with progressive OA (B-E)

of increasing joint loads, impact, or fatigue loading beyond normal physiological levels (Aigner and McKenna, 2002; Blanco et al., 1998). Radin et al. reported that subchondral sclerosis leads to thicker and stiffer bone underlying the cartilage, which induces increased stresses on the cartilage, predisposing the OA joint to progressive damage (Radin et al., 1986). Beyond biomechanical considerations, biological factors play a key role in the initiation and progression of OA. The biomechanical factors previously described (or other unknown factors) result in increased biological activity within the subchondral bone and/or cartilage. Within the subchondral bone, increased bone remodeling results in thicker (sclerotic) bone, causing cartilage thinning, and consequentially increased cartilage stresses. Biochemical markers indicating increased bone remodeling in OA joints have been reported (Bailey and Mansell, 1997; Mansell and Bailey, 1998). It is likely a combination of both biomechanical and biological systemic factors that contribute to the initiation and progression of OA (Dieppe, 1995; Felson et al., 2000; Sharma, 2001).

1.2.3 Bone Density

Despite the appearance of increased bone density seen using x-ray techniques, the sclerotic bone visualized in OA joints is hypomineralized. The tissue density of subchondral cortical and trabecular bone is lower in OA subjects than normal controls (Chappard et al., 2006; Grynpas et al., 1991; Li et al., 1997a; Li and Aspden, 1997). The higher rate of bone remodeling that occurs during the pathologic process (Mansell and Bailey, 1998) results in less mineralized bone and increased osteoid (Burr, 1998; Fazzalari and Parkinson, 1997; Grynpas et al., 1991). These variations in densities have been assessed in the OA hip (Chappard et al., 2006; Li et al., 1997a; Li and Aspden, 1997), and proximal tibia (Ding et al., 2001), among other joints. In subchondral cortical and trabecular bone, the altered OA bone remodeling process leads to increases in bone volume fraction. Recall that apparent density can be calculated as the tissue density multiplied by the bone volume fraction (section 1.1.2.2). As such, although the density of the mineralised tissue is less than non-pathologic bone, the increase in bone volume fraction increases the apparent density of this bone. This may be as large as 50% higher in some joints (Brown et al., 2002; Li and Aspden, 1997).

1.2.4 Mechanical Properties

It has been observed that subchondral bone from joints with early OA has reduced ability to transfer strain-energy (area under the load-displacement curve) during impact loading (Radin et al., 1970). In the joint, this results in increased energy being transferred to other areas of the skeletal system (Johnston, 2010), such as the articular cartilage, leading to higher cartilage stress, breakdown, degradation and OA (Radin et al., 1986, 1973, 1972). The structure and composition of the OA bone is altered during disease progression which contributes to the alteration of mechanical properties related to normal bone (Li et al., 1997b). The increased mineralization, but decreased material density on the outer surface of the trabeculae alter the bending stiffness under compressive loading. There still remains a significant correlation between elastic modulus and apparent density in OA bone; however, the large range of apparent-densities and variations in mineralization that occur in OA bone results in a more linear density-modulus relationship and lower correlation coefficients (Li et al., 1997b).

1.3 FINITE ELEMENT MODELING

1.3.1 Radiographic Techniques

X-ray computed tomography (CT) is a medical imaging modality that uses ionizing radiation projected through an object to collect a series of projections quantified by the object's x-ray attenuation along the beam path. A detector measures the x-rays that pass through the object, allowing for a quantitative map of attenuation values that is directly proportional to the electron density of the object being scanned. In helical clinical CT scanners, the x-ray source rotates around the object allowing for a series of projections to be collected. This collection of projections is reconstructed to create 2-dimensional (2D) image stacks in the three main anatomical directions (axial, sagittal, and coronal). The orthogonal 2D images can be combined into 3D, characterized into volumes and broken down by voxels. In clinical scanners, voxels are generally anisotropic, with in-plane spatial resolutions dependent on the size of the object being scanned. In-plane spatial resolutions can be as fine as 0.1 mm, with the most recent clinical-resolution helical scanners having out-of-plane spatial resolutions of 0.3125 mm. This spatial resolution limits the quantitative data to the apparent-level, in which the density retrieved per voxel is a function of both

bone and other constituents (muscle, fat, marrow, etc.). Micro-CT works in a similar manner, but current cone-beam industrial systems, such as the one used in this thesis (section 1.3.1.2), are capable of spatial resolutions < 0.01 mm. Spatial resolutions in these scanners are again a function of the size of the object being scanned; however, these improvements in spatial resolution allow for local bone architecture to be visualized and tissue density to be quantified.

1.3.2 Quantitative Computed Tomography (QCT)

Quantitative computed tomography (QCT) was introduced in the 1970's as a method of quantifying bone mineral density (BMD) using CT scanners (Isherwood et al., 1976; Rüegsegger et al., 1976). In the years following its introduction, alternative methods of bone mineral density estimation, such as dual-energy x-ray absorptiometry (DXA), gained clinical popularity due to lower levels of ionising radiation dose (Adams, 2009). More recently, QCT has regained usefulness, both clinically and within the research community, for its ability to accurately quantify volumetric BMD (vBMD), compared to the two-dimensional, or areal BMD (aBMD) measurements acquired with DXA. In biomechanics research, this method of accurate vBMD measurement is essential for computational modeling of bone and other structures. Due to the strong relationship between apparent density and elastic modulus (Section 1.1.2.3), QCT provides a quantitative method of determining accurate vBMD that can be translated across CT scanners and settings.

The basis of QCT scanning is that the object, specimen, or patient is scanned with a calibration phantom, which contains rods of varying concentrations of calcium hydroxyapatite (HA), or rods with varying materials from low to high atomic number calibrated against liquid dipotassium phosphate (K_2HPO_4). These provide a consistent density reference between objects, specimens, or patients and allow for scaling of CT attenuation values to known QCT density values (Figure 1.7). The phantoms are not scanner specific and therefore provide a common density reference translatable across all scanners and scan settings. Radiological or quantitative density (ρ_{QCT}) is calculated in units of $mg_{HA}/cm3$ (ρ_{HA}) or $mg_{K2HPO4}/cm3$ (ρ_{K2HPO4}). These imaging-based density measures can then be related to physical methods, such as ash or apparent density using relationships developed within the literature (Section 1.4.6).

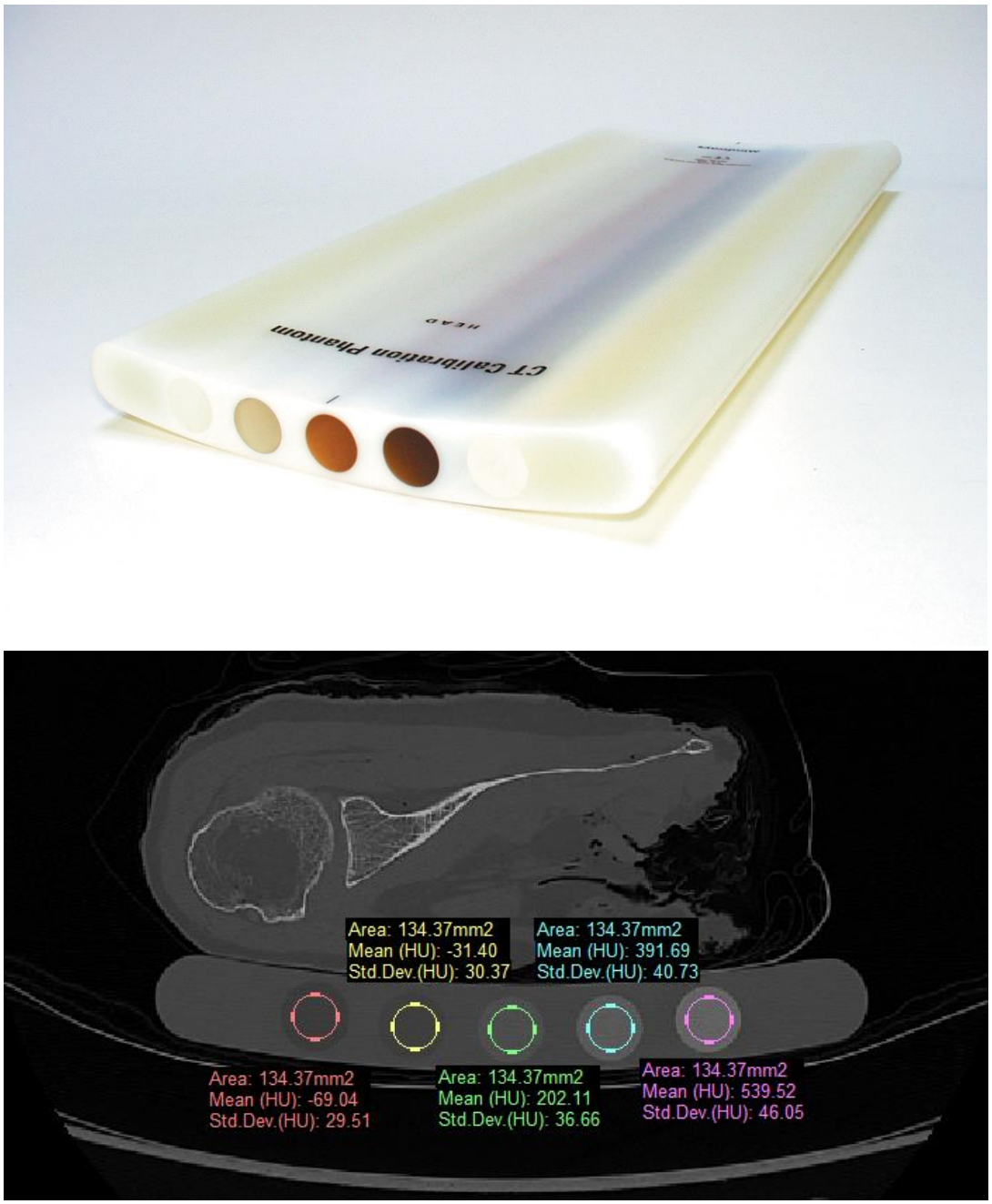

Figure 1.7: A QCT calibration phantom (QCT Pro, Mindways Software, Austin, TX, USA) and sampling of rods of various density

1.3.1.2 Micro-Computed Tomography

Micro-CT systems differ slightly from helical clinical CT-scanners in that the object or specimen is generally placed on a rotating turntable that rotates 360° during scan acquisition. An x-ray tube and detector are fixed on opposite sides of the turntable and 2D projections are collected and used to reconstruct the volumetric 3D image (Figure 1.8). The x-ray beam disperses from the emitter as a cone-beam, which causes a degree of geometric magnification and variations in x-ray energy across the object. The spatial resolution of the object is inherently linked to the size of the specimen, as larger objects limit the proximity of the emitter and detector. As such, the closer the distance that the specimen is from source, the higher the spatial resolution will be. Similar to QCT-clinical scanning, a calibration phantom may be scanned with an object before or after scanning to calibrate the scans to a known density reference. In the present thesis, a micro-CT calibration phantom was not available, and so the same scanner, scanner settings, and scanning protocol was used to ensure consistency between scans. Beyond the scope of this thesis, a comprehensive evaluation of micro-CT parameters that influence image quality is provided by Stauber and Müller (2008).

1.3.2 The Finite Element Method

The finite element (FE) method is a numerical method for solving engineering problems – primarily those with complex geometries in which analytical solutions are difficult to obtain. In the *stiffness matrix method*, the simple Hooke's law stiffness equation is solved element-wise and summed to determine a global stiffness matrix of the solid continuum as a whole. The geometry is discretized into finite elements (Figure 1.9) that simplify the complex geometry. Each individual element has an associated stiffness value related to the geometrical features of the element and its associated elastic modulus. As an example, for a simple bar element, the elemental stiffness is given by the relationship between Hooke's Law and stress-strain:

$$F = kx \rightarrow F = k\Delta L \rightarrow E = \frac{\sigma}{\varepsilon} = \frac{\frac{F}{A}}{\frac{\Delta L}{L}} \rightarrow \frac{EA}{L} = \frac{F}{\Delta L} = k \qquad \text{(Equation1.7)}$$

It can be seen from equation 1.7 that the elemental stiffness, k, is a function of geometrical factors A (area) and L (length) and E (elastic modulus). The element-wise

Figure 1.8: Nikon XT H 225 ST Micro-CT Scanner

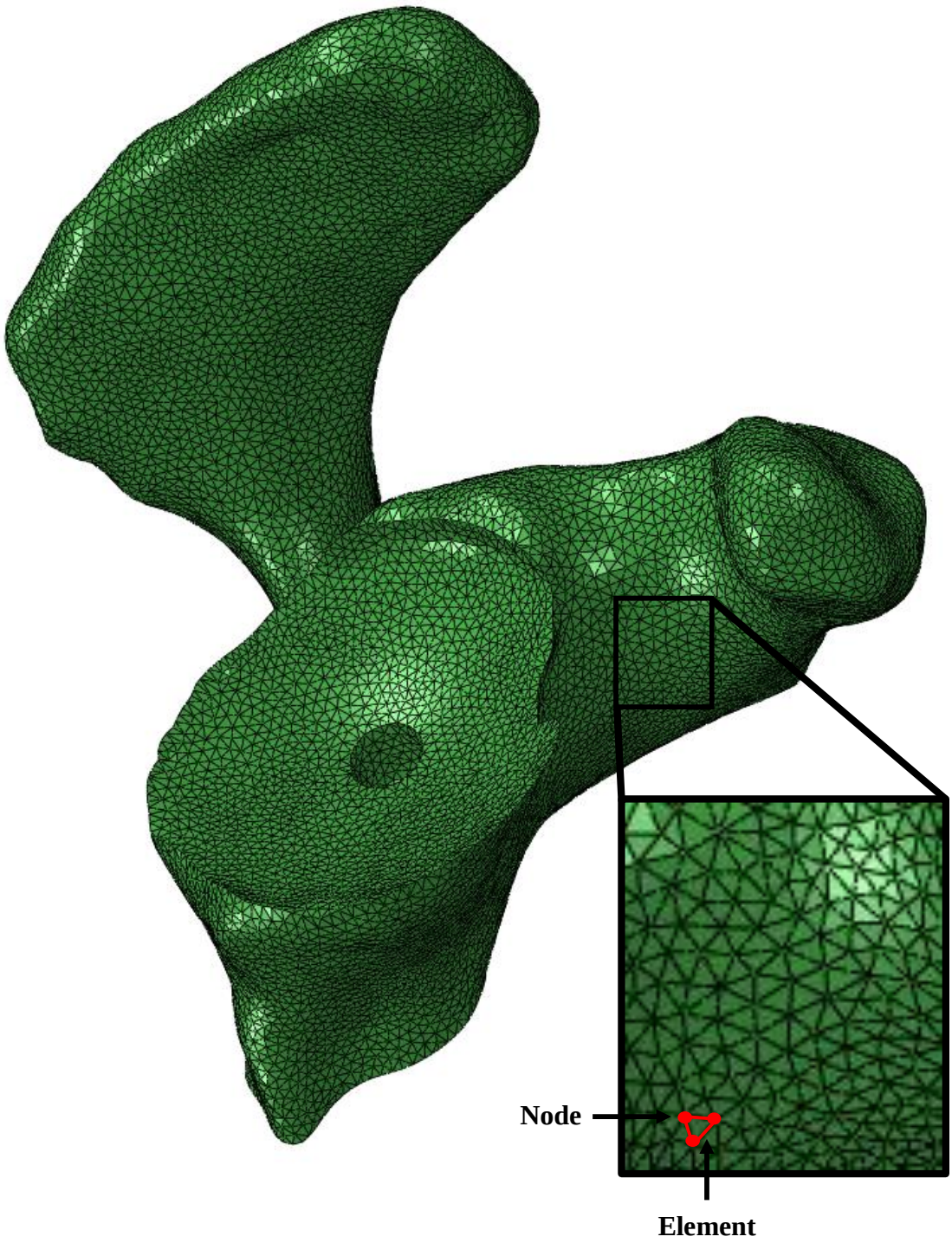

Figure 1.9: A finite element model of a cadaveric scapula, discretized into a tetrahedral mesh, consisting of nodes and elements.

stiffness matrices are combined to form a global stiffness matrix for the entire model. In linear-isotropic models, forces are often applied at the nodes of the model allowing for the equilibrium of a system of linear equations to be solved:

$$\{F\} = [k] * \{U\} \rightarrow \{U\} = [k]^{-1}\{F\} \qquad \text{(Equation 1.8)}$$

where $\{U\}$ is a displacement field vector. In displacement-controlled models, the elemental forces can be determined using the same relationships. These are then combined with element geometry and compatibility equations to determine the elemental strains. Using the constitutive relationship of each element, stresses can then be determined element-wise. This provides a full-field analysis of the displacement, strain, stress and other relevant mechanical properties throughout the entire structure.

1.3.3 Finite Element Mesh

The finite element mesh is a discretization of solid geometry and decreasing its element size – known as *h-type* mesh refinement – allows the approximate solution of the model to converge on the correct solution. Two element types are commonly used in finite element modeling of bone – hexahedral and tetrahedral (Figure 1.10). Hexahedral elements are most commonly used in micro-level FEMs due to direct conversion of isotropic voxels into these brick elements. Hexahedral elements usually use linear integration formulations to improve convergence and reduce computational expense, although higher order integration formulations can be implemented. In micro-level FEMs, higher order hexahedral elements have shown minimal improvements in the accuracy of local stresses and strains (Depalle et al., 2013). Hexahedral elements can also be adapted to more complex geometries, by creating elements with non-uniform edge lengths; however, the complexity associated with automatic mesh generation for these elements and complex geometries limits their usefulness in most bone computational studies. Tetrahedral elements, using linear or quadratic integration formulations are most often used in continuum-level FEMs, but can also be used in micro-level FEMs (Figure 1.11). The advantage of tetrahedral elements is their ability to represent complex curved geometries with smoother surfaces, and their widespread implementation in automatic mesh generators. Linear tetrahedral elements are less common in contemporary FE modeling due to their high stiffness (Cifuentes et al., 1992). Quadratic tetrahedral elements have high accuracy, and excellent convergence

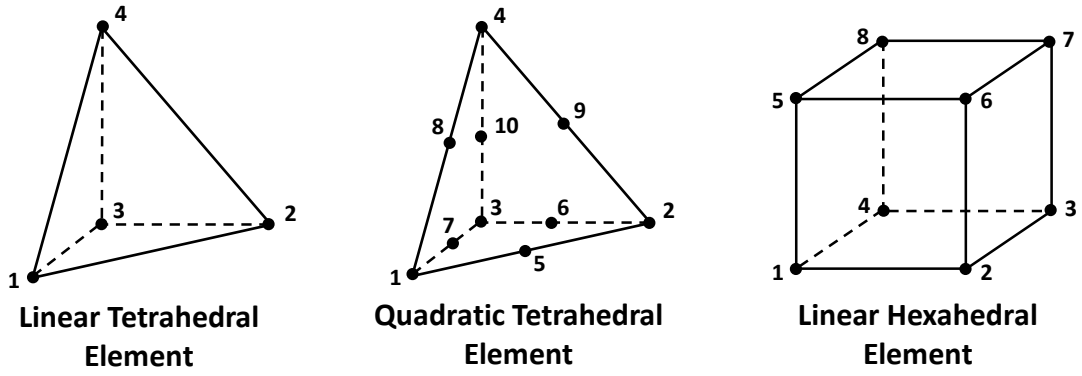

Figure 1.10: Linear hexahedral, linear and quadratic tetrahedral element types

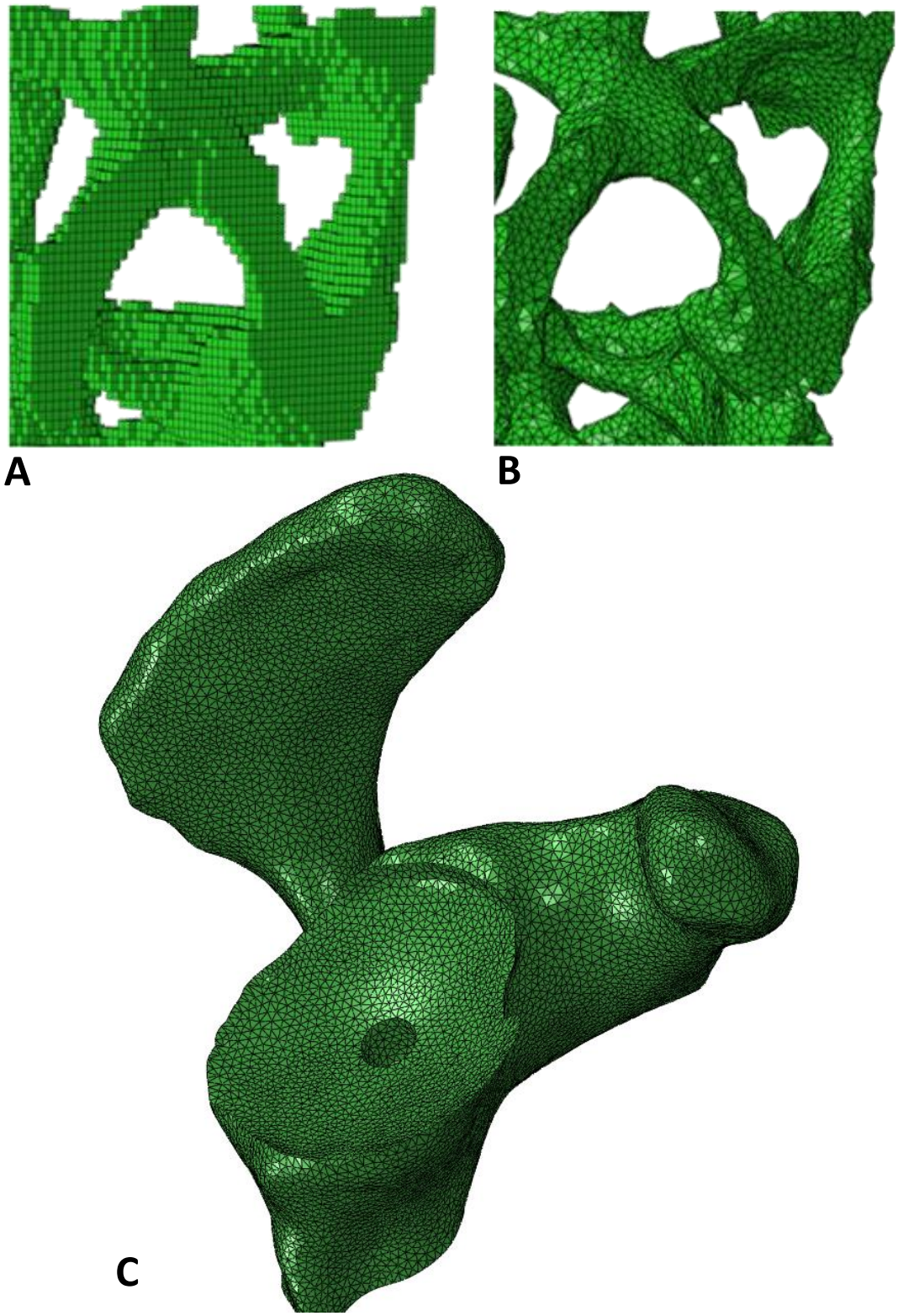

Figure 1.11: Hexahedral (A) and tetrahedral (B) microFEMs and a tetrahedral continuum-level FEM (C)

behaviour and may require less mesh refinement to achieve an accurate solution, provided that geometrical quality is maintained (Burkhart et al., 2013). With all FE types, node numbering is important for element connectivity, maintaining a continuous mesh. The effect of element type in microFEMs will be explored in Chapter 4 and mesh refinement and element type in QCT-FEMs in Chapter 5.

1.3.4 Material Assignment

At the continuum-level, finite element models (FEMs) are assigned mechanical properties based on a continuum of material densities through the bone geometry. These can be applied using a homogeneous elastic modulus for bone, homogeneous distributions with pre-processed separation of cortical and trabecular bone, or a heterogeneous distribution of materials using an (apparent) density-(apparent) modulus relationship (section 1.1.5.1). These may be single relationships that represent the full-range of densities within the bone, or piece-wise functions that account for differences between trabecular and cortical bone. An accurate estimation of bone density and choosing an anatomic location-specific density-modulus relationship is essential for physiologic accuracy in linear-isotropic continuum FEMs (Helgason et al., 2008a; Knowles et al., 2016; Morgan et al., 2003; Schileo et al., 2008). Density-modulus relationships can be assigned using software that is commercially available (Mimics, Materialise, Leuven, BE; Simpleware, Synopsys, UK) or open-source (Bonemat, www.bonemat.org; MITK-GEM, https://simtk.org/projects/mitk-gem). These software packages expand on the simple elemental averaging method, first reported by Zannoni et al. (1999), by overlaying the mesh lattice vertices on the native CT field and applying mechanical properties to the elemental integration points (Zannoni et al., 1999). Within Bonemat, this has been improved using numerical integration (Taddei et al., 2007, 2004), while Mimics and Simpleware use exact volume-weighted elemental averaging. Bonemat can also assign materials using the elastic modulus field, in which the non-linear density-modulus relationship is first applied to the native CT-intensity field, and then the density-modulus relationship is applied. This method has been reported to improve accuracy with experimental surface strain results (Helgason et al., 2008b). Material mapping accuracy may be impacted when mesh density varies greatly in relation to the

native CT voxel dimensions, or at the interface of materials of different densities, due to partial volume effects (PVEs).

In FEM development, PVEs are of the highest concern on the outer cortical shell because this region lies adjacent to muscle and other soft tissue, with vastly different densities. As such, materials mapped to the outer cortical surface may underestimate the true modulus of this bone. PVEs can be accounted for using image processing techniques to remove the outer 'weak-voxel layer,' assigning a uniform modulus to the cortical regions (Helgason et al., 2016), or ensuring the contours of the model do not include PVE voxels. Due to elemental mesh complexity, methods beyond these to eliminate PVEs are limited. This is implemented in open-source software (MITK-GEM).

Alternative to elemental material mapping, a nodal material mapping strategy may be employed (Figure 1.12). The nodal coordinates can either be read as a user subroutine in Abaqus (Simulia, Providence, RI) (Chen et al., 2015, 2010), or as 'field or auxiliary (temperature) variables,' in Abaqus or Ansys (Ansys Inc., USA) (Helgason et al., 2008b). These variables are linearly interpolated to the element gauss integration points in the subsequent FE simulation. In nodal material mapping, tri-linear interpolation of the scalar field is used to map materials directly to the nodes. This is typically implemented in custom-code and so the scalar field can be either the native CT field, or an elastic modulus field. This method has also been used to account for PVEs by determining whether outer nodes are assigned a lower modulus than the nearest internal node (Helgason et al., 2008b), and if so, these outer nodes are assigned the nearest internal node's value (Figure 1.13).

At the micro-level, trabecular geometry is preserved in micro-FEMs, allowing for tissue-level mechanical properties to be defined. These models are most commonly generated using direct-conversion of the micro-CT voxels into hexahedral elements (van Rietbergen et al., 1995), retaining the CT attenuation of each voxel. It is most common for a uniform homogeneous tissue modulus to be assigned to models at this resolution; however, heterogeneous material distributions are increasing in popularity to account for spatial variations in material properties that occur due to bone remodeling (Oftadeh et al., 2015; Wu et al., 2018) (Figure 1.14). These relationships often use direct linear relationships between voxel CT attenuation to apply element-wise tissue moduli (Bourne and Van Der Meulen, 2004; Jaasma et al., 2002), or may use a calibration phantom to

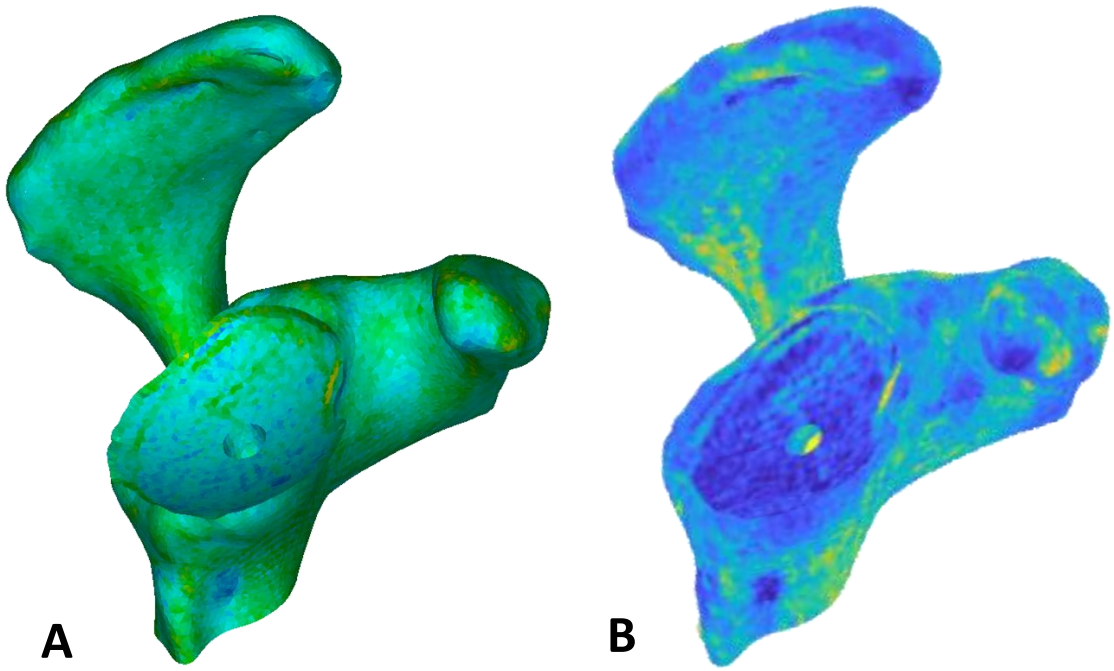

Figure 1.12: Scapular FEMs mapped with elemental (Mimics. v.20.0) (A) or nodal (Matlab, v.R2017a) (B) material mapping strategies

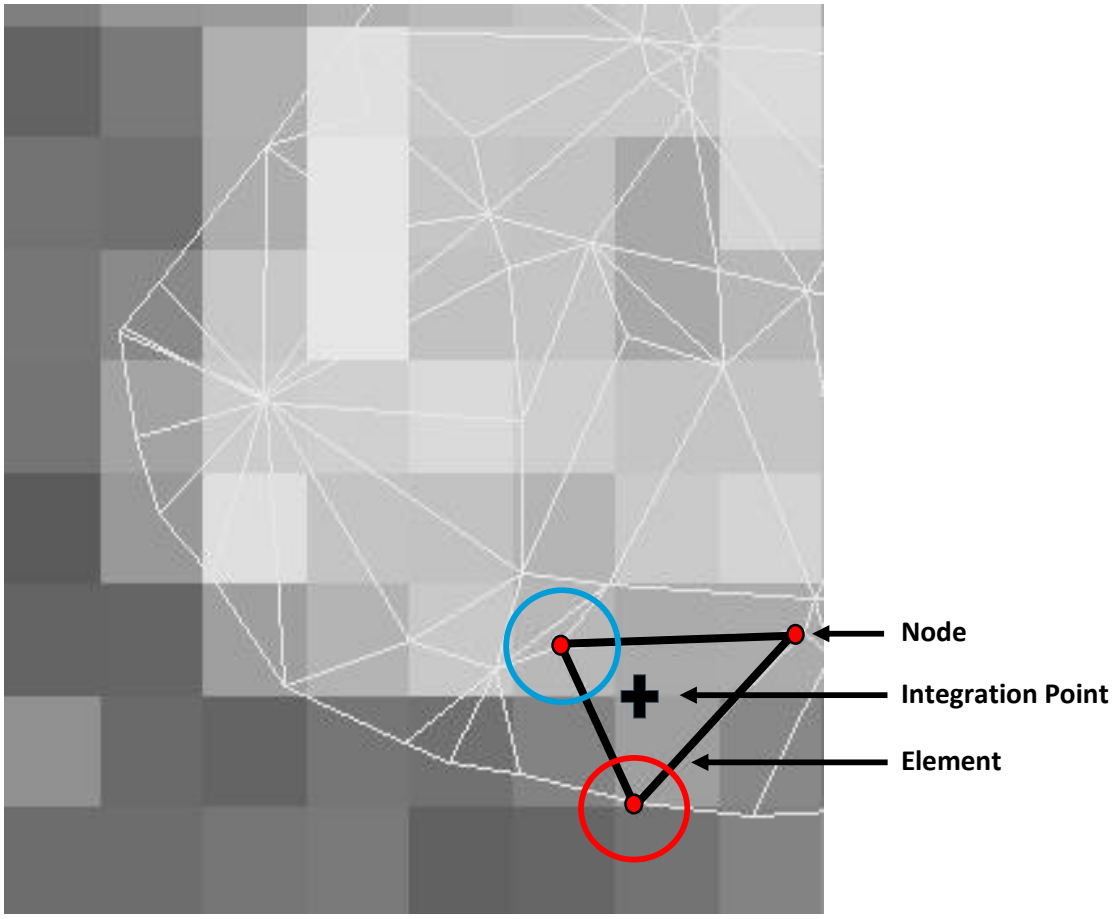

Figure 1.13: A tetrahedral mesh overlaid on native CT voxels

To account for partial volume effect, if the outer surface node (red circle) has a lower assigned modulus than its nearest internal neighbour (blue circle), the modulus of the internal node is assigned to the outer node.

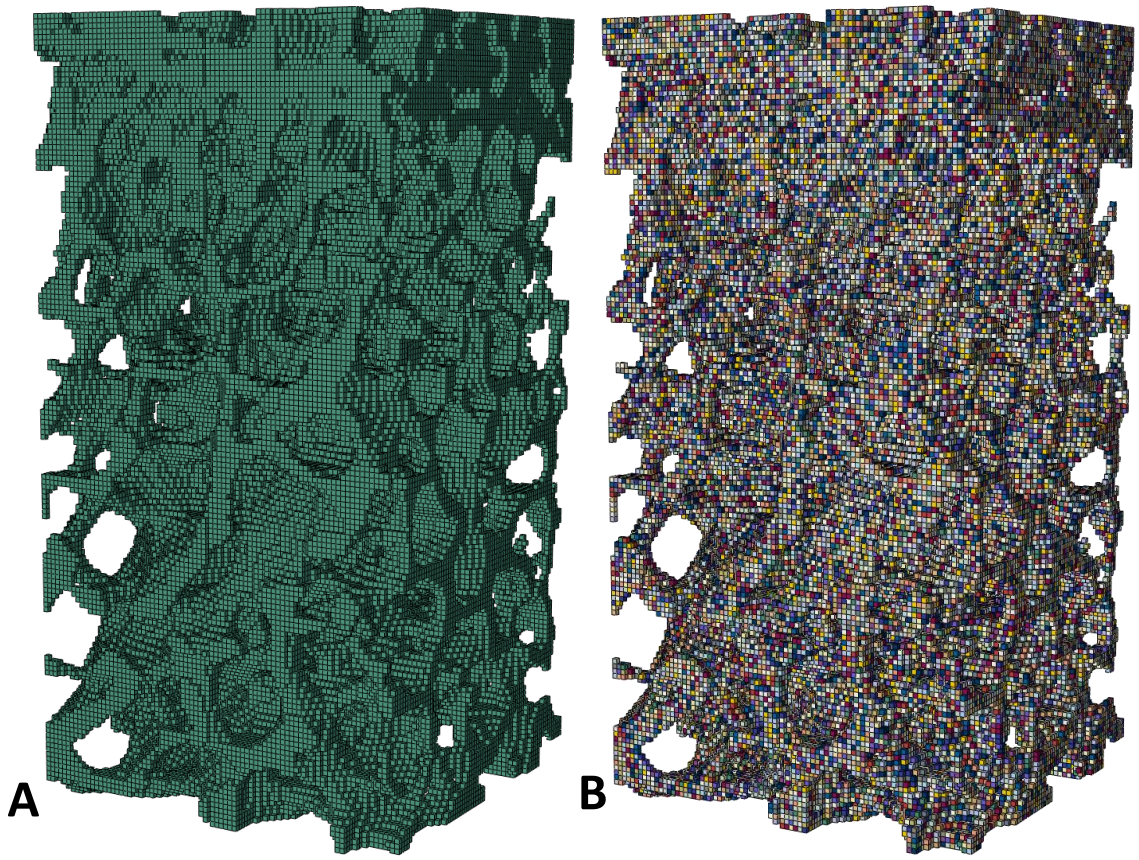

Figure 1.14: Trabecular micro-FEMs with homogeneous (A) or heterogeneous (B) element-wise material properties

assign relationships based on HA content. Although less common, micro-FEMs can be generated with tetrahedral elements and elemental or nodal material mapping strategies.

1.4 EXPERIMENTAL VALIDATION METHODS

A variety of experimental validation methods exist in biomechanics research, with validations primary being performed *in-vitro*, using cadaveric whole bones or small trabecular or cortical core samples taken from various anatomic locations of cadavers. These samples are not limited to cadavers, and the cores (*i.e.*, biopsies) can also be extracted from patients undergoing surgical procedures. The testing methods used provide either local measurements of strain (strain gauges and extensometers), global measures of stiffness, surface displacements and/or strains (digital image correlation – DIC), or full-field displacement and/or strain (digital volume correlation – DVC). Although each method has its advantages and disadvantages, the method chosen for experimental validation of computational models should produce a metric that is equivalent to the output of the computational model. A thorough literature review of the primary testing methods used in bone biomechanical studies was reported by Grassi and Isaksson (2015) – a summary of these methods is provided below.

1.4.1 Stiffness

Bone stiffness measurements are one of the simplest methods of comparing experimental and computational models. Experimentally, this is generally performed by preparing a cadaveric specimen for loading within a hydraulic mechanical or electromechanical material testing frame. For whole bones, the bone is often potted in polymethylmethacrylate (PMMA) bone cement for ease of securing to the testing frame. For bone cores, the ends of the sample can either be potted in PMMA, brass end caps (Keaveny et al., 1994), or compressed between two parallel platens (Helgason et al., 2008a). The actuator of the testing frame applies a tensile, compressive, or torsional load to the sample. A load cell is used to measure the reaction loads and a linear variable displacement transducer (LVDT) measures the displacement of the actuator – rotational variable displacement transducer (RVDT) in the case of torsion. Strain rate is an important consideration during these test, and multiple samples may be loaded with

various strain rates to determine variations. Additionally, because this method uses a machine-mounted load cell and LVDT for force and displacement measurements, machine compliance must be accounted for and used to correct the measured mechanical properties – especially in samples with high stiffness.

1.4.2 Strain Gauges

Strain gauges used in biomechanics date back to the mid-1940's (Gurdjian et al., 1945) and have since become one of the most common methods of experimental strain measurement, providing the gold standard in bone biomechanics (Grassi and Isaksson, 2015). Strain gauges measure changes in voltage or current as the result of resistance changes that occur in a circuit when a portion of its conductive path extends or contracts. Uni-axial strain gauges can be used to determine strains in a single direction, while strain rosettes measure strain in three directions, allowing for the determination of principal strains and their orientations (Grassi and Isaksson, 2015). The main limitation of strain gauges is that they only provide a localized measure of strain on the surface of the outer cortical shell. The non-uniform geometry of bone creates a difficult medium for the attachment of strain gauges. The review by Grassi and Isaksson (2015) provides an excellent overview of the literature in the optimal methods of attaching strain gauges in bone biomechanical studies. Combined with the difficulty in gauge placement and attachment, bone consists of a heterogeneous distribution of material properties that may cause large strain errors for even slight variations in material properties along the length of the gauge. When comparing strains collected experimentally with computational models, it is essential that variations in material are consistent between models and that the strains extracted computationally are extracted in a method that is consistent with the strain output measured experimentally.

1.4.3 Extensometers

The use of extensometers in bone biomechanics have been reported since the early 1950's (Dempster and Liddicoat, 1952). Extensometers provide a local measure of strain by measuring length changes between two fixed ends. In bone biomechanics, these are mainly utilized for testing small trabecular or cortical bone cores within a material testing frame. Two or four extensometer setups minimize the variation in length that may occur in

different regions of the sample (Helgason et al., 2008a). Extensometers with attachment to brass end-caps still provides a gold standard in bone core experimental strain measurement under tensile and compressive loading (Keaveny et al., 1994; Morgan and Keaveny, 2001).

1.4.4 Digital Image Correlation (DIC)

Digital image correlation (DIC) improves surface strain measurements by allowing for full-field surface displacements and strains, instead of localized measures. DIC uses variations in the patterns of digital images taken during pre- and post-loaded states to determine displacement fields. The transformation field between images is determined by maximizing a correlation coefficient, while the images are compared based on pixel intensity variations between states. The accuracy of DIC is dependent on image subset area, pixel shift used to calculate the strain field and image post-processing parameters, such as smoothing and filtering (Grassi and Isaksson, 2015). This method is better than strain gauge or extensometer methods when validating computational models, because the full-field surface measurements can be compared directly to surface node displacements and strains obtained computationally. DIC provides a cost-effective method of increasing the comparative data between models but is still limited to surface displacements and strains.

1.4.5 Digital Volume Correlation (DVC)

Digital volume correlation (DVC) is an extension of DIC and was first reported by (Bay et al., 1999). In DVC, minimization functions are solved on a 3D-subset using intensity variations in the pre- and post-loaded states of the naturally occurring patterns that exist within bone micro-structure. In the review by (Roberts et al., 2014), the main parameters influencing accuracy of DVC are reported. Subset size is the most important parameter affecting measurement precision, a global correlation approach reduces errors compared to local approaches and due to the reliance on the naturally occurring micro-structure of bone, variations in bone micro-structure may influence accuracy and precision.

In this thesis, the software BoneDVC was used to quantify experimental full-field displacements of cadaveric scapulae from micro-CT scans while under varying loads (Chapter 6). BoneDVC is global DVC software that computes a full-field displacement map by superimposing grids on images of the pre- and post-loaded states. The equations

representing deformations are solved at the nodal locations of the grid with intensity and weighting functions to improve accuracy (Dall'Ara et al., 2017, 2014).

1.4.6 Summary of QCT-FEM Experimental Validation Studies

This section provides a summary of QCT-derived FEM studies and the experimental validation metrics used (Table 1.1). Although this is not an exhaustive list of all QCT-based FEM studies in the literature, it is apparent that although significant work has been done in implementing the most contemporary methods of bone density extraction in FEM generation and experimental validation in the femur and spine, a paucity of studies utilizing these methods in alternate anatomic locations exist.

Table 1.1: Summary of QCT-Based Finite Element Studies in the Literature

Author, Year	Anatomic Location	Phantom Type	Densitometric Relationship (g/cm^3)	Density-Modulus Relationship (MPa)	Validation Metric	Peak Voltage (kVp)	Tube Current (mA)/ Time Product (mAs)	Voxel Size (mm)
(Tarala et al., 2011)	Femur	HA	$\rho_{HA} = \rho_{ash}$	NR	Displacement CLS Stem $R^2 = 0.95$ EPOCH Stem $R^2 = 0.88$	NR	NR	NR
(Cong et al., 2011)	Femur	K_2HPO_4	$\rho_{ash} = \rho_{K2HPO4} = -0.009 + 0.0007 * HU$ $\rho_{ash}/\rho_{app} = 0.6$[a]	$E = 14664\rho_{ash}^{1.49}$; $E = 10500\rho_{ash}^{2.29}$ $E = 17546\rho_{ash}^{3}$ $E = 8050\rho_{ash}^{1.16}$ $E = 15000e^{-4.91^{e-2.63\rho ash}}$ $E = 20000e^{-5.19e^{-2.10\rho ash}}$ $E = 55000e^{-5.40e^{-2.63\rho ash}}$	Axial Stiffness $R^2(y=x) = -1.40$ $R^2(y=x) = -4.97$ $R^2(y=x) = -6.93$ $R^2(y=x) = 0.50$ $R^2(y=x) = 0.71$ $R^2(y=x) = 0.69$ $R^2(y=x) = 0.69$	120	216 mAs	0.40 x 0.45 x 0.45
(Dragomir-Daescu et al., 2011)	Femur	K_2HPO_4	$\rho_{ash} = \rho_{K2HPO4} = -9*10^{-3} + 7*10^{-4}*HU$ $\rho_{ash}/\rho_{app} = 0.6$[a]	$E = 14664\rho_{ash}^{1.49}$	Axial Stiffness ($R^2 = 0.87$) Ultimate Load ($R^2 = 0.93$)	120	216 mAs	0.40 x 0.30 to 0.45 x 0.30 to 0.45
(Keyak et al., 2011)	Femur	HA	NR	NR	NR	120	140 mAs	NR
(Trabelsi and Yosibash, 2011)	Femur	K_2HPO_4	$\rho_{ash} = 1.22\rho_{k2HPO4} + 0.0523$[b]	$E_{cort} = 10200\rho_{ash}^{2.01}$ $E_{trab} = 5307\rho_{ash} + 469$	Strain Experimental ($R^2 = 0.982$) MM-based ($R^2 = 0.939$)	NR	NR	NR
(Trabelsi et al., 2011)	Femur	K_2HPO_4	$\rho_{ash} = 1.22\rho_{k2HPO4} + 0.0523$[b]	$E_{cort} = 10200\rho_{ash}^{2.01}$ $E_{trab} = 5307\rho_{ash} + 469$	Local Displacement ($R^2 = 0.871$) Strain ($R^2 = 0.951$) Axial Stiffness ($R^2 = 0.619$)	120	90 mAs	1.0 x 0.488 to 0.547 x 0.488 to 0.547

(Amin et al., 2011)	Femur	European Spine Phantom	NR	NR	NE	NR	NR	2.5 x 0.74 x 0.74
(Op Den Buijs and Dragomir-Daescu 201)	Femur	K_2HPO_4	$\rho_{ash} = \rho_{K2HPO4} = 7.0*10^{-4}HU$[c]	$E = 29800\rho_{ash}^{1.56}$	Axial Stiffness ($R^2 = 0.76$) Strength ($R^2 = 0.71$)	120	216 mA	0.40 x 0.29 to 0.41 x 0.29 to 0.41
(Koivumäki et al., 2012a)	Femur	HA	$\rho_{ash} = \rho_{HA}$	$E = 10095\rho_{ash}$	Fracture Load ($R^2 = 0.87$)	120	100 mAs	0.75 x 0.25 x 0.25
(Shim et al., 2012)	Femur	NR	NR	$E = 6750.3\rho_{ash}^{2.01}$	NE	NR	NR	NR
(Gong et al., 2012)	Femur	HA	ρ_{HA} to ρ_{app} and converted to ρ_{ash}[d] – Equation NR	$E = 0.001$ for $\rho_{ash} = 0$ $E = 33900\rho_{ash}^{2.20}$ for $0 < \rho_{ash} < 0.27$ $E = 5307\rho_{ash} + 469$ for $0.27 < \rho_{ash} < 0.60$ $E = 10200\rho_{ash}^{2.01}$ for $\rho_{ash} > 0.60$	NE	80	280 mA	2.5 x 0.9375 x 0.9375
(Tomaszewski et al., 2012)	Femur	HA	$\rho_{ash} = 0.0633 + 0.887\rho_{HA}$[e]	NR but referenced	NE	NR	NR	NR
(Keaveny et al., 2012)	Femur	K_2HPO_4	NR	NR but referenced	NE	80	280 mAs	3.0 x 0.78 to 0.94 x 0.78 to 0.94
(Koivumäki et al., 2012b)	Femur	HA	NR	NR	Fracture Load ($R^2 = 0.73$)	120	100 mAs	0.75 x 0.25 x 0.25
(Ruess et al., 2012)	Femur	NR	$\rho_{qct} = 10^{-3}*(0.793)*HU$ $\rho_{ash} = 1.22\rho_{K2HPO4} + 0.0523$[b]	$E_{cort} = 10200\rho_{ash}^{2.01}$ $E_{trab} = 5307\rho_{ash} + 469$	Strain ($R^2 = 0.918–0.981$) See paper for specifics by method	120	250 mAs	1.25 x 0.195 x 0.195
(Eberle et al., 2013a)	Femur	K_2HPO_4	$\rho_{ash} = 1.22\rho_{K2HPO4} + 0.0523$[b] $\rho_{HA} = 1.15\rho_{K2HPO4} – 0.0073$[f] $\rho_{ash} = 0.8772\rho_{HA} + 0.0789$ $\rho_{app} = 1.58\ \rho_{ash} + 0.00011$	$E = 10200\rho_{ash}^{2.01}$ $E = 6850\rho_{app}^{1.49}$ $E = 15100\rho_{K2HPO4}^{2.225}$ Displacement (μm) $E = 10200\rho_{ash}^{2.01}$ $E = 6850\rho_{app}^{1.49}$ $E = 15100\rho_{K2HPO4}^{2.225}$ Axial Stiffness $E = 10200\rho_{ash}^{2.01}$ $E = 6850\rho_{app}^{1.49}$ $E = 15100\rho_{K2HPO4}^{2.225}$	Strain Bland-Altman (mean) 9% Bland-Altman (mean) 11% Bland-Altman (mean) 7.9% Bland-Altman (mean) 21% Bland-Altman (mean) 23% Bland-Altman (mean) 1.6% Bland-Altman (mean) 16% Bland-Altman (mean) 2.6% Bland-Altman (mean) 9.6%	120	90 mAs	1.0 x 0.547 x 0.547 OR 1.0 x 0.488 x 0.488

(Eberle et al., 2013b)	Femur	K_2HPO_4	$\rho_{ash} = 1.22\rho_{K2HPO4} + 0.0523$[b] $\rho_{HA} = 1.15\rho_{K2HPO4} - 0.0073$[f] $\rho_{ash} = 0.8772\rho_{HA} + 0.0789$ $\rho_{app} = 1.58\ \rho_{ash} + 0.00011$	$E = 12486\rho_{K2HPO4}^{1.16}$ $E = 8346\rho_{app}^{1.50}$ $E = 8050\rho_{ash}^{1.16}$ $E = 25000e^{-5.40e^{\wedge}-2.10\rho ash}$ $E = 6850\rho_{app}^{1.49}$ $E = 12486\ \rho_{K2HPO4}^{1.16}$ $E = 8346\rho_{app}^{1.50}$ $E = 8050\rho_{ash}^{1.16}$ $E = 25000e^{-5.40e^{\wedge}-2.10\rho ash}$ $E = 6850\rho_{app}^{1.49}$ $E = 12486\ \rho_{K2HPO4}^{1.16}$ $E = 8346\rho_{app}^{1.50}$ $E = 8050\rho_{ash}^{1.16}$ $E = 25000e^{-5.40e^{\wedge}-2.10\rho ash}$ $E = 6850\rho_{app}^{1.49}$	Strain Relative Error (mean) 5% Relative Error (mean) 28% Relative Error (mean) 18% Relative Error (mean) 16% Relative Error (mean) 12% Displacement Relative Error (mean) 10% Relative Error (mean) 40% Relative Error (mean) 3% Relative Error (mean) 29% Relative Error (mean) 26% Stiffness Relative Error (mean) 6% Relative Error (mean) 56% Relative Error (mean) 6% Relative Error (mean) 31% Relative Error (mean) 28%	120	90 mAs	1.0 x 0.547 x 0.547 OR 1.0 x 0.488 x 0.488
(Haider et al., 2013)	Femur	K_2HPO_4	$\rho_{ash} = 0.00106\rho_{K2HPO4} + 0.0389$[g] $\rho_{ash}/\rho_{app} = 0.6$[b]	$E = 6850\rho_{app}^{1.49}$	NE	NR	NR	0.5 x 0.49 x 0.49
(Dall'Ara et al., 2012)	Femur	HA	BMD to BV/TV from µCT	Relation to BV/TV – Equation NR	Axial Stiffness Stance: $R^2 = 0.449$ Side: $R^2 = 0.869$	120	100 mAs	1.0 x 0.33 x 0.33
(Nishiyama et al., 2013)	Femur	HA	$\rho_{ash} = \rho_{HA}$	$E = 10500\rho_{ash}^{2.29}$	Axial Stiffness $R^2 = 0.89$ Failure Load $R^2 = 0.81$	120	60 mAs	0.625 x 0.439 x 0.439
(Kersh et al., 2013)	Femur	HA	BV/TV = 9.3BMD + 3 from µCT[h]	NR	NE	120	100 mA	0.60 x 0.36 x 0.36
(Keyak et al., 2013)	Femur	HA	$\rho_{ash} = 0.0633 + 0.887\rho_{HA}$[i]	$E_{trab} = 14900\rho_{ash}^{1.86}$	NE	120	140 mAs	NR
(Hambli and Allaoui, 2013)	Femur	HA	$\rho_{HA} = 6.932*10^{-4}HU - 5.68*10^{-4}$ $\rho_{ash} = 1.22\rho_{K2HPO4} + 0.0523$[b]	$E = 33900\rho_{ash}^{2.20}$ for $0 < \rho_{ash} < 0.27$ $E = 5307\rho_{ash} + 469$ for $0.27 < \rho_{ash} < 0.60$ $E = 10200\rho_{ash}^{2.01}$ for $\rho_{ash} > 0.60$	Fracture Load $R^2 = 0.943$	120	160 mAs	0.70 x 0.25 x 0.25

(Carballido-Gamio et al., 2013)	Femur	HA & K_2HPO_4	NR	NR	NE	NR	NR	2.5 x 0.74 x 0.74 & 1.0 x 0.98 x 0.98
(Nishiyama et al., 2014)	Femur	HA & K_2HPO_4	$\rho_{ash} = \rho_{HA}$	$E = 10500\rho_{ash}^{2.29}$	NE	120	250 mAs	0.50 x 0.625 x 0.625
(Luisier et al., 2014)	Femur	HA	BMD to BV/TV from µCT[j]	$E_o = 6614$	Ultimate Force Stance: $R^2 = 0.797$ Side: $R^2 = 0.842$	120	100 mA	1.0 x 0.33 x 0.33
(Enns-Bray et al., 2014)	Femur	NR	$\rho_{ash} = \rho_{qCT}$	$E_3 = 10500*\rho_{ash}^{2.29}$ See paper for anisotropic modulus	Axial Stiffness Anisotropic: $R^2 = 0.783$ Isotropic: $R^2 = 0.792$ Ultimate Strength Anisotropic: $R^2 = 0.355$ Isotropic: $R^2 = 0.350$	120	60 mAs	0.625 x 0.625 x 0.625
(Anez-Bustillos et al., 2013)	Femur	HA	NR	Experimentally derived	Axial Rigidity $R^2 = 0.82$ Bending Rigidity $R^2 = 0.86$ Failure Load $R^2 = 0.89$	120	220 mA	3.0 x 0.9375 x 0.9375
(Mirzaei et al., 2014)	Femur	K_2HPO_4	$\rho_{ash} = 1.22\rho_{K2HPO4} + 0.0526$[b]	$E = 33900\rho_{ash}^{2.20}$ for $0 < \rho_{ash} < 0.27$ $E = 5307\rho_{ash} + 469$ for $0.27 < \rho_{ash} < 0.60$ $E = 10200\rho_{ash}^{2.01}$ for $\rho_{ash} > 0.60$	Load $R^2 = 0.809 – 0.886$ See paper for specifics by method	140	80 mAs	1.0 x 0.50 x 0.50
(Arachchi et al., 2015)	Femur	HA	NR	NR	NE	140	206 mAs	2.0 x 0.29 x 0.29
(Kheirollahi and Luo, 2015)	Femur	NR	$\rho_{ash} = 0.04162 + 0.000854HU$	$E = 10500\rho_{ash}^{2.29}$	NE	NR	NR	NR
(Carballido-gamio et al., 2015)	Femur	Both	vBMD reported	NR	NE	NR	NR	2.0 x 0.742 x 0.742 OR 2.5 x 0.938 x 0.938 OR 1.0 x 0.977 x 0.977
(Kaneko et al., 2015)	Femur	HA	$\rho_{ash} = \rho_{HA}$	NR	NE	120	80 mA	NR
(Qasim et al., 2016)		HA & K_2HPO_4	$\rho_{ash} = 0.8772\rho_{HA} + 0.0789$ $\rho_{ash} = 0.6\ \rho_{app}$[g]	$E = 6950\rho_{app}^{1.49}$	See paper for specifics by method	120	80 to 200 mA	0.74 x 0.74 x 0.625

(Oftadeh et al., 2016)	Femur	HA	$\rho_{ash} = 0.0633 + 0.887\rho_{HA}$[i]	Specifics NR, but referenced	Multiple – See paper	120	220 mA	0.9375 x 0.9375 x 3.0
(Michalski et al., 2017)	Femur	HA	ρ_{HA} related to HU NR, but ρ_{HA} to ρ_{ash} using relatonship[n]	$E = 10500\rho_{ash}^{2.29}$	NE	120	280 mAs	0.352 x 0.352 x 1.0
(Varghese et al., 2011)	Femur, Tibia, Humerus, Radius	K_2HPO_4	NR	NR	Strain $R^2 = 0.61 – 0.99$ See paper for specifics by method	80	200 mAs	0.625 x 0.625 x 0.625
(Kopperdahl et al., 2014)	Spine & Femur	HA	BMD related to HU	NR	NE	120	150 mAs	Spine: 1.0 x 1.0 x 1.0 Femur: 1.5 x 1.5 x 1.5
(Kleerekoper et al., 2014)	Spine & Femur	NR	NR	NR	NE	NR	NR	NR
(Keaveny et al., 2014)	Spine & Femur	HA	NR	NR	NE	120	Femur: 170 mAs Spine: 100 mAs	NR
(Zeinali et al., 2010)	Spine	K_2HPO_4	BMD related to HU	$E_z = -34.7+3230\rho_{qct}$ $E_z = -2980\rho_{qct}^{1.05}$ $E_x = E_y = 0.333E_z$	Strength Linear elastic-plastic $R^2 = 0.937$ Linear elastic-perfectly plastic $R^2 = 0.855$ Linear elastic $R^2 = 0.831$ Min. sectional $R^2 = 0.863$	140	400 mA	1.0 x 0.25 x 0.25
(Tawara et al., 2010)	Spine	HA	$\rho_{app} = 0.0$ (HU < −1) $\rho_{app} = (0.733HU + 4.51)*10^{-3}$ (−1≤HU)	E = 0.001 for $\rho_{ash} = 0$ $E = 33900\rho_{ash}^{2.20}$ for $0 < \rho_{ash} < 0.27$ $E = 5307\rho_{ash} + 469$ for $0.27 < \rho_{ash} < 0.60$ $E = 10200\rho_{ash}^{2.01}$ for $\rho_{ash} > 0.60$	NE	120	NR	1.0 x 0.39 x 0.39
(Unnikrishnan and Morgan, 2011)	Spine	HA	ρ_{qct} based	$E_{zz} = -34.7 + 3.230\rho_{qct}$ $E_{xx} = E_{yy} = 0.333$	NE	120	240 mA	0.625 x 0.31 x 0.31

(Christiansen et al., 2011)	Spine	HA	ρ_{qct} based	NR	NE	120	100 to 360 mAs	2.5 x 0.68 x 0.68
(Imai, 2011)	Spine	HA	$\rho_{ash} = \rho_{HA}$	E_{cort} = 10000	NE	120	360 mA	2.0 x 0.35 x 0.35
(Dall'Ara et al., 2012)	Spine	K_2HPO_4	BV/TV using the relationships BV/TV = 0 for BMD < -100 BV/TV = 0.0942*BMD-0.0297 for -100 < BMD < 1061 BV/TV = 1061 for BMD >1061	E = 8780	Strength hFE: R^2 = 0.79 Failure Load hFE: R^2 = 0.78	120	100 mA	0.45 x 0.39 x 0.39
(Wang et al., 2012)	Spine	HA	vBMD based	NR	Strength R^2 = 0.85	120	150 mAs	NR
(Unnikrishnan et al., 2013)	Spine	HA	BMD related to HU	$E_z = -34.7+3230\rho_{qct}$ $E_z = -2980\rho_{qct}^{1.05}$ ρ_{qct} = 0.0527g/cc $E_x = E_y = 0.333E_z$	NE	120	240 mA	0.625 x 0.3125 x 0.3125
(Y. Lu et al., 2014)	Spine	HA & K_2HPO_4	NR	NR	NE	120	360 mAs	0.60 x 0.32 x 0.32 OR 0.30 x 0.18 x 0.18
(Matsuura et al., 2014)	Spine	K_2HPO_4	$\rho_{ash} = \rho_{K2HPO4}$	ρ_{ash} = 0: E = 0.001 $\rho_{ash} > 0$: $E = 1890\ \rho_{ash}^{1.92}$	Fracture Load R^2 = 0.78 Axial Stiffness R^2 = 0.39	120	210 mA	0.40 x 0.30 x 0.30
(Lu et al., 2014)	Spine	HA	BMD related to HU	$E_z = 2980(\rho_{qct}/1000)^{1.05}$ for ρ_{qct} < 52.7 mg_{HA}/cc E_z = = -34.7+3230ρ_{qct} for ρ_{qct} > 52.7 mg_{HA}/cc	NE	90 & 120	100 & 150 mAs	1.3 x 0.30 x 0.30
(Campbell et al., 2017)	Spine	HA	BMD related to HU	NR but, based on Elastic-perfectly plastic behavior[o]	NE	120	100 mAs	0.234 x 0.234 x 1.5
(Anitha et al., 2017)	Spine	HA & K_2HPO_4	$\rho_{app} = 47 + 1.122*HU^m$ $\rho_{ash} = 0.6\ \rho_{app}^g$	$E_z = -349+5.82\rho_{app}$ $E_x = E_y = 0.333E_z$	Fracture Load R^2 = 0.85	120	585 mAs & 78 mA	0.25 x 0.25 x 0.6 OR 0.977 x 0.977 x 0.67

(Hussein et al., 2018)	Spine	HA	BMD related to HU	$E_z = -34.7+3230\rho_{qct}$	Axial Displacement $R^2 = 0.018 – 0.658$	120	210 mA	0.32 x 0.32 x 0.625
(Campoli et al., 2014)	Scapula	NR	$\rho_{app} = HU + 0.00039$	$E = 6850\rho_{app}^{1.49}$	NE	NR	NR	0.6 x 0.6 x 0.6
(Pomwenger et al., 2014)	Scapula	NR	$\rho_{app} = 1.1187*10^{-3}*HU^k$ assumed $\rho_{app} = 0$ no bone & $\rho_{app} = 1.8$ for bone	$E = 1049.45\rho_{app}^2$ $\rho_{app} < 0.35$ $E = 3000\rho_{app}^3$ $\rho_{app} > 0.35$	NE	NR	NR	NR
(Hermida, 2014)	Scapula	K_2HPO_4	NR	$E_{cort} = 20000$	NE	NR	NR	NR
(Knowles et al., 2018)	Scapula	K_2HPO_4	ρ_{K2HPO4} related to HU	$E = 12486\rho_{K2HPO4}^{1.16}$	NE	120	144 mAs	0.488 to 0.639 x 0.488 to 0.639 x 1.25
(Edwards et al., 2013)	Tibia	HA	ρ_{HA} = BMD $\rho_{app}/\rho_{HA} = 0.626$	$E_3 = 6570\rho_{app}^{1.37}$ $E_{min} = 0.01$ $E_1 = 0.574E_3$ $E_2 = 0.577E_3$	Rotational Stiffness $R^2 = 0.920$ Ultimate Strength $R^2 = 0.753$	120	200 mA	0.625 x 0.352 x 0.352
(Nazemi et al., 2015)	Tibia	K_2HPO_4	$\rho_{ash} = 0.55\ \rho_{app}$[g] $\rho_{ash}=0.597\rho_{dry}$[g] $\rho_{real} = 1.8$ g/cc[l] $\rho_{app}=\rho_{real}*BV/TV$ $BMD = 0.904\rho_{ash} – 0.0321$[g] $\rho_{ash} = 1.06*BMD + 0.0389$[g]	 $E = 15520\rho_{app}^{1.93}$ $E = 6570\rho_{app}^{1.37}$ $E = 33200\rho_{ash}^{2.2}$ $E = 4778\rho_{app}^{1.99}$ $E = 3311\rho_{dry}^{1.66}$ $E = 3890\rho_{dry}^2$ $E = 6310(BV/TV)^{2.1}$	Axial Stiffness $R^2 = 0.75$ $R^2 = 0.65$ $R^2 = 0.70$ $R^2 = 0.69$ $R^2 = 0.67$ $R^2 = 0.69$ $R^2 = 0.70$	120	150 mAs	0.5 x 0.5 x 0.5
(Nazemi et al., 2017b)	Tibia	K_2HPO_4	$\rho_{ash} = 0.55\ \rho_{app}$[g] $\rho_{ash}=0.597\rho_{dry}$[g] $\rho_{real} = 1.8$ g/cc[l] $\rho_{app}=\rho_{real}*BV/TV$ $BMD = 0.904\rho_{ash} – 0.0321$[g]	 $E = 15520\rho_{app}^{1.93}$ $E = 6570\rho_{app}^{1.37}$ $E = 33200\rho_{ash}^{2.2}$ $E = 4778\rho_{app}^{1.99}$ $E = 3311\rho_{dry}^{1.66}$ $E = 3890\rho_{dry}^2$ $E = 6310(BV/TV)^{2.1}$ $E_{cort} = 13000\rho_{app} – 3842$ $E_{cort} = 3891\rho_{app}^{2.39}$	Axial Stiffness $R^2 = 0.59$ OR $R^2 = 0.53$ $R^2 = 0.65$ OR $R^2 = 0.60$ $R^2 = 0.65$ OR $R^2 = 0.61$ $R^2 = 0.69$ OR $R^2 = 0.66$ $R^2 = 0.72$ OR $R^2 = 0.68$ $R^2 = 0.71$ OR $R^2 = 0.69$ $R^2 = 0.74$ OR $R^2 = 0.73$	120	150 mAs	0.5 x 0.5 x 0.5

(Nazemi et al., 2017a)	Tibia	K_2HPO_4	$\rho_{ash} = 0.55\ \rho_{app}$[g] $\rho_{ash}=0.597\rho_{dry}$[g] $\rho_{real} = 1.8$ g/cc[l] $\rho_{app}=\rho_{real}$*BV/TV $BMD = 0.904\rho_{ash} - 0.0321$[g]	$E = 6310(BV/TV)^{2.1}$ $E_{cort} = 13000\rho_{app} - 3842$ $E_{cort} = 3891\rho_{app}^{2.39}$	Axial Stiffness $R^2 = 0.75$ $R^2 = 0.77$	120	150 mAs	0.5 x 0.5 x 0.5
McErlain et al., 2011)	Knee	SB3	NR	NR	NE	90	40 mAs	NR
(Dahan et al., 2016)	Humerus	K_2HPO_4	$\rho_{qct} = (0.816*HU+6)*10^{-3}$ OR $\rho_{qct} = (0.807*HU-1.6)*10^{-3}$ $\rho_{ash} = 0.6\rho_{app}$[a]	$E_{cort} = 10200\rho_{ash}^{2.01}$ $\rho_{ash} > 0.486$ $E_{trab} = 2398$ $0.3 < \rho_{ash} > 0.486$ $E_{trab} = 33900\rho_{ash}^{2.2}$ $\rho_{ash} < 0.486$	Strain $R^2 = 0.982$	120	250mAs	0.2 x 0.2 x 1.25
(Synek et al., 2015)	Radius	NR	BMD to BV/TV from µCT	Multiple – Refer to paper	Axial Stiffness Isotropic-Homogeneous $R^2 = 0.500$ Isotropic-Heterogeneous $R^2 = 0.816$ Orthotropic-Heterogeneous $R^2 = 0.807$	140	260 mA	0.63 x 0.20 x 0.20

HA – Hydroxyapatite; K_2HPO_4 – Dipotassium Phosphate; NR- Not Reported; BMD – Bone Mineral Density; BV/TV – Bone Volume/Total Volume; NE – No Experimental; [a](Schileo et al., 2008); [b](Les et al., 1994); [c](Suzuki et al., 1991); [d](Keyak et al., 1997); [e](Keyak et al., 2005); (Faulkner et al., 1993); [g](Keyak et al., 1994a); [h](Dall'Ara et al., 2011); [l](Keyak et al., 2005); [j](Pahr and Zysset, 2009); [k](Gupta and Dan, 2004); [l](Carter and Hayes, 1977); [m](Rho et al., 1995); [n](Kaneko et al., 2004); [o](Keyak, 2001); [p](Goodsitt, 1992)

1.5 THESIS RATIONALE

Computed tomography (CT) data provides invaluable insight in the assessment of bone quality due to the inherent imaging principles. Using this data as input allows for the generation of subject-specific finite element models (FEMs) that provide the basis of many biomechanical studies. The cost-effective nature of FEMs allow for various factors to be assessed in a parametric and systematic manner, not possible with *in-vitro* or *in-vivo* testing methods. Although FEMs are useful, the underlying assumptions (i.e. boundary conditions and material mapping) require validation. While extensive work has been done in validating FEMs of the femur and spine (Helgason et al., 2008a; Knowles et al., 2016), relatively little attention has been given to validating FEMs of the shoulder. Site-specific relationships may increase the accuracy of subject-specific finite element models (Schileo et al., 2008), and although identified as an imminent need (Pomwenger et al., 2014), a validated glenohumeral model does not exist. Incorporating a glenohumeral site-specific relationship, and improving modeling parameters, would significantly improve computational biomechanical studies of the upper limb.

Furthermore, experimental validations of FEMs are only truly validated with respect to the outcome measure in which they are compared. Previous validations have been performed using strain gauges attached to the outer cortical shell of bones, axial stiffness (Enns-Bray et al., 2016; Helgason et al., 2016), or mechanical loading of small trabecular or cortical bone cores with the use of extensometers to measure apparent strain (Helgason et al., 2008a). Recent studies have suggested that misrepresenting boundary conditions has a significant impact on the mechanical response of bone at both the micro-level (Chen et al., 2017), and macro-level (Hussein et al., 2018; Jackman et al., 2015). Incorporating experimental full-field displacements in both the assigned boundary conditions and in the comparisons of experimental and computational models, has the potential to significantly improve the accuracy of FEMs and provide new methods of FEM validation.

Quantifying the variations in bone density and the associated mechanical properties between normal and osteoarthritic (OA) shoulders is also essential to understand the underlying mechanisms that compromise quality of life of individuals living with this

pathologic bone disease. By incorporating high-resolution density and structural variations, FEMs can be improved and adjusted to more accurately reflect this pathologic condition. With the majority of individuals undergoing surgical procedures, such as total shoulder arthroplasty, exhibiting some form of pathologic bone disease, it is essential to include these variations in properties for model accuracy.

1.6 OBJECTIVES AND HYPOTHESES

The overarching goal of this thesis was to improve the accuracy of glenohumeral joint computational simulations by providing validated glenohumeral-specific material mapping relationships. This requires a thorough understanding of the complex mineralization patterns that influence both the local density, bone architecture, and the associated mechanical properties. Although extensive work has been done in improving the accuracy of computational models in other anatomic locations, there has been a paucity of studies evaluating glenohumeral-specific modeling parameters. In order to improve our understanding of glenohumeral joint mechanical loading, and to improve glenohumeral joint simulations, six specific objectives were explored as part of this research. The associated hypothesis follows each objective.

Objective 1: To compare commonly used density-modulus relationships used in finite element modeling of the shoulder. The specific aims were to:

a. Develop a computational methodology to compare and assess quantitative-CT (QCT) derived finite element models (FEMs) to co-registered micro-CT derived FEMs based on mechanical loading;
b. Compare the ability of QCT-FEMs, with varying density-modulus relationships from the literature, to replicate the apparent strain energy density of each co-registered microFEM from glenoid trabecular bone.

Hypothesis 1: Due to the lack of a shoulder-specific density-modulus relationship, all relationships mapped the QCT-FEMs will have linear correlation coefficients below 0.8

and slopes deviating by greater than 0.2 from unity (Y=X), as related to the apparent strain energy density of the co-registered glenoid trabecular microFEMs.

Objective 2: To develop a glenoid-specific trabecular density-modulus relationship. The specific aims were to:

a. Develop a glenoid trabecular bone-specific density-modulus relationship by virtually loading micro-FEMs derived from glenoid trabecular bone;
b. Use the computational methodology described in Objective 1 to compare each derived density-modulus relationship to co-registered QCT-FEMs based on apparent strain energy density.

Hypothesis 2: A glenoid-specific trabecular density-modulus relationship will have linear correlation coefficients greater than 0.9 and a linear relationship near unity (Y=X) between microFEMs and co-registered QCT-FEMs mapped with the glenoid-specific relationship.

Objective 3: To study the effect of image down-sampling, element type and material heterogeneity on microFEM apparent modulus. The specific aims were to:

a. Generate glenoid trabecular microFEMs from images at 32-microns, 64-microns, and simulated 64-micron resolution down-sampled from the 32-micron scans;
b. Compare microFEMs generated with either quadratic tetrahedral or linear hexahedral element types;
c. Compare microFEMs generated with homogeneous or heterogeneous tissue moduli.

Hypothesis 3: MicroFEMs generated from 32-micron scans with tetrahedral elements, and accounting for material heterogeneity, will have lower errors in apparent modulus compared to the other combinations of resolution and element type.

Objective 4: To determine the effect of material mapping strategy on QCT-FEMs of trabecular bone. The specific aims were to:

a. Use the computational methodology described in Objective 1, and the glenoid trabecular density-modulus relationship developed in Objective 2, to compare QCT-FEMs with either linear tetrahedral, quadratic tetrahedral, or linear hexahedral element types;
b. Use the computational methodology described in Objective 1, and the glenoid trabecular density-modulus relationship developed in Objective 2, to compare QCT-FEMs with elemental material mapping of the native Hounsfield (HU) field, nodal material mapping of the native HU field, or nodal material mapping of the elastic modulus I field.

Hypothesis 4: QCT-FEMs mapped with quadratic tetrahedral or linear hexahedral elements will show no difference in the measured apparent modulus when mapped with either elemental or nodal material mapping strategies.

Objective 5: To compare scapular QCT-FEMs mapped with elemental or nodal material mapping strategies, and various density-modulus relationships, to full-field DVC measurements of experimentally loaded cadaveric scapulae within a micro-CT.

Hypothesis 5: Scapular QCT-FEMs generated with the elemental or nodal material mapping strategies, and the glenoid trabecular density-modulus relationship derived in Objective 1, will have the highest correlations with experimental DVC results.

Objective 6: To compare the morphometric and apparent mechanical properties of non-pathologic normal and end-stage osteoarthritic trabecular bone from excised humeral head osteotomies.

Hypothesis 6: End-stage osteoarthritic bone will exhibit significantly larger bone volume fraction and trabecular thickness, with contributive increases in apparent modulus, compared to non-pathologic normal bone.

1.7 THESIS OVERVIEW

Following this introduction, Chapter 2 compares six of the most commonly used density-modulus relationships used in finite element modeling of the shoulder. This chapter also describes a testing methodology, which uses microFEMs derived from co-registered images to compare finite element models (FEMs) derived from quantitative-CT (QCT). Chapter 3 describes the development of a glenoid trabecular density-modulus relationship using the methodology from Chapter 2. Chapter 4 explores the effect of down-sampling, element type, and material heterogeneity in microFEMs. Chapter 5 also uses the methodology from Chapter 2, to compare material mapping strategies and element types in trabecular QCT-FEMs. Chapter 6 presents experimental comparisons of cadaveric scapular models scanned within a micro-CT using digital volume correlation (DVC) to scapular QCT-FEMs with various material mapping strategies and density-modulus relationships. Chapter 7 uses micro-FEMs to compare trabecular morphometric parameters and apparent modulus of patient end-stage osteoarthritic bone versus cadaveric bone serving as the 'normal' cohort. The thesis concludes with a general discussion and conclusions in Chapter 8.

1.8 REFERENCES

Adams, J.E., 2009. Quantitative computed tomography. Eur. J. Radiol. 71, 415–424. Doi:10.1016/j.ejrad.2009.04.074

Aigner, T., McKenna, L., 2002. Molecular pathology and pathobiology of osteoarthritic cartilage. Cell. Mol. Life Sci. 59, 5–18. Doi:10.1007/s00018-002-8400-3

Aitken, G., Bourne, R., Research, Finlay J.B., Rorabeck C.H, 1985. Indentation stiffness of the cancellous bone in the distal human tibia. Clin. Orthop. Rel. Res.

Amin, S., Kopperdhal, D.L., Melton, L.J., Achenbach, S.J., Therneau, T.M., Riggs, B.L., Keaveny, T.M., Khosla, S., 2011. Association of hip strength estimates by finite-element analysis with fractures in women and men. J. Bone Miner. Res. 26, 1593–1600. Doi:10.1002/jbmr.347

Anez-Bustillos, L., Derikx, L.C., Verdonschot, N., Calderon, N., Zurakowski, D., Snyder, B.D., Nazarian, A., Tanck, E., 2013. Finite element analysis and CT-based structural

rigidity analysis to assess failure load in bones with simulated lytic defects. Bone 58, 160–167. Doi:10.1016/j.bone.2013.10.009

Arachchi, S., Pitto, R.P., Anderson, I.A., Shim, V.B., 2015. Analyzing bone remodeling patterns after total hip arthroplasty using quantitative computed tomography and patient-specific 3D computational models 5, 575–582. Doi:10.3978/j.issn.2223-4292.2015.08.03

Arden, N., Nevitt, M.C., 2006. Osteoarthritis: Epidemiology. Best Pract. Res. Clin. Rheumatol. 20, 3–25. Doi:10.1016/j.berh.2005.09.007

Bailey, A., Mansell, J., 1997. Do subchondral bone changes exacerbate or precede articular cartilage destruction in osteoarthritis of the elderly? Gerentology. 43(5), 296-304

Bay, B.K., Smith, T.S., Fyhrie, D.P., Saad, M., 1999. Digital volume correlation: Three-dimensional strain mapping using X-ray tomography. Exp. Mech. 39, 217–226. Doi:10.1007/BF02323555

Bini, F., Marinozzi, A., Marinozzi, F., Patanè, F., 2002. Microtensile measurements of single trabeculae stiffness in human femur. J. Biomech. 35, 1515–9.

Blanco, F.J., Guitian, R., Vazquez-Martul, E., de Toro, F.J., Galdo, F., 1998. Osteoarthritis chondrocytes die by apoptosis: A possible pathway for osteoarthritis pathology. Arthritis Rheum. 41, 284–289.

Bourne, B.C., Van Der Meulen, M.C.H., 2004. Finite element models predict cancellous apparent modulus when tissue modulus is scaled from specimen CT-attenuation. J. Biomech. 37, 613–621. Doi:10.1016/j.jbiomech.2003.10.002

Bouxsein, M.L., Boyd, S.K., Christiansen, B.A., Guldberg, R.E., Jepsen, K.J., Müller, R., 2010. Guidelines for assessment of bone microstructure in rodents using micro-computed tomography. J. Bone Miner. Res. 25, 1468–1486. Doi:10.1002/jbmr.141

Brandt, K.D., Dieppe, P., Radin, E.L., 2008. Etiopathogenesis of Osteoarthritis. Rheum. Dis. Clin. North Am. 34, 531–559. Doi:10.1016/j.rdc.2008.05.011

Brown, S.J., Pollintine, P., Powell, D.E., Davie, M.W.J., Sharp, C.A., 2002. Regional Differences in Mechanical and Material Properties of Femoral Head Cancellous Bone in Health and Osteoarthritis. Calcif. Tissue Int. 71, 227–234. Doi:10.1007/s00223-001-2102-y

Burkhart, T.A., Andrews, D.M., Dunning, C.E., 2013. Finite element modeling mesh quality, energy balance and validation methods: A review with recommendations associated with the modeling of bone tissue. J. Biomech. 46, 1477–1488. Doi:10.1016/j.jbiomech.2013.03.022

Burr, D., 1998. The importance of subchondral bone in osteoarthrosis. Curr. Opin. Rheumatol. 10(3), 256-262

Campoli, G., Bolsterlee, B., van der Helm, F., Weinans, H., Zadpoor, A. a, 2014. Effects of densitometry, material mapping and load estimation uncertainties on the accuracy of patient-specific finite-element models of the scapula. J. R. Soc. Interface 11, 20131146. Doi:10.1098/rsif.2013.1146

Carballido-gamio, J., Bonaretti, S., Saeed, I., Harnish, R., Recker, R., Andrew, J., Keyak, J.H., Harris, T., Khosla, S., Lang, T.F., 2015. Automatic multi-parametric quantification of the proximal femur with quantitative computed tomography 5, 552–568. Doi:10.3978/j.issn.2223-4292.2015.08.02

Carballido-Gamio, J., Harnish, R., Saeed, I., Streeper, T., Sigurdsson, S., Amin, S., Atkinson, E.J., Therneau, T.M., Siggeirsdottir, K., Cheng, X., Melton, L.J., Keyak, J.H., Gudnason, V., Khosla, S., Harris, T.B., Lang, T.F., 2013. Structural patterns of the proximal femur in relation to age and hip fracture risk in women. Bone 57, 290–299. Doi:10.1016/j.bone.2013.08.017

Carter, D., Hayes, W., 1977. The compressive behavior of bone as a two-phase porous structure. J. Bone Jt. Surg. 59(7), 954-962

Chappard, C., Peyrin, F., Bonnassie, A., Lemineur G., Brunet-Imbault, B., Lespessailles, E., Benhamour, C.L. 2006, Subchondral bone micro-architectural alterations in osteoarthritis: a synchrotron micro-computed tomography study. Osteoarthr. Cartil. 14(3), 215-223

Chen, G., Schmutz, B., Epari, D., Rathnayaka, K., Ibrahim, S., Schuetz, M. a., Pearcy, M.J., 2010. A new approach for assigning bone material properties from CT images into finite element models. J. Biomech. 43, 1011–1015. Doi:10.1016/j.jbiomech.2009.10.040

Chen, G., Wu, F.Y., Liu, Z.C., Yang, K., Cui, F., 2015. CoMParisons of node-based and element-based approaches of assigning bone material properties onto subject-

specific finite element models. Med. Eng. Phys. 000, 1–5. Doi:10.1016/j.medengphy.2015.05.006

Chen, Y., Dall'Ara, E., Sales, E., Manda, K., Wallace, R., Pankaj, P., Viceconti, M., 2017. Micro-CT based finite element models of cancellous bone predict accurately displacement once the boundary condition is well replicated: A validation study. J. Mech. Behav. Biomed. Mater. 65, 644–651. Doi:10.1016/j.jmbbm.2016.09.014

Choi, K., Goldstein, S.A., 1992. A coMParison of the fatigue behavior of human trabecular and cortical bone tissue. J. Biomech. 25, 1371–1381. Doi:10.1016/0021-9290(92)90051-2

Choi, K., Kuhn, J.L., Ciarelli, M.J., Goldstein, S.A., 1990. The Elastic Moduli of Human Subchondral Trabecular and Cortical Bone Tissue. J. Biomech. 23, 1103–1113. Doi:10.1016/0021-9290(90)90003-L

Christiansen, B.A., Kopperdahl, D.L., Kiel, D.P., Keaveny, T.M., Bouxsein, M.L., 2011. Mechanical contributions of the cortical and trabecular coMPartments contribute to differences in age-related changes in vertebral body strength in men and women assessed by QCT-based finite element analysis. J. Bone Miner. Res. 26, 974–983. Doi:10.1002/jbmr.287

Ciarelli, M.J., Goldstein, S. a, Kuhn, J.L., Cody, D.D., Brown, M.B., 1991. Evaluation of orthogonal mechanical properties and density of human trabecular bone from the major metaphyseal regions with materials testing and computed tomography. J. Orthop. Res. 9, 674–82. Doi:10.1002/jor.1100090507

Cifuentes, A., and Kalbag, A., 1992. A performance study of tetrahedral and hexahedral elements in 3-D finite element structural analysis. Finite Element Analysis and Design. 12, 313-318

Cong, A., Buijs, J.O. Den, Dragomir-daescu, D., 2011. Medical Engineering & Physics In situ parameter identification of optimal density – elastic modulus relationships in subject-specific finite element models of the proximal femur. Med. Eng. Phys. 33, 164–173. Doi:10.1016/j.medengphy.2010.09.018

Costa, M.C., Tozzi, G., Cristofolini, L., Danesi, V., Viceconti, M., Dall'Ara, E., 2017. Micro finite element models of the vertebral body: Validation of local displacement predictions. PloS One 12, 1–18. Doi:10.1371/journal.pone.0180151

Dahan, G., Trabelsi, N., Safran, O., Yosibash, Z., 2016. Verified and validated finite element analyses of humeri. J. Biomech. 49, 1094–1102. Doi:10.1016/j.jbiomech.2016.02.036

Dall'Ara, E., Barber, D., Viceconti, M., 2014. About the inevitable compromise between spatial resolution and accuracy of strain measurement for bone tissue : A 3D zero-strain study. J. Biomech. 47, 2956–2963. Doi:10.1016/j.jbiomech.2014.07.019

Dall'Ara, E., Pahr, D., Varga, P., Kainberger, F., Zysset, P., 2012. QCT-based finite element models predict human vertebral strength in vitro significantly better than simulated DEXA. Osteoporos. Int. 23, 563–572. Doi:10.1007/s00198-011-1568-3

Dall'Ara, E., Peña-Fernández, M., Palanca, M., Giorgi, M., Cristofolini, L., Tozzi, G., 2017. Precision of Digital Volume Correlation Approaches for Strain Analysis in Bone Imaged with Micro-Computed Tomography at Different Dimensional Levels. Front. Mater. 4. Doi:10.3389/fmats.2017.00031

Dall'Ara, E., Varga, P., Pahr, D., Zysset, P., 2011. A calibration methodology of QCT BMD for human vertebral body with registered micro-CT images. Med. Phys. 38, 2602–2608. Doi:10.1118/1.3582946

Danielsson, P.E., 1980. Euclidean distance mapping. Comput. Graph. Image Process. 14, 227–248. Doi:10.1016/0146-664X(80)90054-4

Dempster, W.T., Liddicoat, R.T., 1952. CoMPact Bone as a Non-Isotropic Material. J. Anat. 91, 331–362.

Depalle, B., Chapurlat, R., Walter-Le-Berre, H., Bou-Saïd, B., Follet, H., 2013. Finite element dependence of stress evaluation for human trabecular bone. J. Mech. Behav. Biomed. Mater. 18, 200–212. Doi:10.1016/j.jmbbm.2012.08.012

Dieppe, P., 1995. The classification and diagnosis of osteoarthritis. Osteoarthritic Disord. 5–12.

Ding, M., Danielsen, C.C., Hvid, I., 2001. Bone density does not reflect mechanical properties in early-stage arthrosis. Acta Orthop. Scand. 72, 181–185. Doi:10.1080/000164701317323444

Dragomir-Daescu, D., Op Den Buijs, J., McEligot, S., Dai, Y., Entwistle, R.C., Salas, C., Melton, L.J., Bennet, K.E., Khosla, S., Amin, S., 2011. Robust QCT/FEA models of proximal femur stiffness and fracture load during a sideways fall on the hip. Ann.

Biomed. Eng. 39, 742–755. Doi:10.1007/s10439-010-0196-y

Eberle, S., Göttlinger, M., Augat, P., 2013a. An investigation to determine if a single validated density – elasticity relationship can be used for subject specific finite element analyses of human long bones. Med. Eng. Phys. 35, 875–883. Doi:10.1016/j.medengphy.2012.08.022

Eberle, S., Göttlinger, M., Augat, P., 2013b. Individual density-elasticity relationships improve accuracy of subject-specific finite element models of human femurs. J. Biomech. 46, 2152–2157. Doi:10.1016/j.jbiomech.2013.06.035

Edwards, W.B., Schnitzer, T.J., Troy, K.L., 2013. Torsional stiffness and strength of the proximal tibia are better predicted by finite element models than DXA or QCT. J. Biomech. 46, 1655–1662. Doi:10.1016/j.jbiomech.2013.04.016

Enns-Bray, W.S., Ariza, O., Gilchrist, S., Widmer Soyka, R.P., Vogt, P.J., Palsson, H., Boyd, S.K., Guy, P., Cripton, P.A., Ferguson, S.J., Helgason, B., 2016. Morphology based anisotropic finite element models of the proximal femur validated with experimental data. Med. Eng. Phys. 38, 1339–1347. Doi:10.1016/j.medengphy.2016.08.010

Enns-Bray, W.S., Bahaloo, H., Fleps, I., Ariza, O., Gilchrist, S., Widmer, R., Guy, P., Pálsson, H., Ferguson, S.J., Cripton, P.A., Helgason, B., 2018. Material mapping strategy to improve the predicted response of the proximal femur to a sideways fall iMPact. J. Mech. Behav. Biomed. Mater. 78, 196–205. Doi:10.1016/j.jmbbm.2017.10.033

Enns-Bray, W.S., Owoc, J.S., Nishiyama, K.K., Boyd, S.K., 2014. Mapping anisotropy of the proximal femur for enhanced image based finite element analysis. J. Biomech. 47, 3272–3278. Doi:10.1016/j.jbiomech.2014.08.020

Ethier, C.R., Simmons, C.A., 2007. Introductory Biomechanics: From Cells to Organisms. Cambridge University Press.

Faulkner, K.G., Glüer, C.C., Grampp, S., Genant, H.K., 1993. Cross-calibration of liquid and solid QCT calibration standards: Corrections to the UCSF normative data. Osteoporos. Int. 3, 36–42. Doi:10.1007/BF01623175

Fazzalari, N.L., Parkinson, I.H., 1997. Fractal Properties of Subchondral Cancellous Bone in Severe Osteoarthritis of the Hip. J. Bone Miner. Res. 12, 632–640.

Doi:10.1359/jbmr.1997.12.4.632

Felson, D., Lawrence, R., Dieppe, P. A., Hirsch, R., Helmick, C. G., Jordan, J. M., & Sowers, M. 2000. Osteoarthritis: new insights. Part 1: the disease and its risk factors. Am Coll Physicians. 133(8), 635-646

Fondrk, M.T., Bahniuk, E.H., Davy, D.T., 1999. A damage model for nonlinear tensile behavior of cortical bone. J. Biomech. Eng. 121, 533–41.

Frost, H., 1960. Presence of microscopic cracks in vivo in bone. Henry Ford Hosp Med Bull 8, 27–35.

Galante, J., Rostoker, W., Ray, R.D., 1970. Physical properties of trabecular bone. Calcif. Tissue Res. 5, 236–246. Doi:10.1007/BF02017552

Goldstein, S.A., Wilson, D.L., Sonstegard, D.A., Matthews, L.S., 1983. The mechanical properties of human tibial trabecular bone as a function of metaphyseal location. J. Biomech. 16, 965–969. Doi:10.1016/0021-9290(83)90097-0

Gong, H., Zhang, M., Fan, Y., Kwok, W.L., Leung, P.C., 2012. Relationships between femoral strength evaluated by nonlinear finite element analysis and BMD, material distribution and geometric morphology. Ann. Biomed. Eng. 40, 1575–1585. Doi:10.1007/s10439-012-0514-7

Grassi, L., Isaksson, H., 2015. Extracting accurate strain measurements in bone mechanics: A critical review of current methods. J. Mech. Behav. Biomed. Mater. 50, 43–54. Doi:10.1016/j.jmbbm.2015.06.006

Gray, H.A., Taddei, F., Zavatsky, A.B., Cristofolini, L., Gill, H.S., 2008. Experimental Validation of a Finite Element Model of a Human Cadaveric Tibia 130, 1–9. Doi:10.1115/1.2913335

Grynpas, M.D., Alpert, B., Katz, I., Lieberman, I., Pritzker, K.P.H., 1991. Subchondral bone in osteoarthritis. Calcif. Tissue Int. 49, 20–26. Doi:10.1007/BF02555898

Gupta, S., Dan, P., 2004. Bone geometry and mechanical properties of the human scapula using computed tomography data. Trends Biomater Artif Organs 17, 61–70.

Gurdjian, E., Lissner, H.R., 1945. Mechanism of head injury as studied by the cathode ray oscilloscope. J Nerv Ment Dis. 102(4), 425

Haider, I.T., Speirs, A.D., Frei, H., 2013. Effect of boundary conditions, iMPact loading and hydraulic stiffening on femoral fracture strength. J. Biomech. 46, 2115–2121.

Doi:10.1016/j.jbiomech.2013.07.004

Hambli, R., Allaoui, S., 2013. A robust 3D finite element simulation of human proximal femur progressive fracture under stance load with experimental validation. Ann. Biomed. Eng. 41, 2515–2527. Doi:10.1007/s10439-013-0864-9

Harada, Y., Wevers, H., Cooke, T.D.V, 1988. Distribution of bone strength in the proximal tibia. J Arthroplasty. 3(2), 167-175

Helgason, B., Gilchrist, S., Ariza, O., Vogt, P., Enns-bray, W., Widmer, R.P., Fitze, T., Pálsson, H., Pauchard, Y., Guy, P., Ferguson, S.J., Cripton, P.A., 2016. The influence of the modulus – density relationship and the material mapping method on the simulated mechanical response of the proximal femur in side-ways fall loading configuration. Med. Eng. Phys, 38, 679–689. Doi:10.1016/j.medengphy.2016.03.006

Helgason, B., Perilli, E., Schileo, E., Taddei, F., 2008a. Mathematical relationships between bone density and mechanical properties: a literature review. Clin Biomech 23, 135–146. Doi:10.1016/j.clinbiomech.2007.08.024

Helgason, B., Taddei, F., Pálsson, H., Schileo, E., Cristofolini, L., Viceconti, M., Brynjólfsson, S., 2008b. A modified method for assigning material properties to FE models of bones. Med. Eng. Phys. 30, 444–453. Doi:10.1016/j.medengphy.2007.05.006

Hermida, J.C., Flores-Hernandez, C., Hoenecke, H.R. and D'Lima, D.D., 2014. Augmented wedge-shaped glenoid component for the correction of glenoid retroversion: a finite element analysis. J Shoulder Elb. Surg., 23(3), 347-354.

Hildebrand, T., Rüegsegger, P., 1997. A new method for the model-independent assessment of thickness in three-dimensional images. J. Microsc. 185, 67–75. Doi:10.1046/j.1365-2818.1997.1340694.x

Hildebrand, T.O.R., Laib, A., Müller, R., Dequeker, J.A.N., Rüegsegger, P., 1999. Direct Three-Dimensional Morphometric Analysis of. J. Bone 14, 1167–1174.

Hodgskinson, R., Currey, J.D., 1993. Separate effects of osteoporosis and density on the strength and stiffness of human cancellous bone. Clin. Biomech. (Bristol, Avon) 8, 262–8. Doi:10.1016/0268-0033(93)90036-H

Hussein, A.I., Louzeiro, D.T., Morgan, E.F., 2018. Differences in Trabecular

Microarchitecture and Simplified Boundary Conditions Limit the Accuracy of Quantitative Computed Tomography-Based Finite Element Models of Vertebral Failure 140, 1–11. Doi:10.1115/1.4038609

Imai, K., 2011. Vertebral fracture risk and alendronate effects on osteoporosis assessed by a computed tomography-based nonlinear finite element method. J. Bone Miner. Metab. 29, 645–651. Doi:10.1007/s00774-011-0281-9

Isherwood, I., Rutherford, R.A., Pullan, B.R., Adams, P.H., 1976. Bone-mineral estimation by computer-assisted transverse axial tomography. Lancet, 2, 712–5.

Jaasma, M.J., Bayraktar, H.H., Niebur, G.L., Keaveny, T.M., 2002. Biomechanical effects of intraspecimen variations in tissue modulus for trabecular bone. J. Biomech. 35, 237–246. Doi:10.1016/S0021-9290(01)00193-2

Jackman, T.M., DelMonaco, A.M., Morgan, E.F., 2015. Accuracy of finite element analyses of CT scans in predictions of vertebral failure patterns under axial compression and anterior flexion. J. Biomech. 1–9. Doi:10.1016/j.jbiomech.2015.12.004

Johnston, J. D. 2011. Development of a novel non-invasive imaging technique for characterizing subchondral bone mineral density and stiffness. Diss. PhD Thesis. Vancouver: University of British Columbia.

Kabel, J., Rietbergen, B. van, Dalstra, M., Odgaard, A., & Huiskes, R., 1999. The role of an effective isotropic tissue modulus in the elastic properties of cancellous bone. J. Biomech. 32(7), 673-680

Kaneko, M., Ohnishi, I., Bessho, M., Matsumoto, T., Ohashi, S., Tobita, K., Nakamura, K., 2015. Prediction of proximal femur strength by a quantitative computed tomography-based finite element method -Creation of predicted strength data of the proximal femur according to age range in a normal population and analysis of risk factors for hip fracture-. Mod. Rheumatol. 26, 151–155. Doi:10.3109/14397595.2015.1046220

Keaveny, T.M., McClung, M.R., Genant, H.K., Zanchetta, J.R., Kendler, D., Brown, J.P., Goemaere, S., Recknor, C., Brandi, M.L., Eastell, R., Kopperdahl, D.L., Engelke, K., Fuerst, T., Radcliffe, H.S., Libanati, C., 2014. Femoral and vertebral strength improvements in postmenopausal women with osteoporosis treated with denosumab.

J. Bone Miner. Res. 29, 158–165. Doi:10.1002/jbmr.2024

Keaveny, T.M., McClung, M.R., Wan, X., Kopperdahl, D.L., Mitlak, B.H., Krohn, K., 2012. Femoral strength in osteoporotic women treated with teriparatide or alendronate. Bone 50, 165–170. Doi:10.1016/j.bone.2011.10.002

Keaveny, T.M., Wachtel, E.F., Ford, C.M., Hayes, W.C., 1994. Differences between the tensile and compressive strength of trabecular bone depend on modulus. J. Biomech. 27, 1137–1146.

Kersh, M.E., Zysset, P.K., Pahr, D.H., Wolfram, U., Larsson, D., Pandy, M.G., 2013. Measurement of structural anisotropy in femoral trabecular bone using clinical-resolution CT images. J. Biomech. 46, 2659–2666. Doi:10.1016/j.jbiomech.2013.07.047

Keyak, J.H., Kaneko, T.S., Tehranzadeh, J., Skinner, H.B., 2005. Predicting proximal femoral strength using structural engineering models. Clin. Orthop. Relat. Res. NA;, 219–228. Doi:10.1097/01.blo.0000164400.37905.22

Keyak, J.H., Lee, I.Y., Skinner, H.B., J.H. Keyak, I.Y. Lee, H.. S., Keyak, Joych H. Lee, I.Y. Skinner, H.., Keyak, J.H., Lee, I.Y., Skinner, H.B., 1994b. Correlations between orthogonal mechanical properties and density of trabecular bone: Use of different densitometric measures. J. Biomed. Mater. Res. 28, 1329–1336.

Keyak, J.H., Rossi, S. a, Jones, K. a, Skinner, H.B., 1997. Prediction of Femoral Fracture Load using Automated Finite Element Modelling. J Biomech 31, 125–133. Doi:10.1016/S0021-9290(97)00123-1

Keyak, J.H., Sigurdsson, S., Karlsdottir, G., Oskarsdottir, D., Sigmarsdottir, A., Zhao, S., Kornak, J., Harris, T.B., Sigurdsson, G., Jonsson, B.Y., Siggeirsdottir, K., Eiriksdottir, G., Gudnason, V., Lang, T.F., 2011. Male-female differences in the association between incident hip fracture and proximal femoral strength: A finite element analysis study. Bone 48, 1239–1245. Doi:10.1016/j.bone.2011.03.682

Kheirollahi, H., Luo, Y., 2015. Assessment of Hip Fracture Risk Using Cross-Section Strain Energy Determined by QCT-Based Finite Element Modeling. Biomed Res. Int. 2015. Doi:10.1155/2015/413839

Kleerekoper, M., Greenspan, S.L., Lewiecki, E.M., Miller, P.D., Kendler, D.L., Maricic, M., Keaveny, T.M., Kopperdahl, D.L., Ruff, V.A., Wan, X., Janos, B., Krohn, K.,

2014. Assessing the Effects of Teriparatide Treatment. J. Bone Jt. Surg. 90, 1–9. Doi:10.1016/S0021-9355(14)74223-7

Knowles, N., Reeves, J.M., Ferreira, L.M., 2016. Quantitative Computed Tomography (QCT) derived Bone Mineral Density (BMD) in finite element studies: a review of the literature. J. Exp. Orthop. 3, 36. Doi:10.1186/s40634-016-0072-2

Knowles, N.K., Ferreira, L.M., Athwal, G.S., 2016. The arthritic glenoid: anatomy and arthroplasty designs. Curr. Rev. Musculoskelet. Med. 9. Doi:10.1007/s12178-016-9314-2

Koivumäki, J.E.M., Thevenot, J., Pulkkinen, P., Kuhn, V., Link, T.M., Eckstein, F., Jämsä, T., 2012a. Ct-based fi nite element models can be used to estimate experimentally measured failure loads in the proximal femur. Bone 50, 824–829. Doi:10.1016/j.bone.2012.01.012

Koivumäki, J.E.M., Thevenot, J., Pulkkinen, P., Kuhn, V., Link, T.M., Eckstein, F., Jämsä, T., 2012b. Cortical bone finite element models in the estimation of experimentally measured failure loads in the proximal femur. Bone 51, 737–740. Doi:10.1016/j.bone.2012.06.026

Kopperdahl, D.L., Aspelund, T., Hoffmann, P.F., Sigurdsson, S., Siggeirsdottir, K., Harris, T.B., Gundason, V., Keaveny, T.M., 2014. Assessment of Incident Spine and Hip Fractures in Women and Men using FEA of CT scans. J. Bone Miner. Res. 29, 570–580. Doi:10.1016/j.devcel.2010.12.007.Peroxiredoxin

Laib, A., Hildebrand, T., Häuselmann, H.J., Rüegsegger, P., 1997. Ridge number density: a new parameter for in vivo bone structure analysis. Bone 21, 541–6.

Les, C.M., Keyak, J., Stover, S.M., Taylor, K.T., Kaneps, A.J., 1994. Estimation of Material Properties in the Equine Metacarpus with use of Quantitative Computed Tomography. Jounral Orthop. Res. 12, 822–833.

Li, B., Aspden, R.M., 1997. Composition and Mechanical Properties of Cancellous Bone from the Femoral Head of Patients with Osteoporosis or Osteoarthritis. J. Bone Miner. Res. 12, 641–651. Doi:10.1359/jbmr.1997.12.4.641

Li, B., Aspden, R.M., 1997a. Mechanical and material properties of the subchondral bone plate from the femoral head of patients with osteoarthritis or osteoporosis. Ann. Rheum. Dis. 56(4), 247-254

Li, B., Aspden, R.M., 1997b. Composition and mechanical properties of cancellous bone from the femoral head of patients with osteoporosis or osteoarthritis. J. Bone. Min. Res. 12(4), 641-651

Lievers, W.B., Petryshyn, A.C., Poljsak, A.S., Waldman, S.D., Pilkey, A.K., 2010a. Specimen diameter and "side artifacts" in cancellous bone evaluated using end-constrained elastic tension. Bone 47, 371–377. Doi:10.1016/j.bone.2010.03.024

Lievers, W.B., Waldman, S.D., Pilkey, A.K., 2010b. Minimizing specimen length in elastic testing of end-constrained cancellous bone. J. Mech. Behav. Biomed. Mater. 3, 22–30. Doi:10.1016/j.jmbbm.2009.02.001

Lu, Engelke, K., P??schel, K., Morlock, M.M., Huber, G., 2014. Influence of 3D QCT scan protocol on the QCT-based finite element models of human vertebral cancellous bone. Med. Eng. Phys. 36, 1069–1073. Doi:10.1016/j.medengphy.2014.05.001

Lu, Y., Engelke, K., Glueer, C.-C., Morlock, M.M., Huber, G., 2014. The effect of in situ/in vitro threedimensional quantitative computed tomography image voxel size on the finite element model of human vertebral cancellous bone. Proc. Inst. Mech. Eng. Part H J. Eng. Med. 228, 1208–1213. Doi:10.1177/0954411914558654

Luisier, B., Dall'Ara, E., Pahr, D.H., 2014. Orthotropic HR-pQCT-based FE models improve strength predictions for stance but not for side-way fall loading compared to isotropic QCT-based FE models of human femurs. J. Mech. Behav. Biomed. Mater. 32, 287–299. Doi:10.1016/j.jmbbm.2014.01.006

Mansell, J., Bailey, A.-T.J. of clinical, 1998. Abnormal cancellous bone collagen metabolism in osteoarthritis. Am Soc Clin Investig.

Maquer, G., Musy, S.N., Wandel, J., Gross, T., Zysset, P.K., 2015. Bone volume fraction and fabric anisotropy are better determinants of trabecular bone stiffness than other morphological variables. J. Bone Miner. Res. 30, 1000–1008. Doi:10.1002/jbmr.2437

Matsuura, Y., Kuniyoshi, K., Suzuki, T., Ogawa, Y., Sukegawa, K., Rokkaku, T., Thoreson, A.R., An, K.-N., Takahashi, K., 2014. Accuracy of specimen-specific nonlinear finite element analysis for evaluation of radial diaphysis strength in cadaver material. Comput. Methods Biomech. Biomed. Engin. 5842, 1–7.

Doi:10.1080/10255842.2014.974579

McElhaney, J.H., 1966. Dynamic response of bone and muscle tissue. J. Appl. Physiol. 21, 1231–1236. Doi:10.1152/jappl.1966.21.4.1231

McErlain, D.D., Milner, J.S., Ivanov, T.G., Jencikova-Celerin, L., Pollmann, S.I., Holdsworth, D.W., 2011. Subchondral cysts create increased intra-osseous stress in early knee OA: A finite element analysis using simulated lesions. Bone 48, 639–646. Doi:10.1016/j.bone.2010.11.010

Mirzaali, M.J., Schwiedrzik, J.J., Thaiwichai, S., Best, J.P., Michler, J., Zysset, P.K., Wolfram, U., 2016. Mechanical properties of cortical bone and their relationships with age, gender, composition and microindentation properties in the elderly. Bone 93, 196–211. Doi:10.1016/j.bone.2015.11.018

Mirzaei, M., Keshavarzian, M., Naeini, V., 2014. Analysis of strength and failure pattern of human proximal femur using quantitative computed tomography (QCT)-based finite element method. Bone 64, 108–114. Doi:10.1016/j.bone.2014.04.007

Morgan, E., Bayraktar, H., Keaveny, T., 2003. Trabecular bone modulus–density relationships depend on anatomic site. J. Biomech.

Morgan, E.F., Keaveny, T.M., 2001. Dependence of yield strain of human trabecular bone on anatomic site. J. Biomech. 34, 569–577.

Morgan, E.F., Unnikrisnan, G.U., Hussein, A.I., 2018. Bone Mechanical Properties in Healthy and Diseased States. Annu. Rev. Biomed. Eng. 20, 119–43. Doi:10.1146/annurev-bioeng-062117-121139

Mueller, K., Trias, A., JBJS, R.R.-, 1966, U., 1966. Bone density and composition: age-related and pathological changes in water and mineral content. Citeseer.

Nazemi, S.M., Amini, M., Kontulainen, S.A., Milner, J.S., Holdsworth, D.W., Masri, B.A., Wilson, D.R., Johnston, J.D., 2015. Clinical Biomechanics Prediction of local proximal tibial subchondral bone structural stiffness using subject-speci fi c fi nite element modeling : Effect of selected density – modulus relationship ☆. JCLB 30, 703–712. Doi:10.1016/j.clinbiomech.2015.05.002

Nishiyama, K.K., Gilchrist, S., Guy, P., Cripton, P., Boyd, S.K., 2013. Proximal femur bone strength estimated by a computationally fast finite element analysis in a sideways fall configuration. J. Biomech. 46, 1231–1236.

Doi:10.1016/j.jbiomech.2013.02.025

Nishiyama, K.K., Ito, M., Harada, a, Boyd, S.K., 2014. Classification of women with and without hip fracture based on quantitative computed tomography and finite element analysis. Osteoporos. Int. 25, 619–26. Doi:10.1007/s00198-013-2459-6

Nordin, M., Frankel, V., 2001. Basic biomechanics of the musculoskeletal system.

Oftadeh, R., Perez-Viloria, M., Villa-Camacho, J.C., Vaziri, A., Nazarian, A., 2015. Biomechanics and Mechanobiology of Trabecular Bone: A Review. J. Biomech. Eng. 137, 010802. Doi:10.1115/1.4029176

Op Den Buijs, J., Dragomir-Daescu, D., 2011. Validated finite element models of the proximal femur using two-dimensional projected geometry and bone density. Comput. Methods Programs Biomed. 104, 168–174. Doi:10.1016/j.cmpb.2010.11.008

Pahr, D.H., Zysset, P.K., 2009. A coMParison of enhanced continuum FE with micro FE models of human vertebral bodies. J. Biomech. 42, 455–462. Doi:10.1016/j.jbiomech.2008.11.028

Parfitt, A.M., Drezner, M.K., Glorieux, F.H., Kanis, J.A., Malluche, H., Meunier, P.J., Ott, S.M., Recker, R.R., 1987. Bone histomorphometry: Standardization of nomenclature, symbols, and units: Report of the asbmr histomorphometry nomenclature committee. J. Bone Miner. Res. Doi:10.1002/jbmr.5650020617

Pomwenger, W., Entacher, K., Resch, H., Schuller-Götzburg, P., 2014. Need for CT-based bone density modelling in finite element analysis of a shoulder arthroplasty revealed through a novel method for result analysis. Biomed. Tech. (Berl). 59, 421–30. Doi:10.1515/bmt-2013-0125

Radin, E., Parker, H. G., Pugh, J. W., Steinberg, R. S., Paul, I. L., & Rose, R. M. 1973. Response of joints to iMPact loading—III: Relationship between trabecular microfractures and cartilage degeneration. J. Biomech. 6(1): 51-57

Radin, E., Paul, I., Rose, R.M, 1972. Role of mechanical factors in pathogenesis of primary osteoarthritis. Lancet, 299, 519-522

Radin, E., Rose, R.M., 1986. Role of subchondral bone in the initiation and progression of cartilage damage. Clin. Orthop. Rel. Res. 213, 34-40

Radin, E.L., Paul, I.L., Tolkoff, M.J., 1970. Subchondral bone changes in patients with

early degenerative joint disease. Arthritis Rheum. 13, 400–405. Doi:10.1002/art.1780130406

Reilly, D.T., Burstein, A.H., 1975. The elastic and ultimate properties of coMPact bone tissue. J. Biomech. 8, 393–405.

Rho, J.Y., Ashman, R.B., Turner, C.H., 1993. Young's modulus of trabecular and cortical bone material: ultrasonic and microtensile measurements. J. Biomech. 26, 111–9.

Rho, J.Y., Tsui, T.Y., Pharr, G.M., 1997. Elastic properties of human cortical and trabecular lamellar bone measured by nanoindentation. Biomaterials 18, 1325–30.

Roberts, B.C., Perilli, E., Reynolds, K.J., 2014. Application of the digital volume correlation technique for the measurement of displacement and strain fields in bone: A literature review. J. Biomech. 47, 923–934. Doi:10.1016/j.jbiomech.2014.01.001

Rüegsegger, P., Elsasser, U., Anliker, M., Gnehm, H., Kind, H., Prader, A., 1976. Quantification of Bone Mineralization Using Computed Tomography. Radiology 121, 93–97. Doi:10.1148/121.1.93

Ruess, M., Tal, D., Trabelsi, N., Yosibash, Z., Rank, E., 2012. The finite cell method for bone simulations: Verification and validation. Biomech. Model. Mechanobiol. 11, 425–437. Doi:10.1007/s10237-011-0322-2

Schileo, E., Dall'Ara, E., Taddei, F., 2008. An accurate estimation of bone density improves the accuracy of subject-specific finite element models. J. ….

Sharma, L., 2001. Local factors in osteoarthritis. Curr. Opin. Rheumatol. 13, 441–446.

Shim, V.B., Pitto, R.P., Anderson, I.A., 2012. Quantitative CT with finite element analysis: Towards a predictive tool for bone remodelling around an uncemented tapered stem. Int. Orthop. 36, 1363–1369. Doi:10.1007/s00264-012-1513-x

Sophia Fox, A.J., Bedi, A., Rodeo, S.A., 2009. The basic science of articular cartilage: structure, composition, and function. Sports Health 1, 461–8. Doi:10.1177/1941738109350438

Stauber, M., Müller, R., 2006. Volumetric spatial decomposition of trabecular bone into rods and plates–a new method for local bone morphometry. Bone 38, 475–84. Doi:10.1016/j.bone.2005.09.019

Suzuki, S., Yamamuro, T., Okumura, H., Yamamoto, I., 1991. Quantitative computed tomography: coMParative study using different scanners with two calibration

phantoms. Br. J. Radiol. 64, 1001–6. Doi:10.1259/0007-1285-64-767-1001

Synek, A., Chevalier, Y., Baumbach, S.F., Pahr, D.H., 2015. The influence of bone density and anisotropy in finite element models of distal radius fracture osteosynthesis: Evaluations and coMParison to experiments. J. Biomech. 48, 4116–4123. Doi:10.1016/j.jbiomech.2015.10.012

Taddei, F., Pancanti, A., Viceconti, M., 2004. An improved method for the automatic mapping of computed tomography numbers onto finite element models. Med. Eng. Phys. 26, 61–69. Doi:10.1016/S1350-4533(03)00138-3

Taddei, F., Schileo, E., Helgason, B., Cristofolini, L., Viceconti, M., 2007. The material mapping strategy influences the accuracy of CT-based finite element models of bones: an evaluation against experimental measurements. Med. Eng. Phys. 29, 973–9. Doi:10.1016/j.medengphy.2006.10.014

Tarala, M., Janssen, D., Telka, a, Waanders, D., Verdonschot, N., 2011. Experimental versus computational analysis of micromotions at the implant-bone interface. Proc. Inst. Mech. Eng. H. 225, 8–15. Doi:10.1243/09544119JEIM825

Tawara, D., Sakamoto, J., Murakami, H., Kawahara, N., Oda, J., Tomita, K., 2010. Mechanical evaluation by patient-specific finite element analyses demonstrates therapeutic effects for osteoporotic vertebrae. J. Mech. Behav. Biomed. Mater. 3, 31–40. Doi:10.1016/j.jmbbm.2009.03.001

Tomaszewski, P.K., van Diest, M., Bulstra, S.K., Verdonschot, N., Verkerke, G.J., 2012. Numerical analysis of an osseointegrated prosthesis fixation with reduced bone failure risk and periprosthetic bone loss. J. Biomech. 45, 1875–1880. Doi:10.1016/j.jbiomech.2012.05.032

Townsend, P.R., Rose, R.M., Radin, E.L., 1975. Buckling studies of single human trabeculae. J. Biomech. 8, 199–201.

Trabelsi, N., Yosibash, Z., 2011. Patient-specific finite-element analyses of the proximal femur with orthotropic material properties validated by experiments. J. Biomech. Eng. 133, 061001. Doi:10.1115/1.4004180

Trabelsi, N., Yosibash, Z., Wutte, C., Augat, P., Eberle, S., 2011. Patient-specific finite element analysis of the human femur-A double-blinded biomechanical validation. J. Biomech. 44, 1666–1672. Doi:10.1016/j.jbiomech.2011.03.024

Ün, K., Bevill, G., Keaveny, T.M., 2006. The effects of side-artifacts on the elastic modulus of trabecular bone. J. Biomech. 39, 1955–1963. Doi:10.1016/j.jbiomech.2006.05.012

Unnikrishnan, G.U., Barest, G.D., Berry, D.B., Hussein, A.I., Morgan, E.F., 2013. Effect of specimen-specific anisotropic material properties in quantitative computed tomography-based finite element analysis of the vertebra. J. Biomech. Eng. 135, 101007–11. Doi:10.1115/1.4025179

Unnikrishnan, G.U., Morgan, E.F., 2011. A New Material Mapping Procedure for Quantitative Computed Tomography-Based, Continuum Finite Element Analyses of the Vertebra. J. Biomech. Eng. 133, 071001. Doi:10.1115/1.4004190

van Rietbergen, B., Weinans, H., Huiskes, R., Odgaard, A., 1995. A new method to determine trabecular bone elastic properties and loading using micromechanical finite-elements models. J. Biomech. 28, 69–81.

Varghese, B., Short, D., Penmetsa, R., Goswami, T., Hangartner, T., 2011. Computed-tomography-based finite-element models of long bones can accurately capture strain response to bending and torsion. J. Biomech. 44, 1374–1379. Doi:10.1016/j.jbiomech.2010.12.028

Wang, X., Sanyal, A., Cawthon, P.M., Palermo, L., Jekir, M., Christensen, J., Ensrud, K.E., Cummings, S.R., Orwoll, E., Black, D.M., Keaveny, T.M., 2012. Prediction of New Clinical Vertebral Fractures in Elderly Men using Finite Element Analysis of CT Scans for the Osteoporotic Fractures in Men (MrOS) Research Group. J Bone Min. Res. J Bone Min. Res 27, 808–816. Doi:10.1002/jbmr.1539

Wolff, J., 1892. The law of bone remodeling. Verlag von August Hirchwald. Berlin.

Wu, D., Isaksson, P., Ferguson, S.J., Persson, C., 2018. Young's modulus of trabecular bone at the tissue level: A review. Acta Biomater. 78, 1–12. Doi:10.1016/j.actbio.2018.08.001

Zannoni, C., Mantovani, R., Viceconti, M., 1999. Material properties assignment to finite element models of bone structures: a new method. Med. Eng. Phys. 20, 735–740. Doi:10.1016/S1350-4533(98)00081-2

Zeinali, A., Hashemi, B., Akhlaghpoor, S., 2010. Noninvasive prediction of vertebral body compressive strength using nonlinear finite element method and an image

based technique. Phys. Medica 26, 88–97. Doi:10.1016/j.ejmp.2009.08.002

Zioupos, P., Hansen, U., Currey, J.D., 2008. Microcracking damage and the fracture process in relation to strain rate in human cortical bone tensile failure. J. Biomech. 41, 2932–9. Doi:10.1016/j.jbiomech.2008.07.025

Zysset, P.K., Sonny, M., Hayes, W.C., 1994. Morphology-mechanical property relations in trabecular bone of the osteoarthritic proximal tibia. J. Arthroplasty 9, 203–16.

CHAPTER 2 – A COMPARISON OF DENSITY-MODULUS RELATIONSHIPS USED IN FINITE ELEMENT MODELING OF THE SHOULDER

OVERVIEW: *Shoulder-specific density-modulus relationships are limited within the literature. As such, a variety of relationships developed for alternate anatomic-locations are used to model the mechanical behavior of continuum-level scapular finite element models (FEMs). This study introduces a computational methodology using continuum-level FEMs derived from quantitative-CT (QCT) data compared to co-registered microFEMs of trabecular bone to compare the most commonly used density-modulus relationships used in continuum-level FEMs of the scapula.*[2]

[2]A version of this work has been accepted: Knowles NK, Langohr GDG, Faieghi M, Nelson A, Ferreira LM. A Comparison of Density-Modulus Relationships Used in Finite Element Modeling of the Shoulder. Medical Engineering and Physics. 2019; 66:40-46

2.1 INTRODUCTION:

Clinical-computed tomography (CT) scans are commonly performed for diagnostics and surgical planning of upper limb orthopaedic surgical procedures. Improvements in surgical procedures, implant designs, understanding of joint biomechanics, and pathologic conditions can be elucidated using clinical-resolution-derived computational finite element models (FEMs). As initial input to these models a constitutive relationship must be chosen that relates the CT-intensity to the bones' mechanical properties, to ensure that the resulting model is an accurate representation of the bone being modeled.

These density-modulus relationships have been shown to result in clinical-resolution-derived whole bone FEMs that are highly correlated with experimental results ($R^2 > 0.90$) (Dahan et al., 2016; Knowles et al., 2016). These relationships are thought to be site-specific, with anatomic site- and subject-specific modeling parameters shown to greatly improve the accuracy of clinical-resolution-derived FEMs (Campoli et al., 2013; Schileo et al., 2008, 2007; Unnikrishnan et al., 2013). However, it is common for relationships developed for one anatomic site, such as the hip, to be used in another, due to a paucity of established relationships. Pooling relationships from multiple anatomic sites to improve the modeling of mechanical properties in alternative sites is one approach to cover a greater density range. However, this method neglects site-specific trabecular architecture, the local distribution of bone, and the geometric contributions from the cortical structure of whole bones.

Anatomic location-specific linear-isotropic density-modulus relationships are commonly used in biomechanics research for accurate material mapping in FEMs derived from commercially available (Mimics, Materialise, Leuven, BE.; Simpleware, Synopsys, Mountain View, CA, USA) and open source (BoneMat; MITK-GEM) software, making these relationships essential to FEM development. A large number of density-modulus relationships exist within the literature (Helgason et al., 2008), with relationships primarily developed by testing physical trabecular and/or cortical bone specimens. However, when mechanically testing specimens, variations in experimental testing protocols have resulted in large systematic errors due to end-artifacts, specimen geometry, misrepresented boundary conditions, and the loss of load-carrying capacity of outer trabeculae due to coring (Bayraktar et al., 2004; Helgason et al., 2008; Ün et al., 2006). To improve model

accuracy and reduce these errors, computational μ-FEMs that account for mineral heterogeneity (Bourne and Van Der Meulen, 2004; Harrison et al., 2008; Jaasma et al., 2002; Renders et al., 2011, 2008; van Ruijven et al., 2007) may provide a robust method of density-modulus development.

A computational methodology has recently been reported that uses μ-FEMs and co-registered QCT-FEMs to compare the loading of trabecular bone cores. This methodology eliminates some of the errors associated with traditional experimental mechanical testing of trabecular bone cores (Chen et al., 2017) and allows for the use of identical boundary conditions across models. Consistent with previous work, this methodology uses apparent strain energy density (SED_{app}) to compare multi-resolution modeling of trabecular bone (Podshivalov et al., 2011). Accounting for trabecular tissue heterogeneity at the micro-level has been shown to improve μ-FEM accuracy by allowing for a more accurate representation of trabecular bending stiffness (Bourne and Van Der Meulen, 2004; Harrison et al., 2008; Jaasma et al., 2002; Renders et al., 2011, 2008). Computationally, this is represented as a heterogeneous distribution of varying tissue modulus and is consistent with studies that have illustrated variations in trabecular tissue density superficially and at the core due to trabecular bone remodeling (Brennan et al., 2009; Oftadeh et al., 2015).

Six relationships are commonly used in shoulder FE studies (Büchler et al., 2002; Carter and Hayes, 1977; Gupta and Dan, 2004; Hayes, 1991; Morgan et al., 2003; Rice et al., 1988), with only a single study having used scapular trabecular bone samples (Gupta and Dan, 2004) for development. Shoulder FE studies lack experimental validation of the FE results, limiting the ability to translate outcomes and compare studies. This study compares these six relationships on the ability to predict SED_{app} in μ-FEMs derived from glenoid trabecular bone.

2.2 METHODS:

2.2.1 Micro Finite Element Model Generation

Fourteen full-arm cadaveric specimens were obtained (7 male; 7 female; mean age 67 ± 8 years). The scapula was removed and denuded of all soft tissues. The glenoid fossa of each

scapula was scanned with a micro-computed tomography scanner (Nikon XT H 225 ST, Nikon Metrology, NV, 95 kVp, 64 µA, 3141 projections, 1000 ms exposure). To include the entire glenoid structure in all scans from the largest to the smallest specimen, a fixed spatial resolution of 32 µm was used. As recommended for numerical convergence in subsequent µ-FEMs, this spatial resolution was less than one-fourth the mean trabecular thickness (Guldberg et al., 1998; Niebur et al., 1999). The images were exported as 16-bit Digital Imaging and Communications in Medicine (DICOM) format, and loaded to medical imaging software (Mimics, V.20.0, Materialise, Leuven, BE).

The raw images were filtered with a Gaussian filter ($\sigma = 1.25$, support = 2) to remove high frequency noise. A specimen-specific threshold was used to separate bone from the surrounding marrow, preserving trabecular geometry (Bouxsein et al., 2010). A three-dimensional stereolithography (STL) model was created and transferred to 3-Matic (V.12.0, Materialise, Leuven, BE). Volumes of interest (VOIs) with 5 mm edge length and 10 mm in length were placed medial to the glenoid articular surface subchondral bone. This size was chosen for consistency between the smallest and largest specimens, while maintaining the recommended 2:1 aspect ratio (Helgason et al., 2008). A maximum number of VOIs were placed in each specimen to ensure only glenoid vault trabecular bone was removed, resulting in 98 ‘virtual cores’ among the 14 specimens. The 3D morphometric measurements for the cores had an average bone volume fraction (bone volume/total volume (BV/TV)) of 0.25 ± 0.08 (range: 0.10 – 0.51), trabecular thickness (Tb.Th) of 0.26 ± 0.05 (range 0.17 – 0.40), trabecular separation (Tb.Sp) of 0.80 ± 0.13 (range: 0.29 – 1.03), and a trabecular number (Tb.N) of 0.93 ± 0.23 (range: 0.53 – 1.52) (Skyscan CTAn, Bruker micro-CT, Kontich, BE).

Each VOI was transferred back to Mimics and registered to the DICOM images, to associate each VOI with the corresponding grayscale intensity of the contained voxels. Region growing with 6-connectivity was used to ensure connected voxels. The central voxel coordinates and associated grayvalues were exported and custom code was used for direct conversion to eight node hexahedral elements (Faieghi et al., 2019). Two tissue moduli cases were considered in µ-FEM development: a homogeneous tissue modulus, and a heterogeneous tissue modulus. In the former, all elements were assigned a uniform modulus of 20 GPa. In the latter, an element-wise material mapping was performed that

used each voxel's grayvalue and a quantitative linear mapping to a reference modulus of 20 GPa, with a slope factor of 1.4 (Bourne and Van Der Meulen, 2004). This resulted in a tissue modulus ranging from 4.3 – 21.5 GPa (16.9 – 39.2% coefficient of variation (COV)), and mean tissue modulus of 9.8 ± 1.0 GPa for all 98 heterogeneous µ-FEMs.

Following the methods described by Knowles et al. (2019), the nodes of the bottom face of the resulting linear-isotropic homogeneous (98 µ-FEMs) and heterogeneous (98 µ-FEMs) were fully constrained, with the top nodes constrained to compressive only loading of 0.5% apparent strain (Morgan and Keaveny, 2001) (Abaqus V.6.14, Simulia, Providence, RI, USA). Custom Matlab (Mathworks Inc., Natick, MA, USA) code generated the Abaqus input file, ensuring identical boundary conditions and loads between models. The apparent strain energy density (SED_{app}) was calculated for each of the 196 µ-FEMs.

2.2.2 Quantitative Computed Tomography (QCT) Finite Element Generation

The 14-cadaveric scapulae were also scanned with a clinical multi-slice CT-scanner (GE Discovery CT750 HD, Milwaukee, WI, USA, 120 kVp, 200 mAs, 320 mm FOV, 0.625 mm isotropic voxels, BONEPLUS convolution kernel). A liquid dipotassium phosphate (K_2HPO_4) calibration phantom (QCT Pro, Mindways Software Inc., Austin, TX, USA) was scanned with each specimen to provide a consistent density scaling reference among specimens (g_{K2HPO4}/cm^3). The DICOM images were loaded into Mimics, a 3D STL model was generated and transferred to 3-Matic. The QCT-model was co-registered to the µ-CT model using iterative closest points fitting. The previously placed uCT VOIs were duplicated and transformed to the QCT coordinate system using the coordinate transform between the two models. Each QCT VOI was transferred back to Mimics and registered to the DICOM images. The VOI size is evenly divisible by the QCT voxel dimensions, ensuring partial volume effects are eliminated during registration.

Custom-written Matlab code generated linear-isotropic models with eight-node hexahedral elements and generated the Abaqus input file, with identical boundary and loading conditions to the µ-FEMs. The code was also used to implement each of the six non-linear density-modulus relationships used in shoulder finite element (FE) studies (Table 2.1). These relationships were applied element-wise, such that each element had a

Table 2.1: Density-Modulus Relationships used in Scapular FE Studies

$E = \alpha\rho^{\beta}$

Reference	Density Measure (ρ)	Density Range (g/cm^3)	Anatomic Location	α	β	r^2
Morgan et al., 2003	Apparent	(0.09 – 0.75)	Pooled	8920	1.83	0.88
Morgan et al., 2003	Apparent	(0.26 – 0.75)	Femoral Neck	6850	1.49	0.85
Gupta and Dan, 2004	Apparent	< 0.35	Scapulae	1050	2	0.403
		0.35 – 1.8		3000	3	0.987
Büchler et al., 2002	Apparent/1.8	n/r	n/r	15000	2	n/r
Carter and Hayes, 1977	Apparent	(0.18 – 2.00 rfg)	Human Tibia & Bovine Femur	2875	3	n/r
Schaffler & Burr 1988	Ash	(0.644 – 0.723)	Bovine Tibia & Femur	60 + 900	2	n/r
	Apparent	< 1.54				
Rice et al., 1988	Apparent	(1.80 – 2.00)	Human & Bovine	90	7.4	n/r
	Apparent	> 1.54				

Density range refers to piecewise density relationships. In brackets are the ranges of physical bone samples tested in the respective studies. Pooled values are from Vertebra (T10-L5), Proximal Tibia, Greater Trochanter, and Femoral Neck. The Büchler et al., 2002 relationship is derived from Hayes, 1991, Reilly et al., 1974, and Rice et al., 1988 and does not report which studies contributed to the relationships. Therefore, density range and anatomic location could not be extracted. Carter and Hayes, 1977 assumes a physiologic strain rate of 0.01/s. n/r – not reported. rfg – read from graph

unique modulus assigned based on its corresponding voxel QCT density. The following equations derived from the co-registered VOIs were developed to convert QCT to apparent density. A linear relationship between the BV/TV of each µ-CT VOI and corresponding QCT density of each co-registered QCT VOI was used to develop equation 2.1. The relationship between BV/TV and apparent density described by Carter and Hayes (1977) was then used to relate the QCT density to apparent density (equation 2.2). This allowed equation 2.3 to be used to convert between QCT and apparent density and resulted in QCT-FEMs with a range of average apparent densities of 0.10 – 0.90 g/cm^3.

$$\rho_{QCT}\ \left[\frac{g_{K2HPO4}}{cm^3}\right] = 0.821\frac{BV}{TV} - 0.003 \qquad \text{(Equation 2.1)}$$

$$\rho_{QCT}\ \left[\frac{g_{K2HPO4}}{cm^3}\right] = 0.821\frac{\rho_{app}}{1.8} - 0.003, \qquad \text{(Equation 2.2)}$$

$$where\ \frac{BV}{TV} = \frac{\rho_{app}}{\rho_{real}},$$

with $\rho_{real} = 1.8\ \left[\frac{g}{cm^3}\right]$ (Carter and Hayes, 1977)

$$\rho_{app}\ \left[\frac{g}{cm^3}\right] = 2.192\rho_{QCT} + 0.007 \qquad \text{(Equation 2.3)}$$

For each QCT-FEM (6 x 98 = 588 models), the apparent strain energy density (SED_{app}) was calculated. The SED_{app} between QCT- and µ-FEMs were used to compare each density-modulus relationship's ability to map the apparent modulus to each virtual core (Figure 2.1). To account for the larger number of cores than specimens, restricted maximum likelihood estimation (REML) linear regression fits were used (Matlab Statistics Toolbox, V. R2017a).

2.3 RESULTS

When considering comparisons between QCT-FEMs and µ-FEMs with a homogeneous tissue modulus, near absolute statistical agreement (Y=X) was observed between the µ-FEMs and the QCT-FEMs using the Morgan et al. (2003) pooled relationship (Table 2.2). Not surprisingly, due to the similarity between the two relationships (Table 2.2), the Gupta & Dan (2004) and Carter & Hayes (1977) models showed near identical REML linear regression fit parameters.

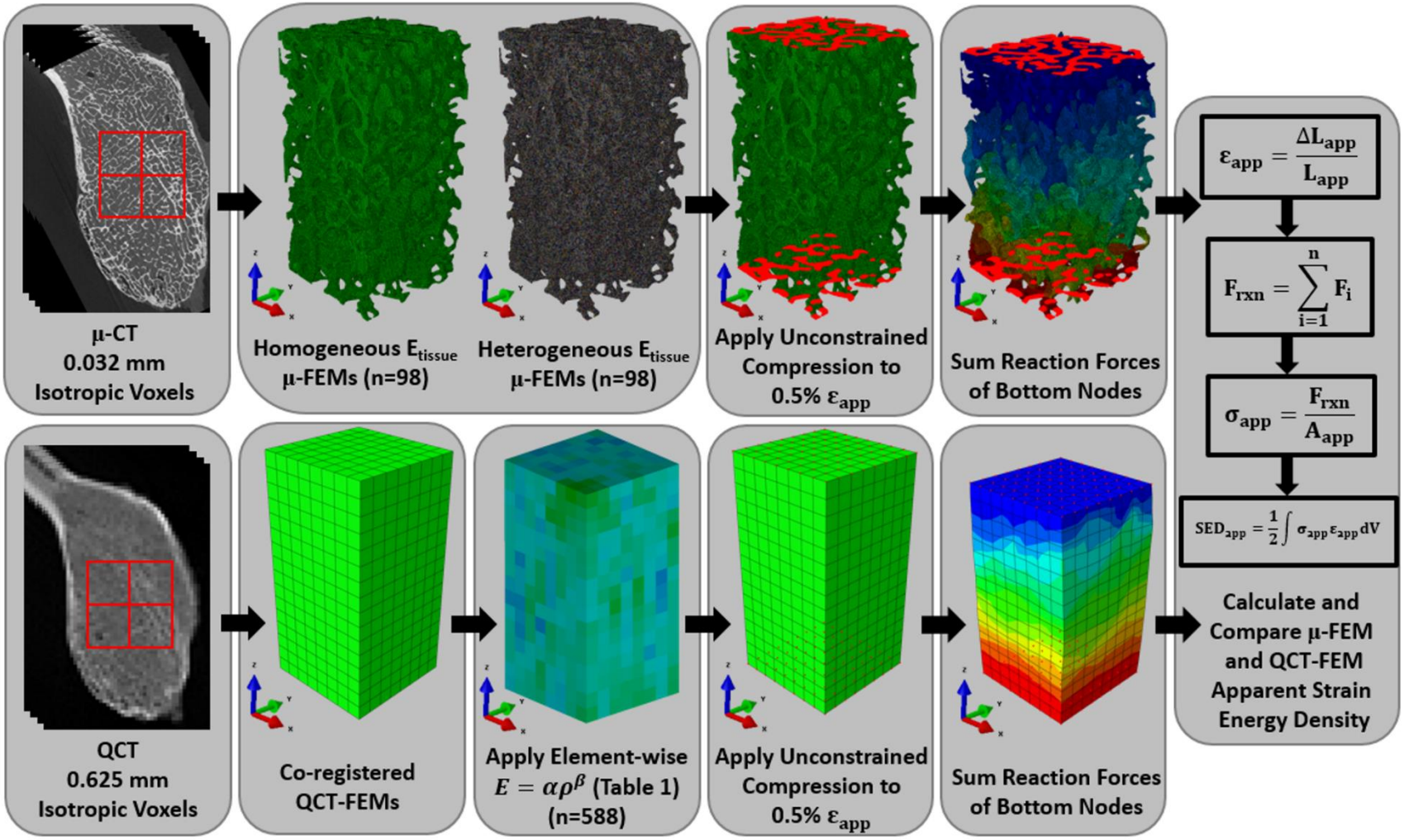

Figure 2.1: The workflow used to create μ-FEMs and QCT-FEMs

Fourteen specimens were used to acquire μ-CT and QCT images. The μ-FEMs were applied either homogeneous (E_{tissue} = 20 GPa) or heterogeneous (E_{tissue} scaled by CT-intensity (Bourne and Van Der Meulen, 2004)), loaded in unconstrained compression and used to determine μ-FEMs apparent strain energy (SED_{app}). Co-registered QCT-FEMs were loaded with identical boundary conditions and the SED_{app} was compared to the μ-FEM SED_{app}.

Table 2.2: Results from restricted maximum likelihood estimation linear regression fits of apparent strain energy (SED_{app}) predictions between QCT-FEMs and homogeneous tissue modulus μ-FEMs (20 GPa)

QCT-FEM SED_{app} = mμ-FEM SED_{app} + b

Author	r^2	m	b	SE	SE/mean
Morgan et al., 2003 – Pooled	0.933	0.979	0.0066	0.0049	17.5%
Morgan et al., 2003 – Femur	0.937	0.739	0.0098	0.0037	14.4%
Gupta and Dan, 2004	0.891	0.326	-0.0013	0.0019	32.2%
Büchler et al., 2002	0.942	0.516	0.0021	0.0023	17.5%
Carter and Hayes, 1977	0.901	0.317	-0.0014	0.0017	31.7%
Schaffler & Burr,1988	0.940	0.105	0.0013	0.0005	13.7%
Rice et al., 1988					

r^2 – coefficient of determination; m – slope of regression line; b – intercept of regression line; SE – standard error of regression; SE/mean – standard error of regression as a percentage of the mean value.

All relationships other than the Morgan et al. (2003) pooled relationship, greatly underestimated the μ-FEM apparent strain energy density (SED_{app}) when considering a homogeneous tissue modulus in the μ-FEMs (Figure 2.2). The Schaffler & Burr (1988) and Rice et al. (1988) relationship had the lowest standard error divided by the mean and the highest coefficient of determination, but greatly underestimated the μ-FEM SED_{app}. The underestimation of SED_{app} was also evident from the Bland-Altman plots for the homogeneous tissue modulus models. Significant proportional error for the Gupta & Dan (2004), Carter & Hayes (1977), and the Schaffler & Burr (1988), Rice et al. (1988) relationships was observed. There was also moderate proportional error for the Büchler et al. (2002) relationship in these comparisons.

The same result with the pooled relationship did not hold true when the heterogeneous tissue modulus was considered in the μ-FEMs. The Büchler et al. (2002) relationship most accurately predicted the SED_{app} for this comparison (Table 2.3). The Gupta & Dan (2004) and Carter & Hayes (1977) relationships again showed near identical REML linear regression fit parameters, and for the heterogeneous case, the Bland-Altman plots were nearly identical (Figure 2.3). Again, the Schaffler & Burr (1988), Rice et al. (1988) relationship had the lowest standard error divided by the mean and the highest coefficient of determination, but greatly underestimated the μ-FEM SED_{app}. The Bland-Altman proportional error illustrates an overestimation in SED_{app} with both Morgan et al. (2003) relationships and proportional error underestimation of SED_{app} with the Schaffler & Burr (1988), Rice et al. (1988) relationship.

2.4 DISCUSSION:

This study compared the six most commonly used density-modulus relationships used in finite element (FE) modeling of the shoulder using a computational methodology with co-registered μ-FEMs. When a homogeneous effective tissue modulus is used in μ-FEMs the results suggest that density-modulus relationships mapped to co-registered QCT-FEMs pooled from multiple anatomic sites, may accurately predict the apparent strain energy density ($SED_{app)}$ of glenoid trabecular bone. When considering a heterogeneous tissue modulus, the Büchler et al. (2002) relationship most accurately predicted the SED_{app} of the μ-FEMs. The differences in SED_{app} between these two relationships and their ability to represent micro-level SED_{app} may be due to variations in the trabecular density range of the samples used in density-modulus relationship development and the resulting heterogeneity of the trabeculae. The μ-FEMs used in this study

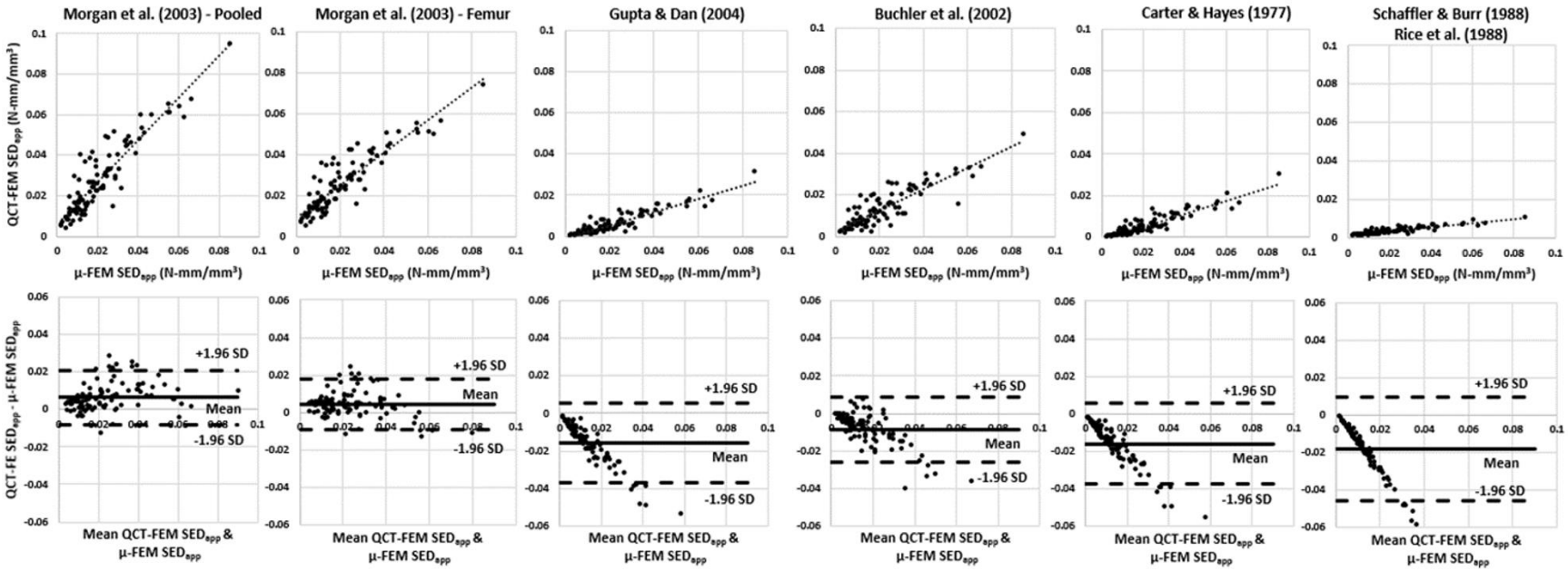

Figure 2.2: Restricted maximum likelihood linear regression fits (upper row) and Bland-Altman plots (lower row) of the of the six density-modulus relationships compared for μ-FEM homogeneous tissue modulus of 20 GPa.

Table 2.3: Results from restricted maximum likelihood estimation linear regression fits of apparent strain energy (SED_{app}) predictions between QCT-FEMs and heterogeneous tissue modulus µ-FEMs

QCT-FEM SED_{app} = mµ-FEM SED_{app} + b

Author	r^2	m	b	SE	SE/mean
Morgan et al., 2003 – Pooled	0.926	1.914	0.0091	0.0052	18.5%
Morgan et al., 2003 – Femur	0.928	1.432	0.0119	0.0040	15.4%
Gupta and Dan, 2004	0.892	0.638	-0.0005	0.0019	32.2%
Büchler et al., 2002	0.935	1.014	0.0034	0.0025	18.7%
Carter and Hayes, 1977	0.900	0.617	-0.0007	0.0018	32.2%
Schaffler & Burr, 1988	0.947	0.211	0.0015	0.0005	12.9%
Rice et al., 1988					

Element-wise material heterogeneity in the µ-FEMs was applied to each model using a slope factor of 1.4 and a reference tissue modulus of 20 GPa (Bourne and Van Der Meulen, 2004). R^2 – coefficient of determination; m – slope of regression line; b – intercept of regression line; SE – standard error of regression; SE/mean – standard error of regression as a percentage of the mean value.

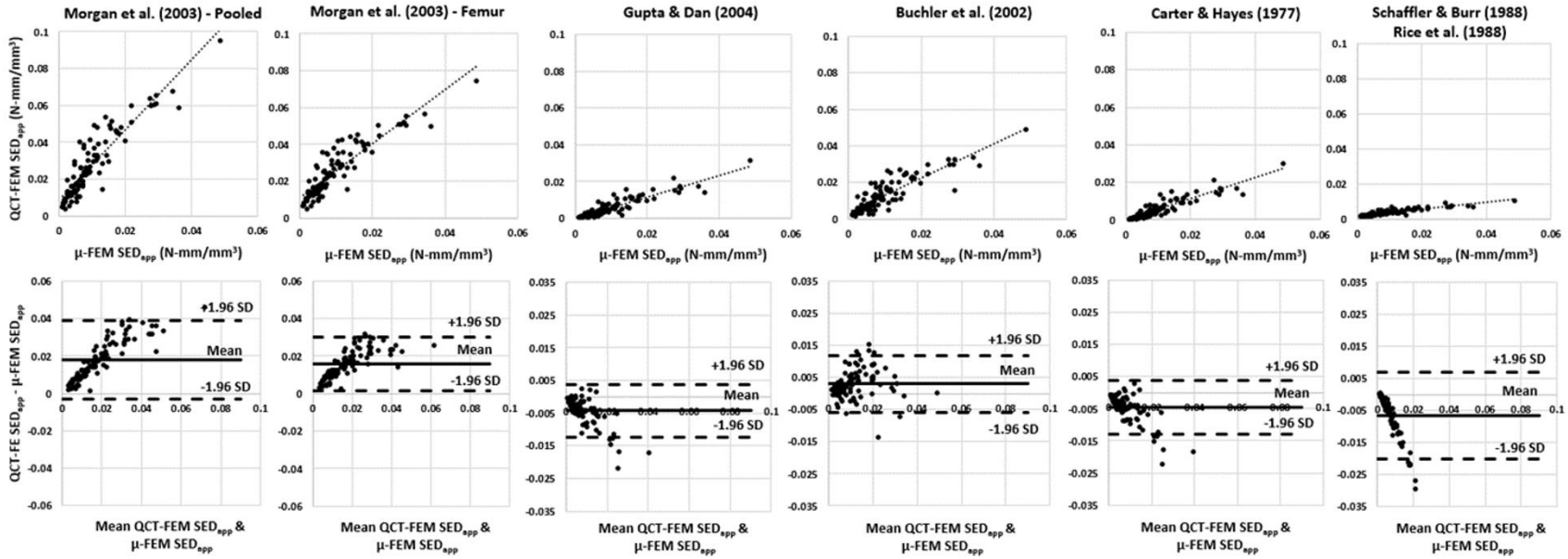

Figure 2.2: Restricted maximum likelihood linear regression fits (upper row) and Bland-Altman plots (lower row) of the of the six density-modulus relationships compared for μ-FEM heterogeneous tissue modulus.

The modulus was applied using a slope factor of 1.4 and a reference tissue modulus of 20 GPa (Bourne and Van Der Meulen, 2004).

were linear isotropic and therefore the arbitrary homogeneous effective tissue modulus can be scaled to determine the 'ideal' modulus for absolute statistical agreement (Y=X). In this case, the ideal effective tissue modulus for the Morgan et al. (2003) pooled relationship was 20.43 GPa, which is consistent with the 20 GPa modulus chosen. Although Morgan et al. (2003) do not report an effective tissue modulus for the pooled samples in their study, they do report an effective tissue modulus of 22 GPa for their relationship developed from femoral neck specimens. Our effective tissue modulus for this same relationship would be 27 GPa, when scaled to reach absolute statistical agreement. When translating micro-level mechanical property relationships to the apparent level, the apparent density is determined by the relationship between apparent modulus and apparent density. For accurate characterization among anatomic sites, this density range must be consistent because it is the only factor that is controlled in the density-modulus mapping to clinical-resolution derived FEMs.

Single anatomic site relationships are typically developed using an average density of a physical bone specimen, resulting in a relatively narrow range of density values. This is especially true in vertebrae, the greater trochanter, and the proximal tibia (ρ_{app} = 0.09 – 0.41) (Morgan et al., 2003). Anatomic sites that experience larger loads typically result in density values that extend to a larger range. When mapping density-modulus relationships derived from clinical-resolution scans, regardless of anatomic site, each voxel incorporates the full range of density values representative of bone, and therefore requires extrapolation beyond the typical range of average densities presented in many density-modulus relationships (Helgason et al., 2008).

It is generally reported that due to variations in trabecular architecture and density by anatomic site, extrapolation beyond the presented density ranges and to alternative anatomic sites, is not recommended (Helgason et al., 2008; Kopperdahl et al., 2002; Morgan et al., 2003). However, the apparent density ranges for the Morgan et al. (2003) relationships (0.26 – 0.75 g/cm^3 for the femoral neck, and 0.09 – 0.75 g/cm^3 for pooled), were consistent with the apparent density range of the samples used in the present study (0.10 – 0.90 g/cm^3). Even though the density range is similar, these relationships ignore the variable contribution of trabecular architecture between anatomic sites. It has been reported that bone volume fraction (BV/TV) accounts for ~90% of the elastic properties of

trabecular bone, with architecture (based on fabric tensor) accounting for ~10% (Maquer et al., 2015). Because BV/TV is inherently related to density, this may indicate that a single density modulus relationship could accurately represent the mechanical properties of trabecular bone, independent of anatomic site. For this to hold true, the density range must be similar and anisotropy must be integrated into the QCT-FEMs. The integration of anisotropy into QCT-FEMs adds a level of complexity that is beyond the scope of many studies and has yet to be compared beyond the patella (Latypova et al., 2016), femur (Enns-Bray et al., 2016), or tibia (Nazemi et al., 2017).

For the Büchler et al. (2002) relationship the apparent density range for the samples used in the development of this relationship is unknown. However, it is possible that the heterogeneous tissue modulus of these samples more closely match the true heterogeneous distribution of the specimens tested in this study and may account for why this relationship was a stronger predictor of heterogeneous µ-FEMs SED_{app}. Load transfer paths are dependent not only on trabecular architecture, but also on the density of individual trabeculae (Ün et al., 2006). As such, multiple studies using experimental results for reference, have found that accounting for mineral heterogeneity in trabeculae improves the accuracy of µ-FEMs compared to homogeneous µ-FEMs (Bourne and Van Der Meulen, 2004; Harrison et al., 2008; Jaasma et al., 2002; Renders et al., 2011, 2008; van Ruijven et al., 2007). The variation in mineralization across the width of trabeculae has significant influence on the bending stiffness, and as such may greatly alter the mechanical properties under compressive loading (Renders et al., 2011). Due to this fact, it is not possible to scale the heterogeneous tissue modulus as with the homogeneous effective tissue modulus. Although the µ-FEM material mapping uses a linear mapping of tissue modulus based on CT-intensity, the distribution of CT-intensity varies by specimen, and the bending stresses are dependent on this tissue modulus distribution at the trabecular level.

The ‘ideal’ density-modulus relationship would result in absolute statistical agreement (Y=X) between µ-FEM and QCT-FEM SED_{app}, which was the primary metric for determining which relationship best mapped the mechanical properties to the QCT-FEMs. Although the Schaffler & Burr (1988) and Rice (1988) relationship had the largest coefficient of determination (r^2) and lowest standard error of regression (SE), the proportional error shown in the Bland-Altman plots was largest for this relationship. The

Morgan et al. (2003) relationships showed similar coefficients of determination (r^2) and standard errors of regression (SE) for both the homogeneous (Table 2.2) and heterogeneous cases (Table 2.3) but had lower bias for the homogeneous case (Figure 2.2), compared to the heterogeneous case (Figure 2.3). If an effective homogeneous tissue modulus is assumed to accurately represent the tissue-level mechanical response of the trabecular bone, then the Morgan et al. (2003) density-modulus relationship from pooled anatomic sites should be used. However, the perhaps more relevant heterogeneous tissue modulus case (Bourne and Van Der Meulen, 2004; Harrison et al., 2008; Jaasma et al., 2002; Renders et al., 2011, 2008; van Ruijven et al., 2007) indicates that the Büchler et al. (2002) density-modulus relationship should be used to model trabecular bone in shoulder FEMs.

A limitation of this study is that physical bone specimens were not directly tested. The wide variety of testing protocols that are reported in density-modulus relationship development (Helgason et al., 2008) provides a confounding bias that is difficult to account for when testing the mapping of constitutive relationships. Although physical bone specimen testing has become the 'gold standard' in density-modulus relationship development, recent literature has shown excellent correlations of µ-FEMs with empirical data (Chen et al., 2017; Costa et al., 2017), indicating that µ-FEMs can accurately determine the apparent mechanical properties of trabecular bone without the need for empirical mechanical testing. The computational methodology used in this study eliminates the systematic error resulting from specimen preparation, end-artifacts, physical measurement error, and stiffness variations that may occur in testing apparatus. This methodology allows for an indirect comparison and determination of the most accurate density-modulus relationships, as suggested by Helgason et al. (2008). To provide external validation with these comparisons, empirical modeling could be combined with µ-FEM development. These models should replicate empirical boundary conditions using digital volume correlation (DVC) and compare full-field DVC results to computational results (Chen et al., 2017).

2.5 CONCLUSION:

Further studies should be performed to determine whether these relationships can be translated to whole bones. This may provide insight into the predictive capabilities of using

pooled or custom density-modulus relationships in the mapping of mechanical properties in future clinical-resolution derived FEMs of the shoulder.

2.6 REFERENCES:

Bayraktar, H.H., Morgan, E.F., Niebur, G.L., Morris, G.E., Wong, E.K., Keaveny, T.M., 2004. CoMParison of the elastic and yield properties of human femoral trabecular and cortical bone tissue. J. Biomech. 37, 27–35. Doi:10.1016/S0021-9290(03)00257-4

Bourne, B.C., Van Der Meulen, M.C.H., 2004. Finite element models predict cancellous apparent modulus when tissue modulus is scaled from specimen CT-attenuation. J. Biomech. 37, 613–621. Doi:10.1016/j.jbiomech.2003.10.002

Bouxsein, M.L., Boyd, S.K., Christiansen, B.A., Guldberg, R.E., Jepsen, K.J., M??ller, R., 2010. Guidelines for assessment of bone microstructure in rodents using micro-computed tomography. J. Bone Miner. Res. 25, 1468–1486. Doi:10.1002/jbmr.141

Brennan, O., Kennedy, O.D., Lee, T.C., Rackard, S.M., O'Brien, F.J., 2009. Biomechanical properties across trabeculae from the proximal femur of normal and ovariectomised sheep. J. Biomech. 42, 498–503. Doi:10.1016/j.jbiomech.2008.11.032

Büchler, P., Ramaniraka, N.A., Rakotomanana, L.R., Iannotti, J.P., Farron, A., 2002. A finite element model of the shoulder: application to the coMParison of normal and osteoarthritic joints. Clin. Biomech. 17, 630–639. Doi:10.1016/S0268-0033(02)00106-7

Campoli, G., Weinans, H., van der Helm, F., Zadpoor, A. a, 2013. Subject-specific modeling of the scapula bone tissue adaptation. J. Biomech. 46, 2434–41. Doi:10.1016/j.jbiomech.2013.07.024

Carter, D., Hayes, W., 1977. The compressive behavior of bone as a two-phase porous structure. J. Bone Jt. Surg. 59(7), 954-962

Chen, Y., Dall′Ara, E., Sales, E., Manda, K., Wallace, R., Pankaj, P., Viceconti, M., 2017. Micro-CT based finite element models of cancellous bone predict accurately displacement once the boundary condition is well replicated: A validation study. J. Mech. Behav. Biomed. Mater. 65, 644–651. Doi:10.1016/j.jmbbm.2016.09.014

Costa, M.C., Tozzi, G., Cristofolini, L., Danesi, V., Viceconti, M., Dall'Ara, E., 2017. Micro finite element models of the vertebral body: Validation of local displacement

predictions. PloS One 12, 1–18. Doi:10.1371/journal.pone.0180151

Dahan, G., Trabelsi, N., Safran, O., Yosibash, Z., 2016. Verified and validated finite element analyses of humeri. J. Biomech. 49, 1094–1102. Doi:10.1016/j.jbiomech.2016.02.036

Enns-Bray, W.S., Ariza, O., Gilchrist, S., Widmer Soyka, R.P., Vogt, P.J., Palsson, H., Boyd, S.K., Guy, P., Cripton, P.A., Ferguson, S.J., Helgason, B., 2016. Morphology based anisotropic finite element models of the proximal femur validated with experimental data. Med. Eng. Phys. 38, 1339–1347. Doi:10.1016/j.medengphy.2016.08.010

Faieghi, M., Knowles, N.K., Tutunea-fatan, O.R., Ferreira, L.M., 2019. Fast Generation of Cartesian Meshes from Micro-Computed Tomography Data. Comput. Aided Des. Appl. 16, 161–171.

Guldberg, R.E., Hollister, S.J., Charras, G.T., 1998. The Accuracy of Digital Image-Based Finite Element Models. J. Biomech. Eng. 120, 289. Doi:10.1115/1.2798314

Gupta, S., Dan, P., 2004. Bone geometry and mechanical properties of the human scapula using computed tomography data. Trends Biomater Artif Organs 17, 61–70.

Harrison, N.M., McDonnell, P.F., O'Mahoney, D.C., Kennedy, O.D., O'Brien, F.J., McHugh, P.E., 2008. Heterogeneous linear elastic trabecular bone modelling using micro-CT attenuation data and experimentally measured heterogeneous tissue properties. J. Biomech. 41, 2589–2596. Doi:10.1016/j.jbiomech.2008.05.014

Hayes, W.C., 1991. Biomechanics of cortical and tubecular bone: implications for assessment of fracture risk, in: Basic Orthopaedic Biomechanics. Raven Press, New York, pp. 93–142.

Helgason, B., Perilli, E., Schileo, E., Taddei, F., 2008. Mathematical relationships between bone density and mechanical properties: a literature review. Clin. … 23, 135–146. Doi:10.1016/j.clinbiomech.2007.08.024

Jaasma, M.J., Bayraktar, H.H., Niebur, G.L., Keaveny, T.M., 2002. Biomechanical effects of intraspecimen variations in tissue modulus for trabecular bone. J. Biomech. 35, 237–246. Doi:10.1016/S0021-9290(01)00193-2

Knowles, N., Langohr, G.D.G., Faieghi, M., Nelson, A., Ferreira, L.M., 2019. Development of a validated glenoid trabecular density-modulus relationship. J. Mech.

Behav. Biomed. Mat. 90, 140-145

Knowles, N., Reeves, J.M., Ferreira, L.M., 2016. Quantitative Computed Tomography (QCT) derived Bone Mineral Density (BMD) in finite element studies: a review of the literature. J. Exp. Orthop. 3, 36. Doi:10.1186/s40634-016-0072-2

Kopperdahl, D.L., Morgan, E.F., Keaveny, T.M., 2002. Quantitative computed tomography estimates of the mechanical properties of human vertebral trabecular bone. J. Orthop. Res. 20, 801–805. Doi:10.1016/S0736-0266(01)00185-1

Latypova, A., Maquer, G., Elankumaran, K., Pahr, D., Zysset, P., Pioletti, D.P., Terrier, A., 2016. Identification of elastic properties of human patellae using micro-finite element analysis. J. Biomech. 49, 3111–3115. Doi:10.1016/j.jbiomech.2016.07.031

Maquer, G., Musy, S.N., Wandel, J., Gross, T., Zysset, P.K., 2015. Bone volume fraction and fabric anisotropy are better determinants of trabecular bone stiffness than other morphological variables. J. Bone Miner. Res. 30, 1000–1008. Doi:10.1002/jbmr.2437

Morgan, E., Bayraktar, H., Keaveny, T., 2003. Trabecular bone modulus–density relationships depend on anatomic site. J. Biomech. 36(7), 897-904

Morgan, E.F., Keaveny, T.M., 2001. Dependence of yield strain of human trabecular bone on anatomic site . J. Biomech. 34, 569–577.

Nazemi, S.M., Kalajahi, S.M.H., Cooper, D.M.L., Kontulainen, S.A., Holdsworth, D.W., Masri, B.A., Wilson, D.R., Johnston, J.D., 2017. Accounting for spatial variation of trabecular anisotropy with subject-specific finite element modeling moderately improves predictions of local subchondral bone stiffness at the proximal tibia. J. Biomech. 59, 101–108. Doi:10.1016/j.jbiomech.2017.05.018

Niebur, G.L., Yuen, J.C., Hsia, A.C., Keaveny, T.M., 1999. Convergence Behavior of High-Resolution Finite Element Models of Trabecular Bone. J. Biomech. Eng. 121, 629. Doi:10.1115/1.2800865

Oftadeh, R., Perez-Viloria, M., Villa-Camacho, J.C., Vaziri, A., Nazarian, A., 2015. Biomechanics and Mechanobiology of Trabecular Bone: A Review. J. Biomech. Eng. 137, 010802. Doi:10.1115/1.4029176

Podshivalov, L., Fischer, A., Bar-Yoseph, P.Z., 2011. 3D hierarchical geometric modeling and multiscale FE analysis as a base for individualized medical diagnosis of bone structure. Bone 48, 693–703. Doi:10.1016/j.bone.2010.12.022

Renders, G.A.P., Mulder, L., Langenbach, G.E.J., van Ruijven, L.J., van Eijden, T.M.G.J., 2008. Biomechanical effect of mineral heterogeneity in trabecular bone. J. Biomech. 41, 2793–2798. Doi:10.1016/j.jbiomech.2008.07.009

Renders, G.A.P., Mulder, L., van Ruijven, L.J., Langenbach, G.E.J., van Eijden, T.M.G.J., 2011. Mineral heterogeneity affects predictions of intratrabecular stress and strain. J. Biomech. 44, 402–407. Doi:10.1016/j.jbiomech.2010.10.004

Rice, J., Cowin, S., Bowman, J., 1988. On the dependence of the elasticity and strength of cancellous bone on apparent density. J. Biomech. 155-168

Schileo, E., Dall'Ara, E., Taddei, F., 2008. An accurate estimation of bone density improves the accuracy of subject-specific finite element models. J. Biomech. 41(11), 2483-2491

Schileo, E., Taddei, F., Malandrino, A., Cristofolini, L., Viceconti, M., 2007. Subject-specific finite element models can accurately predict strain levels in long bones. J. Biomech. 40, 2982–2989. Doi:10.1016/j.jbiomech.2007.02.010

Ün, K., Bevill, G., Keaveny, T.M., 2006. The effects of side-artifacts on the elastic modulus of trabecular bone. J. Biomech. 39, 1955–1963. Doi:10.1016/j.jbiomech.2006.05.012

Unnikrishnan, G.U., Barest, G.D., Berry, D.B., Hussein, A.I., Morgan, E.F., 2013. Effect of specimen-specific anisotropic material properties in quantitative computed tomography-based finite element analysis of the vertebra. J. Biomech. Eng. 135, 101007–11. Doi:10.1115/1.4025179

van Ruijven, L.J., Mulder, L., van Eijden, T.M.G.J., 2007. Variations in mineralization affect the stress and strain distributions in cortical and trabecular bone. J. Biomech. 40, 1211–1218. Doi:10.1016/j.jbiomech.2006.06.004

CHAPTER 3 – DEVELOPMENT OF A VALIDATED GLENOID TRABECULAR DENSITY-MODULUS RELATIONSHIP

OVERVIEW: *This chapter describes the development of a trabecular density-modulus relationship, specific to glenoid trabecular bone. This was accomplished using simulated loading of micro finite element models and compared to co-registered quantitative computed tomography generated finite element models. The accuracy of the derived relationships were compared on the basis of apparent strain energy density between the models at the two hierarchical levels.*[3]

[3]A version of this work has been published: Knowles NK, Langohr GDG, Athwal GS, Faieghi M, Nelson A, Ferreira LM. Development of a Validated Glenoid Density-Modulus Relationship. The Journal of the Mechanical Behavior of Biomedical Materials. 2019; 90:140-145

3.1 INTRODUCTION:

Subject-specific finite element models (FEMs) are a valuable tool in biomechanical research. Highly correlated relationships exist between CT-intensity and bone mechanical properties, allowing for mechanical properties to be accurately modeled using clinical-resolution CT images (Knowles et al., 2016). These density-modulus relationships depend on bone architecture and mineralization, and are therefore site-specific (Helgason et al., 2008; Morgan et al., 2003). As such, previous studies have determined that anatomic site-specific and subject-specific modeling parameters increase the accuracy of FEMs derived with clinical-resolution scans (Campoli et al., 2013; Schileo et al., 2008, 2007; Unnikrishnan et al., 2013). This allows for patient-specific computational modeling or development of population-based statistical shape models.

Most reported density-modulus relationships are determined from mechanical testing of small bone cores. Testing protocols have suffered from potentially high end-artifact errors due to specimen preparation, off-axis coring, and misrepresentation of boundary conditions (Chen et al., 2017). This may result in calculation of a transverse modulus, limiting the accuracy of previously developed relationships (Bayraktar et al., 2004; Helgason et al., 2008). Additionally, coring of trabecular bone samples inherently disturbs the outer trabeculae, reducing or eliminating these trabeculae's load carrying capacity. These side-artifacts have been suggested to greatly influence the determination of modulus, and subsequently density-modulus relationships. Ün et al. report implications for all modulus development, especially those with low density, and the correction factors developed within should be used to adjust previously developed moduli (Ün et al., 2006).

A possible additional source of error arises in relationship development due to systematic error in density measures (Knowles et al., 2016; Zioupos et al., 2008). Accurate bone density measurements are required as the initial input in density-modulus relationships, and therefore, the effect of variations in density measures between studies is difficult to elucidate. Direct relationships between computational derived density provided by quantitative computed tomography (QCT) and mechanical properties has the potential to minimize these errors and may optimize development of density-modulus relationships (Kopperdahl et al., 2002), and the associated material mapping accuracy.

Although recognized as an imminent need (Pomwenger et al., 2014), a validated density-modulus relationship specific to the shoulder does not exist, potentially limiting the accuracy of clinical-resolution derived shoulder FEMs. As such, previous FE studies of the scapular side of the shoulder have used density-modulus relationships developed for alternate anatomical locations. None of these studies have provided experimental validation of the FE results, limiting translation of outcomes and comparisons among studies. The objective of this study was to develop a validated glenoid trabecular density-modulus relationship using computational comparisons between micro-computed tomography (μ-CT) FEMs and co-registered QCT-FEMs.

3.2 METHODS:

3.2.1 Specimens and Computed Tomography Scanning

Fourteen cadaveric scapulae (7 male, 7 female) were denuded of soft tissue. Each specimen was scanned with a cone-beam μ-CT scanner (Nikon XT H 225 ST, Nikon Metrology, NV) with the largest field of view (FOV) possible to capture the entire glenoid structure in the largest specimen. For consistency, uniform parameters were used for all subsequent specimens, regardless of specimen size. This resulted in a spatial resolution of 32 μm, which was less than one-fourth the mean trabecular thickness recommended for numerical convergence (Guldberg et al., 1998; Niebur et al., 1999). Microarchitectural information is provided in Table 3.1.

Subsequently, all specimens were scanned with a multi-slice clinical CT-scanner (GE Discovery CT750 HD, Milwaukee, WI, USA) with isotropic voxels (Table 3.2). A dipotassium phosphate (K_2HPO_4) (QCT Pro, Mindways Software Inc., Austin, TX, USA) calibration phantom was scanned with each specimen during clinical scanning. This phantom consists of five rods of varying low and high atomic number materials calibrated against liquid K_2HPO_4 and water solutions. This provided a consistent density reference between specimens, and for scaling CT-attenuation values to known QCT- density values (g_{K2HPO4}/cm^3). Because the QCT phantom is not scanner specific for calibration, it provides a density reference required for the relationships developed to be translatable to any bone scanned in another scanner, provided the scan settings remain similar.

Table 3.1: Microarchitectural information measurements for the samples tested

n	BV/TV	Tb.Th (mm)	Tb.Sp (mm)	Tb.N (1/mm)
98	0.25 ± 0.08	0.26 ± 0.05	0.80 ± 0.13	0.93 ± 0.23
	(0.10 – 0.51)	(0.17 – 0.40)	(0.29 – 1.03)	(0.53 – 1.52)

Values are mean ± standard deviation (range). All values were calculated using SkyScan CTAn (Bruker micro-CT, Kontich, BE) based on 3D morphometric calculations. BV/TV – Bone Volume/Total Volume; Tb.Th – Trabecular Thickness; Tb.Sp – Trabecular Separation; Tb.N – Trabecular Number

Table 3.2: Scan Parameters for Micro- and Quantitative-Computed Tomography Specimen Scanning

Parameter	Micro-CT Scans	Quantitative-CT Scans
Voxel Size (isotropic) (μm^3)	32	625
Peak Voltage (kVp)	95	120
Current (mA)	0.064	200
Projections	3141	n/a
Exposure (ms)	1000	1460
Calibration Phantom	None	K_2HPO_4
Convolution Kernel	n/a	BONEPLUS

The µ-CT images were exported as 16-bit digital imaging and communications in medicine (DICOM) files and loaded to medical imaging software (Mimics®, Materialize, V.20.0, Leuven, BE) for finite element (FE) pre-processing. High frequency noise was removed from the images using an embedded Gaussian blur filter ($\sigma = 1.25$, support = 2). A specimen-specific threshold of the maximum gray value was used to best preserve trabecular bone architecture (Bouxsein et al., 2010). Segmentation from the surrounding marrow was performed using region growing with embedded 6-connectivity to ensure that all voxels were connected for FEM development. A three-dimensional (3D) stereolithography (STL) model of the scapula was generated and transferred to 3-Matic (Materialize, V.12.0, Leuven, BE) for placement of volumes of interest (VOIs).

3.2.2 Micro-Computed Tomography Image Processing and Finite Element Model Generation

The VOIs measuring 10x5x5 mm were positioned medially adjacent to the subchondral bone in each specimen. This size was chosen to provide adequate depth for smaller trabecular glenoid vaults in female scapulae, while maintaining the recommended 2:1 aspect ratio (Helgason et al., 2008). The VOI was evenly divisible by the QCT voxel dimensions (0.625 mm) to avoid partial volume error effects in the QCT-FEMs. A maximum number of VOIs were placed in each specimen to ensure that only trabecular architecture was present, resulting in 98 ‘virtual bone cores’ for the 14 specimens. The VOIs were transferred to Mimics, registered to the DICOM images, and voxel coordinates and grayscale intensity values were exported. Using custom-written code, eight node brick elements (C3D8) were constructed per voxel, while the modulus of each element was inherited from the corresponding voxel’s grayscale intensity value (Faieghi et al., 2019).
Two cases of µ-FEMs were considered: a homogeneous tissue modulus, and a heterogeneous tissue modulus scaled by CT-intensity. For the homogeneous case, a uniform modulus of 20 GPa was applied to all elements in each µ-FEM (98 µ-FEMs). In the heterogeneous µ-FEMs, a model-specific heterogeneous element-wise material mapping was applied to each element using a quantitative linear mapping of tissue modulus to CT-intensity with a slope factor of 1.4, and a reference tissue modulus of 20 GPa (98 µ-

FEMs). This method has been shown to provide the best agreement between experimental and simulated modulus (Table 3.3) (Bourne and Van Der Meulen, 2004).

Each of the 98 homogeneous µ-FEMs and 98 heterogeneous µ-FEMs were fully constrained on the medial edge and compressively loaded to 0.5% apparent strain (Abaqus V.6.14, Simulia, Providence, RI, USA). Custom Matlab (V. R2017a, Mathworks Inc., Natick, MA) code generated the Abaqus input files to ensure reproducibility of the boundary and loading conditions. The apparent stress and strain were used to calculate the apparent modulus (E_{app}), and subsequently the apparent strain energy density (SED_{app}), for each µ-FEM. The apparent stress was determined using the measured reaction force and apparent area (25 mm^2) of the µ-FEMs. A uniform displacement (0.05 mm) was used to apply the 0.5% apparent strain (0.005 ε_{app}) as determined from the core gauge length (10 mm). The SED_{app} was calculated using the computational strain energy output and the core apparent volume (250 mm^3), which is equivalent to the area under the apparent stress – apparent strain curve (Figure 3.1).

3.2.3 Density-Modulus Relationship Development and Quantitative-Computed Tomography Finite Element Model Generation

The QCT images in DICOM format were loaded into Mimics and pre-processed to create a filled scapular STL model, which was transferred to 3-Matic. This model was co-registered to the µ-CT derived scapula using iterative closest points fitting. The same VOIs previously placed were co-registered using the coordinate transformation from the µ-CT and QCT coordinate systems. This allowed for precise placement of the VOIs in the QCT images when registered to the clinical DICOM images in Mimics. The resulting QCT VOIs consisted of 1024 voxels. Similar custom written Matlab code was developed for direct conversion to eight-node brick elements (C3D8), while allowing for element-wise density-modulus mapping by converting the Hounsfield (HU) values to QCT density (g_{K2HPO4}/cm^3) and applying the derived density-modulus relationships. This code also produced identical boundary and loading conditions to the µ-FEMs for each QCT-FEM. The apparent modulus (E_{app}) for each µ-FEM was plotted as a function of the mean QCT density (g_{K2HPO4}/cm^3) for each virtual bone core. To determine density-modulus fitting accuracy and for consistency with other density modulus relationships developed in

Table 3.3: Heterogeneous tissue modulus by specimen for μ-FEMs

Specimen	Sex	Age	Mean (MPa)	Maximum (MPa)	Coefficient of Variation (%)
1	F	62	10339 ± 551	19951 ± 332	33
2	F	68	8766 ± 513	19998 ± 713	37
3	F	69	9495 ± 618	19998 ± 382	34
4	F	60	10036 ± 577	19999 ± 800	34
5	M	80	9156 ± 772	20000 ± 504	34
6	M	72	9949 ± 700	20017 ± 1097	33
7	M	78	8956 ± 659	19999 ± 362	35
8	F	73	8426 ± 320	19999 ± 124	35
9	M	50	11073 ± 304	20000 ± 669	30
10	F	66	9048 ± 423	19998 ± 145	35
11	F	65	8819 ± 250	20055 ± 342	32
12	M	73	11622 ± 253	19999 ± 1216	23
13	M	58	10559 ± 370	19999 ± 593	18
14	M	64	9728 ± 402	20000 ± 316	27

Values are mean ± standard deviation (SD) by specimen; however, each of the 98 μ-FEMs had a model-specific element-wise tissue modulus. The SD for coefficient of variation in all specimens was zero.

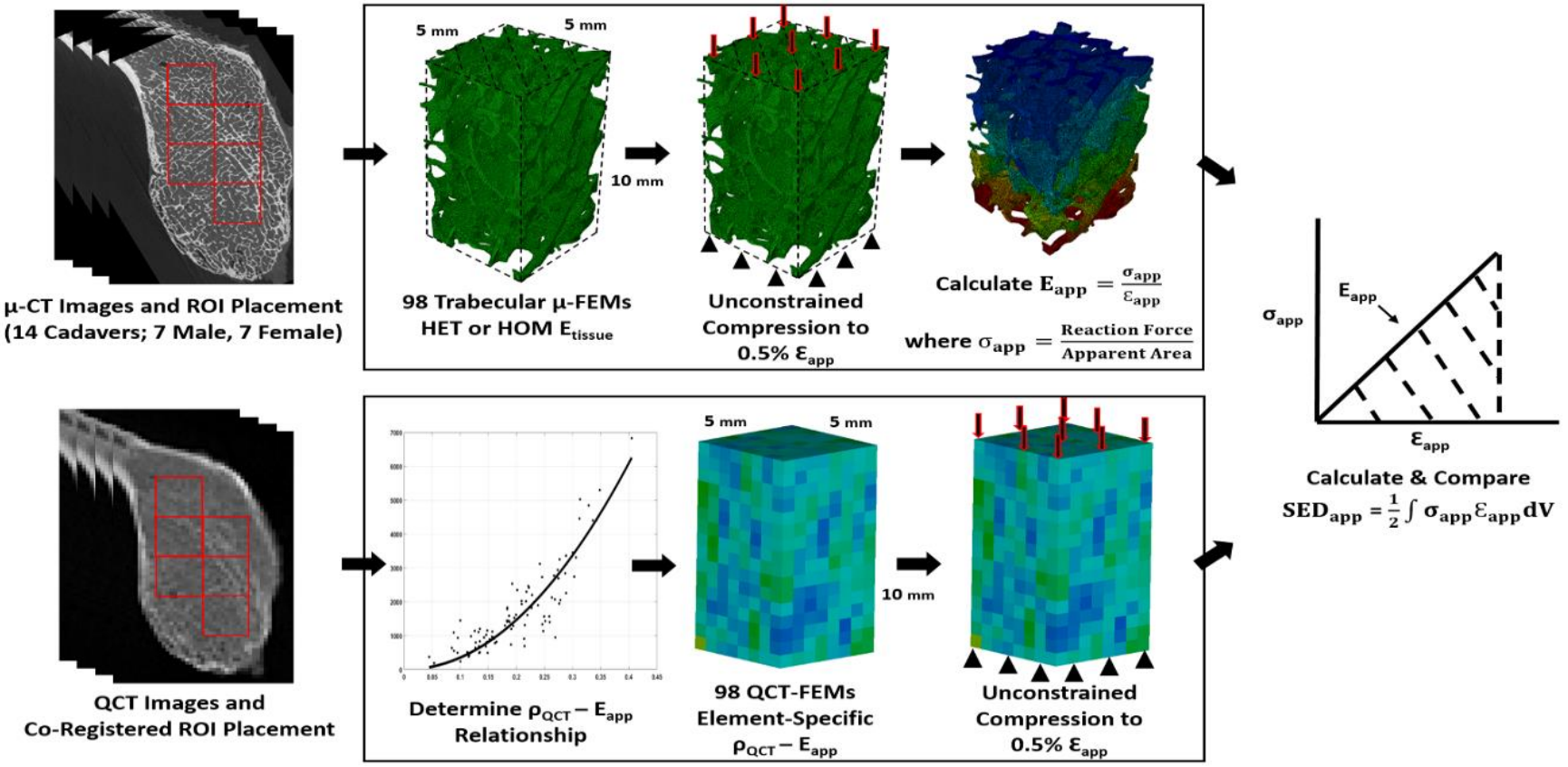

Figure 3.1: The complete workflow for validation of a glenoid-specific density- modulus relationship using apparent modulus derived from co-registered trabecular μ-FEMs

Unconstrained and compressed μ-FEMs, with either a homogeneous (HOM) or heterogeneous (HET) tissue modulus, were first completed to determine the apparent modulus of each of the 98 trabecular cores. Cores were co-registered to QCT images and used to determine the QCT-density of each core. This provided the QCT-density-apparent modulus relationship that was mapped to each of the 98 QCT-FEMs on an element-wise basis. The apparent strain energy density was compared between the μ-FEMs and corresponding QCT-FEMs as validation.

the literature (Helgason et al., 2008; Kopperdahl et al., 2002; Morgan et al., 2003), three homogeneous relationships were developed. An ordinary least squares regression power fit (OLS), an identical 'fixed' ordinary least squares regression power fit through minimum and maximum values of 0 and 20 GPa (FOLS), and a power fit with coefficients derived from restricted maximum likelihood estimation linear regression log-transformed data (LOG). The µ-FEM heterogeneous tissue modulus case used an OLS regression power fit (Figure 3.2).

The relationships can also be adapted for use with apparent density (hydrated weight of bone tissue/apparent volume of core) using the relationships developed from the 98 co-registered VOIs (Equation 3.1-3.3):

$$\rho_{QCT}\ \left[\frac{g_{K2HPO4}}{cm^3}\right] = 0.821\frac{BV}{TV} - 0.003 \qquad \text{(Equation 3.1)}$$

$$\rho_{QCT}\ \left[\frac{g_{K2HPO4}}{cm^3}\right] = 0.821\frac{\rho_{app}}{1.8} - 0.003, \qquad \text{(Equation 3.2)}$$

$$where\ \frac{BV}{TV} = \frac{\rho_{app}}{\rho_{real}},$$

with $\rho_{real} = 1.8\ \left[\frac{g}{cm^3}\right]$ (Carter and Hayes, 1977)

$$\rho_{app}\ \left[\frac{g}{cm^3}\right] = 2.192\rho_{QCT} + 0.007 \qquad \text{(Equation 3.3)}$$

Each of the 4 relationships in Figure 3.2 was used to map element-wise modulus to each of the 392 QCT-FEMs (4 relationships x 98 QCT-FEMs = 392), using the custom Matlab code. The boundary conditions were replicated, and each QCT-FEM was identically compressively loaded to 0.5% strain. Apparent strain energy density (SED_{app}) between µ-FEMs and QCT-FEMs were used as validation. To account for more samples than donors, restricted maximum likelihood estimation (REML) linear regression fits were used to compare µ-FEM SED_{app} and QCT-FEM SED_{app} for each relationship (Kopperdahl et al., 2002). As discussed above, it has been suggested that coring of bone samples for modulus determination underestimates the *in-vivo* modulus due to side-artifacts created by the loss of load-caring capacity of outer-trabeculae (Ün et al., 2006). The measured modulus can

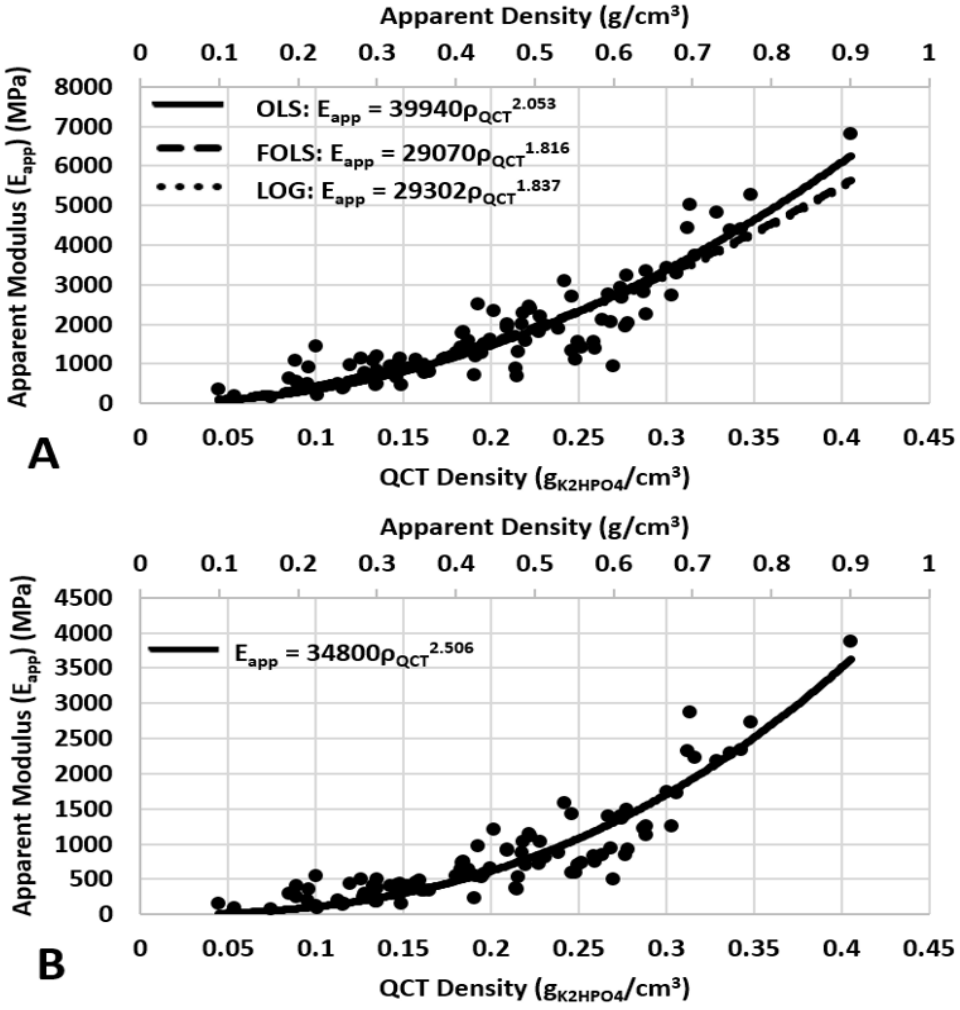

Figure 3.2: Density-modulus relationships for homogeneous µ-FEM tissue

Three fitting methods were compared for this case: ordinary least squares regression power fit (OLS), fixed ordinary least squares regression power fit through a minimum modulus of 0 GPa and maximum of 20 GPa (FOLS), and a least squares regression power fit with coefficients derived from log-transformed data (LOG) **(A)**. The heterogeneous µ-FEM tissue modulus used an ordinary least squares regression power fit **(B)**.

be corrected by accounting for this loss of load carrying capacity using a correction factor (Equation 3.4):

$$\alpha = \frac{E_{corrected}}{E_{measured}} = \left(\frac{1}{1-2\beta}\right)^2, where\ \beta = \frac{a*Tb.Sp^* + b}{W}$$ (Ün et al., 2006) (Equation 3.4)

The linear coefficients are empirically determined to be a = 0.51 and b = -0.13. Although these were originally derived for cylindrical specimens, the authors state the equation is translatable to cubic specimens by using edge width, W. They also report that results can be extrapolated to alternate anatomic locations because Tb.Sp is mechanistically related to side-artifact. Equation 3.4 was applied to each of the four density-modulus relationships developed for the homogeneous and heterogeneous tissue modulus cases for translation into whole bone scapular models.

3.3 RESULTS:

The trabecular-specific glenoid density-modulus relationships were $E = 39940\rho_{qct}^{2.053}$, $E = 29070\rho_{qct}^{1.816}$, $E = 29302\rho_{qct}^{1.837}$, for the homogeneous tissue modulus OLS, FOLS, and LOG, respectively. For the heterogeneous tissue modulus, the relationship was $E = 34800\rho_{qct}^{2.506}$. The OLS homogeneous relationship was corrected to $E = 38780\rho_{qct}^{1.88}$. Only the OLS homogeneous relationship was corrected because it was the most accurate homogeneous density-modulus relationship. The heterogeneous relationship was corrected to $E = 32790\rho_{qct}^{2.307}$. These relationships are thought to be representative of whole scapula mechanical property mapping.

The restricted maximum likelihood estimation (REML) linear regression fits of SED_{app} showed high correlations for all three homogeneous relationships; however, no relationship accurately predicted µ-FEM SED_{app}. When the µ-FEMs accounted for the heterogeneous tissue modulus based on CT-intensity (Table 3.3), there was near absolute statistical agreement between the QCT-FEM SED_{app} and µ-FEM SED_{app} (Figure 3.3 & Table 3.4). The Bland-Altman plots indicate a decrease of outliers present when heterogeneous tissue moduli are considered in µ-FEMs.

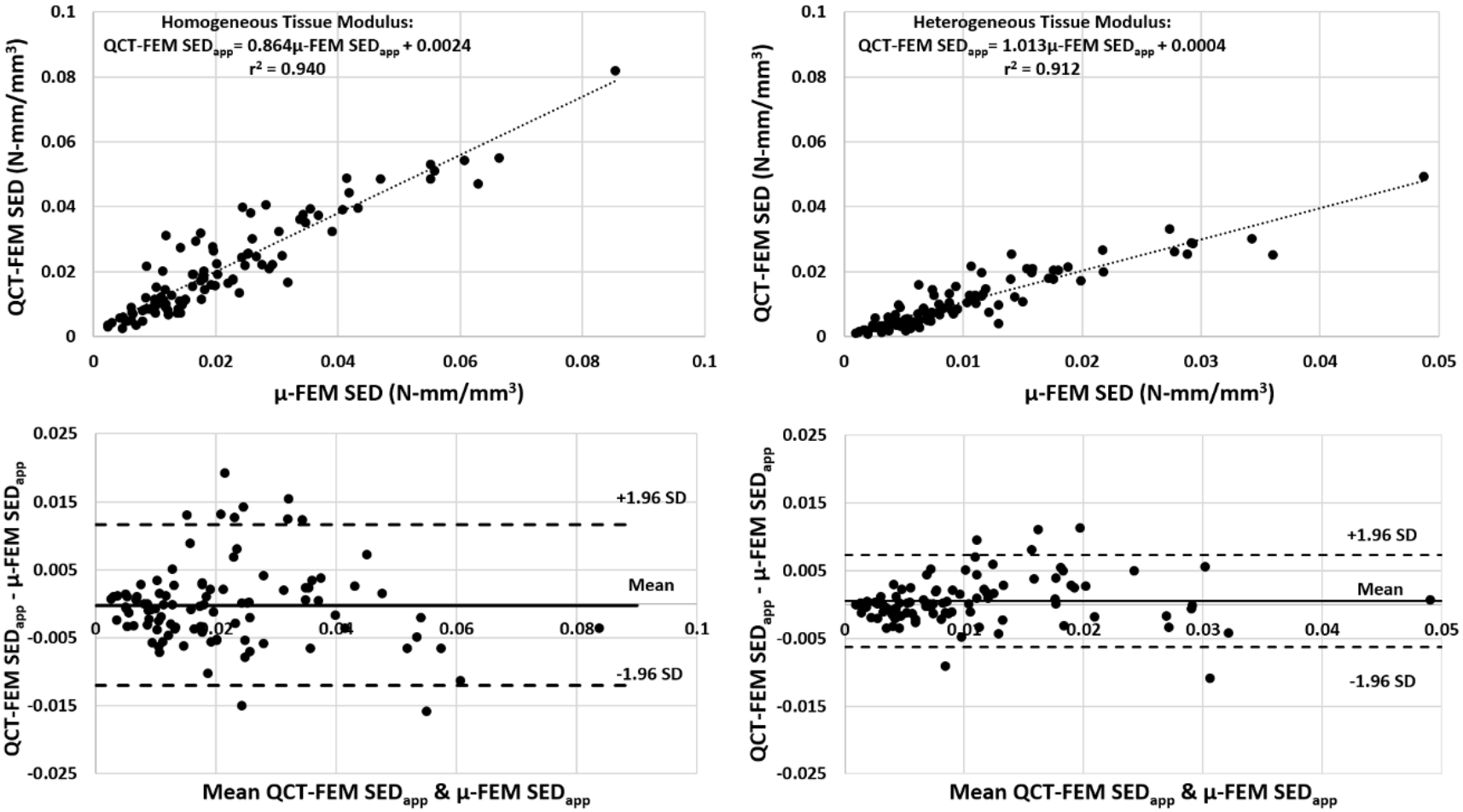

Figure 3.3: Restricted maximum likelihood estimation linear regression fits and Bland-Altman plots of the ordinary least squares regression fit apparent strain energy density (SED_{app})

Comparison for homogeneous (left) and heterogeneous (right) μ-FEM tissue moduli.

Table 3.4: Results from restricted maximum likelihood estimation linear regression fits of apparent strain energy (SED_{app}) predictions between QCT-FEMs and μ-FEMs

QCT-FEM SED_{app} = mμ-FEM SED_{app} + b

μ-FEM	r^2	m	b	SE	SE/mean
Homogeneous OLS	0.940	0.864	0.0024	0.0040	18.6%
Homogeneous FOLS	0.945	0.757	0.0046	0.0034	16.1%
Homogeneous LOG	0.945	0.752	0.0043	0.0034	16.1%
Heterogeneous OLS	0.912	1.013	0.0004	0.0028	26.6%

SE – Standard error of regression; OLS – Ordinary least squares regression power fit; FOLS – Fixed ordinary least squares regression power fit; LOG – Least squares regression fit parameters derived from log-transformed data

3.4 DISCUSSION:

This study used a new computational methodology for the development of density-modulus relationships using µ-CT and co-registered QCT derived FEMs. This allows for a direct comparison of the mechanical properties of trabecular architecture and density to be translated to linear isotropic QCT derived FEMs. Although only linear isotropic density-modulus material mapping was considered in this study, this methodology could potentially be translated to validate bone strength and fracture using similar µ-FEMs and co-registered QCT-FEMs. The predictive capabilities of this translation into clinically derived models has the potential to greatly improve fracture prediction in patient populations.

The results of this study suggest that glenoid trabecular density-modulus relationships mapped to QCT-FEMs based on homogeneous effective tissue moduli in µ-FEMs under predict apparent strain energy density (SED_{app}). When considering density-modulus relationships derived from µ-FEMs accounting for a heterogeneous distribution of tissue moduli, near absolute statistical agreement (Y = X) was found in SED_{app}. This enforces the point that load transfer paths are dependent on both the density distribution of individual trabeculae as well as trabecular architecture (Ün et al., 2006). In linear-isotropic QCT-FEMs, the mechanical properties are determined solely from the CT-intensity and associated QCT-density of each voxel. As such, it is essential that density-modulus relationships used to map mechanical properties to the bone are directly related to QCT-density representative of the site-specific distribution of trabecular orientation, architecture, and mineralization. The goal of which is to ensure that the mapped mechanical properties are most representative of the bone being modeled.

It has been suggested that material heterogeneity has a minimal influence on the apparent modulus (E_{app}) of trabecular bone (Gross et al., 2011). However, multiple studies have reported large variations between homogeneous and heterogeneous tissue modulus µ-FEMs (Bourne and Van Der Meulen, 2004; Harrison et al., 2008; Jaasma et al., 2002; Renders et al., 2011, 2008; van Ruijven et al., 2007). Renders et al. (2011) reported that stresses were increased near trabecular surfaces versus the core, suggesting trabecular bending occurring when loaded in compression (Renders et al., 2011). In an earlier study, these same authors found a decrease in apparent modulus (E_{app}) of 21% compared to

homogeneous models (E_{tissue} = 9 GPa) when tested in compression. The present study found that E_{app} decreased 41% – 68% between heterogeneous and homogeneous (E_{tissue} = 20 GPa) µ-FEMs, which is consistent when accounting for the increased tissue modulus in the present study. It has also been reported that variations in stresses and strains between the heterogeneous and homogenous models were found to be small in cortical bone, but large in trabecular bone, indicating the need to accurately model material heterogeneity in trabecular µ-FEMs (van Ruijven et al., 2007).

Only a single study has reported trabecular density-modulus relationships specific to the shoulder (Gupta and Dan, 2004). Data from a subsequent study of reported experimental apparent density and modulus values from scapular trabecular bone samples were used to determine statistical piece-wise relationships, with apparent bone density ρ_{app} < 0.36 g/cm^3 having a power coefficient of 2, and ρ_{app} > 0.36 g/cm^3 having a power coefficient of 3. These coefficients are consistent with the range of power coefficients found in the present study. However, due to the lack of empirical measurements in the aforementioned study, direct comparisons are not possible.

The results of the present study are consistent with previous results derived from alternative anatomic locations (Helgason et al., 2008). These studies have found trabecular density-modulus relationships are best fit by power fit regression models with exponential coefficients in the range of 1.7 to 2.5, for the density range in the present study (ρ_{app} = 0.1 – 0.9 g/cm^3). Similarly, the E_{app} values determined for µ-FEMs with a homogeneous effective tissue modulus of 20 GPa were most consistent with samples taken from the femoral neck (E_{app} = 185 – 6826 MPa). When heterogeneous tissue modulus was considered in the µ-FEMs, E_{app} more closely matched values from pooled anatomical sites (E_{app} = 76 – 3891 MPa), especially in the lower density range (Figure 3.2) (Morgan et al., 2003).

More recent development of density-modulus relationships have focused on experimental validation primarily of whole long bone cadaveric specimens (Austman et al., 2009; Dahan et al., 2016; Eberle et al., 2013). These validations and density-modulus relationships are primary dictated by the mechanical response of cortical bone. Although this may provide the desired loading response for some physiological conditions, these relationships minimize the contribution of trabecular bone architecture and density on load

transfer. Accurate modeling of this load transfer is essential when considering implants that are supported by the trabecular bone (such as all-polyethylene glenoid components). Furthermore, the trabecular bone is primarily responsible for fracture and failure, and as such, bone remodeling. Eliminating the contribution of trabecular mechanical properties in density-modulus material mapping has the potential to provide inaccurate fracture, failure, stress and strain response in clinical-derived FEMs.

A limitation of this study is that physical bone specimens were not mechanically tested, and therefore a physical subject-specific tissue modulus, or effective tissue modulus could not be derived. However, the potentially significant inaccuracies and error resulting from end-artifacts, misrepresented boundary conditions and sample preparation, are minimized or eliminated using the purely computational method in the present study (Chen et al., 2017). Micro-FEMs have been extensively validated over the past decade (Bauer et al., 2014; Bevill and Keaveny, 2009; Chen et al., 2017; Gong et al., 2012; Harrison et al., 2008; Jaasma et al., 2002; Renders et al., 2011, 2008; van Ruijven et al., 2007), allowing for the generation of independent models in which to validate co-registered QCT-FEMs. The use of linear isotropic models allows for the homogeneous tissue modulus derived µ-FEM relationships to be scaled to any tissue modulus once a glenoid specific value is determined. Although the relationships developed were shown to have excellent statistical agreement for the density range tested and the relationships were corrected for the loss of load carrying capacity due to side-artifacts, the translation to whole bone specimens requires further evaluation. As determined in other studies (Dahan et al., 2016; Hambli and Allaoui, 2013; Trabelsi and Yosibash, 2011), piece-wise density-modulus relationships that account for specific density ranges may more accurately model the mechanical response of whole bones derived from clinical-resolution scans.

3.5 CONCLUSION:

The density-modulus relationships derived in this study have the potential to greatly improve accuracy in shoulder FE studies. A glenoid-specific density-modulus relationship accounting for trabecular bone architecture is essential to properly model load transfer paths for accurate prediction of bone mechanical response to loading. The corrected relationships can be adapted to whole bone scapular models or used with piece-wise

functions that account for mechanical variations due to density differences in trabecular and cortical bone. Site-specific modeling techniques can be used for patient-specific modeling and adapted for population-based statistical shape models.

3.6 REFERENCES:

Austman, R.L., Milner, J.S., Holdsworth, D.W., Dunning, C.E., 2009. Development of a customized density–modulus relationship for use in subject-specific finite element models of the ulna. Proc. Inst. Mech. Eng. Part H J. Eng. Med. 223, 787–794. Doi:10.1243/09544119JEIM553

Bayraktar, H.H., Morgan, E.F., Niebur, G.L., Morris, G.E., Wong, E.K., Keaveny, T.M., 2004. CoMParison of the elastic and yield properties of human femoral trabecular and cortical bone tissue. J. Biomech. 37, 27–35. Doi:10.1016/S0021-9290(03)00257-4

Bourne, B.C., Van Der Meulen, M.C.H., 2004. Finite element models predict cancellous apparent modulus when tissue modulus is scaled from specimen CT-attenuation. J. Biomech. 37, 613–621. Doi:10.1016/j.jbiomech.2003.10.002

Bouxsein, M.L., Boyd, S.K., Christiansen, B.A., Guldberg, R.E., Jepsen, K.J., Müller, R., 2010. Guidelines for assessment of bone microstructure in rodents using micro-computed tomography. J. Bone Miner. Res. 25, 1468–1486. Doi:10.1002/jbmr.141

Campoli, G., Weinans, H., van der Helm, F., Zadpoor, A. a, 2013. Subject-specific modeling of the scapula bone tissue adaptation. J. Biomech. 46, 2434–41. Doi:10.1016/j.jbiomech.2013.07.024

Carter, D., Hayes, W., 1977. The compressive behavior of bone as a two-phase porous structure. J. Bone Jt. Surg. 59(7), 954-962

Chen, Y., Dall′Ara, E., Sales, E., Manda, K., Wallace, R., Pankaj, P., Viceconti, M., 2017. Micro-CT based finite element models of cancellous bone predict accurately displacement once the boundary condition is well replicated: A validation study. J. Mech. Behav. Biomed. Mater. 65, 644–651. Doi:10.1016/j.jmbbm.2016.09.014

Dahan, G., Trabelsi, N., Safran, O., Yosibash, Z., 2016. Verified and validated finite element analyses of humeri. J. Biomech. 49, 1094–1102. Doi:10.1016/j.jbiomech.2016.02.036

Eberle, S., Göttlinger, M., Augat, P., 2013. An investigation to determine if a single

validated density – elasticity relationship can be used for subject specific finite element analyses of human long bones. Med. Eng. Phys. 35, 875–883. Doi:10.1016/j.medengphy.2012.08.022

Faieghi, M., Knowles, N.K., Tutunea-fatan, O.R., Ferreira, L.M., 2019. Fast Generation of Cartesian Meshes from Micro-Computed Tomography Data Computer Aided Design & Applications. 16(1), 161–171.

Gong, H., Zhang, M., Fan, Y., Kwok, W.L., Leung, P.C., 2012. Relationships between femoral strength evaluated by nonlinear finite element analysis and BMD, material distribution and geometric morphology. Ann. Biomed. Eng. 40, 1575–1585. Doi:10.1007/s10439-012-0514-7

Gross, T., Pahr, D.H., Peyrin, F., Zysset, P.K., 2011. The Influence of Mineral Heterogeneity on the Apparent Elastic Properties of Human Cancellous Bone: a Micro-CT-based Finite Element study. 2011 ORS Annu. Meet. 15, 1137–1144.

Guldberg, R.E., Hollister, S.J., Charras, G.T., 1998. The Accuracy of Digital Image-Based Finite Element Models. J. Biomech. Eng. 120, 289. Doi:10.1115/1.2798314

Gupta, S., Dan, P., 2004. Bone geometry and mechanical properties of the human scapula using computed tomography data. Trends Biomater Artif Organs 17, 61–70.

Hambli, R., Allaoui, S., 2013. A robust 3D finite element simulation of human proximal femur progressive fracture under stance load with experimental validation. Ann. Biomed. Eng. 41, 2515–2527. Doi:10.1007/s10439-013-0864-9

Harrison, N.M., McDonnell, P.F., O'Mahoney, D.C., Kennedy, O.D., O'Brien, F.J., McHugh, P.E., 2008. Heterogeneous linear elastic trabecular bone modelling using micro-CT attenuation data and experimentally measured heterogeneous tissue properties. J. Biomech. 41, 2589–2596. Doi:10.1016/j.jbiomech.2008.05.014

Helgason, B., Perilli, E., Schileo, E., Taddei, F., 2008. Mathematical relationships between bone density and mechanical properties: a literature review. Clin. Biomech. 23, 135–146. Doi:10.1016/j.clinbiomech.2007.08.024

Jaasma, M.J., Bayraktar, H.H., Niebur, G.L., Keaveny, T.M., 2002. Biomechanical effects of intraspecimen variations in tissue modulus for trabecular bone. J. Biomech. 35, 237–246. Doi:10.1016/S0021-9290(01)00193-2

Knowles, N.K., Reeves, J.M., Ferreira, L.M., 2016. Quantitative Computed Tomography

(QCT) derived Bone Mineral Density (BMD) in finite element studies: a review of the literature. J. Exp. Orthop. 3, 36. Doi:10.1186/s40634-016-0072-2

Kopperdahl, D.L., Morgan, E.F., Keaveny, T.M., 2002. Quantitative computed tomography estimates of the mechanical properties of human vertebral trabecular bone. J. Orthop. Res. 20, 801–805. Doi:10.1016/S0736-0266(01)00185-1

Morgan, E., Bayraktar, H., Keaveny, T., 2003. Trabecular bone modulus–density relationships depend on anatomic site. J. Biomech. 36(7), 897-904. Doi.org/10.1016/S0021-9290(03)00071-X

Niebur, G.L., Yuen, J.C., Hsia, A.C., Keaveny, T.M., 1999. Convergence Behavior of High-Resolution Finite Element Models of Trabecular Bone. J. Biomech. Eng. 121, 629. Doi:10.1115/1.2800865

Pomwenger, W., Entacher, K., Resch, H., Schuller-Götzburg, P., 2014. Need for CT-based bone density modelling in finite element analysis of a shoulder arthroplasty revealed through a novel method for result analysis. Biomed. Tech. (Berl). 59, 421–30. Doi:10.1515/bmt-2013-0125

Renders, G.A.P., Mulder, L., Langenbach, G.E.J., van Ruijven, L.J., van Eijden, T.M.G.J., 2008. Biomechanical effect of mineral heterogeneity in trabecular bone. J. Biomech. 41, 2793–2798. Doi:10.1016/j.jbiomech.2008.07.009

Renders, G.A.P., Mulder, L., van Ruijven, L.J., Langenbach, G.E.J., van Eijden, T.M.G.J., 2011. Mineral heterogeneity affects predictions of intratrabecular stress and strain. J. Biomech. 44, 402–407. Doi:10.1016/j.jbiomech.2010.10.004

Schileo, E., Dall'Ara, E., Taddei, F., 2008. An accurate estimation of bone density improves the accuracy of subject-specific finite element models. J. Biomech. 41(11). 2483-2491. Doi.org/10.1016/j.jbiomech.2008.05.017

Schileo, E., Taddei, F., Malandrino, A., Cristofolini, L., Viceconti, M., 2007. Subject-specific finite element models can accurately predict strain levels in long bones. J. Biomech. 40, 2982–2989. Doi:10.1016/j.jbiomech.2007.02.010

Trabelsi, N., Yosibash, Z., 2011. Patient-specific finite-element analyses of the proximal femur with orthotropic material properties validated by experiments. J. Biomech. Eng. 133, 61001. Doi:10.1115/1.4004180

Ün, K., Bevill, G., Keaveny, T.M., 2006. The effects of side-artifacts on the elastic modulus

of trabecular bone. J. Biomech. 39, 1955–1963. Doi:10.1016/j.jbiomech.2006.05.012

Unnikrishnan, G.U., Barest, G.D., Berry, D.B., Hussein, A.I., Morgan, E.F., 2013. Effect of specimen-specific anisotropic material properties in quantitative computed tomography-based finite element analysis of the vertebra. J. Biomech. Eng. 135, 101007–11. Doi:10.1115/1.4025179

van Ruijven, L.J., Mulder, L., van Eijden, T.M.G.J., 2007. Variations in mineralization affect the stress and strain distributions in cortical and trabecular bone. J. Biomech. 40, 1211–1218. Doi:10.1016/j.jbiomech.2006.06.004

Zioupos, P., Cook, R.B., Hutchinson, J.R., 2008. Some basic relationships between density values in cancellous and cortical bone. J. Biomech. 41, 1961–1968. Doi:10.1016/j.jbiomech.2008.03.025

CHAPTER 4 – THE EFFECT OF MATERIAL HETEROGENEITY, ELEMENT TYPE, AND DOWN-SAMPLING ON TRABECULAR STIFFNESS IN MICRO FINITE ELEMENT MODELS

OVERVIEW: *This chapter compares micro finite element models (FEMs) generated from 32 micron, 64 micron, 64 micron down-sampled microCT images, on the basis of apparent modulus under simulated unconstrained compression. The effect of element type and material heterogeneity are also explored.*[4]

[4]A version of this work has been published: Knowles NK, Ip K, Ferreira LM. The Effect of Material Heterogeneity, Element Type, and Down-Sampling on Trabecular Stiffness in Micro Finite Element Models. Annals of Biomedical Engineering. 2018; 47(2): 615-623

4.1 INTRODUCTION:

Trabecular bone is most active in bone remodeling and is therefore less mineralized (Oftadeh et al., 2015). This remodeling occurs most on the trabeculae surface (Brennan et al., 2009), altering trabecular material strength, thereby changing the bending stiffness (Renders et al., 2011). In pathologic joints and/or joints with replacement components, variations in joint loads may increase trabecular fracture risk due to altered bone formation/resorption.

To determine variations in trabecular mechanical properties, such as the function of trabecular architecture, mineralization, and volume fraction, linear and non-linear micro finite element models (µFEMs) have shown increasingly high correlations with empirical models (Bayraktar et al., 2004; Dall'Ara et al., 2017; Palanca et al., 2017). As the initial input for many non-linear trabecular µFEMs, the apparent modulus, E_{app}, of experimentally tested bone cores are combined with linear elastic µFEMs E_{app} to determine an effective (homogeneous) tissue modulus (Bayraktar et al., 2004; Oftadeh et al., 2015; van Rietbergen et al., 1995). An arbitrary tissue modulus E_i, is used to scale the ratio of experimental apparent modulus, E_{exp}, and finite element apparent modulus, E_{FEM}, to back-calculate the 'real' effective tissue modulus, E_{tissue} (Equation 4.1).

$$E_{tissue} = \frac{E_{exp}}{E_{FEM}} E_i \qquad \text{(Equation 4.1)}$$

These models then use this homogeneous effective E_{tissue} and direct conversion of the micro-CT (µCT) voxels into hexahedral elements in µFEMs for bone strength predictions and failure analysis. Although these voxel-based models are the 'gold standard' for µFEMs, they neglect the contribution of material heterogeneity found *in-vivo*. Trabeculae are heterogeneous, with increased tissue modulus at the core and decreased modulus superficially, due to surface bone remodeling (Brennan et al., 2009; Oftadeh et al., 2015; Renders et al., 2011). Accounting for trabecular material heterogeneity has been shown to improve empirical-µFEM correlations by allowing for more realistic trabecular bending stiffness (Bourne and Van Der Meulen, 2004; Harrison et al., 2008; Jaasma et al., 2002; Renders et al., 2011, 2008; van Ruijven et al., 2007), but comparisons across image resolutions and element types have not been made.

Preclinical and clinical bone strength predictions can be elucidated by understanding bone mechanics at a variety of hierarchical levels (Palanca et al., 2017). As

such, down-sampled µCT images are often used to make comparisons across image resolutions (Bauer et al., 2014; Bevill and Keaveny, 2009; Lu, 2015; Lu et al., 2014; Palanca et al., 2017) and to reduce computational resource burden, especially in non-linear analyses. Down-sampling not only alters the trabecular architecture, but inherently alters the CT-intensity of each trabeculae. In homogeneous µFEMs, this has been shown to have negligible effect on stiffness and strength due to trabecular architectural changes (Bevill and Keaveny, 2009). However, the effect of CT-intensity variations on computationally derived apparent modulus (E_{app}) in heterogeneous µFEMs, or comparisons between the 'gold standard' voxel-based hexahedral µFEMs and increasingly common tetrahedral µFEMs, has not been discussed.

The objectives of this study were to compare trabecular E_{app} among i) hexahedral and tetrahedral µFEMs, ii) µFEMs generated from 32 µm, 64 µm, and 64 µm down-sampled from 32 µm µCT scans, and iii) µFEMs with homogeneous and heterogeneous tissue moduli.

4.2 METHODS:

4.2.1 Specimens and Finite Element Model Generation

Fourteen cadaveric scapulae were denuded of soft tissue (7 male; 7 female; mean age 67 ± 8 years). The use of these specimens was approved by the Western University Health Sciences Research Ethics Board (HSREB) (File# 105912). Micro-CT scans at two spatial resolutions were acquired (Nikon XT H 225 ST, Nikon Metrology, NV) for each scapula (Table 4.1). These images maintained the recommended one-fourth mean trabecular thickness for numerical convergence, shown to have less than 7% error in mechanical properties when down-sampled to half the original scan resolution (Niebur et al., 1999). The raw DICOM images were filtered to remove high frequency noise (Gaussian filter: σ = 1.25, support = 2) (Mimics v. 20.0, Materialise, Leuven, BE). Virtual bone cores were extracted from the glenoid vault, medial to the subchondral bone, maintaining the recommended 2:1 aspect ratio (Helgason et al., 2008), to create µFEMs from the 32 µm, 64 µm, and down-sampled 64 µm scans. Custom code was used to generate µFEMs with 8-node hexahedral elements (HEX8), while maintaining the bone volume fraction (BV/TV) of each 'gold standard' HEX8 32 µm model (Table 4.2). A surface mesh of each virtual

core was also generated (Mimics v. 20.0) and volume meshed as a 10-node tetrahedral (TET10) µFEM (Abaqus v.6.14, Simulia, Providence, RI). A target element edge length (48 µm in the 32 µm µFEMs and 64 µm in the 64 µFEMs) of at least one-fourth mean trabecular thickness was used to ensure trabecular geometry was maintained, uniform material mapping, and numerical convergence. Three-dimensional morphometric parameters are provided in Table 4.2.

4.2.2 Material Property Assignment and Boundary Conditions

All µFEMs were given either a homogeneous tissue modulus of 20 GPa, or a heterogeneous tissue modulus scaled by CT-intensity. For the hexahedral µFEMs, custom-code was used to generate the Abaqus input files and apply the material properties (Faieghi et al., 2019). The heterogeneous tissue modulus was applied based on the CT-intensity of the µCT images with a reference (maximum) tissue modulus of 20 GPa and a slope factor of 1.4 (Table 4.3). This slope factor has been shown to have the best agreement between empirical and computational models in mapping material heterogeneity in trabecular µFEMs (Bourne and Van Der Meulen, 2004). The materials were applied with a material bin of one (Pegg and Gill, 2016), resulting in a varying number of unique materials per specimen based on CT-intensity at each scan spatial resolution (Tables 4.3 & 4.4). For the tetrahedral µFEMs, the same reference tissue modulus and slope factor was used for each heterogeneous µFEM (Mimics v. 20.0). The maximum number of allowable materials were applied, resulting in a mean tissue modulus and unique number of materials shown in Tables 4.3 and 4.4, respectively. Differences in the number of materials are attributed to variations in the direct method of material assignment used in hexahedral µFEMs and numerical integration of the tetrahedral mesh on the native HU scaler-field used for tetrahedral µFEMs.

Simulated unconstrained compression to 0.5% apparent strain was performed along the medial-lateral direction of each µFEM. The boundary conditions were applied with custom-code to generate the Abaqus input files (Matlab v. R2017a, Natick, RI, USA) and were therefore identical between all µFEMs. The apparent modulus (E_{app}) of each µFEM was calculated and compared. The highest resolution (32 µm) HEX8 µFEMs provide the comparative ‘gold standard’ for all other µFEMs and were used to determine differences

Table 4.1: Parameters for Micro-Computed Tomography Scans

Parameter	**Micro-CT Scans**	
Voxel Size (isotropic) (μm^3)	32	64
Peak Voltage (kV)	95	95
Current (µA)	64	64
Projections	3141	3141
Exposure (ms)	1000	1000

Table 4.2: Three-dimensional morphometric parameters of the specimens compared

N = 14	32 µm	64 µm	p-value vs. 32 µm	DS 64 µm	p-value vs. 32 µm	p-value vs. 64 µm
BV/TV	0.243 ± 0.103 (0.099 – 0.457)	0.244 ± 0.104 (0.104 – 0.464)	.915[a]	0.241 ± 0.103 (0.091 – 0.450)	**.036**[a]	.133[a]
Tb.Th (mm)	0.258 ± 0.059 (0.174 – 0.357)	0.309 ± 0.060 (0.216 – 0.407)	**< .001**[a]	0.285 ± 0.059 (0.185 – 0.385)	**< .001**[a]	**< .001**[a]
Tb.Sp (mm)	0.780 ± 0.123 (0.577 – 0.996)	0.864 ± 0.146 (0.654 – 1.127)	**< .001** [b]	0.838 ± 0.124 (0.664 – 1.050)	**< .001**[a]	**< .001**[b]
Tb.N (1/mm)	0.918 ± 0.254 (0.532 – 1.506)	0.749 ± 0.230 (0.355 – 1.222)	**< .001**[a]	0.801 ± 0.246 (0.440 – 1.367)	**< .001**[a]	**< .001**[a]
SMI	0.999 ± 0.657 (-0.395 – 1.872)	1.297 ± 0.708 (-0.349 – 2.216)	**< .001**[a]	1.151 ± 0.780 (-0.890 – 2.027)	**.013** [b]	**< .001**[b]

Values are mean ± SD (range). All 3D morphometric parameters were calculated with SkyScan CTAn (Bruker micro-CT, Kontich, BE). Bone Volume Fraction (BV/TV); Trabecular Thickness (Tb.Th); Trabecular Separation (Tb.Sp); Trabecular Number (Tb.N); Structure Model Index (SMI). [a] Paired t-test. [b] Wilcoxon signed rank test. Significant values ($p < .05$) are bolded.

Table 4.3: Heterogeneous μ-FEM tissue modulus by specimen based on CT-intensity

Specimen	Sex	Age	Hexahedral (HEX8) Mean Tissue Modulus (MPa)			Tetrahedral (TET10) Mean Tissue Modulus (MPa)		
			32 μm	64 μm	DS 64 μm	32 μm	64 μm	DS 64 μm
1	F	62	10683 ± 3566	9610 ± 3006	10921 ± 2982	10825 ± 3306	9708 ± 2812	10889 ± 2972
2	F	68	8444 ± 3129	9034 ± 3131	9418 ± 2967	8488 ± 2828	9023 ± 2749	9688 ± 2638
3	F	69	10812 ± 3691	11159 ± 3207	10649 ± 3133	10482 ± 3406	10981 ± 3048	10486 ± 3062
4	F	60	9753 ± 3374	8811 ± 3009	9480 ± 3048	10074 ± 3070	9208 ± 2827	9471 ± 2922
5	M	80	8782 ± 2832	10135 ± 2400	9833 ± 2476	9859 ± 2741	10459 ± 2371	10182 ± 2429
6	M	72	9075 ± 2748	9660 ± 1870	9064 ± 2013	10499 ± 2662	10167 ± 1973	10990 ± 2358
7	M	78	9653 ± 3448	10081 ± 3145	9716 ± 2977	9404 ± 3138	10080 ± 2949	9734 ± 2843
8	F	73	8044 ± 2785	8703 ± 2263	8297 ± 2310	8431 ± 2547	9149 ± 2187	8541 ± 2229
9	M	50	11234 ± 3486	11350 ± 2160	11870 ± 2502	11242 ± 3122	11497 ± 2077	12198 ± 2370
10	F	66	9208 ± 3145	10841 ± 2816	10128 ± 2866	9300 ± 2916	10812 ± 2642	10129 ± 2720
11	F	65	8664 ± 2699	11515 ± 1806	10150 ± 2319	9189 ± 2512	11918 ± 1846	10532 ± 2244
12	M	73	11579 ± 2755	11466 ± 2405	12007 ± 2336	12058 ± 2510	11703 ± 2340	12815 ± 2273
13	M	58	10297 ± 1745	10305 ± 1687	11176 ± 1474	11344 ± 1728	11040 ± 1793	11963 ± 1640
14	M	64	9928 ± 2659	12047 ± 2236	11352 ± 2227	9983 ± 2418	12277 ± 2186	11544 ± 2093
			9725 ± 3004	**10336 ± 2510**	**10290 ± 2545**	**10084 ± 2779**	**10573 ± 2414**	**10654 ± 2485**

Values are mean ± standard deviation. DS – Down-sampled

Table 4.4: Average number of elements and mean number of unique materials for µFEMs

N = 14	Hexahedral			Tetrahedral		
	32 µm	**64 µm**	**DS 64 µm**	**32 µm**	**64 µm**	**DS 64 µm**
Number of Elements (millions)	1.89 ± 0.82 (0.77 – 3.56)	0.23 ± 0.10 (0.10 – 0.44)	0.28 ± 0.10 (0.09 – 0.43)	4.35 ± 1.57 (1.96 – 6.82)	1.82 ± 0.82 (0.68 – 3.52)	1.89 ± 0.86 (0.79 – 3.65)
Number of Materials (thousands)	13.34 ± 1.42 (9.75 – 15.37)	11.02 ± 1.79 (8.02 – 13.22)	10.93 ± 1.60 (7.23 – 12.63)	8.63 ± 0.34 (8.18 – 9.39)	8.79 ± 0.48 (7.82 – 9.39)	8.48 ± 0.55 (6.87 – 8.99)
Required Memory to Minimize I/O (GB)	93.37 ± 76.93 (15.74 – 299.05)	6.25 ± 4.76 (1.31 – 18.43)	6.36 ± 5.07 (1.20 – 19.56)	257.39 ± 155.12 (60.48 – 574.09)	89.400 ± 72.96 (15.81 – 274.65)	98.33 ± 87.39 (16.45 – 327.27)

Values are mean ± standard deviation (Range). DS – Down-sampled

in mean E_{app} and errors in E_{app} as a function of trabecular thickness (Tb.Th) and bone volume fraction (BV/TV).

4.3 RESULTS

Significant differences were found in all three-dimensional morphometric parameters between the µFEMs at all scan spatial resolutions. Trabecular thickening occurred as scan spatial resolution was decreased but the amount of thickening was not consistent between the two 64 µm models. Similar results were observed between other morphometric parameters (Table 4.2). The mean tissue modulus mapped to hexahedral µFEMs was consistently lower than tetrahedral µFEMs. For 32 µm µFEMs the mean difference was 359 ± 225 MPa lower, 64 µm µFEMs 237 ± 96 MPa lower and down-sampled 64 µm µFEMs 364 ± 60 MPa lower (Table 4.3). Tetrahedral µFEMs consistently had a larger number of elements but a lower number of mapped materials than hexahedral µFEMs (Table 4.4). For equal number of elements, the tetrahedral µFEMs (64 µm and DS 64 µm) had similar memory requirements to hexahedral µFEMs (32 µm). The increase in memory requirements for tetrahedral models was proportional to the increase in the number of elements (Table 4.4).

Compared to the 'gold standard' HEX8 32 µm µFEMs with a homogeneous tissue modulus, the E_{app} of TET10 32 µm µFEMs decreased by a mean 7% (Figure 4.2A). The HEX8 µFEMs generated from the down-sampled 64 µm and scanned 64 µm E_{app} decreased by a mean 24% and 33%, respectively. The E_{app} of the corresponding TET10 models decreased by a mean 32% and 43%, respectively. Decreases in mean E_{app} was reduced when a heterogeneous tissue modulus was considered in all µFEMs (Figure 4.2B). The TET10 32 µm µFEMs E_{app} decreased by a mean 1%, and TET10 down-sampled 64 µm and scanned 64 µm E_{app} decreased by a mean 24% and 37%, respectively. The HEX8 down-sampled 64 µm and scanned 64 µm, had lower mean E_{app} decreases of 18%, and 28%, respectively.

The error in E_{app} as a function of trabecular thickness (Tb.Th) was larger for µFEMs generated from the scanned 64 µm, than the down-sampled 64 µm µFEMs (Figure 4.3). The errors were lowest for Tb.Th greater than 0.225 mm and for µFEMs generated.

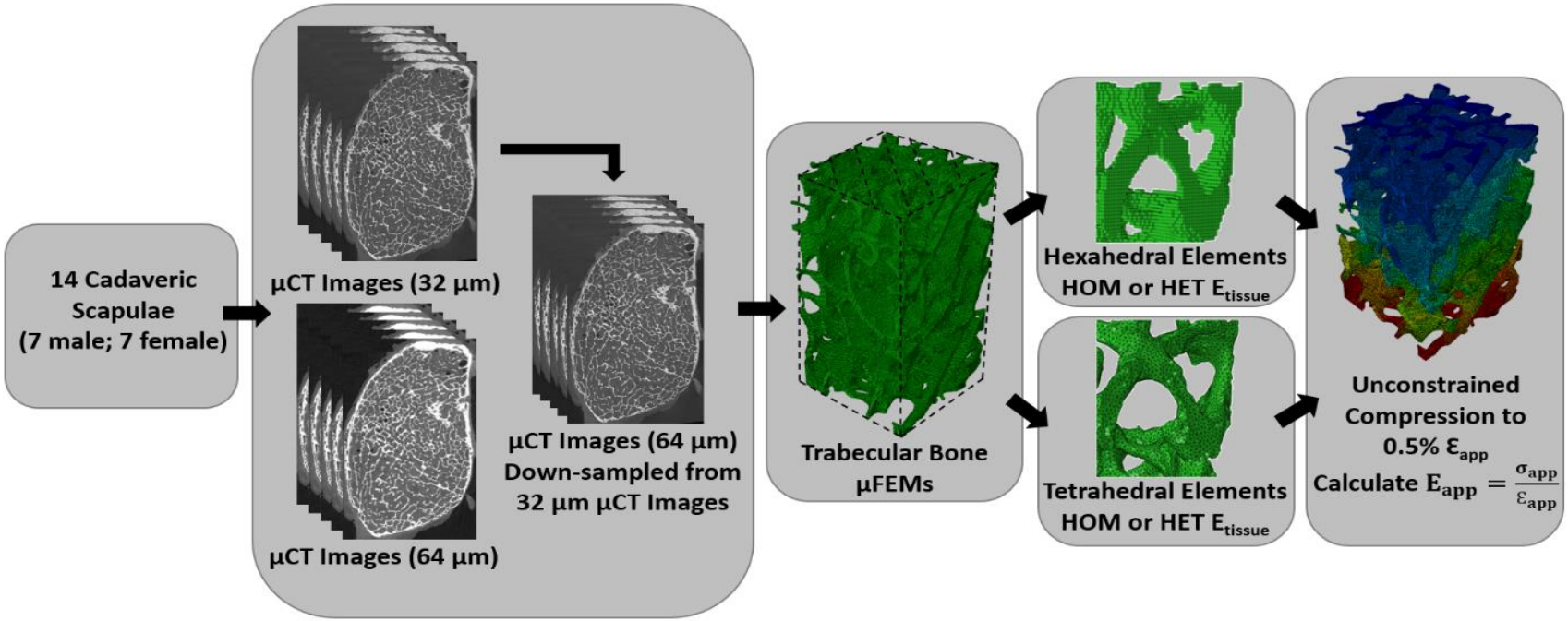

Figure 4.1: The complete workflow for comparison of the apparent modulus (E_{app}) of trabecular bone μFEMs from cadaveric scapulae

Three image spatial resolutions were used to generate μFEMs, with hexahedral or tetrahedral elements and homogeneous (HOM) or heterogeneous (HET) tissue moduli (E_{tissue}). A total of 168 μFEMs were compared.

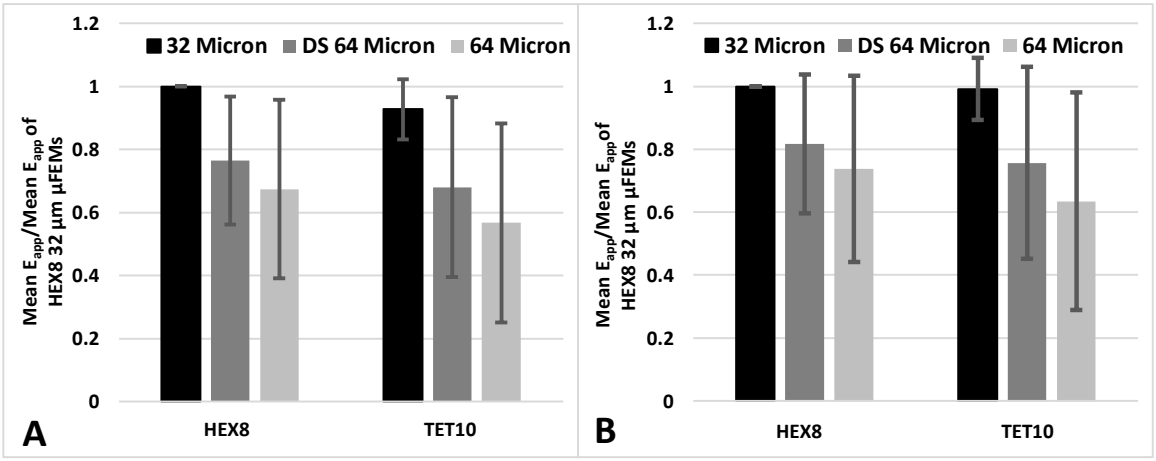

Figure 4.2: Mean error in apparent modulus (E_{app}) of µFEMs

FEMs generated from 32 µm, 64 µm or down-sampled 64 µm micro-CT scans with hexahedral (HEX8) or tetrahedral (TET10) elements and a homogeneous (A) or heterogeneous (B) tissue modulus. Error bars are ± SD (n=14).

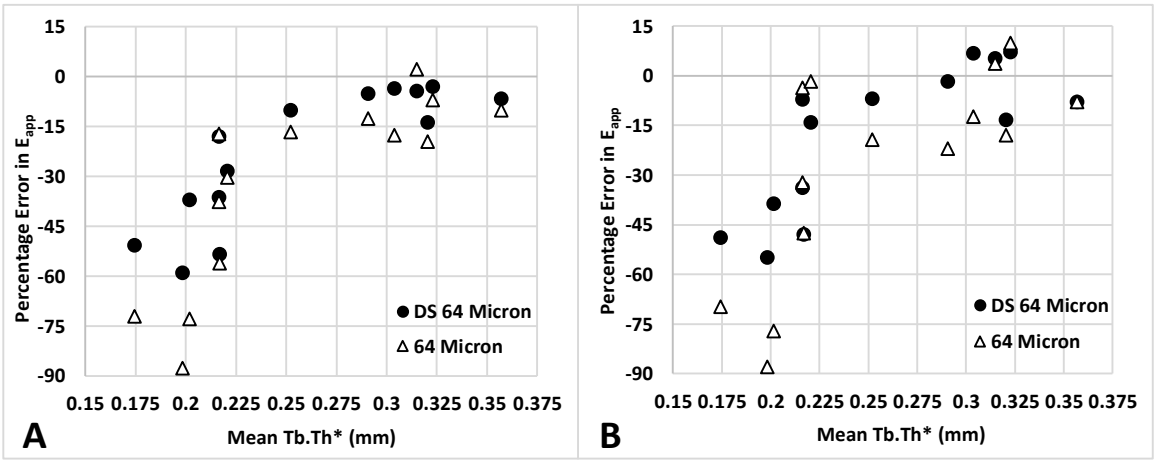

Figure 4.3: Percentage error in apparent modulus (E_{app}) compared to 32 µm HEX8 µFEMs

FEMs generated from 64 µm or down-sampled 64 µm µCT scans with hexahedral elements and a homogeneous (A) or heterogeneous (B) tissue modulus, as a function of the 32 µm trabecular thickness (Tb.Th)

with heterogeneous tissue moduli. The error in E_{app} as a function of volume fraction (BV/TV) for hexahedral µFEMs was lower above 0.225 for µFEMs with both homogeneous and heterogeneous tissue moduli and was lower for the down-sampled 64 µm µFEMs (Figure 4.4). For tetrahedral µFEMs, E_{app} error as a function of BV/TV was again lowest above 0.225, and lower for down-sampled 64 µm µFEMs compared to 64 µm µFEMs (Figure 4.5). The lowest errors occurred for the 32 µm µFEMs with both homogeneous and heterogeneous tissue moduli.

4.4 DISCUSSION:

This study compared the apparent modulus (E_{app}) of linear isotropic µFEMs generated with hexahedral or tetrahedral elements from 32 µm, 64 µm, or down-sampled 64 µm µCT scans, with a homogeneous or heterogeneous tissue modulus. It was found that except at the highest spatial resolution, tetrahedral elements underestimate E_{app}. Down-sampling to half the original scan spatial resolution is not equivalent in E_{app} to µFEMs generated from scans at that spatial resolution and both models underestimate the E_{app} of the highest spatial resolution models. Across µFEMs generated from all spatial resolutions, accounting for trabecular material heterogeneity decreased errors in E_{app}.

The mechanical properties of µFEMs generated from hexahedral and tetrahedral elements have been reported (Cyganik et al., 2014), with the authors concluding that their data suggests there is no basis that element type influenced the accuracy of the numerical solution. However, direct comparisons between trabecular µFEMs created with each element type were not performed in their study, limiting the ability to elucidate which element type provides greater accuracy. Differences in the apparent mechanical properties of hexahedral element formulations (linear, quadratic, and reduced integration) have also been discussed (Depalle et al., 2013), indicating that variations in E_{app} are negligible between linear and quadratic hexahedral elements at both one half and one quarter the original voxel size, but are significantly lower when reduced integration linear hexahedral elements are used. Our comparison of linear hexahedral and quadratic tetrahedral elements in the same samples indicate that hexahedral elements have lower errors than tetrahedral elements, but if a heterogeneous tissue modulus is used, tetrahedral elements are comparable to hexahedral elements at high spatial resolutions (Figure 4.2B).

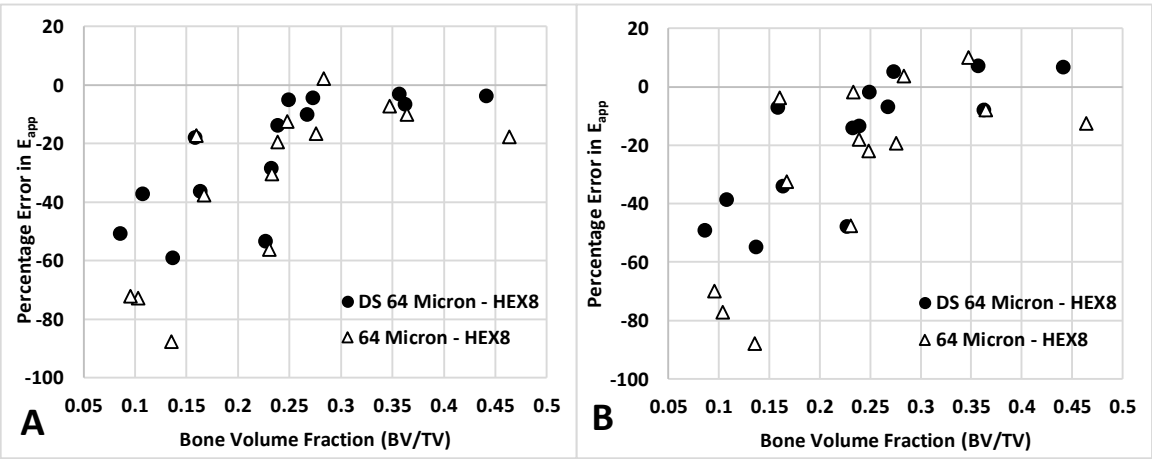

Figure 4.4: Percentage error in apparent modulus (E_{app}) compared to 32 µm HEX8 µFEMs

FEMs generated from 64 µm or down-sampled 64 µm µCT scans with hexahedral elements and a homogeneous (A) or heterogeneous (B) tissue modulus, as a function of volume fraction (BV/TV).

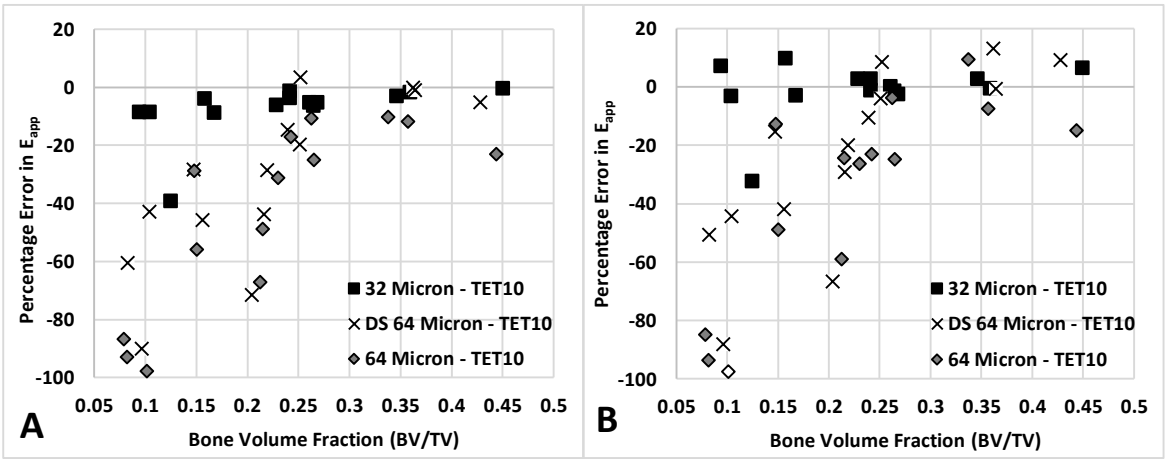

Figure 4.5: Percentage error in apparent modulus (E_{app}) compared to 32 µm HEX8 µFEMs

FEMs generated from 64 µm or down-sampled 64 µm µCT scans with tetrahedral elements and a homogeneous (A) or heterogeneous (B) tissue modulus, as a function of volume fraction (BV/TV).

Voxel-based μFEMs are the gold standard in trabecular bone modeling because the hexahedral elements are directly created from the voxels of the scanned bone and inherently retain the voxel CT-intensity for use in homogeneous or heterogeneous μFEMs. These linear elements have minimal computational expense and have shown excellent correlations with empirical results (Bayraktar et al., 2004; Dall'Ara et al., 2017; Palanca et al., 2017). With contemporary automatic tetrahedral mesh generators, μFEM pre-processing between tetrahedral and hexahedral models is now nearly equivalent. For non-homogeneous tetrahedral μFEMs, finite element pre-processing software, such as that used in this study (Mimics V. 20.0, Materialise, Leuven, BE), also incorporate semi-automated material assignment using mapping of the CT-intensity scaler field, further simplifying tetrahedral FEM pre-processing. In the present study a larger number of tetrahedral elements was used to ensure at least one-fourth mean trabecular thickness elements were used to maintain trabecular geometry, uniform material mapping, and numerical convergence (Niebur et al., 1999). This increase in the number of elements added to the increased computational expense of these quadratic μFEMs (Table 4). It was expected that due to this increased degrees of freedom (DOF) of these μFEMs, at least equivalent results to hexahedral μFEMs would occur. However, this was only observed in μFEMs at the highest spatial resolution (32 μm) but not in μFEMs derived from lower spatial resolution (64 μm and down-sampled 64 μm). This suggests that although the pre-processing time and computational expense of the two element types are nearly equal, there is little benefit to using tetrahedral elements.

Decreases in trabecular bone apparent mechanical properties have been shown in high volume fraction femoral μFEMs (Bevill and Keaveny, 2009), and low volume fraction greater trochanter and vertebral μFEMs (Bevill and Keaveny, 2009; Depalle et al., 2013). In their high-volume fraction (BV/TV = 0.25 ± 0.06) femoral μFEMs, Bevill and Keaveny (2009) found decreases in E_{app} of less than 5% when coarsened to one half the high resolution μFEMs. When considering the subset of their low BV/TV samples the error increased greatly. We found the lowest errors occurred for BV/TV > 0.225. Depalle et al. (2013) used low volume fraction vertebral specimens (BV/TV = 0.08 ± 0.03) and found negligible variations in E_{app} between high- and low-resolution μFEMs. This result

compared to the present study may be partially explained by the differences in their high-resolution μFEMs (20 μm) and ours (32 μm).

Microarchitectural parameters are not the same between resampled images and images scanned at low-resolution (Kim et al., 2004). This is concerning, because bone mechanical properties from different hierarchical levels are often used to make conclusions about bone mechanical properties, and down-sampled images are often used to reduce computational resources, especially for non-linear modeling and fracture analysis. Depalle et al. (2013) found μFEM trabecular stress distribution was most sensitive to image resolution, suggesting in their linear models that this is due to stress concentrations caused by trabecular stiffening errors. This is partially due to trabecular thickening that occurs when down-sampling. In the present study, increased trabecular thickness was found for both the scanned 64 μm and down-sampled 64 μm μFEMs. Compared to the 32 μm μFEMs, the thickening was significantly different in both 64 μm μFEMs. There was also a significant difference between the two 64 μm μFEMs (Table 4.2). Intuitively, thickened trabeculae would result in increased specimen stiffness, especially when a homogeneous tissue modulus was used. This however was not the case, indicating that trabecular architecture and load transfer is more complex. Errors in apparent modulus were improved when material heterogeneity was considered, partially because the superficial regions of the thickened trabeculae have less influence on bending stiffness and thereby minimize these stiffening errors. The near identical E_{app} between the hexahedral and tetrahedral μFEMs at 32 μm indicates that the differences in heterogeneous material mapping strategies between element types can model material heterogeneity equivalently if μFEMs are derived from scan spatial resolutions that are high enough to reduce errors induced by partial volume effects.

Accounting for material heterogeneity has been shown to improve stress and strain predications in μFEMs (Bourne and Van Der Meulen, 2004; Harrison et al., 2008; Jaasma et al., 2002; Renders et al., 2011, 2008; van Ruijven et al., 2007). Stresses are increased near trabecular surfaces versus the core, suggesting trabecular bending occurring when loaded in compression (Renders et al., 2011), and is consistent with studies that have used nanoindentation showing increased tissue modulus at the trabecular core compared to the surface (Brennan et al., 2009). In a study comparing homogeneous and heterogeneous

trabecular µFEMs, a decrease in E_{app} of 21% was found between µFEMs accounting for material heterogeneity compared to homogeneous models (E_{tissue} = 9 GPa) when tested in compression (Renders et al., 2008). It has also been shown that variations in stresses and strains are small in cortical bone, but large in trabecular bone between homogenous and heterogeneous models, further illustrating the need to accurately model material heterogeneity in trabecular µFEMs (van Ruijven et al., 2007).

Recent studies have compared and validated trabecular mechanical loading between physical specimens and linear-isotopic µFEMs generated from down-sampled images, and/or µFEMs with homogeneous tissue moduli using digital volume correlation (DVC) (Chen et al., 2017; Costa et al., 2017; Dall'Ara et al., 2017; Palanca et al., 2017). These µFEMs have been found to accurately predict empirical displacements, but quantitative strain measurements are less accurate between empirical models and µFEMs. The results of the present study suggest that the difficulties in extracting meaningful strain measurements from µFEMs might be partially due to the lack of material heterogeneity and/or the use of µFEMs generated from down-sampled images. Comparison with empirical models using DVC and high-resolution µFEMs that account for material heterogeneity may improve strain predictions.

Although bone volume fraction was used as the metric to ensure consistency between models, a significant difference was found between the down-sampled 64 µm and 32 µm models. Although statistically different, the difference in BV/TV was 0.002, and likely contributed less to variations in E_{app} than the significant variations in trabecular architecture. At lower bone volume fractions and resolutions, tetrahedral µFEM generation inherently loses trabecular connectivity. When pre-processing these µFEMs with connected trabeculae by removing 'floating regions' – required for numerical convergence – can result in a significant reduction in relative volume fraction compared to hexahedral models derived from the voxel threshold in the raw images. The extent in which load carrying trabeculae are compromised is unknown and may account for why tetrahedral µFEMs with low volume fractions have large errors in E_{app} (Figure 4.5). It has been shown that down-sampled models have increased trabecular spacing and trabecular thickening but the variation in apparent mechanical properties seems to be minimized at higher trabecular thicknesses (Depalle et al., 2013). Comparable results were obtained in the present study.

A limitation of this study is that physical trabecular bone cores were not mechanically tested. Although physical trabecular specimen testing has been used extensively for E_{app} calculation, the variability in comparing empirical models and µFEMs due to variations in boundary conditions adds a level of complexity beyond the scope of the present study. The purely computational methodology used in the present study is similar to other hierarchical µFEM studies (Bevill and Keaveny, 2009; Depalle et al., 2013), and allows for direct comparison of models that differ only by the parameters derived from the scan spatial resolution (CT-intensity and voxel size) used to derive µFEMs.

4.5 CONCLUSION:

Due to an underestimation in bone stiffness, consideration should be taken when using down-sampled scans to elucidate preclinical or clinical bone fracture and failure. The results of this study have shown that apparent modulus is not equivalent to high spatial resolution µFEMs when µFEMs are generated from down-sampled images or from images scanned at the down-sampled spatial resolution. Also, hexahedral and tetrahedral µFEMs are only equivalent at the highest scan spatial resolution. Accounting for material heterogeneity decreases errors at all scan spatial resolutions. These results question the accuracy of using a homogeneous effective tissue modulus in linear and non-linear µFEMs. Future work should focus on determination of the local effects of down-sampling on trabecular stiffness using full-field DVC-based empirical comparisons.

4.6 REFERENCES:

Bauer, J.S., Sidorenko, I., Mueller, D., Baum, T., Issever, A.S., Eckstein, F., Rummeny, E.J., Link, T.M., Raeth, C.W., 2014. Prediction of bone strength by µcT and MDCT-based finite-element-models: How much spatial resolution is needed? Eur. J. Radiol. 83, e36–e42. Doi:10.1016/j.ejrad.2013.10.024

Bayraktar, H.H., Morgan, E.F., Niebur, G.L., Morris, G.E., Wong, E.K., Keaveny, T.M., 2004. CoMParison of the elastic and yield properties of human femoral trabecular and cortical bone tissue. J. Biomech. 37, 27–35. Doi:10.1016/S0021-9290(03)00257-4

Bevill, G., Keaveny, T.M., 2009. Trabecular bone strength predictions using finite element analysis of micro-scale images at limited spatial resolution. Bone 44, 579–584.

Doi:10.1016/j.bone.2008.11.020

Bourne, B.C., Van Der Meulen, M.C.H., 2004. Finite element models predict cancellous apparent modulus when tissue modulus is scaled from specimen CT-attenuation. J. Biomech. 37, 613–621. Doi:10.1016/j.jbiomech.2003.10.002

Brennan, O., Kennedy, O.D., Lee, T.C., Rackard, S.M., O'Brien, F.J., 2009. Biomechanical properties across trabeculae from the proximal femur of normal and ovariectomised sheep. J. Biomech. 42, 498–503. Doi:10.1016/j.jbiomech.2008.11.032

Chen, Y., Dall'Ara, E., Sales, E., Manda, K., Wallace, R., Pankaj, P., Viceconti, M., 2017. Micro-CT based finite element models of cancellous bone predict accurately displacement once the boundary condition is well replicated: A validation study. J. Mech. Behav. Biomed. Mater. 65, 644–651. Doi:10.1016/j.jmbbm.2016.09.014

Costa, M.C., Tozzi, G., Cristofolini, L., Danesi, V., Viceconti, M., Dall'Ara, E., 2017. Micro finite element models of the vertebral body: Validation of local displacement predictions. PloS One 12, 1–18. Doi:10.1371/journal.pone.0180151

Cyganik, Ł., Binkowski, M., Kokot, G., Rusin, T., Popik, P., Bolechała, F., Nowak, R., Wróbel, Z., John, A., 2014. Prediction of Young's modulus of trabeculae in microscale using macro-scale's relationships between bone density and mechanical properties. J. Mech. Behav. Biomed. Mater. 36, 120–134. Doi:10.1016/j.jmbbm.2014.04.011

Dall'Ara, E., Peña-Fernández, M., Palanca, M., Giorgi, M., Cristofolini, L., Tozzi, G., 2017. Precision of Digital Volume Correlation Approaches for Strain Analysis in Bone Imaged with Micro-Computed Tomography at Different Dimensional Levels. Front. Mater. 4. Doi:10.3389/fmats.2017.00031

Depalle, B., Chapurlat, R., Walter-Le-Berre, H., Bou-Saïd, B., Follet, H., 2013. Finite element dependence of stress evaluation for human trabecular bone. J. Mech. Behav. Biomed. Mater. 18, 200–212. Doi:10.1016/j.jmbbm.2012.08.012

Faieghi, M., Knowles, N.K., Tutunea-fatan, O.R., Ferreira, L.M., 2019. Fast Generation of Cartesian Meshes from Micro-Computed Tomography Data 16, 161–171.

Harrison, N.M., McDonnell, P.F., O'Mahoney, D.C., Kennedy, O.D., O'Brien, F.J., McHugh, P.E., 2008. Heterogeneous linear elastic trabecular bone modelling using micro-CT attenuation data and experimentally measured heterogeneous tissue

properties. J. Biomech. 41, 2589–2596. Doi:10.1016/j.jbiomech.2008.05.014

Helgason, B., Perilli, E., Schileo, E., Taddei, F., 2008. Mathematical relationships between bone density and mechanical properties: a literature review. Clin. … 23, 135–146. Doi:10.1016/j.clinbiomech.2007.08.024

Jaasma, M.J., Bayraktar, H.H., Niebur, G.L., Keaveny, T.M., 2002. Biomechanical effects of intraspecimen variations in tissue modulus for trabecular bone. J. Biomech. 35, 237–246. Doi:10.1016/S0021-9290(01)00193-2

Kim, D.G., Christopherson, G.T., Dong, X.N., Fyhrie, D.P., Yeni, Y.N., 2004. The effect of microcomputed tomography scanning and reconstruction voxel size on the accuracy of stereological measurements in human cancellous bone. Bone 35, 1375–1382. Doi:10.1016/j.bone.2004.09.007

Lu, Y., 2015. Influence of the specimen scan condition on the finite element voxel model of human vertebral cancellous bone. Comput. Methods Biomech. Biomed. Eng. Imaging Vis. 3, 172–176. Doi:10.1080/21681163.2014.947385

Lu, Y., Engelke, K., Glueer, C.-C., Morlock, M.M., Huber, G., Lu, Engelke, K., Glueer, C.-C., Morlock, M.M., Huber, G., 2014. The effect of in situ/in vitro threedimensional quantitative computed tomography image voxel size on the finite element model of human vertebral cancellous bone. Proc. Inst. Mech. Eng. Part H J. Eng. Med. 228, 1208–1213. Doi:10.1177/0954411914558654

Niebur, G.L., Yuen, J.C., Hsia, A.C., Keaveny, T.M., 1999. Convergence Behavior of High-Resolution Finite Element Models of Trabecular Bone. J. Biomech. Eng. 121, 629. Doi:10.1115/1.2800865

Oftadeh, R., Perez-Viloria, M., Villa-Camacho, J.C., Vaziri, A., Nazarian, A., 2015. Biomechanics and Mechanobiology of Trabecular Bone: A Review. J. Biomech. Eng. 137, 010802. Doi:10.1115/1.4029176

Palanca, M., Bodey, A.J., Giorgi, M., Viceconti, M., Lacroix, D., Cristofolini, L., Dall'Ara, E., 2017. Local displacement and strain uncertainties in different bone types by digital volume correlation of synchrotron microtomograms. J. Biomech. 58, 27–36. Doi:10.1016/j.jbiomech.2017.04.007

Pegg, E.C., Gill, H.S., 2016. An open source software tool to assign the material properties of bone for ABAQUS finite element simulations. J. Biomech. 49, 3116–3121.

Doi:10.1016/j.jbiomech.2016.07.037

Renders, G.A.P., Mulder, L., Langenbach, G.E.J., van Ruijven, L.J., van Eijden, T.M.G.J., 2008. Biomechanical effect of mineral heterogeneity in trabecular bone. J. Biomech. 41, 2793–2798. Doi:10.1016/j.jbiomech.2008.07.009

Renders, G.A.P., Mulder, L., van Ruijven, L.J., Langenbach, G.E.J., van Eijden, T.M.G.J., 2011. Mineral heterogeneity affects predictions of intratrabecular stress and strain. J. Biomech. 44, 402–407. Doi:10.1016/j.jbiomech.2010.10.004

van Rietbergen, B., Weinans, H., Huiskes, R., Odgaard, A., 1995. A new method to determine trabecular bone elastic properties and loading using micromechanical finite-elements models. J. Biomech. 28, 69–81.

Van Ruijven, L.J., Mulder, L., van Eijden, T.M.G.J., 2007. Variations in mineralization affect the stress and strain distributions in cortical and trabecular bone. J. Biomech. 40, 1211–1218. Doi:10.1016/j.jbiomech.2006.06.004

CHAPTER 5 – MICRO-LEVEL APPARENT MODULUS CAN BE ACCURETLY MODELED BY QCT FINITE ELEMENT MODELS BASED ON MATERIAL MAPPING STRATEGY AND ELEMENT TYPE

OVERVIEW: *This chapter evaluates QCT finite element models (FEMs) with elemental or nodal material mapping, and linear hexahedral, linear tetrahedral, or quadratic tetrahedral elements ability to replicate the apparent modulus of co-registered microFEMs.*

5.1 INTRODUCTION:

The mapping of bone mechanical properties based on CT-attenuation, with heterogeneous materials and bone geometry defined from clinical-resolution CT scans, is the basis of subject-specific finite element modeling (FEM). In order to assign an accurate material distribution to the FE mesh, constitutive relationships that relate bone density (ash, apparent, or radiological) to apparent modulus are used (Helgason et al., 2008a; Knowles et al., 2016). Most reported density-modulus relationships are derived using mechanical testing of trabecular bone cores with extensive empirical validation to evaluate the accuracy of these constitutive relationships applied to FEMs at the whole bone level (Helgason et al., 2008a; Knowles et al., 2016). However, these validation studies are generally limited to strain gauge measurements on the outer cortical shell, which precludes direct comparisons within trabecular bone. As well, strain gauges placed on the cortical shell have shown larger errors when compared to computational results, partially due to the influence of partial volume effects (PVEs) in models derived from clinical-resolution CT (Helgason et al., 2016).

In addition to the multitude of density-modulus relationships that exist, it is also important to consider how these are applied to the FE mesh. At the whole bone level, while hexahedral elements allow for a direct conversion from a CT voxel to an FE element, tetrahedral elements are often preferred due to their ability to generate continuous geometry contours. However, as a trade-off, the strategy required to assign bone material properties to a tetrahedral element based on the attenuation from the CT scalar field becomes increasingly complex. The effects due to material mapping strategy (elemental or nodal) have been reported; however, at a lesser extent compared to density-modulus relationships (Chen et al., 2015, 2010, Helgason et al., 2016, 2008b; Taddei et al., 2007; Wille et al., 2012). A recent study reported a computational methodology that compares trabecular µFEMs to co-registered quantitative-CT (QCT)-FEMs derived from direct conversion of isotropic voxels into hexahedral elements (Knowles et al., 2018). This direct conversion method retains within each element the voxel CT-intensity and, if the constitutive relationship remains unchanged, a direct comparison of material mapping strategy is possible.

To assign density-modulus relationships to FE elements, commercially available software, such as (Mimics, Materialise, Leuven, BE), use automated tetrahedral mesh generation and exact volume-weighted elemental averaging based on the CT scalar field. This mapping method can be applied to both hexahedral and tetrahedral elements but is limited to the native Hounsfield (HU) scalar field. An alternative nodal material mapping strategy is to assign material properties based on the nodes relative position within the CT scalar field. The nodal coordinates can either be read as a user subroutine in Abaqus (Simulia, Providence, RI),(Chen et al., 2015, 2010) or as 'field or auxiliary (temperature) variables,' in Abaqus or Ansys (Ansys Inc., USA) (Helgason et al., 2008b). These variables are linearly interpolated to the element gauss integration points in the subsequent FE simulation. In nodal material mapping, tri-linear interpolation of the scalar field is used to map materials directly to the nodes. This is typically implemented in custom-code and so the scalar field can be either the native HU field, or an elastic modulus E field, in which the non-linear empirical density-modulus relationship is applied to the scalar field prior to mapping. The latter 'E field' has been shown to have improved correlations with empirical surface strain results (Helgason et al., 2008b; Taddei et al., 2007). This method has also been used to account for PVEs by determining whether outer nodes are assigned a lower modulus than the nearest internal node (Helgason et al., 2008b), and if so, these outer nodes are assigned the nearest internal nodes value.

The objective of this study was to determine the effect of material mapping strategy on computational models of trabecular bone, by using a validated density-modulus relationship (Knowles et al., 2019) derived directly from trabecular bone CT scans. The associated hierarchical computational methodology eliminates the influence of PVEs and the potential for confounding bias from cortical strain measurements, by using μFEMs as a gold standard for computational simulation of trabecular bone's mechanical response.

5.2 METHODS:

5.2.1 Specimens, Computed Tomography Scans and Constitutive Relationship

Fourteen cadaveric scapulae were denuded of soft tissue (7 male; 7 female; mean age 67 ± 8 years). Micro-CT (32 μm isotropic voxels, 95 kV, 64 μA, 3141 projections, 1000 ms exposure; Nikon XT H 225 ST, Nikon Metrology, NV) and QCT (0.625 mm isotropic

voxels, 120 kVp, 200 mA, BONEPLUS convolution kernel; GE Discovery CT750 HD, Milwaukee, WI, USA) scans were acquired for each scapula. A dipotassium phosphate (K_2HPO_4) (QCT Pro, Mindways Software Inc., Austin, TX, USA) calibration phantom was scanned with each specimen during QCT scans. The constitutive relationship was derived using virtual bone cores from the same specimens developed in a prior study (Knowles et al., 2019).

$$E = 34800\rho_{qct}^{2.506} \quad \text{(Equation 5.1)}$$

5.2.2 Finite Element Model Generation and Material Mapping Strategies

The μCT images were filtered to remove high frequency noise (Gaussian filter: $\sigma = 1.25$, support = 2) (Mimics v. 20.0, Materialise, Leuven, BE). Rectangular virtual bone cores with 5 mm edges and 10 mm long, maintaining the recommended 2:1 aspect ratio (Helgason et al., 2008a), were extracted medial to the glenoid subchondral bone for each specimen (n=14). Custom code was used for direct conversion to 8-node hexahedral elements (Faieghi et al., 2019). The μFEMs were sufficient in size and resolution to maintain the recommended one-fourth mean trabecular thickness for numerical convergence (Guldberg et al., 1998; Niebur et al., 1999). Microarchitectural information for the cores in this study is presented in Table 5.1. The μFEMs were assigned a heterogeneous tissue modulus based on CT-intensity of the corresponding cores (Bourne and Van Der Meulen, 2004). Unconstrained compression was applied to each of the 14 μFEMs to 0.5% apparent strain, in order to determine μFEM apparent modulus E_{app} (Abaqus v.6.14).

To investigate the sensitivity of variables used during assignment of material properties to QCT-FEMs, co-registered QCT-FEMs were developed for each of the 14 bone cores. Hexahedral QCT-FEMs (HEX8) were created using similar custom code (Matlab v. R2017a, Providence, RI) for direct conversion to 8-node brick elements from the QCT voxels. Tetrahedral QCT-FEMs were also created with either linear tetrahedral (TET4) or quadratic tetrahedral (TET10) elements, at 3 mesh densities (edge lengths: 0.625 mm, 0.46875 mm, 0.3125 mm) (3-Matic v. 12.0, Materialise, Leuven, BE & Abaqus

Table 5.1: Microarchitectural information measurements for he samples tested

n	BV/TV	Tb.Th (mm)	Tb.Sp (mm)	Tb.N (1/mm)
14	0.24 ± 0.09	0.26 ± 0.05	0.80 ± 0.12	0.89 ± 0.24
	(0.10 – 0.36)	(0.17 – 0.33)	(0.65 – 1.00)	(0.57 – 1.46)

Values are mean ± standard deviation (range). All values were calculated using SkyScan CTAn (Bruker micro-CT, Kontich, BE) based on 3D morphometric calculations. BV/TV – Bone Volume/Total Volume; Tb.Th – Trabecular Thickness; Tb.Sp – Trabecular Separation; Tb.N – Trabecular Number

v.6.14). These edge lengths correspond to 1, ¾, and ½ the QCT voxel dimensions, and were selected to determine if mesh density influences the outcomes by material mapping strategy. Three material mapping strategies were used to map Equation 5.1 to the corresponding QCT-FEMs:

i) Exact volume weighted elemental averaging of the native HU scalar field (MIMICS).

ii) Field variable node-based mapping of the native HU scalar field (NB HU).

iii) Field variable node-based mapping of the E scalar field (NB E).

For HEX8, TET4, and TET10 models, exact volume-weighted elemental averaging of the HU scalar field defined mapping to the model elements using commercially available software (Mimics v. 20.0). For HEX8, TET4, and TET10 node-based models, tri-linear interpolation was used to determine the nodal material properties using either the native HU scalar field or the E field (Matlab v. R2017a). Mimics does not allow for conversion of the native HU scalar field to E scalar field, and therefore this comparison was made only in the node-based models. For all QCT-FEMs, custom code generated an Abaqus input file with identical boundary conditions to the corresponding µFEMs (Matlab v. R2017a). All QCT-FEMs were equally compressed unconstrained to 0.5% apparent strain, and the apparent modulus (E_{app}) was compared to the corresponding 14 µFEMs (Figure 5.1).

The QCT density of each hexahedral mesh, with element size equal to the voxel dimensions, was used to compare the QCT density mapping between tetrahedral meshes and exact volume-weighted elemental averaging to the native HU scalar field or nodal tri-linear integration of the HU scalar field. Plots of each element type, material mapping strategy, and displacement fields under compression were completed to show the variations between models. To determine if bone volume fraction (BV/TV) influenced the QCT-FEM prediction of µFEM E_{app}, percent error was calculated and plotted for each material mapping strategy, element type and element density. Finally, linear regression was performed to compare QCT-FEM predicted E_{app} and µFEM E_{app} using coefficient of determination (r^2), slope (m), y-intercept (b), standard error of regression (SE), and SE/mean. These are further illustrated using Bland-Altman plots.

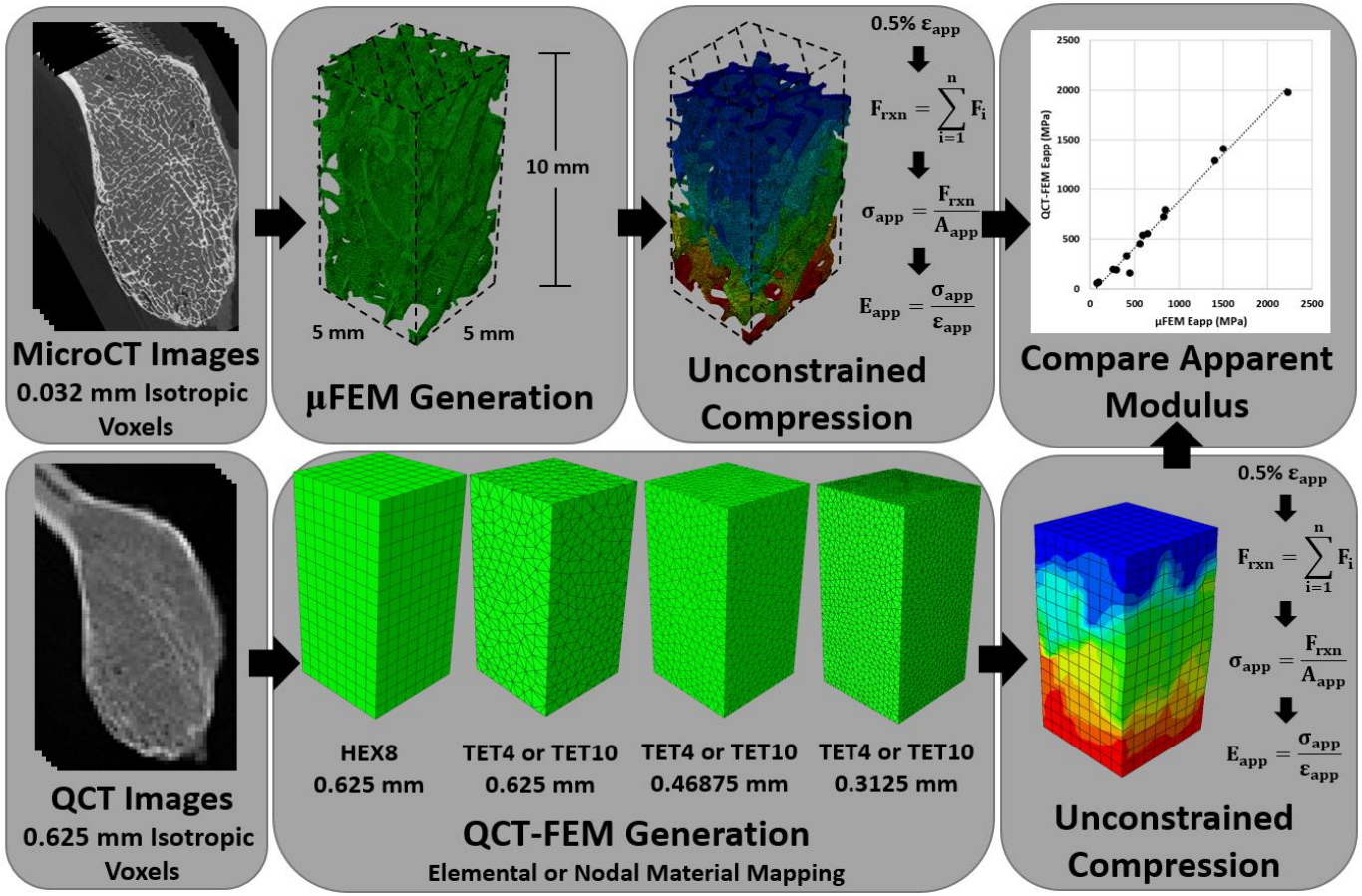

Figure 5.1: The complete workflow used to coMPare apparent modulus (E_{app}) between μFEMs and co-registered QCT-FEMs generated with different mesh types, densities and material mapping strategies

5.3 RESULTS

The mean QCT density error between the tetrahedral and corresponding hexahedral mesh was 2.4±2.7%, 4.3±4.4%, and 1.6±2.5%, for mesh densities of 0.3125, 0.46875, and 0.625 mm, respectively (Figure 5.2A). When comparing tri-linear interpolated nodal material mapping, four-node linear (TET4) and ten-node quadratic (TET10) tetrahedral meshes map materials differently, most likely due to the variation in number of nodes and their relative location within the CT scalar field. The QCT density error for TET4 mesh densities of 0.3125, 0.46875, and 0.625 mm was 0.4±1.6%, 3.5±3.3%, and 2.0±2.2%, respectively when compared to the hexahedral mesh. For the TET10 mesh, errors were -0.6±1.4%, 2.0±1.4%, 0.2±1.9% with densities of 0.3125, 0.46875, and 0.625 mm, respectively (Figure 5.2B).

Qualitatively, the material mapping strategy applied to the hexahedral or tetrahedral QCT-FEMs varied by both element type and tetrahedral mesh density (Figure 5.3). This was also observed in the displacement field during compression. The most pronounced variation was visible among hexahedral elements and material mapping using either Mimics, node-based HU, or node-based E field. Variations in displacement maps were also apparent by tetrahedral element type (TET4 or TET10) and material mapping strategy but were less pronounced between element density.

When assessing the percent errors in E_{app} as a function of bone volume fraction (BV/TV) by material mapping strategy, errors were lowest for HEX8 QCT-FEMs mapped with Mimics (Figure 5.4). This mapping strategy also has the lowest errors for both TET4 and TET10 QCT-FEMs, especially at larger bone volume fractions. The node-based material mapping using the HU field generally showed lower errors for TET4 QCT-FEMs with 0.625 mm elements. The node-based E field mapping had the lowest errors for QCT-FEMs with TET10 elements but had greater errors than the other two mapping strategies for all element types.

Comparing linear regression of the HEX8 QCT-FEMs compared to the corresponding µFEMs (Table 5.2), indicated that QCT-FEMs mapped with Mimics had the closest agreement to the µFEMs, representing an over-estimation in E_{app} of 1.4%. For HEX8 elements, the node-based material mapping strategy using the native HU-field had the highest r^2, lowest SE and represented an underestimation in E_{app} for these cores of 4.6%.

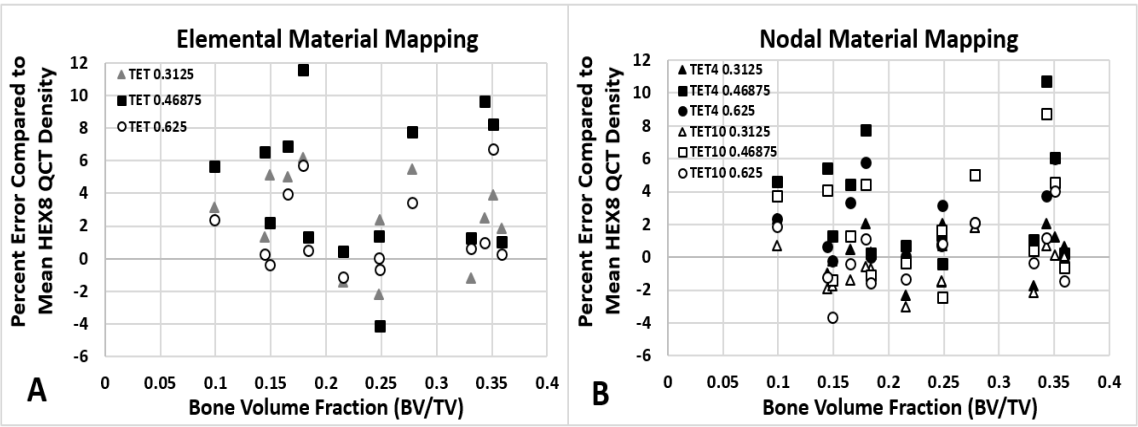

Figure 5.2: Percent error in QCT density mapping for tetrahedral elements compared to hexahedral (HEX8) elements as a function of bone volume fraction

Comparison using elemental exact volume-weighted elemental averaging (Mimics V. 20.0) **(A)**, and nodal tri-linear interpolation (Matlab V. R2017a) **(B)**. All hexahedral meshes are 0.625 mm isotropic, equal to the QCT voxel dimensions. Elemental material mapping is independent of tetrahedral mesh type (TET4 or TET10). Nodal material mapping varied by tetrahedral element type (TET4 or TET10) due to the number of nodes and their relative position in the QCT scalar field.

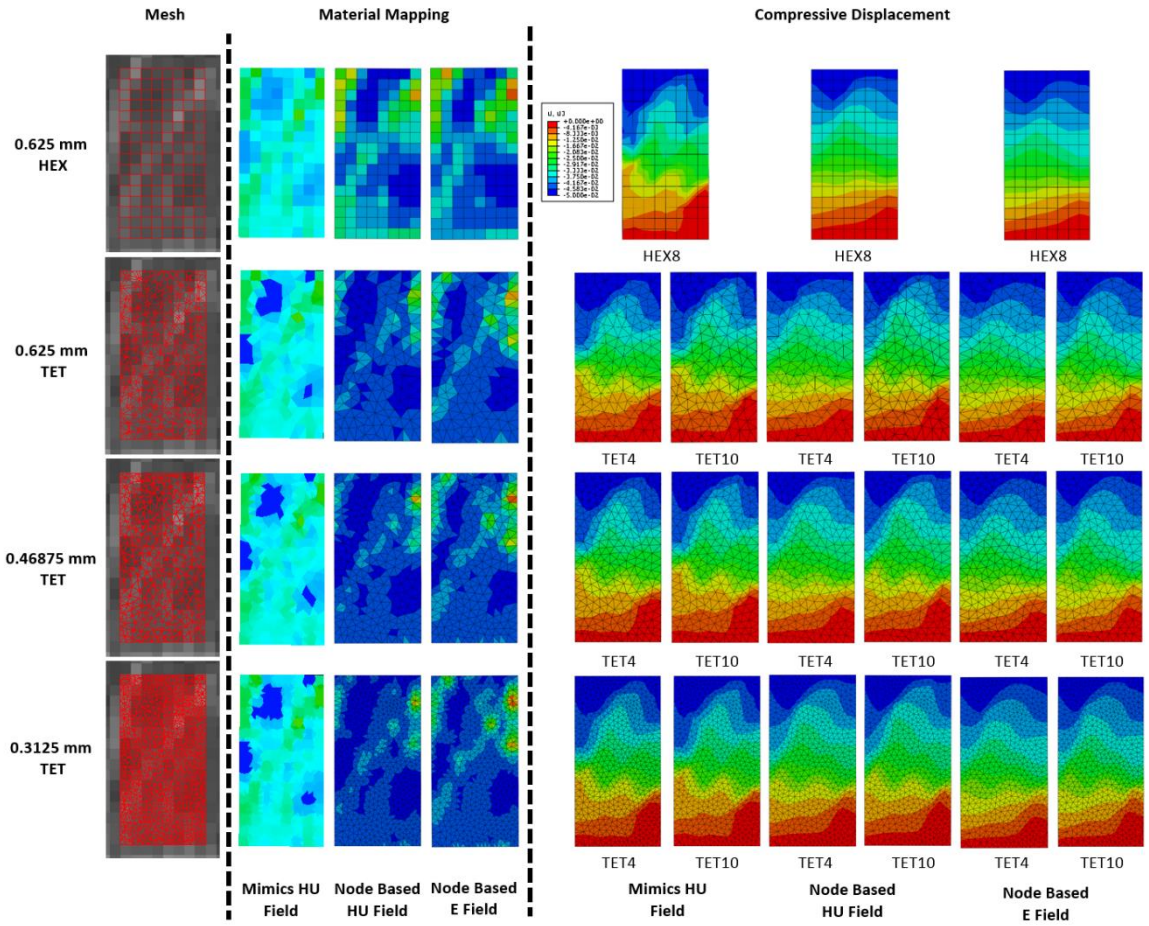

Figure 5.3: Representations of element mesh type, material mapping, and compressive displacement in QCT-FEMs

The hexahedral (HEX8) and tetrahedral (TET4 & TET10) meshes overlaid on the QCT image. Color maps of the apparent modulus mapped to each QCT-FEM using the different material mapping strategies. Corresponding displacement maps of representative QCT-FEMs using hexahedral (top) and coarse (0.625 mm), medium (0.46875 mm), and fine (0.3125 mm) tetrahedral elements. The apparent strain of 0.5% was applied along the long-axis of each FEM. Note: slight variations in material mapping color maps may occur due to rendering variations in Mimics and field variable output in Abaqus (node-based models).

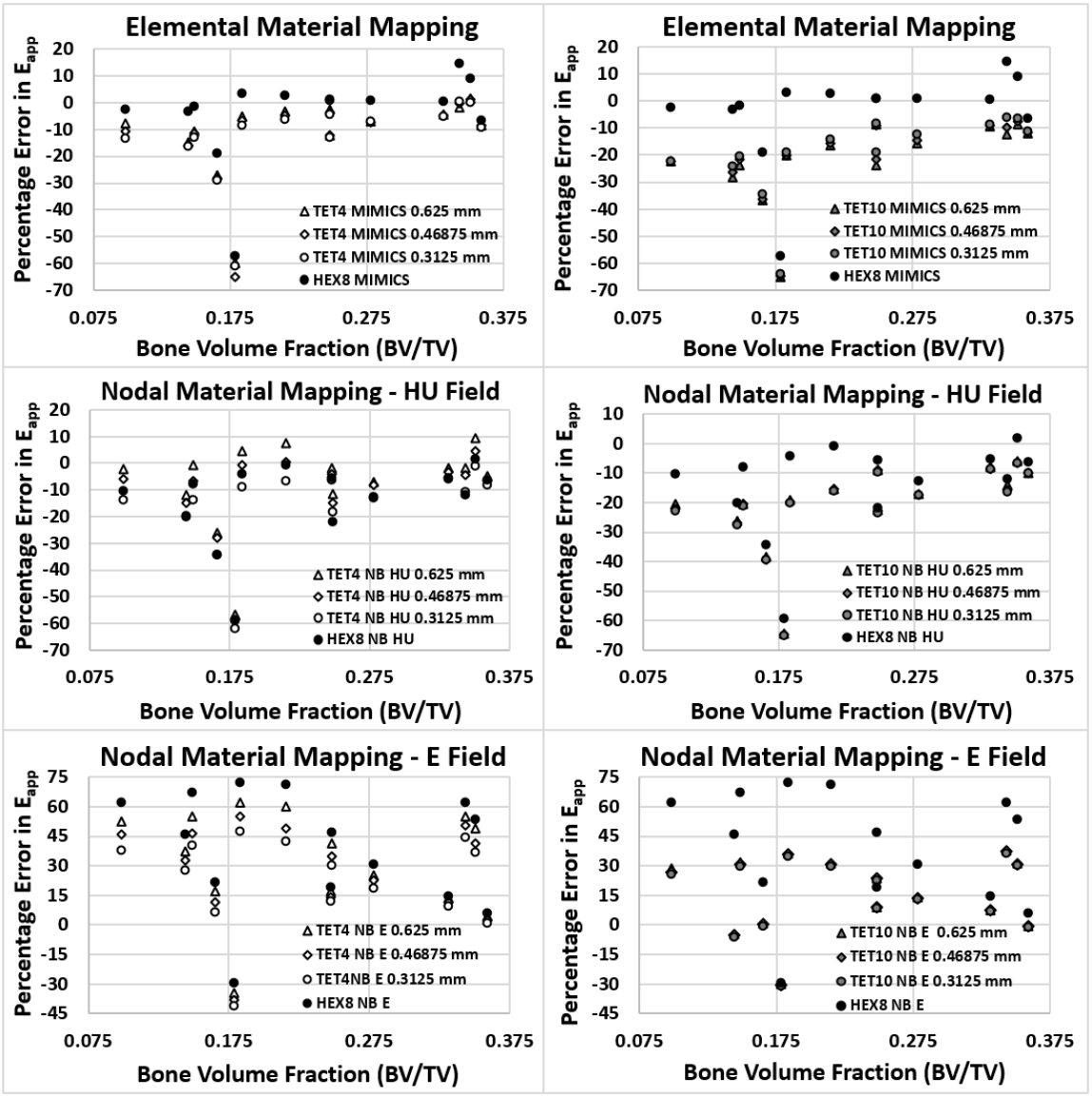

Figure 5.4: Percent error of QCT-FEMs compared to corresponding µFEMs as a function of bone volume fraction (BV/TV)

Results are by material mapping strategy: exact volume-weighted elemental averaging of the native HU field using Mimics, node-based using the HU-field, and node-based using E-field.

Table 5.2: Linear regression of apparent modulus (E_{app}) of QCT-FEMs as a function µFEM E_{app} for hexahedral (HEX8) elements and different material mapping strategies

QCT-FEM E_{app} = m x µFEM E_{app} + b

FEM	r^2	m	b	SE (MPa)	SE/mean
QCT HEX8 MIMICS	0.972	1.014	-17.94	109	15.1 %
QCT HEX8 Node-Based HU	0.984	0.954	-44.20	78	12.0 %
QCT HEX8 Node-Based E	0.903	1.175	-106.50	244	25.4%

SE – Standard error of regression

The same material mapping strategy, but using the E-field, overestimated E_{app} by 17.5%, and had the largest SE and lowest r^2.

The Bland-Altman plots (Figure 5.5) for the HEX8 QCT-FEMs showed the least bias for QCT-FEMs mapped with Mimics. The node-based HU-field had increased error and the node-based E-field had significant proportional error.

When TET10 elements were used in the QCT-FEMs, Mimics provided the best mapping strategy for TET10 elements with an underestimation in E_{app} of 6.4% at the smallest mesh density (Table 5.4). Linear regression parameters for TET10 elements were comparable between Mimics mapped models and node-based HU models. Errors were again largest for node-based E-field mapping.

Bland-Altman plots of TET10 comparisons (Figure 5.6) further illustrate the similarities between Mimics mapped QCT-FEMs and node-based HU-field mapped QCT-FEMs. The proportional error is again evident with node-based E-field mapped QCT-FEMs and is consistent across mesh densities.

TET4 elements showed the least error of all the mapping strategies, with the lowest error for node-based HU-field mapping at a mesh density of 0.625 mm (Table 5.3). This error of 1.5% occurred at a mesh density equal to that of the QCT voxel dimensions.

Contrary to the linear regression results, the Bland-Altman plots for the TET4 comparisons show the least bias for the QCT-FEMs mapped with Mimics (Figure 5.7). The node-based HU-field with a mesh density of 0.3125 mm was the closest coMParison to the Mimics elemental results. As with the other two element types, proportional error was evident for the node-based E-field material mapping.

5.4 DISCUSSION:

This study compared elemental (MIMICS) and nodal (NB HU & NB E) material mapping strategies used to map a validated density-modulus relationship to QCT-FEMs, with co-registered µFEMs as the gold standard for micro-level loading. By using a constitutive relationship developed specifically for these virtual cores, it was found that QCT-FEMs with hexahedral elements closely matched predictions of E_{app} provided by µFEMs when elemental mapping was performed using Mimics.

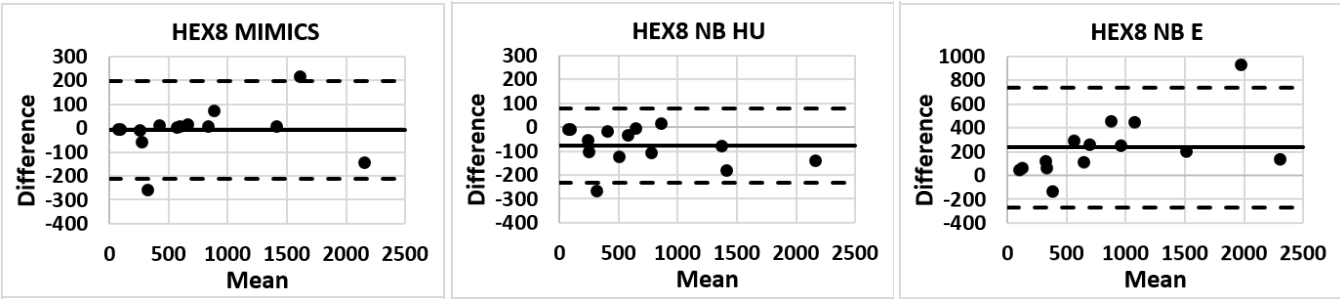

Figure 5.5: Bland-Altman plots of QCT-FEMs and µFEMs for QCT hexahedral elements (HEX8) with Mimics, node-based HU (NB HU) or node-based E (NB E) material mapping

Note the scale change in the NB E plots.

Table 5.3: Linear regression of apparent modulus (E_{app}) of QCT-FEMs as a function µFEM E_{app} for linear tetrahedral (TET4) or quadratic tetrahedral (TET10) elements and different material mapping strategies

QCT-FEM E_{app} = m x µFEM E_{app} + b

FEM	r^2	m	b	SE (MPa)	SE/mean
QCT TET10 MIMICS					
0.625 mm	0.987	0.917	-58.78	66	11.2%
0.46875 mm	0.987	0.925	-57.53	67	10.9%
0.3125 mm	0.987	0.936	-55.57	69	11.0%
QCT TET10 Node-Based HU					
0.625 mm	0.986	0.927	-61.36	69	11.3%
0.46875 mm	0.986	0.923	-61.91	70	11.5%
0.3125 mm	0.986	0.921	-62.69	71	11.7%
QCT TET10 Node-Based E					
0.625 mm	0.946	1.093	38.53	165	19.8%
0.46875 mm	0.947	1.091	36.95	163	19.6%
0.3125 mm	0.949	1.089	34.53	160	19.4%
QCT TET4 MIMICS					
0.625 mm	0.984	0.961	-32.06	77	11.5%
0.46875 mm	0.982	0.965	-38.38	83	12.5%
0.3125 mm	0.983	0.964	-39.55	79	11.9%
QCT TET4 Node-Based HU					
0.625 mm	0.983	0.985	-25.32	82	11.9%
0.46875 mm	0.985	0.970	-33.79	76	11.3%
0.3125 mm	0.986	0.944	-45.62	72	11.2%
QCT TET4 Node-Based E					
0.625 mm	0.916	1.154	87.27	222	24.0%
0.46875 mm	0.923	1.135	70.78	208	23.2%
0.3125 mm	0.931	1.113	59.15	191	22.0%

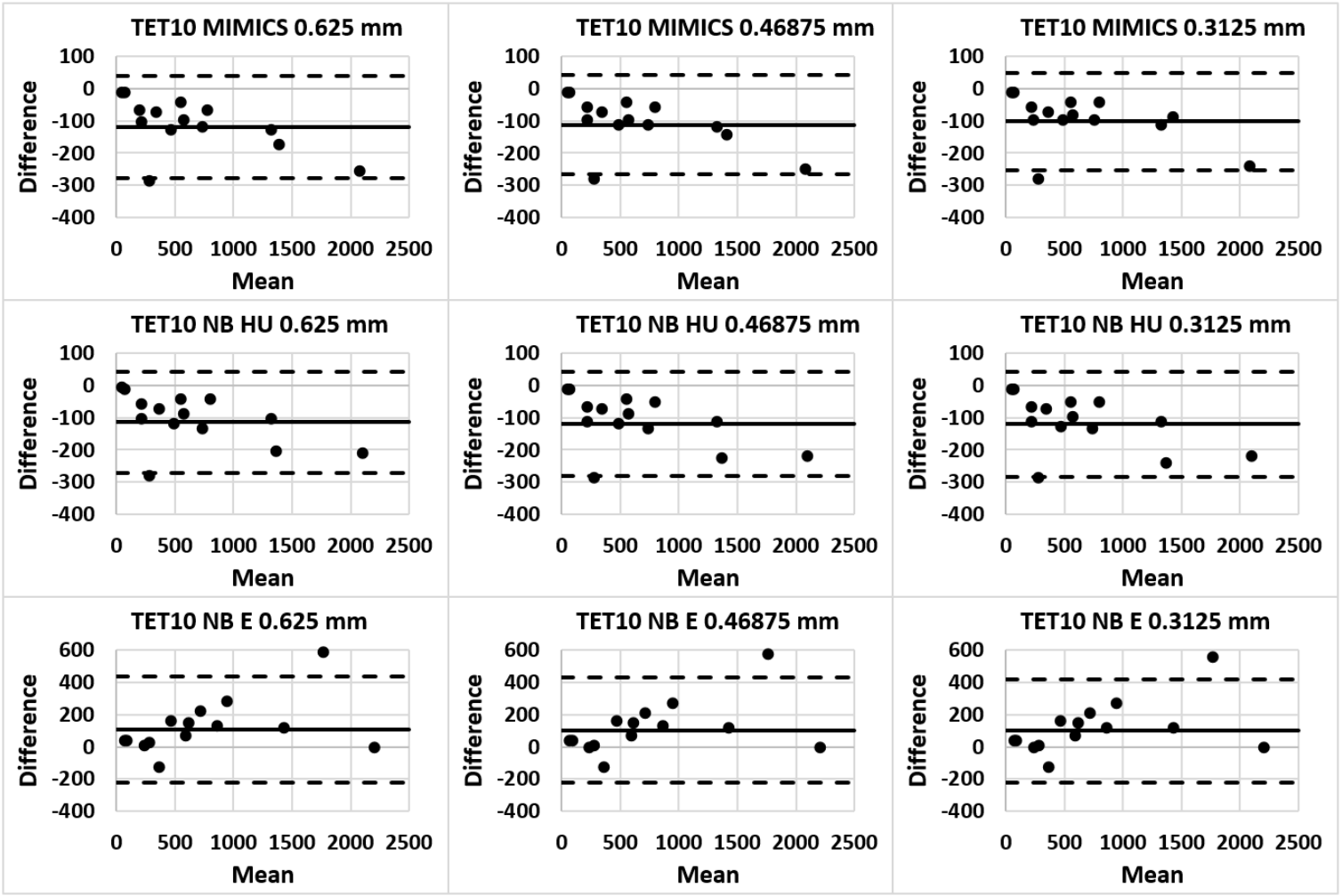

Figure 5.6: Bland-Altman plots of QCT-FEMs and µFEMs for QCT tetrahedral elements (TET10) with Mimics, node-based HU (NB HU) or node-based E (NB E) material mapping

Note the scale change in the NB E plots.

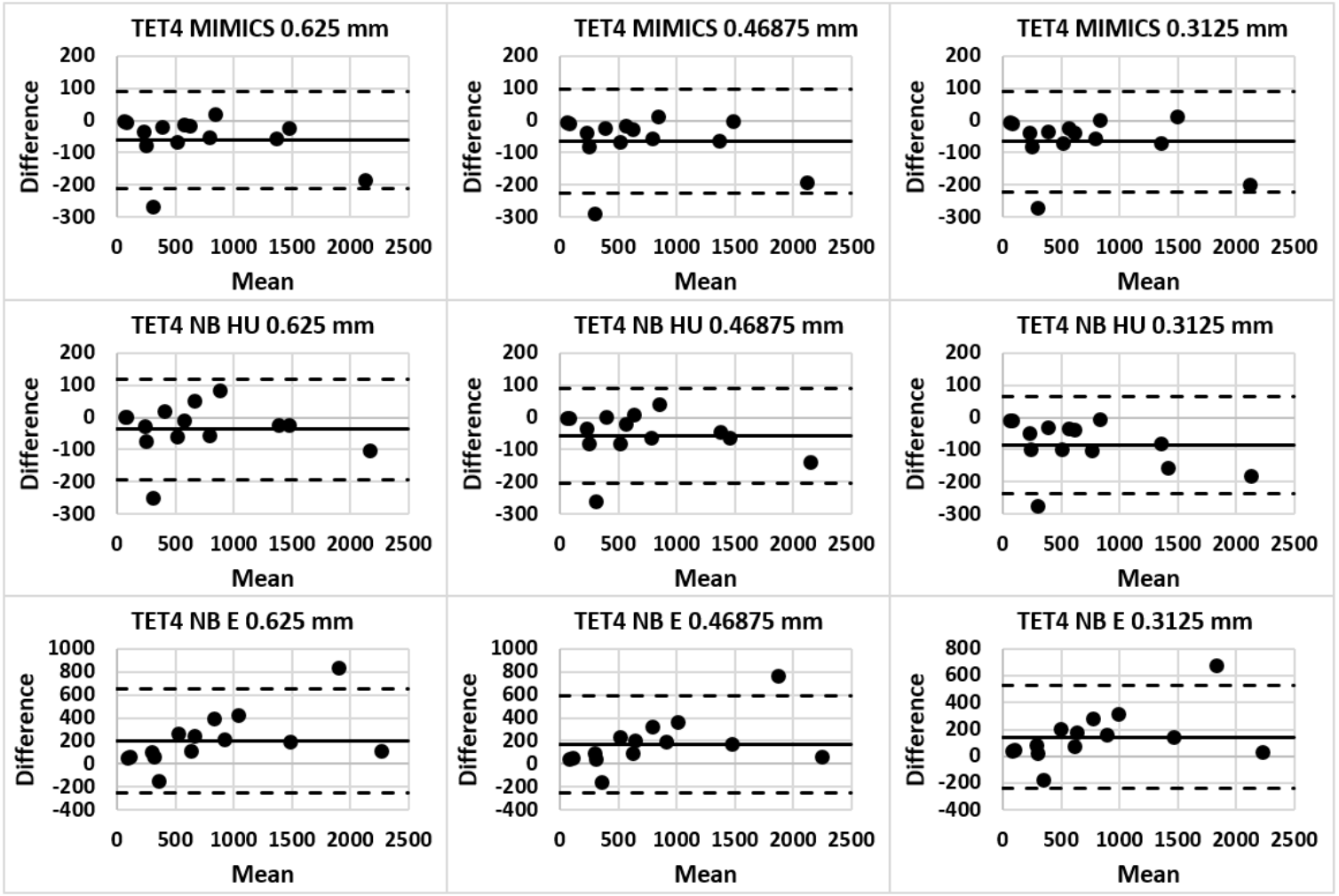

Figure 5.7: Bland-Altman plots of QCT-FEMs and µFEMs for QCT tetrahedral elements (TET4) with Mimics, node-based HU (NB HU) or node-based E (NB E) material mapping

Note the scale change in the NB E plots.

This mapping strategy also showed lower errors with linear and quadratic tetrahedral elements compared to node-based material mapping strategies. The node-based material mapping strategy using the native HU-field showed comparable results to Mimics elemental mapping when quadratic tetrahedral elements were used (TET10). This suggests that when choosing TET10 elements, either material mapping strategy can replicate the micro-level apparent loading model.

The first step in accurately mapping an empirically-derived non-linear constitutive relationship to a clinical-resolution FEM is to extract an accurate density for each voxel. Using a calibration phantom and extracting a calibrated QCT density can eliminate some of the systematic error between density measures (Knowles et al., 2016). However, the subsequent assignment of material properties to the FEM mesh can also have a dramatic effect, especially for tetrahedral elements. It was found that errors of greater than 10% in mean QCT density can occur simply by altering the material mapping strategy, element type, and/or mesh density (Figure 5.2). This adds a level of complexity in determining a converged mesh, especially when the outcome measures are stresses and/or strains, which may be significantly altered by variations in local material properties induced by the modeling parameters.

Material mapping strategy is inherently influenced by the local QCT density; therefore, it is essential to ensure that an accurate representation of local density is captured in the QCT scans. Measured QCT density varies greatly with CT scan settings (Giambini et al., 2015; Reeves et al., 2018), and because many existing density-modulus relationships in the literature use apparent or ash density related to apparent modulus (Helgason et al., 2008a), it is important to ensure that the scan settings, density measure, and/or density conversions are consistent with the modeling parameters chosen (Knowles et al., 2016). Variations in the mapped materials and corresponding compressive displacement maps (Figure 5.3) indicate that material mapping strategy is generally independent of bone volume fraction, but local bone response may be dependent on the individual QCT density of the elements within each core. It is therefore essential that, aside from the chosen material mapping strategy, it is understood that variations in settings used to acquire the QCT images can have significance influence on the whole bone apparent strength and stiffness (Dragomir-Daescu et al., 2015).

When comparing apparent modulus results (E_{app}) between QCT-FEMs and µFEMs by material mapping strategy, element type, and element density, it was found that elemental material mapping using Mimics was universally the best predictor of the micro-level loading. This is an important finding because commercially available software using this method simplifies the modeling by incorporating image processing, mesh generation, and material mapping to a single software platform. Open-source material mapping software (BoneMat, www.bonemat.org) also exists for elemental material mapping and makes use of either HU or E scalar fields; however, from our experience with this software, the vtk rectilinear grid used to map the scalar properties to the mesh was misaligned, and due to lack of user-integration this could not be rectified. Addressing this issue and completing these comparisons with this software would be beneficial to the computational biomechanics' community, since this software provides both scalar fields with an elemental mesh. Alternatively, more recent open-source software (MITK-GEM) may also provide an effective method of implementing these material mapping methods.

Elemental material mapping provides a distinct material property for each element within the FE mesh, but this can require significant pre-processing of the mesh to minimize partial volume effects (PVEs) on the outer surface of whole bones (Helgason et al., 2016). PVEs can have a dramatic effect at the interface between the outer cortical shell and the surrounding soft tissue/air, by significantly reducing the modulus of elements falling within these voxels. Methods exist to attempt to account for this by creating a separate mask of the cortex and assigning a uniform homogeneous material with shell (Bessho et al., 2007) or solid elements (Helgason et al., 2016). The weighted mapping of the tetrahedral mesh to the scalar field may result in cortical elements that are less influenced by partial volume if the mesh density is fine and the 'weak voxel layer' has been removed using image processing steps (Helgason et al., 2016). Recently, different material mapping strategies and image processing methods have been described to elucidate the contributive factors of the perceived 'errors' of this 'weak voxel layer' on whole bone FEMs (Helgason et al., 2016). The outer geometry can also be eroded using image processing techniques, but this compromises geometrical accuracy. Collectively these methods may reduce the effects of cortical density variations on the mechanical response of the bone, at a cost of greatly increasing pre-processing time.

A perhaps simpler method is to adopt a node-based material mapping strategy that requires custom code for implementation with either hexahedral or tetrahedral meshes. The method employed in this study uses tri-linear interpolation of the CT-scalar field to assign material properties to the nodes. It assigns these as field variables in Abaqus, which interpolates the values to the Gauss integration points during simulation. This method could also be adapted to automatically assign the material property to the integration point, without the need for the FE-solver to perform this step. An additional benefit to a nodal material mapping strategy is that partial volume effects (PVEs) can be easily identified and corrected using the values obtained during mapping. If outer nodes on a cortical region are assigned a value lower than an internal node (due to PVEs), then the outer node is simply assigned the nearest internal node's value (Helgason et al., 2008b). Nodal material mapping can also be used in bone remodeling simulations by updating the nodal material as a function of outputs (eg. bone strain energy density) using a user-defined sub-routine.

The material mapping strategy inherently influences the mechanical response of the bone and is perhaps most relevant in whole bones at the bone's surface due to PVEs (Helgason et al., 2016). Although the results of this study are not influenced by PVEs due to the trabecular bone cores with isotropic voxels that match the chosen element dimensions, previous studies have validated material mapping strategies by using empirical surface strain measured using strain gauges attached to the cortical bone surface. If the corresponding computational model used in the validation underestimates the 'true' cortical modulus, then the accuracy of this validation may be compromised. This may be one explanation for why 'E field' has been shown to have improved correlations with empirical surface strain results (Dahan et al., 2016; Taddei et al., 2007). As observed in the present study, this mapping strategy tends to overestimate the elemental apparent modulus, which may artificially overestimate the true cortical surface modulus.

The simple elemental averaging method, first reported by Zannoni et al. (1999), was later updated with improved HU mapping of the CT scalar field onto the FE mesh using numerical integration (Taddei et al., 2004). With tetrahedral elements that vary in mesh density, this method was reported to eliminate issues with simple elemental averaging that may significantly influence the accuracy of the mapped materials. This is the method used in the open-source material mapping software, BoneMat. It has also been suggested

that accuracy in mapping may be lost with tetrahedral elements when mesh density varies greatly (especially in relation to the native CT voxel dimensions) and/or at the interface of materials that vary greatly in density, due to PVEs. It was found in this study that Mimics exact volume-weighted elemental averaging of the native HU field accurately replicates the micro–level mechanical loading, both by element type and element mesh density.

A strength of this study is that the density-modulus relationship, μFEMs, and QCT-FEMs were all derived from the same 14 cadaveric specimens. This removes the uncertainty of attempting to replicate the experimental techniques used in subsequent studies (e.g. boundary conditions, density measures, bone quality) (Helgason et al., 2016, 2008a). This study however was purely computational and used μFEMs for validation. Although empirical validation is often performed, this present methodology eliminates systematic errors that has been recently reported when attempting to replicate boundary conditions between empirical bone core loading and computational models (Chen et al., 2017). Mechanical stiffness and strength using exclusively μFEMs have been reported and validated extensively over the past decade (Bauer et al., 2014; Bevill and Keaveny, 2009; Depalle et al., 2013; Gong et al., 2016).

A limitation of this study is that only the apparent mechanical properties of the trabecular cores were considered. Although this provides an indirect comparative analysis of the mechanical response of the bone at the micro- and macro-scale based on displacements and forces, the local stresses and strains were not assessed. It is clear from the variation in the compressive displacement field results, and the associated material mapping, that variations in local stresses and strains may also occur. It is essential that this aspect be considered in the future, as recent work using digital volume correlation (DVC) has determined that bone displacements can be accurately modeled using current FEM methods (Costa et al., 2017), but local strain measurements tend to have relatively large errors (Dall'Ara et al., 2017; Palanca et al., 2017). To have direct relevance to clinical outcomes and fracture analysis, it has been suggested that these DVC comparisons be completed on the whole bone level (Jackman et al., 2016).

5.5 CONCLUSION:

This study further illustrates the importance of choosing an accurate material mapping strategy based on model parameters. If element type is carefully considered, the material mapping strategies assessed here can provide desired results. It was shown that the current methods used to map material properties based on exact volume-weighted elemental averaging of the native HU field can accurately represent the micro-level apparent mechanical properties of human trabecular bone. If modeling parameters are carefully considered, node-based mapping of the HU field, accounting for PVEs, may also provide accurate mechanical response of trabecular bone.

5.6 REFERENCES:

Bauer, J. S., I. Sidorenko, D. Mueller, T. Baum, A. S. Issever, F. Eckstein, E. J. Rummeny, T. M. Link, and C. W. Raeth. 2014. Prediction of bone strength by μcT and MDCT-based finite-element-models: How much spatial resolution is needed? Eur. J. Radiol. 83:e36–e42,

Bessho, M., I. Ohnishi, J. Matsuyama, T. Matsumoto, K. Imai, and K. Nakamura. 2007. Prediction of strength and strain of the proximal femur by a CT-based finite element method. J. Biomech. 40:1745–1753

Bevill, G., and T. M. Keaveny. Trabecular bone strength predictions using finite element analysis of micro-scale images at limited spatial resolution. 2009. Bone 44:579–584,

Bourne, B. C., and M. C. H. Van Der Meulen. 2004.Finite element models predict cancellous apparent modulus when tissue modulus is scaled from specimen CT-attenuation. J. Biomech. 37:613–621

Chen, G., B. Schmutz, D. Epari, K. Rathnayaka, S. Ibrahim, M. a. Schuetz, and M. J. Pearcy. 2010. A new approach for assigning bone material properties from CT images into finite element models. J. Biomech. 43:1011–1015

Chen, G., F. Y. Wu, Z. C. Liu, K. Yang, and F. Cui. 2015. CoMParisons of node-based and element-based approaches of assigning bone material properties onto subject-specific finite element models. Med. Eng. Phys. 37(8):1–5

Chen, Y., E. Dall′Ara, E. Sales, K. Manda, R. Wallace, P. Pankaj, and M. Viceconti. 2017. Micro-CT based finite element models of cancellous bone predict accurately displacement once the boundary condition is well replicated: A validation study. J. Mech. Behav. Biomed. Mater. 65:644–651

Costa, M. C., G. Tozzi, L. Cristofolini, V. Danesi, M. Viceconti, and E. Dall'Ara. 2017. Micro finite element models of the vertebral body: Validation of local displacement predictions. PloS One 12:1–18

Dahan, G., N. Trabelsi, O. Safran, and Z. Yosibash. 2016. Verified and validated finite element analyses of humeri. J. Biomech. 49:1094–1102

Dall'Ara, E., M. Peña-Fernández, M. Palanca, M. Giorgi, L. Cristofolini, and G. Tozzi. 2017. Precision of Digital Volume Correlation Approaches for Strain Analysis in Bone Imaged with Micro-Computed Tomography at Different Dimensional Levels. Front. Mater. 4:31

Depalle, B., R. Chapurlat, H. Walter-Le-Berre, B. Bou-Saïd, and H. Follet. 2013. Finite element dependence of stress evaluation for human trabecular bone. J. Mech. Behav. Biomed. Mater. 18:200–212

Dragomir-Daescu, D., C. Salas, S. Uthamaraj, and T. Rossman. 2015. Quantitative computed tomography-based finite element analysis predictions of femoral strength and stiffness depend on computed tomography settings. J. Biomech. 48:153–161

Faieghi, M., N. K. Knowles, O. R. Tutunea-fatan, and L. M. Ferreira. 2019. Fast Generation of Cartesian Meshes from Micro-Computed Tomography Data. Comput. Aided Des. Appl. 16:161–171

Giambini, H., D. Dragomir-Daescu, P. M. Huddleston, J. J. Camp, K.-N. An, and A. Nassr. 2015. The Effect of Quantitative Computed Tomography Acquisition Protocols on Bone Mineral Density Estimation. J. Biomech. Eng. 137:1–6

Gong, H., L. Wang, Y. Fan, M. Zhang, and L. Qin. 2016. Apparent- and Tissue-Level Yield Behaviors of L4 Vertebral Trabecular Bone and Their Associations with Microarchitectures. Ann. Biomed. Eng. 44:1204–1223

Guldberg RE, Hollister SJ, Charras GT. 1998. The Accuracy of Digital Image-Based Finite Element Models. J Biomech Eng. 120:289.

Helgason, B., S. Gilchrist, O. Ariza, P. Vogt, W. Enns-Bray, R. P. Widmer, T. Fitze, H.

Pálsson, Y. Pauchard, P. Guy, S. J. Ferguson, and P. A. Cripton. 2016. The influence of the modulus-density relationship and the material mapping method on the simulated mechanical response of the proximal femur in side-ways fall loading configuration. Med. Eng. Phys. 38:679–689

Helgason, B., E. Perilli, E. Schileo, and F. Taddei. 2008a. Mathematical relationships between bone density and mechanical properties: a literature review. Clin. Biomech. 23:135–146

Helgason, B., F. Taddei, H. Pálsson, E. Schileo, L. Cristofolini, M. Viceconti, and S. Brynjólfsson. 2008b. A modified method for assigning material properties to FE models of bones. Med. Eng. Phys. 30:444–453

Jackman, T. M., A. I. Hussein, C. Curtiss, P. M. Fein, A. Camp, L. De Barros, and E. F. Morgan. 2016. Quantitative, 3D Visualization of the Initiation and Progression of Vertebral Fractures under Compression and Anterior Flexion. J. Bone Miner. Res. 31:777–788

Knowles, N. K., G. D. G. Langohr, M. Faieghi, and A. Nelson. 2019. Development of a validated glenoid trabecular density-modulus relationship. J. Mech. Behav. Biomed. Mater. 90:140-145

Knowles, N. K., J. M. Reeves, and L. M. Ferreira. 2016.Quantitative Computed Tomography (QCT) derived Bone Mineral Density (BMD) in finite element studies: a review of the literature. J. Exp. Orthop. 3:36

Niebur GL, Yuen JC, Hsia AC, Keaveny TM. 1999. Convergence Behavior of High-Resolution Finite Element Models of Trabecular Bone. J Biomech Eng. 121:629.

Palanca, M., A. J. Bodey, M. Giorgi, M. Viceconti, D. Lacroix, L. Cristofolini, and E. Dall'Ara. 2017. Local displacement and strain uncertainties in different bone types by digital volume correlation of synchrotron microtomograms. J. Biomech. 58:27–36

Reeves, J. M., N. K. Knowles, G. S. Athwal, and J. A. Johnson. 2018. Methods for post Hoc quantitative computed tomography bone density calibration: Phantom-only and regression. J. Biomech. Eng. 140

Taddei, F., A. Pancanti, and M. Viceconti. 2004. An improved method for the automatic mapping of computed tomography numbers onto finite element models. Med. Eng.

Phys. 26:61–69

Taddei, F., E. Schileo, B. Helgason, L. Cristofolini, and M. Viceconti. 2007. The material mapping strategy influences the accuracy of CT-based finite element models of bones: an evaluation against experimental measurements. Med. Eng. Phys. 29:973–9

Wille, H., E. Rank, and Z. Yosibash. 2012.Prediction of the mechanical response of the femur with uncertain elastic properties. J. Biomech. 45:1140–1148

Zannoni, C., R. Mantovani, and M. Viceconti. 1999. Material properties assignment to finite element models of bone structures: a new method. Med. Eng. Phys. 20:735–740

CHAPTER 6 – MATERIAL MAPPING OF QCT-DERIVED SCAPULAR MODELS: A COMPARISON WITH MICRO-CT LOADED CADAVERS USING DIGITAL VOLUME CORRELATION

OVERVIEW: *This chapter describes the experimental comparison of scapular models loaded within a microCT scanner and analyzed with digital volume correlation (DVC) to QCT-FEMs mapped with different density-modulus relationships and material mapping strategies, using DVC-driven boundary conditions.*[6]

[6]A version of this work has been submitted for publication**:** Knowles NK**,** Kusins J, Faieghi M, Ryan M, Dall'Ara E, Ferreira LM. Material Mapping of QCT-Derived Scapular Models: A Comparison with Micro-CT Loaded Cadavers using Digital Volume Correlation. Annals of Biomedical Engineering (ABME-S-19-00191)

6.1 INTRODUCTION:

Subject-specific finite element models (FEMs) allow for a variety of biomechanical and clinical conditions to be tested in a highly repeatable manner. The accuracy of these FEMs is improved by accurately mapping density using quantitative computed tomography (QCT) and by choosing a constitutive relationship that relates density to mechanical properties. Although QCT-derived FEMs have become common practice in contemporary computational studies of whole bones, many of the density-modulus relationships used at the whole bone level were derived using mechanical loading of small trabecular or cortical bone cores (Helgason et al., 2008a; Knowles et al., 2016). These cores are mechanically loaded to derive an apparent modulus, which is related to each core's mean apparent or ash density. Using these relationships to convert the QCT Hounsfield units into equivalent bone mineral density (BMD) and then into apparent or ash density for whole bones composed of both cortical and trabecular bone may introduce error in the FEM development process (Knowles et al., 2016).

To determine mechanical properties, most studies use traditional mechanical testing methods by measuring force and apparent strain using an extensometer attached to brass end caps to quantify apparent strain of the deformed core (Keaveny et al., 1994; Morgan and Keaveny, 2001). However, recent work performed with in-situ mechanical testing (within a scanning device) has shown that it is very important to carefully assign the boundary conditions (BC) in order to obtain accurate predictions of local displacements within the trabecular bone (Chen et al., 2017). Moreover, using a combination of time-lapsed mechanical testing and digital volume correlation (DVC) approaches can provide precise estimations of the full-field specimen deformation, something not available with standard mechanical testing. As such, a recent computational methodology was proposed that developed a glenoid-specific trabecular density-modulus relationship by comparing QCT-FEMs to co-registered micro-FEMs (Knowles et al., 2019). This methodology eliminates experimental uncertainties present in previous density-modulus development and may provide a more accurate mapping of modulus to trabecular bone in subsequent QCT-FEMs.

Beyond the choice of density-modulus relationship, the material mapping strategy also influences model accuracy (Taddei et al., 2007). Recent methods have been proposed,

evaluating elemental and nodal mapping strategies and pre-processing methods to compare the effect of density-modulus relationships and material mapping strategy on the performance of femoral QCT-FEMs (Enns-Bray et al., 2018; Helgason et al., 2016). Although these validations provide a comprehensive and robust testing methodology, they are limited to comparisons lying on the cortical shell and global stiffness measurements. Additionally, the BCs are limited to those measured with load cells or surface displacement registrations with optical tracking or digital image correlation. Recent studies on spine segments have found improvements between QCT-FEMs and experimental results when BCs are derived using local displacements measured by DVC (Hussein et al., 2018; Jackman et al., 2015).

To improve methods used to compare density-modulus relationships and material mapping strategies, this study used experimental loading of scapular models within a micro-CT. Experimental boundary conditions were replicated in QCT-FEMs using DVC, and the predictions of QCT-FEMs were compared to experimental loading results based on reaction forces. Moreover, the predictive accuracy of the QCT-FEMs was tested for different material mapping strategies in order to identify the best modeling approach.

6.2 METHODS:

6.2.1 Specimens and QCT Scanning

Six fresh-frozen cadaveric full arms (3 male; 3 female; mean age: 68±10 years) were scanned with a multi-slice clinical CT-scanner (GE Discovery CT750 HD, Milwaukee, WI, USA) using clinical settings (pixel size: 0.625 mm to 0.668 mm, slice thickness: 0.625 mm, 120 kVp, 200 mA, BONEPLUS). A dipotassium phosphate (K_2HPO_4) calibration phantom (QCT Pro, Mindways Software Inc., Austin, TX, USA) was scanned with each specimen to determine specimen-specific QCT-density relationships. The QCT density distribution for each specimen is provided in Figure 6.1. Following scanning, each scapula was denuded of all soft-tissues and fixed at its medial aspect by potting in polymethylmethacrylate (PMMA). The glenoid surface was then reamed to expose the trabecular bone using a hemispherical total shoulder arthroplasty reamer in order to ensure a uniform surface for

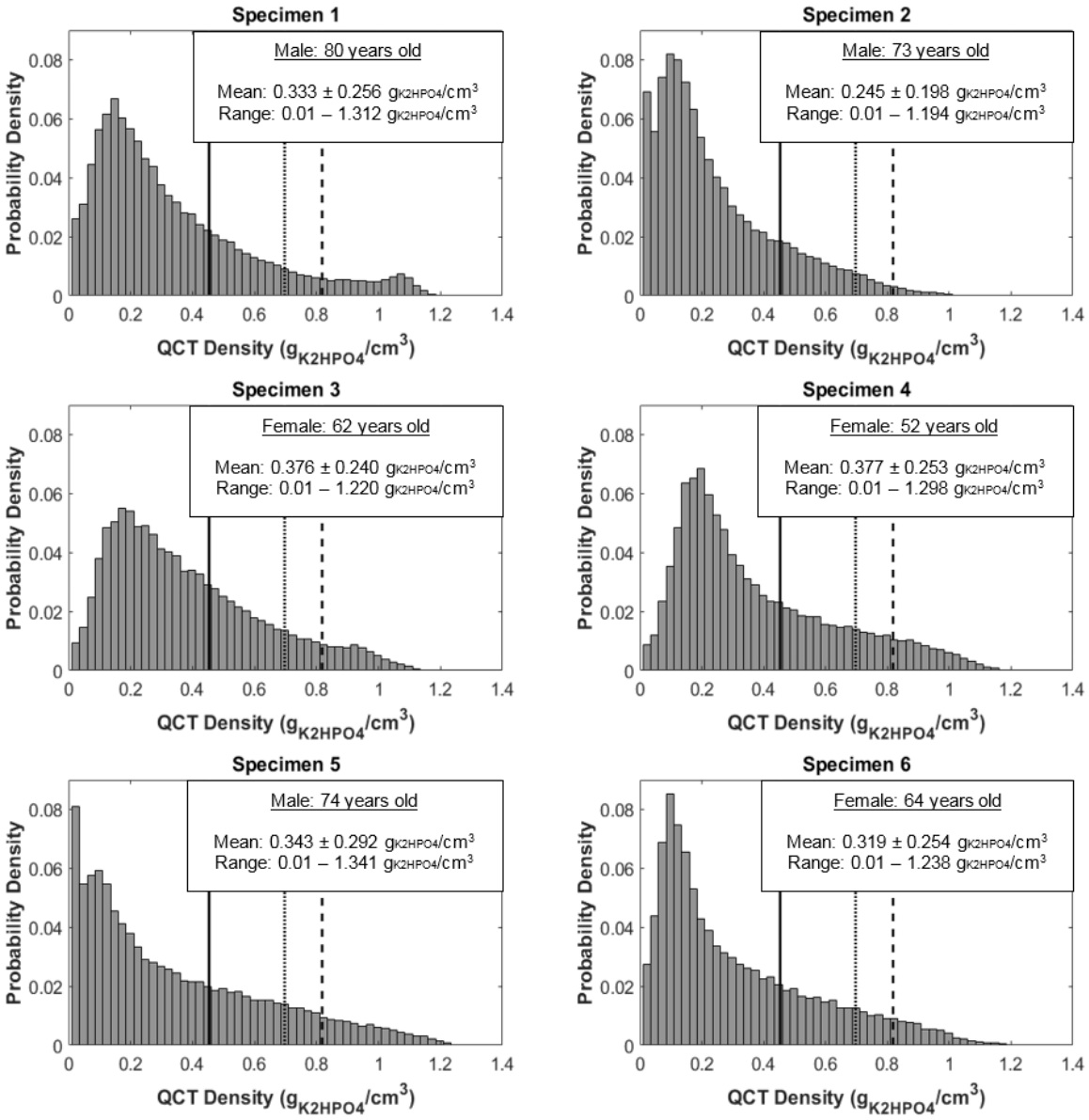

Figure 6.1: Histogram plots of the QCT density distribution in each of the six specimens
The lines represent transition between trabecular and cortical material mapping at 0.453 g_{K2HPO4}/cm^3 (relationships 1, 4, 7, 10, 14) (solid black line), 0.818 g_{K2HPO4}/cm^3 (relationships 2, 5, 8, 11, 14) (dashed black line), or 0.697 g_{K2HPO4}/cm^3 (relationship 15) (dotted black line).

loading. The medial PMMA potted surface was parallel to the reamed glenoid surface to ensure off-axis loads were minimized during compressive loading.

6.2.2 Experimental Loading and MicroCT Scanning

Each specimen was mounted in a custom hexapod parallel robot designed to apply loads to the glenoid through a 48 mm diameter Delrin® hemisphere (Figure 6.2). The hexapod's six linear servo-motors were augmented with carbon fibre rods to produce a radiolucent section for compatibility with a cone beam scanner and the load applicator was extended with an acrylic cylinder to avoid metal artifact. A 6-degree-of-freedom load cell (Mini 45, ATI Industrial Automation, NC, USA), integrated into the hexapod's loading platform, was used to target experimental applied loads. The hexapod was placed within a cone-beam microCT scanner (Nikon XT H 225 ST, Nikon Metrology, NV), each specimen was hydrated with phosphate-buffered saline solution, wrapped in saline-soaked tissue and a pre-load of 10 N was applied. A pre-load scan was acquired (33.5 μm isotropic voxels, 95 kVp, 64 μA, 3141 projections, 1000 ms exposure) after 20 minutes to allow proper relaxation of the loaded structure. The field of view (FOV) within the microCT varied by specimen, due to size, but included the entire glenoid vault and partial scapular body for all specimens (Figure 6.2). Following the pre-loaded scan, a compressive load to a target 500 N was performed. A scan with identical settings was performed at this post-loaded state. Identical loading regimes were performed for all six scapular specimens.

6.2.3 Image Post-Processing and Digital Volume Correlation (DVC)

The pre- and post-loaded scans were post-processed to provide 8-bit images of the bone using a specimen specific threshold (Mimics v.20.0, Materialise, Leuven, BE & ImageJ) (Schneider et al., 2012). These images were registered elastically using the Bone-DVC software (Dall'Ara et al., 2017). Bone-DVC is a global DVC software that computes a full-field displacement map by superimposing a regular grid with nodal spacing on the undeformed (pre-loaded state) and deformed (post-loaded state) images. The registration equations are solved at the nodes of the grid by assuming linear displacements within each grid cell. An optimised smoothing coefficient is used to regularize the displacement field.

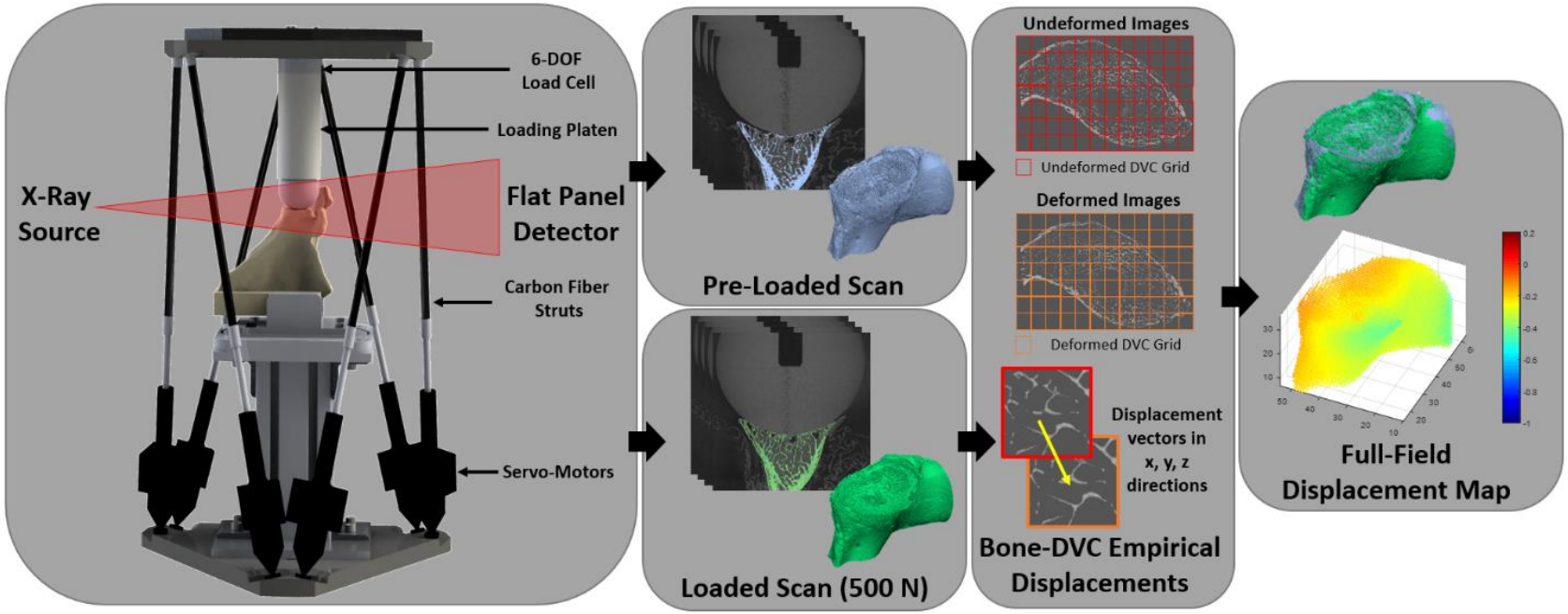

Figure 6.2: The workflow to determine full-field experimental displacements of cadaveric scapulae

A custom CT-compatible hexapod robot was used to applied compressive loads. Pre- and post-loaded scans were acquired and Bone-DVC (Dall'Ara et al., 2014) was used to compare the two states. An experimental full-field displacement map was used for comparison with the QCT-FEM nodal displacements.

This approach was shown to improve the accuracy of bone strain and displacement measurements for different bone structures at different image resolutions (Comini et al., 2019; Dall'Ara et al., 2017, 2014). Moreover, Bone-DVC has previously been used to validate the outputs of different FEM approaches for trabecular bone (Chen et al., 2017), vertebral bodies (Costa et al., 2017), and mouse tibia (Oliviero et al., 2018). In the first specimen, two pre-loaded scans were acquired and compared to determine the optimal DVC nodal spacing, with the assumption that displacements were zero for these two scans (Dall'Ara et al., 2017). A nodal spacing of 30, equivalent to a sub-volume size of ≈1 mm was found to provide the best compromise between the spatial resolution of the displacement measurement and its precision (<2.5 μm in the x, y, and z direction). Bone-DVC was used to determine the full-field displacements for all six cadaveric specimens (Figure 6.2).

6.2.4 QCT-FEM Generation and Boundary Conditions

To replicate the DVC-experimental results in subsequent QCT-FEMs, the scapula was cropped to include only the region included in the DVC results. The entire coracoid was included in the QCT-FEMs because our previous studies have shown that removal of this structure greatly influences the loading characteristics of the scapula (Knowles et al., 2018). The QCT- FEMs were generated from each corresponding QCT scan that was acquired at clinical resolution. The model's glenoid surface was virtually subtracted to match the reamed glenoid of each cadaveric specimen. This QCT model was aligned to a 3D model of the experimental scapula using iterative closest points registration (3-matic v.12.0, Materialise, Leuven, BE). Similar to the co-registration method previously described (Knowles et al., 2019a), the coordinate transform between the clinical-scans and the micro-CT scans were used to ensure computational forces and displacements matched the experimental setup. A triangular surface mesh of each model was created with a target 1 mm edge length and optimal 60-degree angles between edges (Burkhart et al., 2013). Surface meshes were transferred to Abaqus (v.6.14, Simulia, Providence, RI) and meshed with 10-node tetrahedral elements.

To accurately replicate the boundary conditions of each QCT-FEM, DVC-driven BCs were applied on both the articular and the medial cropped surfaces (Figure 6.3). Custom Matlab code (v. R2017a, Mathworks, Natick, MA) was used to create these DVC-driven BCs in the Abaqus input file. Tri-linear interpolation of the DVC displacement-field was performed to assign

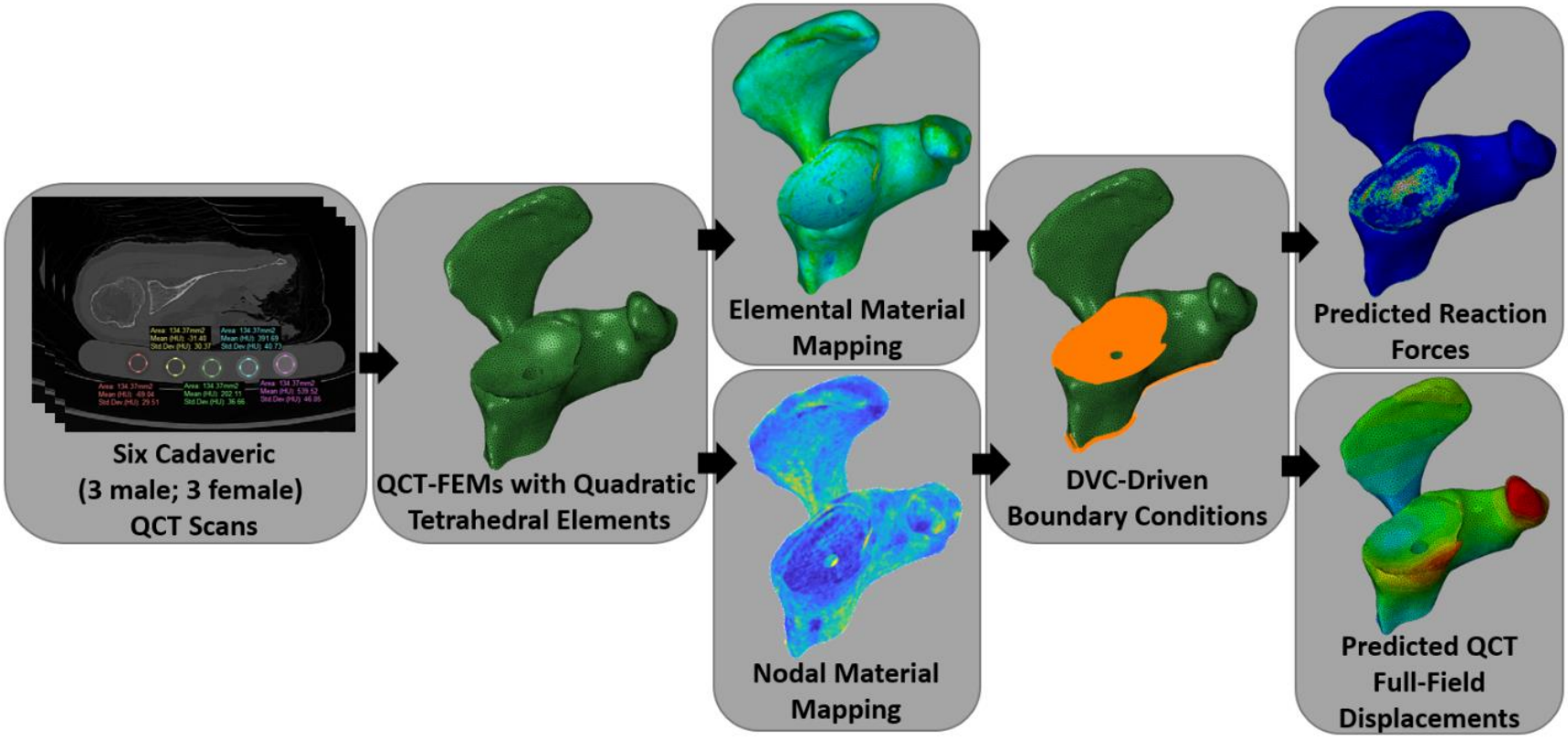

Figure 6.3: The workflow to determine full-field QCT-FEM displacements and reaction forces of cadaveric scapulae

QCT scans were acquired for six cadaveric specimens using a dipotassium phosphate calibration phantom. These images were used to generate QCT-FEMs with quadratic tetrahedral elements. Each of the fifteen density-modulus relationships (Table 1) were mapped using either elemental or nodal material mapping strategies. DVC-driven boundary conditions were applied to the articular and medial cropped surfaces. Reaction forces and full-field displacement of QCT-FEMs were compared to experimental DVC.

displacement boundary conditions in the x, y, and z directions to the tetrahedral nodes of the medial and glenoid articular surface.

6.2.5 Density-Modulus Relationships and Material Mapping Strategies

Fifteen density-modulus relationship combinations were compared with variations in the density ranges of the trabecular and cortical mapping (Table 6.1). The five primary relationships developed in the literature were derived from trabecular/cortical bone cores (relationships 3, 6, 9, 12, 15). Relationship 15 used a transition between trabecular and cortical bone of 1.54 g/cm^3 and was the only one of the primary relationships that had a trabecular/cortical piecewise relationship. This was included as it is a common relationship reported in shoulder FEM studies (Knowles et al., 2019b). Relationships 1, 4, 7, 10, and 13 used a transition from trabecular to cortical bone at an apparent density of 1 g/cm^3 (QCT equivalent density of 0.453 g_{K2HPO4}/cm^3) (Gray et al., 2008). Relationships 2, 5, 8, 11, and 14, assumed a uniform modulus of 20,000 MPa for all bone with an apparent density greater than the mean apparent density of cortical bone (ρ_{app} > 1.8 g/cm^3; QCT equivalent density of 0.818 g_{K2HPO4}/cm^3) (Carter and Hayes, 1977). These fifteen relationships were mapped using either elemental (Mimics v. 20.0) or nodal (Matlab, v.R2017a) material mapping strategies. The former is implemented in commercial software and uses exact volume element averaging of the tetrahedral mesh overlaid on the native CT-scaler field. The latter was implemented in custom code using tri-linear interpolation of the tetrahedral nodal coordinates within the native CT-scaler field. This nodal mapping strategy code also accounted for partial volume effects (PVEs) by assigning surface nodes a modulus equal to the nearest internal nodes, if this node's modulus was higher than the PVE affected surface node (Helgason et al., 2008b). In total, there were 90 elemental-mapped QCT-FEMs and 90 nodal-mapped QCT-FEMs for comparison.

6.2.6 QCT and DVC Model Comparisons

The nodal reaction forces were extracted from each QCT-FEM to determine which density-modulus relationship and material mapping strategy most accurately replicated the experimental reaction forces, measured with the load cell. Custom-code (Matlab v. R2017a) summed the reaction forces that occurred at the articular and medial surfaces of the DVC-Driven QCT-FEM. The code was used to verify that the QCT-FEM reaction forces were in equilibrium (forces were

Table 6.1: Density-Modulus Relationships

	Density Range	ρ-E Relationship
1	$\rho_{qct} < 0.453$ g_{k2HPO4}/cm^3	$^{a}E_{trab} = 32790 * \rho_{qct}^{2.307}$
	$\rho_{qct} \geq 0.453$ g_{k2HPO4}/cm^3	$^{b}E_{cort} = 10200 * \rho_{ash}^{2.01}$
2	$\rho_{qct} < 0.818$ g_{k2HPO4}/cm^3	$^{a}E_{trab} = 32790 * \rho_{qct}^{2.307}$
	$\rho_{qct} \geq 0.818$ g_{k2HPO4}/cm^3	$E_{cort} = 20\,000\ MPa$
3	$\rho_{qct} < 0.818$ g_{k2HPO4}/cm^3	$^{a}E_{trab} = 32790 * \rho_{qct}^{2.307}$
	$\rho_{qct} \geq 0.818$ g_{k2HPO4}/cm^3	$^{a}E_{cort} = 32790 * \rho_{qct}^{2.307}$
4	$\rho_{qct} < 0.453$ g_{k2HPO4}/cm^3	$^{c}E_{trab} = 38780 * \rho_{qct}^{1.88}$
	$\rho_{qct} \geq 0.453$ g_{k2HPO4}/cm^3	$^{b}E_{cort} = 10200 * \rho_{ash}^{2.01}$
5	$\rho_{qct} < 0.818$ g_{k2HPO4}/cm^3	$^{c}E_{trab} = 38780 * \rho_{qct}^{1.88}$
	$\rho_{qct} \geq 0.818$ g_{k2HPO4}/cm^3	$E_{cort} = 20\,000\ MPa$
6	$\rho_{qct} < 0.818$ g_{k2HPO4}/cm^3	$^{c}E_{trab} = 38780 * \rho_{qct}^{1.88}$
	$\rho_{qct} \geq 0.818$ g_{k2HPO4}/cm^3	$^{c}E_{cort} = 38780 * \rho_{qct}^{1.88}$
7	$\rho_{app} < 1.0$ g/cm^3	$^{d}E_{trab} = 8920 * \rho_{app}^{1.83}$
	$\rho_{app} \geq 1.0$ g/cm^3	$^{b}E_{cort} = 10200 * \rho_{ash}^{2.01}$
8	$\rho_{app} < 1.8$ g/cm^3	$^{d}E_{trab} = 8920 * \rho_{app}^{1.83}$
	$\rho_{app} \geq 1.8$ g/cm^3	$E_{cort} = 20\,000\ MPa$
9	$\rho_{app} < 1.8$ g/cm^3	$^{d}E_{trab} = 8920 * \rho_{app}^{1.83}$
	$\rho_{app} \geq 1.8$ g/cm^3	$^{d}E_{cort} = 8920 * \rho_{app}^{1.83}$
10	$\rho_{app} < 1.0$ g/cm^3	$^{e}E_{trab} = 15000 * \left(\frac{\rho_{app}}{1.8}\right)^2$
	$\rho_{app} \geq 1.0$ g/cm^3	$^{b}E_{cort} = 10200 * \rho_{ash}^{2.01}$
11	$\rho_{app} < 1.8$ g/cm^3	$^{e}E_{trab} = 15000 * \left(\frac{\rho_{app}}{1.8}\right)^2$
	$\rho_{app} \geq 1.8$ g/cm^3	$E_{cort} = 20\,000\ MPa$
12	$\rho_{app} < 1.8$ g/cm^3	$^{e}E_{trab} = 15000 * \left(\frac{\rho_{app}}{1.8}\right)^2$
	$\rho_{app} \geq 1.8$ g/cm^3	$^{e}E_{cort} = 15000 * \left(\frac{\rho_{app}}{1.8}\right)^2$
13	$\rho_{app} < 1.0$ g/cm^3	$^{f}E_{trab} = 60 + 900 * \rho_{app}^{2}$
	$\rho_{app} \geq 1.0$ g/cm^3	$^{b}E_{cort} = 10200 * \rho_{ash}^{2.01}$
14	$\rho_{app} < 1.8$ g/cm^3	$^{f}E_{trab} = 60 + 900 * \rho_{app}^{2}$
	$\rho_{app} \geq 1.8$ g/cm^3	$E_{cort} = 20\,000\ MPa$
15	$\rho_{app} < 1.54$ g/cm^3	$^{f}E_{trab} = 60 + 900 * \rho_{app}^{2}$
	$\rho_{app} \geq 1.54$ g/cm^3	$^{g}E_{cort} = 90 * \rho_{app}^{7.4}$

Density-modulus relationships are from: [a,c]Knowles et al. (2019); [b]Keller et. al (1994) [d]Morgan et al. (2003); [e]Büchler et al., (2002); [f]Schaffler and Burr (1988); [g]Rice et al. (1988)

equal and opposite) and furthermore the sum of predicted forces occurring at the articular surface was compared to the experimental load. The difference between these was plotted as percentage error for each of the fifteen density-modulus relationship by specimen. The percentage errors in reaction force were also plotted against mean mapped modulus for the different trabecular and cortical mapping density-modulus relationships.

The QCT-FEM nodal displacements were compared to the full-field experimental DVC displacement results as the gold standard, using linear regression. The QCT-FEM nodes were region averaged within a sub-volume cubic size of 1 mm dependent on the location of the DVC nodal locations before comparing to DVC displacements to account for the increased number of FEM nodes to DVC grid points (Jackman et al., 2015). The regions where the displacements were compared were cropped to include only the volume of the scapula included in DVC assessment. The DVC-driven nodes at the BCs were removed from the displacement comparisons, as previously described (Jackman et al., 2015). Outliers were removed using the 5x the cooks distance method previously described (Costa et al., 2017). Linear regression was used to compare the region averaged QCT-FEM nodal displacement results to the full-field DVC displacement results in the x (UX), y (UY), and z (UZ), directions.

6.3 RESULTS

Nearly identical linear regression results between displacements predicted by QCT-FEMs mapped with elemental or nodal material mapping strategies and experimental DVC measurements (Table 6.2). The lowest slope was in the y-direction (0.86), which also had the lowest r-squared values (0.82). Root mean square error (RMSE) and max error were 0.018 mm and 0.039 mm for all Cartesian directions, respectively.

The target experimental load magnitude for each specimen was 500 N. The actual measured load magnitudes after relaxation, but prior to scanning for each specimen were 496 N, 449 N, 491 N, 491 N, 487 N, and 480 N, for specimens 1 to 6, respectively. The computational reaction forces showed large variation across all specimens and density-modulus relationships when an elemental material mapping strategy was used (Figure 6.4A). The percentage error in computational reaction forces ranged from 37% to 719% in specimen 1, -27% to 439% in specimen 2, 7% to 550% in specimen 3, -46% to 274% in

Table 6.2: Linear regression results of QCT-FEM and DVC experimental nodal displacement fields

Displacement Direction	Material Mapping Strategy	Slope	Intercept	r^2	RMSE (mm)	Max Error (mm)
UX	Elemental	0.94 – 1.06	-0.020 – 0.002	0.97 – 1.00	0.003 – 0.013	0.010 – 0.038
	Nodal	0.94 – 1.06	-0.020 – 0.002	0.97 – 1.00	0.003 – 0.013	0.010 – 0.039
UY	Elemental	0.86 – 1.05	-0.011 – 0.009	0.82 – 1.00	0.003 – 0.010	0.008 – 0.038
	Nodal	0.86 – 1.04	-0.012 – 0.010	0.82 – 1.00	0.003 – 0.010	0.007 – 0.036
UZ	Elemental	1.00 – 1.06	-0.005 – 0.010	0.94 – 1.00	0.003 – 0.018	0.009 – 0.037
	Nodal	1.00 – 1.06	-0.005 – 0.010	0.94 – 1.00	0.002 – 0.018	0.008 – 0.037

Values are range of six specimens and fifteen density-modulus relationship combinations

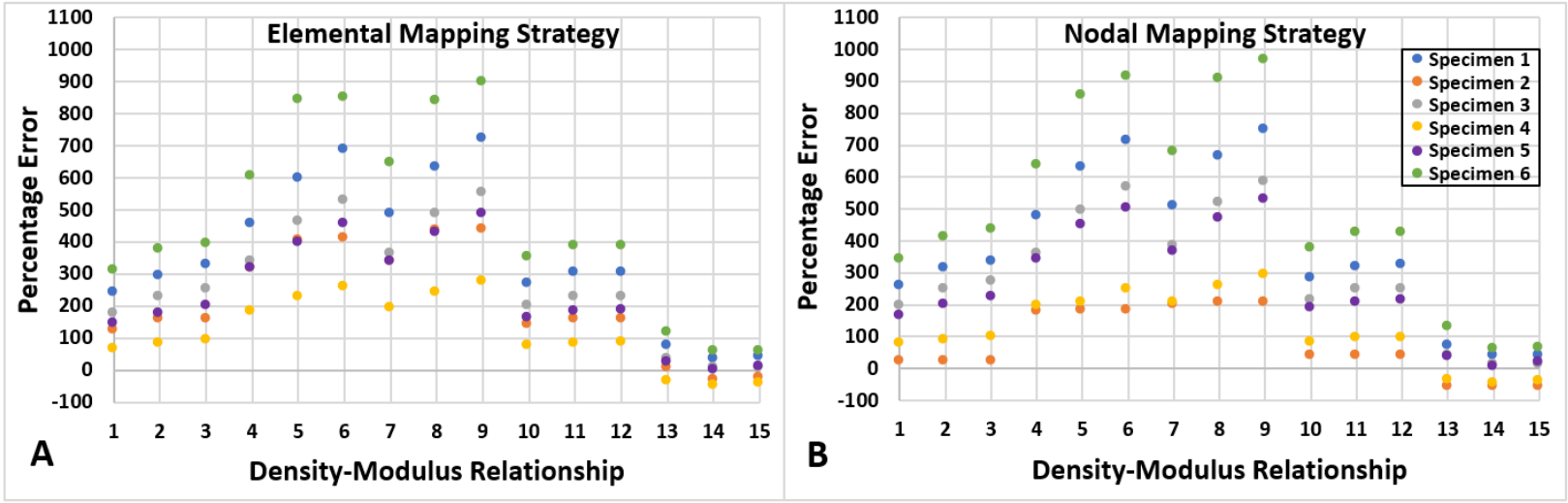

Figure 6.4: Percentage error plots between experimentally loaded scapular specimens and QCT-FEMs

QCT-FEMs were generated with fifteen different density-modulus relationships and elemental **(A)** or nodal **(B)** material mapping strategies (Table 6.1).

specimen 4, -3% to 486% in specimen 5, 57% to 899% in specimen 6. For this material mapping strategy, specimens 1, 3, 5, 6 had the lowest percentage errors, of 37%, 7%, -3%, and 57% respectively, when relationship 14 was used in the QCT-FEMs. Specimens 2 and 4 had a slightly lower percentage errors of 3% and 38% respectively, when using relationship 13.

Similarly, when using a nodal material mapping strategy (Figure 6.4B), there were large variations among specimens when mapped using different material mapping strategies. With this material mapping strategy, the percentage errors in computational reaction forces ranged from 40% to 749% in specimen 1, -59% to 210% in specimen 2, 12% to 587% in specimen 3, -44% to 292% in specimen 4, -4% to 531% in specimen 5, 59% to 965% in specimen 6. For this material mapping strategy, specimens 1, 3, 5, and 6 had the lowest percentage errors of 40%, 12%, 4%, and 59% respectively, when relationship 14 was used in the QCT-FEMs. Specimen 4 had a slightly lower percentage error of 36% using relationship 13 and specimen 2 had the lowest percentage error of 58% when relationships 1, 2, or 3 were used.

Comparing percentage errors in reaction force for each relationship and mean mapped modulus, the relationships that used a trabecular to cortical transition of apparent density of 1 g/cm^3 (QCT equivalent density of 0.453 g_{K2HPO4}/cm^3) and associated trabecular and cortical material mapping showed overall lower mapped modulus than the remaining relationships (Figure 6.5). The percentage errors using these density-modulus relationships were also lowest, with relationship 13 being best for both elemental and nodal material mapping. With a nodal material mapping strategy, comparable errors were observed with relationships 1 and 10. Relationships 4 and 7 had the highest mean mapped modulus and the highest percentage errors. When a trabecular to cortical transition at an apparent density 1.8 g/cm^3 (QCT equivalent density of 0.818 g_{K2HPO4}/cm^3) and a uniform cortical modulus of 20,000 MPa was used, the mapped modulus increased for all relationships except relationship 14 (the Schaffler and Burr trabecular relationship). Similarly, this trabecular relationship has the lowest percentage errors and similar results were observed with lower percentage errors with relationships 2 and 11 (equivalent trabecular mapping to relationships 1 and 10) for nodal material mapping. Nearly identical results were observed when trabecular derived relationships were applied across the entire density range

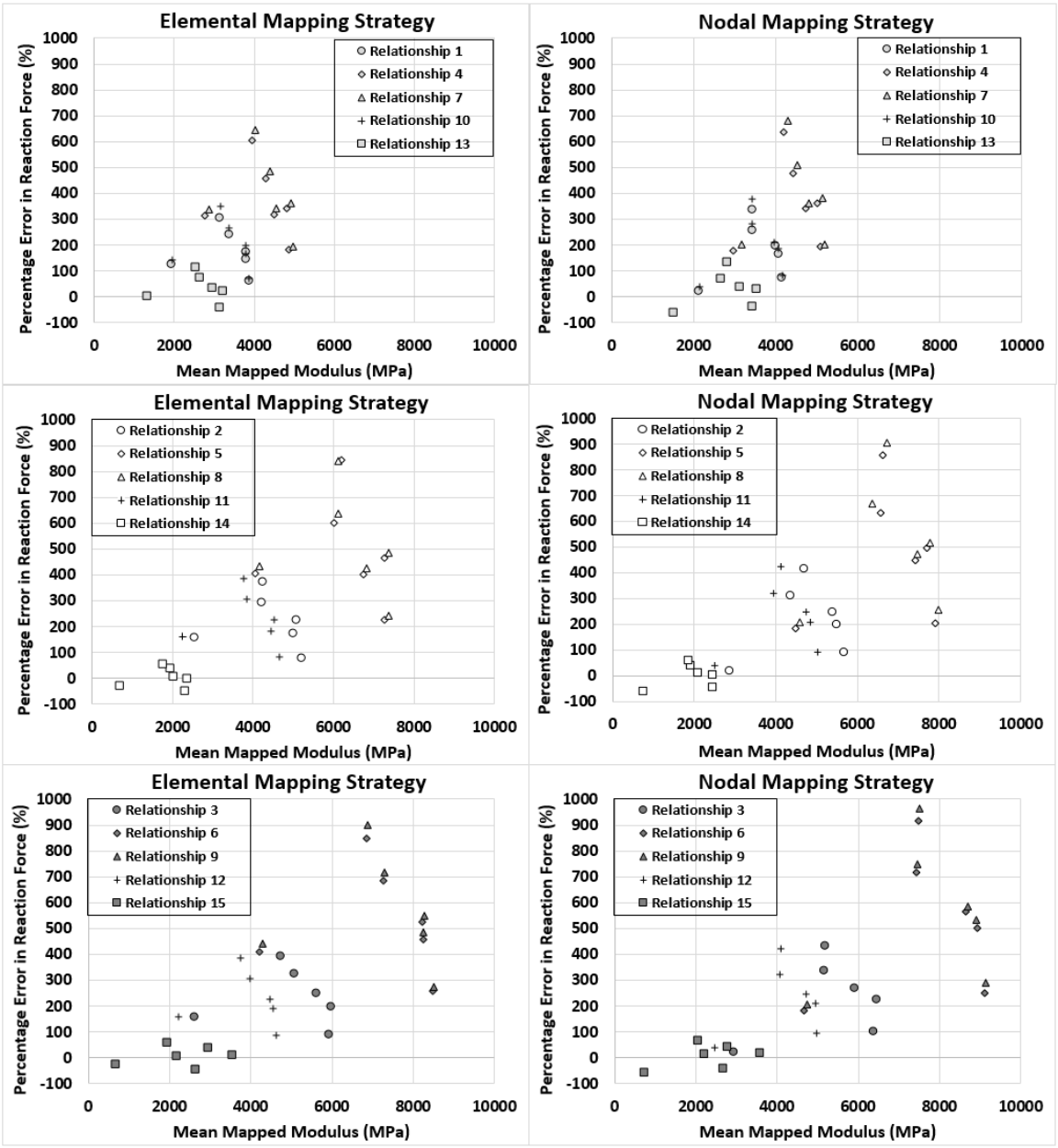

Figure 6.5: Percentage error plots between experimentally loaded scapular specimens and QCT-FEMs

QCT-FEMs were generated with fifteen different density-modulus relationships and elemental **(A)** or nodal **(B)** material mapping strategies (Table 6.1). Relationships 1, 4, 7, 10, 14 use a transition between trabecular and cortical material mapping at 0.453 g_{K2HPO4}/cm^3, relationships 2, 5, 8, 11, 14 at 0.818 g_{K2HPO4}/cm^3 or relationship 15 at 0.697 g_{K2HPO4}/cm^3.

(relationships 3, 6, 9, 12) for both elemental and nodal material mapping. These relationships mapped the highest mean modulus and had the highest percentage errors in reaction forces.

6.4 DISCUSSION:

This study compared density-modulus relationships and material mapping strategies used in QCT-derived finite element modeling (FEM) using DVC-driven boundary conditions. Using DVC-driven boundary conditions allowed the QCT-FEMs to accurately replicate the experimental measured loads based on density-modulus relationship and material mapping strategy. There were large variations among the compared density-modulus relationships, with percentage errors in FEM reaction loads of up to 965%. Computational QCT-FEMs with the best material mapping were able to replicate the experimental loads to within 3% with elemental material mapping and within 4% with nodal material mapping. There were only modest variations among specimens when either elemental or nodal material mapping strategies were used, indicating that either material mapping strategy can accurately replicate experimental loading of the scapula, provided an accurate density-modulus relationship is chosen.

This is important, because nodal material mapping can be easily implemented in custom-code used to generate QCT-FEMs and can easily be modified to account for partial volume effects (PVEs), as was done in the present study. Although with current FE-solvers these properties are generally assigned using field variables, nodal material mapping also allows for the mapping of heterogeneous distributions of materials in meshless models. At the micro-level, these models require significantly less computational resources and therefore allow for comparisons of very high-resolution models and/or non-linear models. This may be relevant at the continuum-level by allowing for larger model comparisons, especially those requiring larger computational resources such as those with contact or non-linear fracture and failure.

The trabecular relationships 3, 6, 9, and 12, were developed using trabecular bone specimens, with the density range extrapolated to include cortical density mapping. As such, these relationships significantly overestimate the upper range modulus mapping and resulted in the highest percentage errors in reaction force (Figure 6.5). Accounting for a

transition of trabecular to cortical bone at an apparent density of 1 g/cm^3 (relationships 1, 4, 7, 10, and 13) showed decreases in percentage errors for both elemental and nodal material mapping strategies. The relationships that used a mean cortical apparent density of 1.8 g/cm^3 (relationships 2, 5, 8, 11, and 14) and a uniform modulus of 20,000 MPa for elements above this value, showed similar results to the trabecular density-modulus mapping relationships, except for relationship 14 which has the lowest percentage errors for most specimens depending on material mapping strategy. These results may suggest that trabecular density-modulus relationships accurately map the mechanical properties of the trabecular bone within the trabecular density range, but there needs to be more accurate cortical density-modulus relationships developed to accurately replicate the mechanical response of the cortical bone. Further investigation into these piecewise relationships are needed.

Generalized trabecular density-modulus relationships from pooled anatomic locations have been reported (Morgan et al., 2003), and although not recommended, these relationships are often used in order to replicate material mapping in alternate anatomic locations because samples from multiple sites span a larger density range. This ignores the contribution of local trabecular morphology and its influence on trabecular modulus. In the present study, the trabecular density-modulus relationships used in 7, 8, 9, were developed from pooled anatomic sites and these relationships showed the greatest percentage errors in reaction forces for both elemental and nodal material mapping strategies. This may suggest that the local contribution of trabecular bone cannot be ignored in development of density-modulus relationships and that a generalized relationship for all anatomic sites is not possible. These relationships also mapped the highest modulus to the QCT-FEMs, providing QCT-FEMs that were much stiffer than the experimentally loaded specimens.

The trabecular relationships 1 to 6 were glenoid-specific (Knowles et al., 2019a). Interestingly, these relationships did not show the best agreement in replicating the experimental forces in these specimens. Although these relationships were developed using glenoid trabecular bone as an input, a relatively large tissue modulus was assumed in the models used to derive the density-modulus relationships (~10 GPa for relationships 1, 2, 3 and 20 GPa for relationships 4, 5 and 6). This fact may partially account for the overestimation in QCT-FEM loads when mapped with these relationships. Relationships

13, 14, 15 showed the lowest percentage errors in reaction force. The trabecular mapping used in these relationships provides the lowest modulus mapping of the trabecular bone, indicating that at the whole-bone level, the true modulus is likely on the lower range of reported values. Although this trabecular relationship provided the closest reaction forces to experimental results, it overestimated the forces in specimens 1 and 6 and underestimated forces in specimens 2 and 4 when using both an elemental and nodal mapping strategy. This indicates that the specimen-specific density distributions (Figure 6.1) may play an important role in the accuracy associated with material mapping.

Specimen 2 had the lowest mean density, standard deviation and the lowest amount of bone in the cortical density ranges (0.453 g_{K2HPO4}/cm^3 or 0.818 g_{K2HPO4}/cm^3 depending on trabecular/cortical transition). This specimen had the lowest percentage errors with a nodal material mapping strategy and the glenoid-specific trabecular density-modulus relationships (1, 2 ,3). This suggests that within smaller density ranges, this trabecular density-modulus relationship may accurately map the modulus. With relationships 13, 14, 15, this specimen's whole bone modulus is underestimated, which may contribute to the larger errors. Specimens 2 and 6 have similar distributions, but different results in reaction force percentage errors. Specimen 6 has the largest range of densities and had the worst percentage errors for all relationships, while specimen 2 had the lowest percentage errors of all specimens for both mapping strategies. Specimens 1, 3, and 4 had varying results depending on the density-modulus relationship used. As mentioned, not only the density-modulus relationship, but also the individual distribution of densities within a specimen may contribute to the large variability seen across specimens. This has been observed in whole bones of the radius (Austman et al., 2009, 2008) and femur (Eberle et al., 2013a, 2013b) and indicates that density-modulus relationships may require alternative methods in development at the whole bone level. Not captured in the density histograms are the local distributions of densities and geometrical factors of the bone, both of which may significantly contribute to the accuracy of the QCT-FEMs to replicate experimental loading.

As assumed, applying varying constitutive relationships to map the mechanical properties of bone did not have a large effect on local displacement predictions generated by scapula QCT-FEMs. Regardless of the relationship selected, excellent agreement

between the local experimental displacement measurements and QCT-FEM predictions were obtained, with both material mapping strategies. However, within the same models, large variations in reaction forces were observed. It has recently been suggested that local variations may be attributed to differences in bone micro-architecture (Hussein et al., 2018); however, the good agreement achieved with full-field displacements in the present study suggest that in QCT-FEMs this may not be true. Considering all density-modulus relationships had nearly identical full-field displacement linear regression results, further studies should be performed to elucidate the contributive variation in local mechanical properties of QCT-FEMs.

A strength of this study is that experimental boundary conditions were replicated in QCT-FEMs using DVC-driven boundary conditions. Replicating experimental boundary conditions has shown significant improvements in improving the accuracy of whole-bone QCT-FEMs (Hussein et al., 2018; Jackman et al., 2015), and have recently been reported as a main limitation in even the most robust studies that compare material mapping strategies and density-modulus relationship comparisons (Helgason et al., 2016). The main limitation of this study is the small sample size. Due to the complexity associated with the experimental protocol required to generate DVC-derived BCs, the current study was limited in sample size to six specimens. However, the use of DVC-derived BCs along with local DVC measurements provided a highly-controlled experimental measure that allowed for the evaluation of multiple density-modulus relationships and material mapping strategies with high confidence that otherwise would not be possible.

6.5 CONCLUSION:

This study compared density-modulus relationships and material mapping strategies of scapular QCT-FEMs with DVC-driven boundary conditions to experimentally loaded scapular models. It was found that elemental and nodal material mapping strategies are both able to accurately replicate experimental full-field displacements and reactions forces. Further investigation is required to determine the specimen-specificity of density-modulus mapping in scapular QCT-FEMs, the transition zone between trabecular and cortical material mapping and associated piecewise relationships, and whether improved cortical density-modulus relationship development improves linear-isotropic QCT-FEM accuracy.

6.6 REFERENCES:

Austman, R.L., Milner, J.S., Holdsworth, D.W., Dunning, C.E., 2009. Development of a customized density–modulus relationship for use in subject-specific finite element models of the ulna. Proc. Inst. Mech. Eng. Part H J. Eng. Med. 223, 787–794. Doi:10.1243/09544119JEIM553

Austman, R.L., Milner, J.S., Holdsworth, D.W., Dunning, C.E., 2008. The effect of the density-modulus relationship selected to apply material properties in a finite element model of long bone. J. Biomech. 41, 3171–6. Doi:10.1016/j.jbiomech.2008.08.017

Burkhart, T.A., Andrews, D.M., Dunning, C.E., 2013. Finite element modeling mesh quality, energy balance and validation methods: A review with recommendations associated with the modeling of bone tissue. J. Biomech. 46, 1477–1488. Doi:10.1016/j.jbiomech.2013.03.022

Carter, D., Hayes, W., 1977. The compressive behavior of bone as a two-phase porous structure. J. Bone Jt. Surg. 59(7), 954-962

Chen, Y., Dall′Ara, E., Sales, E., Manda, K., Wallace, R., Pankaj, P., Viceconti, M., 2017. Micro-CT based finite element models of cancellous bone predict accurately displacement once the boundary condition is well replicated: A validation study. J. Mech. Behav. Biomed. Mater. 65, 644–651. Doi:10.1016/j.jmbbm.2016.09.014

Comini, F., Palanca, M., Cristofolini, L., Ara, E.D., 2019. Uncertainties of synchrotron microCT-based digital volume correlation bone strain measurements under simulated deformation. J. Biomech. C, 1–6. Doi:10.1016/j.jbiomech.2019.01.041

Costa, M.C., Tozzi, G., Cristofolini, L., Danesi, V., Viceconti, M., Dall'Ara, E., 2017. Micro finite element models of the vertebral body: Validation of local displacement predictions. PloS One 12, 1–18. Doi:10.1371/journal.pone.0180151

Dall'Ara, E., Barber, D., Viceconti, M., 2014. About the inevitable compromise between spatial resolution and accuracy of strain measurement for bone tissue : A 3D zero-strain study. J. Biomech. 47, 2956–2963. Doi:10.1016/j.jbiomech.2014.07.019

Dall'Ara, E., Peña-Fernández, M., Palanca, M., Giorgi, M., Cristofolini, L., Tozzi, G., 2017. Precision of Digital Volume Correlation Approaches for Strain Analysis in Bone Imaged with Micro-Computed Tomography at Different Dimensional Levels.

Front. Mater. 4. Doi:10.3389/fmats.2017.00031

Eberle, S., Göttlinger, M., Augat, P., 2013a. An investigation to determine if a single validated density – elasticity relationship can be used for subject specific finite element analyses of human long bones. Med. Eng. Phys. 35, 875–883. Doi:10.1016/j.medengphy.2012.08.022

Eberle, S., Göttlinger, M., Augat, P., 2013b. Individual density-elasticity relationships improve accuracy of subject-specific finite element models of human femurs. J. Biomech. 46, 2152–2157. Doi:10.1016/j.jbiomech.2013.06.035

Enns-Bray, W.S., Bahaloo, H., Fleps, I., Ariza, O., Gilchrist, S., Widmer, R., Guy, P., Pálsson, H., Ferguson, S.J., Cripton, P.A., Helgason, B., 2018. Material mapping strategy to improve the predicted response of the proximal femur to a sideways fall iMPact. J. Mech. Behav. Biomed. Mater. 78, 196–205. Doi:10.1016/j.jmbbm.2017.10.033

Gray, H.A., Taddei, F., Zavatsky, A.B., Cristofolini, L., Gill, H.S., 2008. Experimental Validation of a Finite Element Model of a Human Cadaveric Tibia, J. Biomech. Eng. 130, 1–9. Doi:10.1115/1.2913335

Helgason, B., Gilchrist, S., Ariza, O., Vogt, P., Enns-Bray, W., Widmer, R.P., Fitze, T., Pálsson, H., Pauchard, Y., Guy, P., Ferguson, S.J., Cripton, P.A., 2016. The influence of the modulus-density relationship and the material mapping method on the simulated mechanical response of the proximal femur in side-ways fall loading configuration. Med. Eng. Phys. 38, 679–689. Doi:10.1016/j.medengphy.2016.03.006

Helgason, B., Perilli, E., Schileo, E., Taddei, F., 2008a. Mathematical relationships between bone density and mechanical properties: a literature review. Clin. Biomech. 23, 135–146. Doi:10.1016/j.clinbiomech.2007.08.024

Helgason, B., Taddei, F., Pálsson, H., Schileo, E., Cristofolini, L., Viceconti, M., Brynjólfsson, S., 2008b. A modified method for assigning material properties to FE models of bones. Med. Eng. Phys. 30, 444–453. Doi:10.1016/j.medengphy.2007.05.006

Hussein, A.I., Louzeiro, D.T., Morgan, E.F., 2018. Differences in Trabecular Microarchitecture and Simplified Boundary Conditions Limit the Accuracy of

Quantitative Computed Tomography-Based Finite Element Models of Vertebral Failure 140, 1–11. Doi:10.1115/1.4038609

Jackman, T.M., DelMonaco, A.M., Morgan, E.F., 2015. Accuracy of finite element analyses of CT scans in predictions of vertebral failure patterns under axial compression and anterior flexion. J. Biomech. 1–9. Doi:10.1016/j.jbiomech.2015.12.004

Keaveny, T.M., Wachtel, E.F., Ford, C.M., Hayes, W.C., 1994. Differences between the tensile and compressive strength of trabecular bone depend on modulus. J. Biomech. 27, 1137–1146.

Knowles, N., Langohr, G.D.G., Faieghi, M., Nelson, A., 2018. Development of a validated glenoid trabecular density-modulus relationship. J. Mech. Beh. . Biomed. Mat. 90, 140-145

Knowles, N.K., Langohr, G.D.G., Athwal, G.S., Ferreira, L.M., 2018. Polyethylene glenoid component fixation geometry influences stability in total shoulder arthroplasty. Comput. Methods Biomech. Biomed. Engin. 0, 1–9. Doi:10.1080/10255842.2018.1551526

Knowles, N.K., Langohr, G.D.G., Faieghi, M., Nelson, A., Ferreira, L.M., 2019. A CoMParison of Density-Modulus Relationships Used in Finite Element Modeling of the Shoulder. Med. Eng. Phys. In-Press.

Knowles, N.K., Reeves, J.M., Ferreira, L.M., 2016. Quantitative Computed Tomography (QCT) derived Bone Mineral Density (BMD) in finite element studies: a review of the literature. J. Exp. Orthop. 3, 36. Doi:10.1186/s40634-016-0072-2

Morgan, E., Bayraktar, H., Keaveny, T., 2003. Trabecular bone modulus–density relationships depend on anatomic site. J. Biomech. 36(7), 897-904

Morgan, E.F., Keaveny, T.M., 2001. Dependence of yield strain of human trabecular bone on anatomic site. J. Biomech. 34, 569–577.

Oliviero, S., Giorgi, M., Ara, E.D., 2018. Journal of the Mechanical Behavior of Biomedical Materials Validation of fi nite element models of the mouse tibia using digital volume correlation. J. Mech. Behav. Biomed. Mater. 86, 172–184. Doi:10.1016/j.jmbbm.2018.06.022

Schneider, C.A., Rasband, W.S., Eliceiri, K.W., 2012. NIH Image to ImageJ: 25 years of

image analysis. Nat. Methods 9, 671–675. Doi:10.1038/nmeth.2089

Taddei, F., Schileo, E., Helgason, B., Cristofolini, L., Viceconti, M., 2007. The material mapping strategy influences the accuracy of CT-based finite element models of bones: an evaluation against experimental measurements. Med. Eng. Phys. 29, 973–9. Doi:10.1016/j.medengphy.2006.10.014

CHAPTER 7 – MORPHOLOGICAL AND APPARENT-LEVEL STIFFNESS VARIATIONS BETWEEN NORMAL AND OSTEOARTHRITIC BONE

OVERVIEW: *This chapter compares the morphometric and apparent modulus of non-pathologic normal bone and end-stage osteoarthritic trabecular bone from the humeral head. Excised humeral heads were collected for patients undergoing total shoulder arthroplasty and humeral heads were excised from cadaveric specimens to match these osteotomies. Apparent modulus between groups was compared using micro finite element models.*[7]

[7] A version of this work has been submitted for publication**:** Knowles NK**,** Kusins J, Columbus MP, Athwal GS, Ferreira LM. Morphological and Apparent-Level Stiffness Variations Between Normal and Osteoarthritic Bone. Bone. BONE-D-19-00349

7.1 INTRODUCTION:

Osteoarthritis (OA) is characterized by joint morphological changes during pathological progression and biomechanical changes to the subchondral bone (Arden and Nevitt, 2006). These symptomatic biomechanical changes lead to joint stiffness and reduced range of motion, causing pain and functional loss. Morphological variations that occur within the joint include loss of articular cartilage, subchondral bone sclerosis, subchondral cyst formation, with abnormal bone turnover, leading to osteophyte formation and synovial inflammation (Brandt et al., 2008). Patients with progression to end-stage OA of the shoulder are often treated with joint replacements with a variety of humeral replacement options. Humeral head resurfacing replaces only the articular surface with a prosthetic component, while long- and short-stem designs, and more recently, stemless designs, require excision of the humeral head. These different designs all require some amount of pathologic bone to remain in order to support the fixation of the chosen prosthetic component.

Despite the appearance of increased bone density in OA bone observed using x-ray techniques, the sclerotic bone in OA joints is hypomineralized. The tissue density of subchondral cortical and trabecular bone is lower in OA subjects than normal controls (Burr and Gallant, 2012). The higher rate of bone remodeling that occurs as part of the pathologic process (Mansell et al., 1998) results in less mineralized bone and increased osteoid (Burr and Gallant, 2012). In OA subchondral cortical and trabecular bone, this altered bone remodeling process leads to increases in bone volume fraction. As such, although the tissue density of the mineralized tissue is less than non-pathologic bone, the increase in bone volume fraction increases the apparent density (Brown et al., 2002; Burr and Gallant, 2012; Li and Aspden, 1997). In computational modeling at clinical-level resolution, this apparent density (as related to bone volume fraction at the micro-level) is directly related to elastic modulus (and strength) by material mapping using density-modulus relationships. Although the morphometric variations in the end-stage OA humeral head have been reported (Pawson et al., 2015), variations in the mechanical properties that occur between non-pathologic age-matched ‘normal’ bone, and end-stage pathologic OA bone have not.

The density-modulus relationships used in the computational modeling of bones are most often derived using mechanical testing of normal cadaveric bone. This presents a possible source of error in patient-specific computational modeling due to the lack of OA bone mechanical properties characterization. The accuracy of these models, especially those used in the development of joint replacement components, could be improved by increasing our understanding of the differences in morphometric parameters and mechanical properties between the two groups. As such, this study quantified morphometric parameters and mechanical properties in end-stage OA patient humeral heads and age-matched non-pathologic 'normal' humeral heads.

7.2 METHODS:

7.2.1 Patient and Control Group Demographics and MicroCT Imaging

Humeral head osteotomies were collected from patients undergoing total shoulder arthroplasty (TSA) for end-stage osteoarthritis (OA) (n=24; mean age: 67 ± 10 years old; 15 males; 9 females) in accordance with institutional ethics (HSREB#: 113023). Age-matched non-pathologic cadavers (n=18; mean age: 66 ± 8 years old; 8 males; 10 females) were used as the control group, with humeral heads excised at the cartilage junction to replicate the OA group. Each humeral head was scanned with a cone-beam microCT scanner (Nikon XT H 225 ST, Nikon Metrology, NV) with an isotropic spatial resolution of 20 µm. All heads were scanned with consistent settings of 95 kV, 80 µA, 3141 projections, and 1000 ms exposure.

7.2.2 MicroCT Image Processing

MicroCT images were exported as 16-bit DICOMs and processed using medical imaging software (Mimics®, Materialise, V.20.0, Leuven, BE). A Gaussian blur filter was used to remove high frequency noise (σ = 0.75, support = 2). A specimen-specific gray-value threshold was used to best preserve trabecular bone architecture (Bouxsein et al., 2010). A 5 mm diameter, 10 mm long virtual core was extracted in the medial-lateral direction, adjacent to the subchondral bone. In patients with significant subchondral cyst formation, the cores were extracted directly below the cysts. This size was chosen to ensure consistency between models from the smallest to largest specimens. Connectivity was

ensured using embedded region growing with 6-connectivity. The spatial coordinates of each voxel were extracted for finite element model (FEM) generation, and 2D image stacks of the segmented region were extracted for morphometric calculations.

7.2.3 Morphometric Analysis

The 2D image stacks were processed in ImageJ (Schneider et al., 2012) to create binary images of each virtual core, which were processed with bone analysis software (SkyScan CTAn, Bruker micro-CT, Kontich, BE) for 3D morphometric analysis. The bone volume fraction (BV/TV), trabecular thickness (Tb.Th), trabecular separation (Tb.Sp), and trabecular number (Tb.N) were calculated for the complete cores, and also separately for four subdivided equal regions from proximal to distal (Figure 7.1 inset).

7.2.4 Micro Finite Element Model (FEM) Generation

Custom-code was used to generate micro-finite element models (μFEMs) (Faieghi et al., 2019) with isotropic 20 μm hexahedral elements for each voxel in the segmented virtual cores (van Rietbergen et al., 1995). An arbitrary modulus of 1 GPa was assigned to each element. Simulated unconstrained compression to 0.5% apparent strain was performed in the medial-lateral direction to determine the apparent modulus (E_{app}) of each μFEM (Knowles et al., 2019). The modulus of 1 GPa was scaled in the linear isotropic models to 20 GPa and apparent modulus-bone volume fraction relationships ($E_{app} = \alpha(BV/TV)^{\beta}$) were developed using the calculated E_{app} and the BV/TV of each μFEM. These were plotted and compared between OA and normal groups (Figure 7.1). The additional morphometric parameters (Tb.Th, Tb.Sp, and Tb.N) were also compared to apparent modulus using linear regression.

7.2.4 Statistical Analysis

Bone morphometric parameters were summarized as mean and standard deviation for the complete cores, and separately for the four proximal to distal regions for each of the two groups. Parameters in the complete core were compared using unpaired t-tests or Mann-Whitney Rank Sum tests for non-parametric data. The regional morphometric parameters

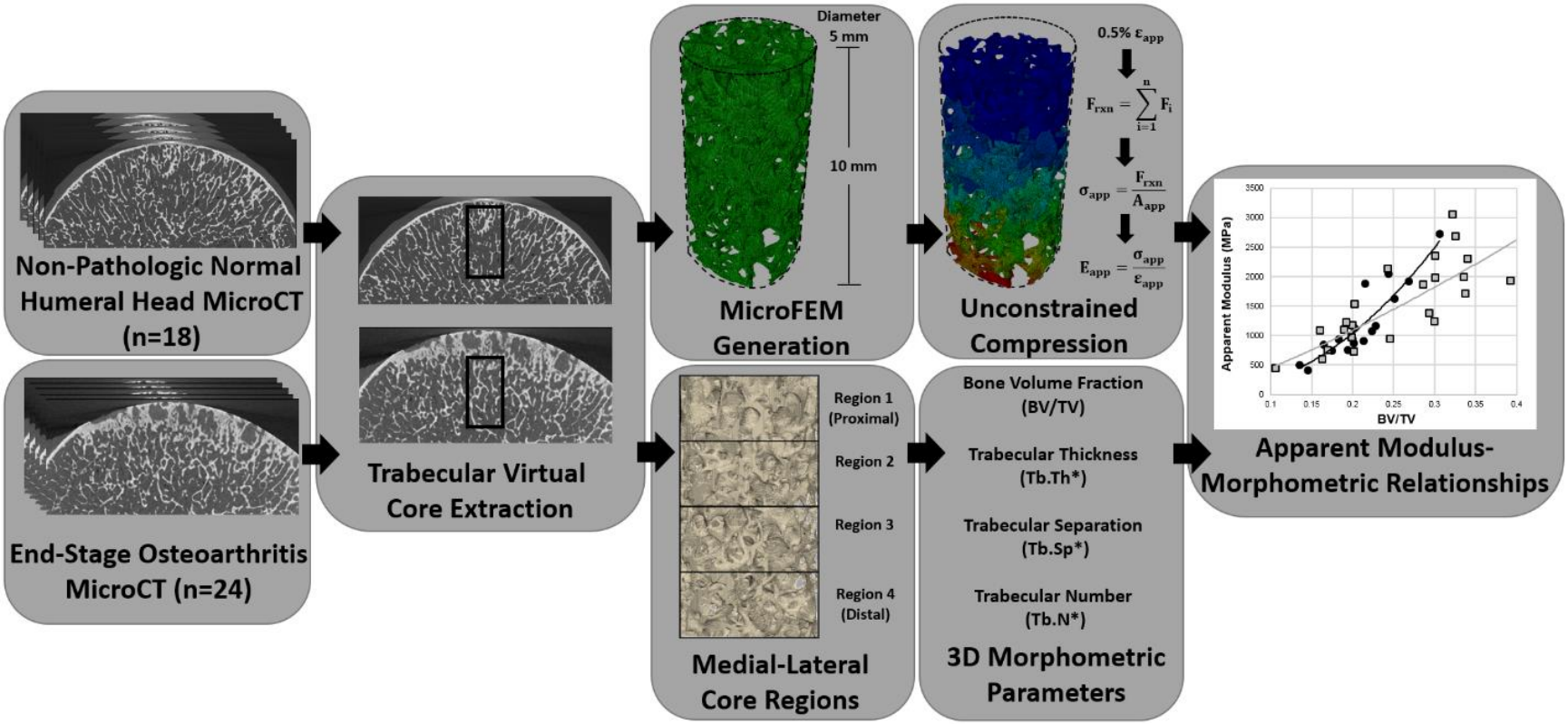

Figure 7.1: The workflow from microCT image collection (20 µm isotropic voxels), virtual core extraction, apparent modulus and morphometry analysis used to coMPare non-pathologic normal bone and end-stage OA bone

were compared using two-way ANOVAs with region and group as factors. Between-group comparisons were tabulated, and within-group comparisons are discussed. Linear regression was performed for morphometric parameters and apparent modulus versus age, and for apparent modulus versus morphometric parameters. Apparent modulus versus bone volume fraction were plotted and compared using power-fit regressions.

7.3 RESULTS

The morphometric analysis for the two groups and regions is provided in Table 7.1. For the complete cores, significant differences between groups were only present in mean trabecular thickness ($p = .034$). Comparing regional variations in bone morphometric parameters showed the greatest regional variations in the most proximal region (Region 1), with significant differences between groups in all morphometric parameters ($p \leq .018$). For region 2, only bone volume fraction was significantly different between groups ($p = .045$). Regions 3 and 4 showed no significant differences in any of the characterized morphometric parameters.

For pairwise comparisons, considering bone volume fraction, significant differences occurred in the normal group between regions 1 and 4 ($p = .003$), but no other regional variations occurred. In the OA group, regional significant differences in BV/TV occurred between regions 1 and 4 ($p < .001$), 1 and 3 ($p <.001$), 1 and 2 ($p <.001$), and 2 and 4 ($p <.001$). For mean trabecular thickness, there were no significant differences in regional variations within the normal group, but significant differences in the OA group occurred between regions 1 and 4 ($p < .001$), 1 and 3 ($p < .001$), 1 and 2 ($p = .002$). Significant differences occurred in trabecular separation between regions 1 and 4 ($p <.001$), 1 and 3 ($p = .007$), and 2 and 4 ($p =.009$) in the normal group, and regions 1 and 4 ($p =.009$), 1 and 3 ($p <.001$), 1 and 2 ($p <.001$), 2 and 4 ($p <.001$), and 2 and 3 ($p = .004$) in the OA group. Similarly, significant differences in trabecular number occurred between regions 1 and 4 ($p <.001$), 1 and 3 ($p =.010$), and 2 and 4 ($p = .001$) of the normal group, and all regions of the OA group ($p \leq .014$). Linear regression fits of morphometric parameters versus age are presented in figure 7.2, apparent modulus versus age in figure 7.3 and linear regression fits of E_{app} versus morphometric parameters in figure 7.4. The linear fit between trabecular thickness (Tb.Th) showed variations between the normal and OA groups in

Table 7.1: Three-dimensional morphometric parameters of trabecular cores from normal and OA groups

Region	Group	BV/TV	p-value	Tb.Th (mm)	p-value	Tb.Sp (mm)	p-value	Tb.N (1/mm)	p-value
Entire	Normal	0.21 ± 0.04	.055[b]	0.196 ± 0.017	**.034[b]**	0.756 ± 0.080	.292[b]	1.052 ± 0.167	.440[a]
Core	OA	0.26 ± 0.08		0.235 ± 0.062		0.733 ± 0.101		1.093 ± 0.116	
1	Normal	0.25 ± 0.06	**<.001[c]**	0.198 ± 0.022	**<.001[c]**	0.647 ± 0.104	**.003[c]**	1.249 ± 0.248	**.018[c]**
(Proximal)	OA	0.38 ± 0.16		0.264 ± 0.088		0.542 ± 0.121		1.394 ± 0.227	
2	Normal	0.22 ± 0.05	**.045[c]**	0.197 ± 0.021	.079[c]	0.693 ± 0.092	.166[c]	1.114 ± 0.210	.122[c]
	OA	0.27 ± 0.16		0.220 ± 0.059		0.650 ± 0.101		1.200 ± 0.187	
3	Normal	0.19 ± 0.05	.373[c]	0.192 ± 0.019	.456[c]	0.735 ± 0.086	.900[c]	0.999 ± 0.190	.352[c]
	OA	0.21 ± 0.07		0.201 ± 0.044		0.735 ± 0.109		1.053 ± 0.185	
4	Normal	0.17 ± 0.04	.888[c]	0.188 ± 0.023	.982[c]	0.789 ± 0.071	.798[c]	0.882 ± 0.144	.735[c]
(Distal)	OA	0.17 ± 0.06		0.188 ± 0.036		0.792 ± 0.126		0.914 ± 0.202	

Values are mean ± SD. BV/TV – Bone Volume/Total Volume; Tb.Th – Trabecular Thickness; Tb.Sp – Trabecular Separation; Tb.N – Trabecular Number. Significant values ($p < .05$) are bolded. [a]Unpaired t-test [b]Mann-Whitney Rank Sum Test [c]Two-way ANOVA with Holm-Sidak Pairwise Comparisons.

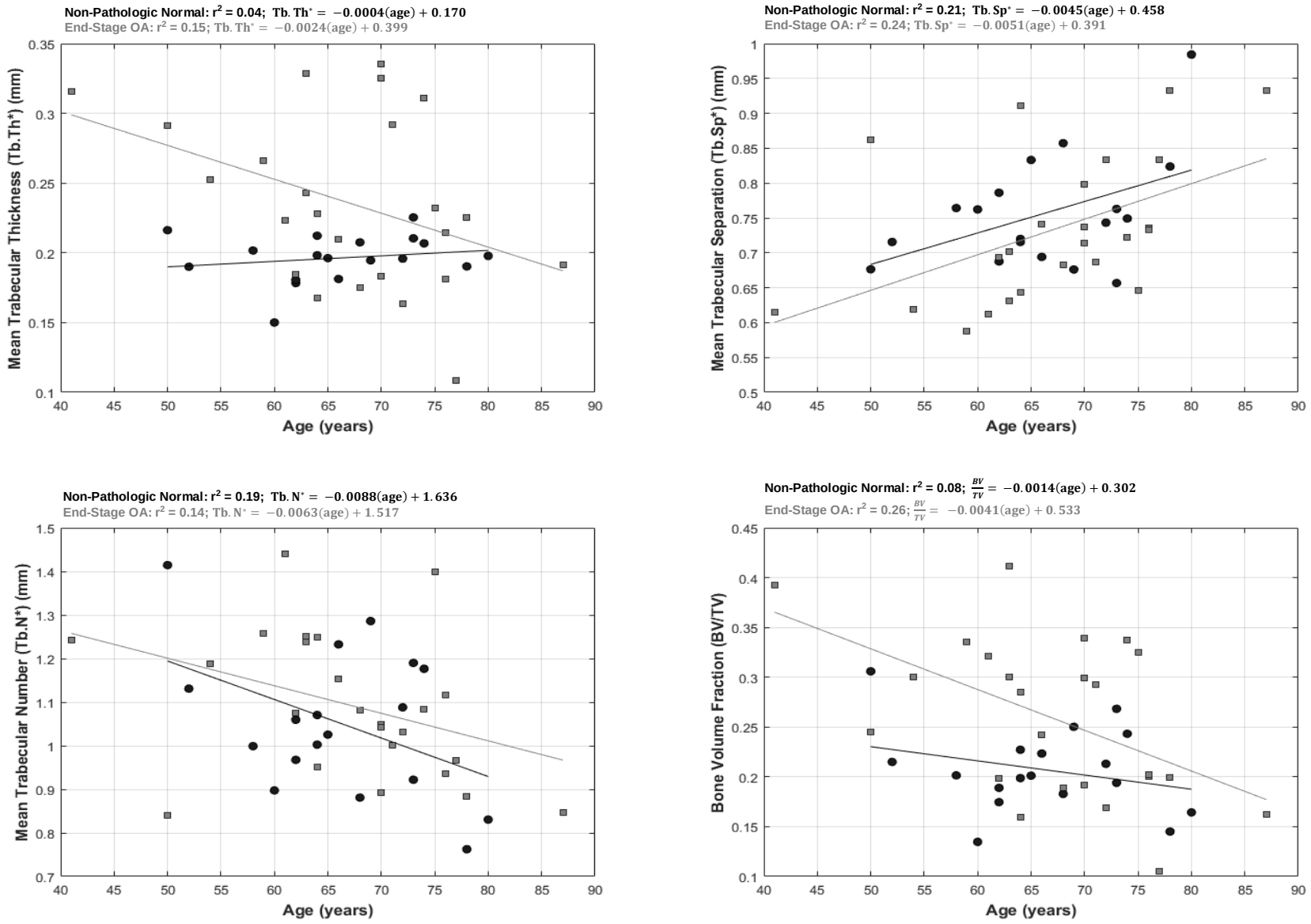

Figure 7.2: Morphometric parameters versus age for non-pathologic normal and end-stage OA groups

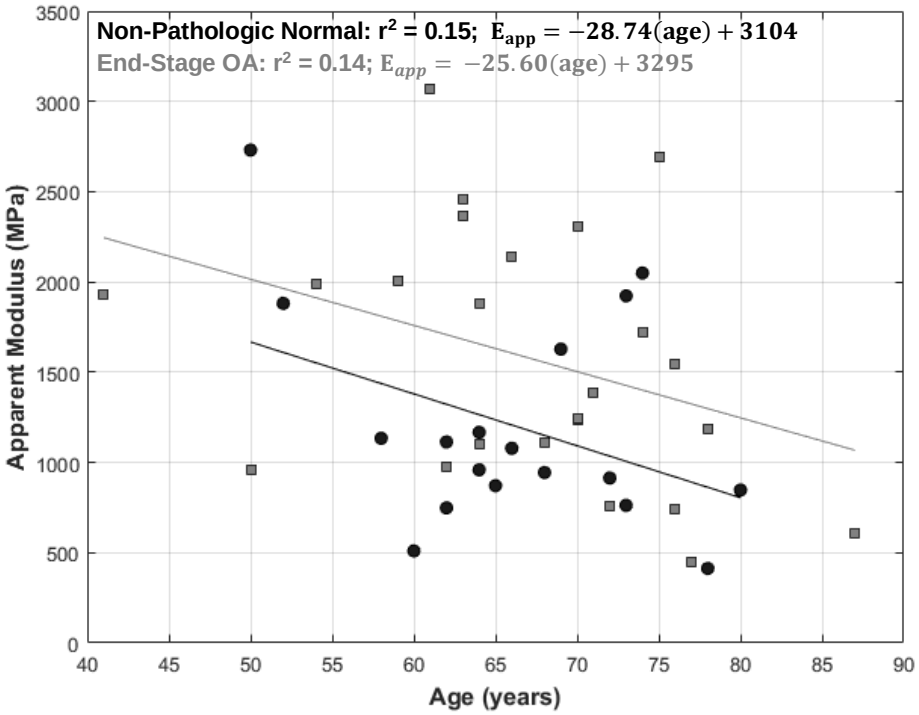

Figure 7.3: Apparent modulus versus age for non-pathologic normal and end-stage OA groups

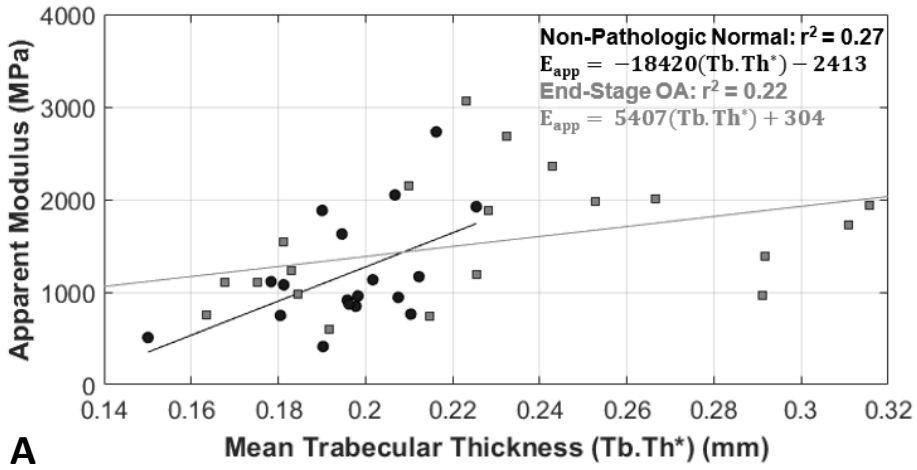

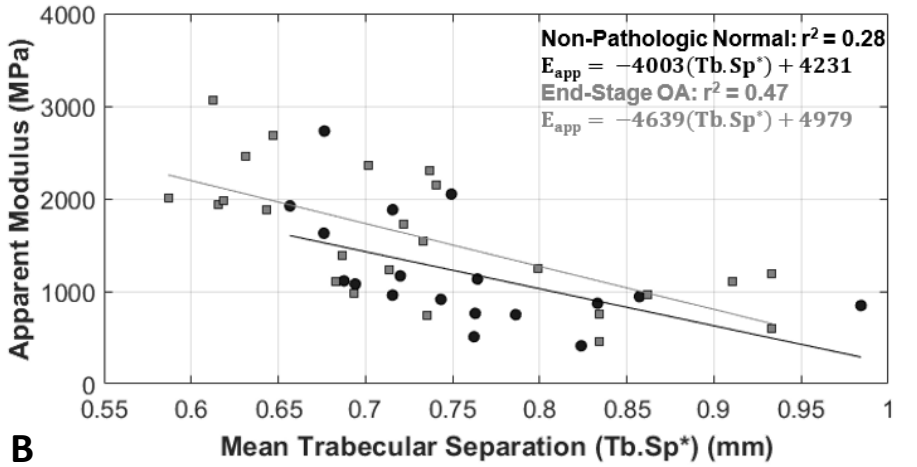

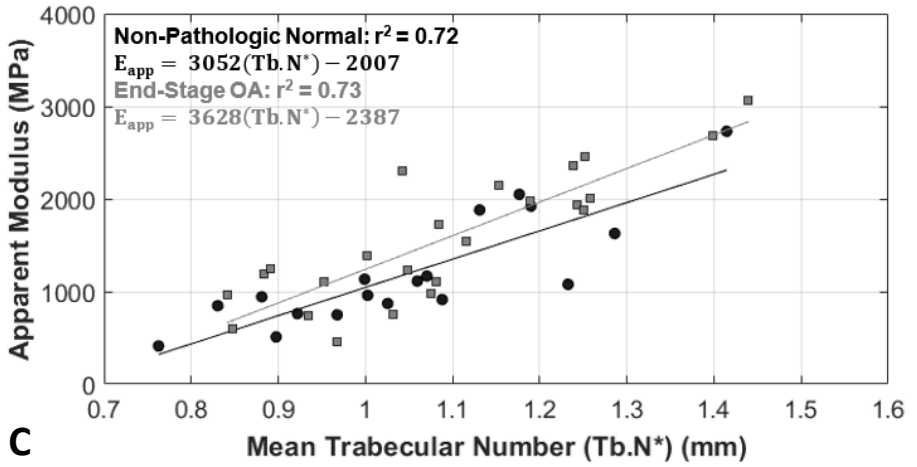

Figure 7.4: Linear regression plots of trabecular thickness (A), trabecular separation (B), and trabecular number (C) versus apparent modulus for non-pathologic normal and end-stage OA

Both slope and intercept, with the greatest deviations from the normal group occurring with mean Tb.Th values above 0.225 mm. The slope and intercept for both E_{app} versus trabecular separation (Tb.Sp) and trabecular number (Tb.N) differed between groups, but the general linear relationship remained consistent over the entire range of values. Power-law regression fits were used to determine the relationships between E_{app} and bone volume fraction (BV/TV) (Figure 7.5). The non-pathologic normal cadaveric group was best fit by a power-law relationship ($E_{app} = 37260(BV/TV)^{2.215}$), while OA bone exhibited a more linear relationship ($E_{app} = 7058(BV/TV)^{1.109}$). For BV/TV lower than 0.25, both groups had similar E_{app}, with deviations occurring in the higher BV/TV of the end-stage OA group.

7.4 DISCUSSION:

This study compared the microarchitectural and apparent modulus of non-pathologic normal bone and end-stage osteoarthritic (OA) bone. Regional variations in morphometric parameters were observed between groups in only the most proximal regions of the analyzed cores. Within-group variations were observed for all morphometric parameters in each the normal and OA groups. Correlating the apparent modulus to morphometric parameters (Figure 7.4) showed interesting similarities in the linear regression trends between both groups for mean trabecular separation and mean trabecular number. Power-law regression fits of apparent modulus and bone volume fraction for the non-pathologic normal group was consistent with the literature, which reports best fits with an exponent between 2 and 3 (Hodgskinson and Currey, 1993; Zysset et al., 1994). This trend did not persist in the end-stage OA group, which was best fit with a nearly linear exponent. Most of the variation between the two groups occurred at a bone volume fraction above 0.25.

The differences in fitting parameters is not only important to characterize the mechanical property variations between groups, it is essential for accurate material property assignment in patient-specific finite element models (FEMs). Due to the strong relationships between bone volume fraction (or apparent-density) and apparent modulus (Carter and Hayes, 1977), density-modulus relationships are used to map a continuum of element-wise materials to FEMs derived from clinical-resolution CT. These linear-isotropic models are important in characterizing a variety of biomechanical scenarios,

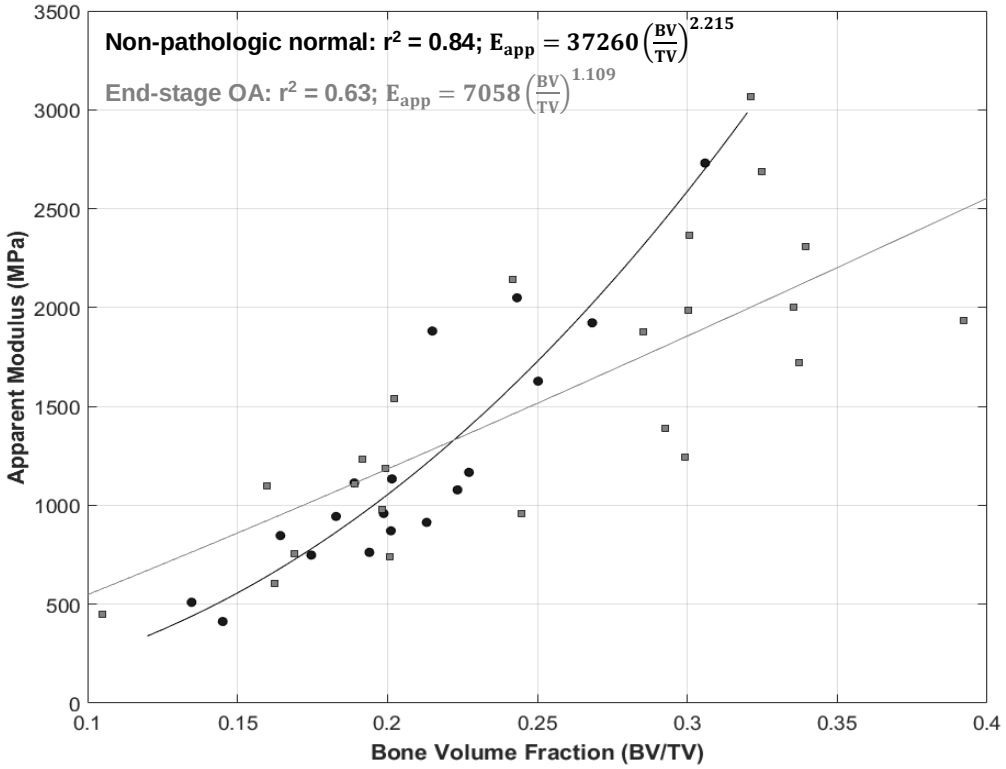

Figure 7.5: Power-law regression fits of apparent modulus and bone volume fraction (BV/TV) for non-pathologic normal and end-stage OA groups.

including joint replacement component design. Because up to 90% of the variation in mechanical properties of trabecular bone can be explained by bone volume fraction (Maquer et al., 2015), linear-isotropic continuum-level FEMs are essential in patient-specific design. With the expanding clinical availability of patient CT scans, the implementation of patient-specific modeling in the clinical workflow is an increasing reality. In the present study, it was found that variations in morphometric parameters between the two groups occurred only in the most proximal regions, and slightly deeper for bone-volume fraction, which indicates that in the lower bone-volume fraction regions of OA bone, the material mapping relationships derived using non-pathologic normal bone may be accurate. This is an important finding because the OA humeral heads used in this study represent end-stage OA patients undergoing joint replacement surgery. The virtual trabecular cores extracted from these heads represent pathologic bone that would be removed and discarded prior to the humeral joint replacement component being placed. Assuming the underlying trabecular bone retains similar architecture and bone volume fraction as the distal regions of the cores tested in this study, then it is reasonable to assume that density-modulus relationships derived for non-pathologic normal bone may be used to map the trabecular modulus in FEMs for OA patients. This would be relevant when modeling joint replacement components with short or stemless designs. Of course, one would also have to account for cortical variations as part of the pathologic process, and the geometrical considerations that must be made during whole-bone modeling.

There have been a paucity of studies pertaining to the material mapping of osteoarthritic shoulders. The few studies that have investigated OA bone report fractionally reducing glenoid trabecular bone mechanical properties (Hermida, 2014; Lacroix et al., 2014) based on experimental testing of rheumatoid glenoid bone (Frich et al., 1997). In contrast, the results of this study suggest that not only should the modulus of OA bone not be reduced by a factor, but that OA bone volume fractions greater than 0.25 should be mapped with a density-modulus relationship that is linear instead of an exponential fit. However, the power-fit regression for the end-stage OA group was not as good of predictor of apparent modulus from bone volume fraction ($r^2 = 0.63$), compared to non-pathologic normals ($r^2 = 0.84$). This is most likely due to the increased variation that occurs at high bone-volume fractions. Quantifying more localized structural differences between groups

would be advantageous to elucidate the contributive factors that lead to mechanical property variations between the two groups.

Comparing microarchitectural parameters by age (Figure 7.2), we found similar results to femoral OA samples in both bone volume fraction and trabecular thickness (Perilli et al., 2007), the only two similar metrics shared between these studies. We also found similar linear regression fits between apparent modulus and age for both the non-pathologic normal group and end-stage OA group (Figure 7.3), with the OA group having higher apparent modulus, but both groups decreasing by age. This is interesting because the same trend did not occur with bone volume fraction and age (Figure 7.4). Within the normal group, there was only a very slight decrease in BV/TV with age, but a more pronounced decrease in BV/TV with age occurred in the OA group. Although the entire OA group consisted of end-stage OA, the progression of the disease including subchondral mineralization, cyst formation, and bone remodeling varied by patient. Although the linear regression parameters are consistent between the two groups, the low coefficient of determination results indicate that in order to make definitive conclusions about the predictive capabilities of these regression models, larger sample sizes are needed. We however found similar trends in our apparent modulus versus bone volume fraction results to reports of apparent stiffness versus density variations between normal and OA bone in the hip, that consisted of much larger sample sizes (Burr and Gallant, 2012; Li and Aspden, 1997).

A limitation of this study is that a uniform homogeneous trabecular tissue modulus was chosen to represent the tissue-level properties of μFEMs. It has been reported that accounting for material heterogeneity has minimal influence on E_{app} (Gross et al., 2011); however, it has also been shown that accounting for local trabecular material heterogeneity may significantly alter the local mechanical properties of trabecular bone. Accounting for material heterogeneity may also allow for more accurate local predictions of fracture and failure between non-pathologic and end-stage OA bone. Heterogeneous μFEMs could be combined with experimental loading of trabecular cores, with boundary conditions derived using digital volume correlation (DVC), which has been shown to improve the accuracy of compressive loading of bone cores (Chen et al., 2017; Bourne and Van Der Meulen, 2004; Jaasma et al., 2002; Renders et al., 2011, 2008). Accurate heterogeneous mapping at the

micro-level can be improved using a relationship between calibration phantom tissue-mineral density (TMD) and modulus. A calibration phantom was not available to quantify TMD in this study, but due to the hypomineralized nature of the OA bone (Burr and Gallant, 2012), quantifying this metric in future comparisons would be helpful.

7.5 CONCLUSION:

The differences and similarities in microarchitectural parameters and apparent mechanical properties between non-pathologic normal bone and end-stage osteoarthritic (OA) bone shown in this study, improve our understanding of the progression of OA and its effect on trabecular architectural and mechanical properties. Understanding how these structural changes influence computational model generation and the mapping of material properties in patient-specific finite element models, has the potential to improve the accuracy of computational models of OA patients. This allows for a variety of improvements to many biomechanical conditions including, but not limited to, joint replacement component design and fracture and failure analysis.

7.6 REFERENCES:

Arden, N., Nevitt, M.C., 2006. Osteoarthritis: Epidemiology. Best Pract. Res. Clin. Rheumatol. 20, 3–25. Doi:10.1016/j.berh.2005.09.007

Bourne, B.C., Van Der Meulen, M.C.H., 2004. Finite element models predict cancellous apparent modulus when tissue modulus is scaled from specimen CT-attenuation. J. Biomech. 37, 613–621. Doi:10.1016/j.jbiomech.2003.10.002

Bouxsein, M.L., Boyd, S.K., Christiansen, B.A., Guldberg, R.E., Jepsen, K.J., M??ller, R., 2010. Guidelines for assessment of bone microstructure in rodents using micro-computed tomography. J. Bone Miner. Res. 25, 1468–1486. Doi:10.1002/jbmr.141

Brandt, K.D., Dieppe, P., Radin, E.L., 2008. Etiopathogenesis of Osteoarthritis. Rheum. Dis. Clin. North Am. 34, 531–559. Doi:10.1016/j.rdc.2008.05.011

Brown, S.J., Pollintine, P., Powell, D.E., Davie, M.W.J., Sharp, C.A., 2002. Regional Differences in Mechanical and Material Properties of Femoral Head Cancellous Bone in Health and Osteoarthritis. Calcif. Tissue Int. 71, 227–234. Doi:10.1007/s00223-001-2102-y

Burr, D.B., Gallant, M.A., 2012. Bone remodelling in osteoarthritis. Nat. Rev. Rheumatol. 8, 665–673. Doi:10.1038/nrrheum.2012.130

Carter, D., Hayes, W., 1977. The compressive behavior of bone as a two-phase porous structure. J. Bone Jt. Surg. 59(7), 594-962

Chen, Y., Dall'Ara, E., Sales, E., Manda, K., Wallace, R., Pankaj, P., Viceconti, M., 2017. Micro-CT based finite element models of cancellous bone predict accurately displacement once the boundary condition is well replicated: A validation study. J. Mech. Behav. Biomed. Mater. 65, 644–651. Doi:10.1016/j.jmbbm.2016.09.014

Faieghi, M., Knowles, N.K., Tutunea-fatan, O.R., Ferreira, L.M., 2019. Fast Generation of Cartesian Meshes from Micro-Computed Tomography Data. Comput. Aided Des. Appl. 16, 161–171.

Frich, H., Jensen, N.C., Odgaard, A., Pedersen, C.M., Sojbjerg, J.O., Dalstra, M., 1997. Bone strength of the glenoid and material properties. J. Shoulder Elbow. Surg

Gross, T., Pahr, D.H., Peyrin, F., Zysset, P.K., 2011. The Influence of Mineral Heterogeneity on the Apparent Elastic Properties of Human Cancellous Bone: a SR-microCT-based Finite Element study. 2011 ORS Annu. Meet. 15, 1137–1144.

Hermida, J., 2014. Augmented wedge-shaped glenoid component for the correction of glenoid retroversion: a finite element analysis. J. Shoulder Elbow Surg. 23(3), 347-354

Hodgskinson, R., Currey, J.D., 1993. Separate effects of osteoporosis and density on the strength and stiffness of human cancellous bone. Clin. Biomech. 8, 262–8. Doi:10.1016/0268-0033(93)90036-H

Jaasma, M.J., Bayraktar, H.H., Niebur, G.L., Keaveny, T.M., 2002. Biomechanical effects of intraspecimen variations in tissue modulus for trabecular bone. J. Biomech. 35, 237–246. Doi:10.1016/S0021-9290(01)00193-2

Knowles, N., Langohr, G.D.G., Faieghi, M., Nelson, A., 2018. Development of a validated glenoid trabecular density-modulus relationship. J. . Mech. Behav. Biomed. Mat. 90, 140-145

Lacroix, D., Murphy, L.A., Prendergast, P.J., 2014. Three-Dimensional Finite Element Analysis of Glenoid Replacement Prostheses : A CoMParison of Keeled and Pegged Anchorage Systems. J. Biomech. Eng. 122, 430–436.

Li, B., Aspden, R.M., 1997. Composition and Mechanical Properties of Cancellous Bone from the Femoral Head of Patients with Osteoporosis or Osteoarthritis. J. Bone Miner. Res. 12, 641–651. Doi:10.1359/jbmr.1997.12.4.641

Mansell, J., Jason, P., Bailey, A.J., 1998. Abnormal cancellous bone collagen metabolism in osteoarthritis. Am Soc Clin Investig. 101(8), 1596-1603

Maquer, G., Musy, S.N., Wandel, J., Gross, T., Zysset, P.K., 2015. Bone volume fraction and fabric anisotropy are better determinants of trabecular bone stiffness than other morphological variables. J. Bone Miner. Res. 30, 1000–1008. Doi:10.1002/jbmr.2437

Pawson, D.J., Glanzmann, M., Luechinger, R., Müller, R., Stok, K.S., 2015. Quantitative morphometric patterns in cartilage and bone from the humeral heads of end-stage osteoarthritis patients. Osteoarthr. Cartil. 23, 1377–1387. Doi:10.1016/j.joca.2015.04.009

Perilli, E., Baleani, M., Öhman, C., Baruffaldi, F., Viceconti, M., 2007. Structural parameters and mechanical strength of cancellous bone in the femoral head in osteoarthritis do not depend on age. Bone 41, 760–768. Doi:10.1016/j.bone.2007.07.014

Renders, G.A.P., Mulder, L., Langenbach, G.E.J., van Ruijven, L.J., van Eijden, T.M.G.J., 2008. Biomechanical effect of mineral heterogeneity in trabecular bone. J. Biomech. 41, 2793–2798. Doi:10.1016/j.jbiomech.2008.07.009

Renders, G.A.P., Mulder, L., van Ruijven, L.J., Langenbach, G.E.J., van Eijden, T.M.G.J., 2011. Mineral heterogeneity affects predictions of intratrabecular stress and strain. J. Biomech. 44, 402–407. Doi:10.1016/j.jbiomech.2010.10.004

Schneider, C.A., Rasband, W.S., Eliceiri, K.W., 2012. NIH Image to ImageJ: 25 years of image analysis. Nat. Methods 9, 671–675. Doi:10.1038/nmeth.2089

van Rietbergen, B., Weinans, H., Huiskes, R., Odgaard, A., 1995. A new method to determine trabecular bone elastic properties and loading using micromechanical finite-elements models. J. Biomech. 28, 69–81.

Zysset, P.K., Sonny, M., Hayes, W.C., 1994. Morphology-mechanical property relations in trabecular bone of the osteoarthritic proximal tibia. J. Arthroplasty 9, 203–16.

CHAPTER 8 – GENERAL DISCUSSION AND CONCLUSIONS

OVERVIEW: *This chapter revisits the objectives and hypotheses of the research and contextualizes the research within the current literature and gaps within. The questions answered by this work and those opened are discussed. Strengths and limitations are detailed, and future directions are explored.*

8.1 SUMMARY:

Computational models provide a cost-effective and repeatable method of analysing a variety of basic science and clinically motivated problems. These models; however, are dependent on validation and characterization with respect to the outcome measures they intend to simulate. There has been a marked improvement in quantitative imaging methods used in biomechanics research in recent years, such as quantitative-CT (QCT) and wide-spread use of microCT; however, there are a paucity of studies that use these contemporary methods of image acquisition in finite element model (FEM) generation of the shoulder (section 1.4.6) (Knowles et al., 2016). Similarly, recent advances in experimental testing methods, such as digital volume correlation (DVC), provide a direct measurement of the experimental full-field mechanical response of bone under load, which can be used to drive FEM boundary conditions, and also incorporate full-field comparisons that are directly relatable to FEM output. These methods of experimental validations have been reported in the vertebrae (Hussein et al., 2018; Jackman et al., 2015), synthetic bone (Madi et al.,2013),

femur (Ridzwan et al., 2018), and bone cores (Bay et al., 1999; Chen et al., 2017; Liu and Aspden, 2007; Zauel et al., 2006), but in the shoulder have only been reported to quantify glenoid implant micromotion (Sukjamsri et al., 2015). Moreover, DVC validations have not been reported with FEM comparisons in the shoulder. Furthermore, although most patients undergoing surgical procedures, such as total shoulder arthroplasty, exhibit some form of pathologic bone disease, and bone pathology, such as osteoarthritis (OA), it is seldom modeled in shoulder FEM studies. The few computational studies that account for pathologic bone in the shoulder fractionally reduce the elastic modulus of the pathologic group by a percentage (Hermida et al., 2014; Lacroix et al., 2014) based on observations of bone strength in rheumatoid glenoid bone (Frich et al., 1997). This is not an accurate representation of pathologic OA bone, as the increased bone turnover increases bone volume fraction, resulting in increased apparent density and associated strength (Burr and Gallant, 2012; Li and Aspden, 1997). Using modern advances in imaging modalities, FEM development methods, and the most recent advances in experimental methods, this thesis provides a body of work that advances shoulder QCT-FEMS using material mapping, density-modulus relationship development, parameter selection, and integration of pathologic variations in bone properties.

The first objective of this research was to develop a computational methodology to assess trabecular QCT-derived FEMs compared to co-registered trabecular microFEMs (Objective 1a) and use this methodology to compare density-modulus relationships from the literature mapped to QCT-FEMs. The ability of the QCT-FEMs to replicate apparent strain energy density (SED_{app}) of the co-registered microFEMs (modeled with homogeneous or heterogeneous material properties) was used to determine the accuracy of each relationship. Hypothesis 1 stated that due to the lack of shoulder-specific density-modulus relationships in the literature, linear correlation coefficients would be less than 0.8 and slopes would deviate from unity (Y=X) by greater than 0.2. The results of Chapter 2 contradict these hypotheses, with homogeneous microFEMs comparisons indicating the best relationship had a linear correlation coefficient of 0.933 and a slope of 0.979 (Morgan et al., 2003). Similarly, when considering tissue heterogeneity in the microFEMs, a different relationship best compared to heterogeneous microFEMs with a correlation coefficient of 0.935 and a slope of 1.014 (Büchler et al., 2002). These represent errors

compared to the microFEMs of 2.1% and 1.4% for homogeneous and heterogeneous microFEM SED_{app} comparisons, respectively. This indicated that given comparisons between microFEMs and QCT-FEMs, non-site-specific density-modulus relationships may accurately replicate the elastic modulus of trabecular FEMs. The methodology developed allows for direct comparison or development of density-modulus relationships in all anatomic locations.

The second objective was to develop a glenoid-specific trabecular density-modulus relationship (Objective 2a), using the same co-registered computational methodology from Objective 1 (Objective 2b). Although the relationships from Chapter 2 showed strong correlations with microFEM SED_{app}, the translation of these relationships to whole-bone scapular models was unknown. Development of a glenoid-specific trabecular density-modulus relationship, in Chapter 3, allowed for the 'correction' of side-artifact that may underestimate the true modulus of cored samples at the whole bone-level, due to damage that occurs on the outer trabeculae (Ün et al., 2006). Although it has been shown that side-artifact has little influence in cored samples greater than 8.3 mm in diameter (Lievers et al., 2010), all samples in the studies from Chapter 2 vary in core size, aspect ratio, anatomic-location, species, and testing method. These limitations were overcome in Chapter 2, and in the development of the glenoid-specific density-modulus relationship (Chapter 3) by using virtual cores that were all tested in a consistent manner, with a uniform rectangular geometry of 5 mm edge length and 10 mm long, to ensure consistency between cadaveric specimens of different sizes. The rectangular geometry ensured isotropic voxels for both the QCT-FEMs and microFEMs. The relationships were characterized using microFEMs with either homogenous or heterogeneous tissue-moduli. It was hypothesised that linear correlation coefficients would be greater than 0.9 and slopes near unity (Y=X) (Hypothesis 2). This held true for the homogeneous relationship for correlation coefficient (0.940), but not slope (0.864); however, held true for both with the heterogeneous relationship (correlation coefficient: 0.912; slope: 1.013). Although this only represents a modest improvement in accuracy of 0.01% over the best relationship from Chapter 2, both of the glenoid-specific trabecular density-modulus relationships characterized in this chapter were corrected for the influence of side-artifact for use in whole-bone scapular FEM studies. This is the only study to directly characterize glenoid trabecular bone loading

at a both the continuum- and micro-level, improving on the purely theoretical glenoid density-modulus relationship of Gupta & Dan (2004) with the development of the trabecular glenoid density-modulus relationship. It also allowed for the development of QCT-density based relationships, minimizing the influence of error in density conversions.

The third objective was to further investigate microFEMs by comparing the effect of model generation from varied spatial resolution microCT images (Objective 3a), hexahedral or tetrahedral elements (Objective 3b), and material heterogeneity (Objective 3c). Hypothesis 3 stated that microFEMs generated from 32-micron scans with tetrahedral elements, and accounting for material heterogeneity, will have lower errors in apparent modulus compared to the other combinations of resolution and element type. This was confirmed in Chapter 4. It was found that when using tetrahedral elements, only microFEMs generated at the highest spatial resolution (32 micron) and accounting for material heterogeneity, were able to replicate the apparent strain energy density of the gold-standard hexahedral homogeneous microFEMs. Large percentage errors also occurred for microFEMs generated from images at half the spatial resolution (64 micron and down-sampled 64 micron) with the 64 micron-derived microFEMs differing from each other in apparent modulus. This indicates that careful consideration should be taken when generating microFEMs and for the highest microFEMs accuracy, the highest possible spatial resolution images should be used as microFEM input, accounting for material heterogeneity.

In order to explore the objectives of Chapter 5, QCT-FEM element type was first compared to microFEM SED_{app} using the methodology from Chapter 2 and the validated glenoid-specific trabecular density-modulus relationship from Chapter 3 (Objective 4a). The secondary objective was to evaluate elemental and nodal material mapping of trabecular QCT-FEMs (Objective 4b). The hypothesis that QCT-FEMs mapped with quadratic tetrahedral or linear hexahedral elements will show no difference in the measured apparent modulus when mapped with either elemental or nodal material mapping strategies (Hypothesis 4) was partially confirmed in Chapter 5. The QCT-FEMs with hexahedral elements showed similar linear regression parameters compared to the microFEM SED_{app} when mapped with elemental (r^2 = 0.972; slope = 1.014) or nodal material mapping strategies (r^2 = 0.984; slope = 0.954), but slightly worse linear regression results when

using quadratic tetrahedral elements for elemental (r^2 = 0.987; slope = 0.936) or nodal material mapping strategies (r^2 = 0.986; slope = 0.927). Ultimately, there was little variation between hexahedral versus quadratic tetrahedral element types, or elemental versus nodal material mapping strategies, indicating that for trabecular QCT-FEMs these element types and material mapping strategies can accurately replicate microFEM SED_{app}. Chapter 5 improves our understanding of QCT-FEM element type and material mapping, directly to the trabecular bone that can be used to evaluate trabecular bone loading at a variety of hierarchical levels. These comparisons are important because multi-level FEMs are used for bone strength predictions and can be translated to clinical evaluation.

The fifth objective was to compare experimentally loaded scapular cadavers within a microCT to scapular QCT-FEMS mapped with different density-modulus relationships and material mapping strategies using digital volume correlation (DVC) (Objective 5). It was hypothesized that QCT-FEMs generated with the glenoid-specific trabecular density modulus relationship developed in Chapter 3 would have the highest correlations with experimental DVC results (Hypothesis 5). This did not hold true. The relationship that had the lowest percentage errors for the six specimens tested was the one that had the lowest standard error of regression, but highest proportional error in Chapter 2 (Rice et al., 1988; Schaffler and Burr, 1988). This indicated that the true modulus of trabecular bone may have been overestimated when developing the glenoid-specific trabecular density modulus relationship (Chapter 3); however, the effect of cortical material mapping, geometry, and specimen-specificity of material mapping is unknown with this relatively low sample size. The results of Chapter 6 indicate that due to the strong relationships between QCT-FEM and DVC full-field displacements, either material mapping strategy can replicate the experimental loading of scapular cadaveric bone under these conditions. Further evaluation, with increased sample size is required to determine the optimal density-modulus relationship and piecewise transition between trabecular and cortical bone for whole-bone scapular QCT-FEMs.

The final objective of this thesis was to compare the morphometric and apparent mechanical properties between non-pathologic normal and end-stage osteoarthritic (OA) bone (Objective 6). The hypothesis that end-stage OA bone will exhibit larger bone volume fractions and associated apparent modulus (Hypothesis 6) held true, but differences in bone

volume fraction only persisted in the most proximal aspects of the cores tested. Further depths of the pathologic and normal bone showed no significant differences in any of the trabecular bone morphometric parameters. This indicates that the adaptive changes that occur as the result of pathologic OA only persist in the bone below the subchondral region. Although it was expected that an OA-specific density-modulus relationship – exhibiting more linearity – would more accurately represent trabecular OA bone, this may only be required if the pathologic subchondral bone is being modeled. In cases where the pathologic humeral head is removed, such as with humeral joint replacements, humeral trabecular density-modulus relationships developed using non-pathologic normal bone may accurately represent the linear elastic response of the OA trabecular bone. Further evaluation into the geometrical factors and cortical bone response of pathologic whole humeri still need to be explored.

8.2 STRENGTHS AND LIMITATIONS:

The multi-resolution comparative computational and experimental scapular loading methodologies described in this thesis represent some of the only experimental validations in shoulder FEM studies within the literature. The use of QCT and microCT imaging data as input to FEM generation are routine in modeling of the spine and femur (Table 1.1), but not commonly used in shoulder FEMs. The relatively large sample size of virtual cores (n=98) used to compare and develop density-modulus relationships (Chapters 2 & 3) allowed for robust statistical comparisons between co-registered FEMs. The advancements in shoulder site-specific modeling provided from these comparisons and development of the glenoid-specific trabecular density-modulus relationship presented in this thesis move shoulder FEM generation in-line with other anatomic locations. Although when applied to scapular whole-bones, the glenoid-specific trabecular density-modulus relationship was not found to be superior, it remains unknown as to whether this was due to inaccuracies in trabecular modeling, cortical modeling, bone geometry, or other unknown factors. One explanation is the trabecular tissue modulus chosen in model development was too large.

Given the limited data to inform accurate trabecular tissue modulus selection, the upper end of reported values (20 GPa) (Wu et al., 2018) was used for homogeneous models, and a CT-intensity scaled value with a reference of 20 GPa was used for heterogeneous

models (Bourne and Van Der Meulen, 2004). As mentioned, these values were perhaps too large, based on the experimental DVC comparison results of Chapter 6. To determine a more accurate homogeneous trabecular tissue modulus, back-calculation may be used by experimentally loading trabecular bone cores that use DVC-driven boundary conditions (Chen et al., 2017). This may eliminate some fo the uncertainty and variability that has occurred in previous experimental measures of trabecular tissue modulus. In the present studies, the difficulty in extracting uniform trabecular bone samples from the relatively small glenoid vault led to the development of the purely computational comparative methodology of Chapter 2, and used in Chapters 3, 4, and 5.

While the computational methodology was consistent with experimental methods used to develop density-modulus relationships in alternate anatomic locations (Helgason et al., 2008), the comparisons of trabecular bone cores used within this thesis are limited to apparent-level mechanical properties. There are inevitably local variations that occur at the micro-level due to trabecular bone load-sharing that alter the local stresses and strains of individual trabeculae. Although not evaluated as part of this thesis, large local variations in stresses and strains have been shown to occur when comparing homogeneous and heterogeneous microFEMs (Harrison et al., 2008; Renders et al., 2011, 2008). Evaluation of these local parameters in future studies may improve out understanding of trabecular bone loading, including fracture and failure. As input, the most accurate FEMs mapped with validated material properties, such as those developed within, are necessary for accurate strength predictions in linear and non-linear studies.

The models and relationships developed as part of this thesis were only evaluated as linear-isotropic FEMs. Despite the fact that bone volume fraction (and apparent density) has been suggested to account for up to 90% of the variation in mechanical properties of bone (Carter and Hayes, 1977; Maquer et al., 2015), recent improvement in accounting for anisotropy at the continuum-level has been reported (Chandran et al., 2017; Enns-Bray et al., 2016, 2014; Latypova et al., 2016; Nazemi et al., 2016; Trabelsi and Yosibash, 2011). Although in many QCT-FEMs this adds a level of complexity to model development, the further evaluation of anisotropic QCT-FEMs may further increase the accuracy of these models.

At the time of microCT scanning, a microCT calibration phantom was not available, and therefore, consistency between models was ensured by using uniform imaging parameters and fields of view (FOV). This meant that for microFEM generation with heterogeneous tissue modulus, only a relationship based on CT-intensity could be used (Bourne and Van Der Meulen, 2004). This limits the available comparison of bone mineral content (BMC) of samples tested and a specimen-specific threshold for model generation based on calibrated volumetric bone mineral density (vBMD). As such, a uniform threshold-based segmentation method was used to generate microFEMs. This method has shown that qualitatively selected thresholds produce repeatable results in estimating bone volume fraction, which is expected to minimize errors in the chosen minimum threshold among models (Christiansen, 2016), since this is the primary metric for generating repeatable models, and was used to ensure comparable model generation in Chapter 4. The use of a microCT phantom would be most beneficial in the comparative analysis of non-pathologic normal bone and end-stage OA bone (Chapter 7), allowing for quantitative comparisons of BMC, among the other quantitative morphometric parameters.

The experimental DVC-based comparisons presented in Chapter 6 is the first known study to use this contemporary experimental testing method for comparison of density-modulus relationships and material mapping strategies. More robust conclusions can be elucidated by allowing for full-field comparisons of QCT-FEMs and experimental microCT-based loading. Although the sample size is relatively small, the use of DVC-derived boundary conditions (BCs) and full-field results provide a new paradigm in the experimental validation of QCT-FEMs. This methodology can be adopted for all anatomic locations and allows for a variety of mechanical properties to be evaluated.

Finally, Chapter 7 provides the first quantitative comparison of non-pathologic normal and end-stage osteoarthritic bone and apparent modulus of humeral bone. The differences and similarities in morphometric and apparent mechanical properties developed in this study allow for more accurate material mapping of trabecular bone in subsequent FEM studies. These comparisons are essential for the implementation of computational modeling into the clinical workflow.

8.3 FUTURE DIRECTIONS

The studies included in this thesis provide considerable improvements in QCT-based FEMs of the shoulder; however, the questions answered as part of this thesis have led to a large number of questions still to be answered.

First, with the advancements in DVC analysis and improvements in the associated algorithms, comparative analysis between physical trabecular (or cortical) bone cores and computational models can now be completed. The methodology described in Chapter 2 could be expanded to include experimental loading of bone cores with DVC-driven BCs, with full-field DVC comparisons. This would allow for comparative local analysis of stresses and strains that can be used to inform fracture risk. This method would also allow for more accurate homogeneous tissue modulus generation by back-calculation with the most accurate microFEMs (van Rietbergen et al., 1995). The difficulty and complexity in measuring heterogeneous tissue modulus of individual trabeculae (Oftadeh et al., 2015; Wu et al., 2018) currently limits the usefulness of accurately modeling material heterogeneity; however, improvements in imaging methods and computational modeling may allow for more accurate representations of heterogeneity at the tissue-level in the future.

Secondly, the effect of non-linear modeling parameters was not evaluated as part of this thesis. Expanding the density-modulus relationships to density-modulus-fabric-tensor relationships that account for the local anisotropy of bone, may further improve model accuracy. A workflow and development of these relationships into open-source software, such as MITK-GEM, would provide a tremendous benefit to the computational biomechanics community. A consistent open-source platform for model development has the potential to provide vast improvements in our understanding of bone biomechanics, joint replacement component design, and clinical evaluation.

Thirdly, only trabecular density-modulus relationships were primarily evaluated as part of this research. It became apparent during the experimental/computational comparisons in Chapter 6, that accurate modeling of the trabecular/cortical transition and/or the modeling of cortical bone, may largely contribute to the specimen-specific

variations that were observed among relationships. As such, future studies using the aforementioned methods should also be performed on cortical bone specimens to ensure that the mapping parameters used for this bone type are being accurately modeled at the whole-bone level. It may also be advantageous to perform density-modulus relationship development at the whole-bone-level, as this has shown improved outcomes versus experimental results (Austman et al., 2009), but appears to show more subject-specific relationships using optimization methods (Eberle et al., 2013). Machine learning techniques, such as neural networks (Nazemi et al., 2017), also provide an interesting framework for density-modulus development of whole-bones and combined with full-field experimental DVC results for comparison, may provide a new paradigm in density-modulus relationship developments at the whole-bone-level.

Finally, further comparisons among normal and pathologic bone within the shoulder should be completed to ensure that computational models are most representative of the clinical conditions that are being modeled. Variations in micro-level bone architecture were observed with increases in apparent-level mechanical properties in pathologic regions. Exploring how these contributive factors, including cortical bone and bone gross morphological changes alter the mechanical response of pathologic bone is essential to ensure model accuracy and for the implementation of computational models into the clinical workflow.

8.4 SIGNIFICANCE:

With an aging population and as the prevalence of surgical procedures involving the shoulder increases, biomechanical computational models provide an important tool in improving our understanding of both basic science and clinical conditions. With modern improvements in imaging modalities, computational model accuracy, and clinical need, the integration of computational modeling into the clinical workflow may guide surgeons during surgical evaluation and intervention, leading to improved patient outcomes. The present work contributes significantly to the improvement of shoulder computational studies, making these studies comparable with those of other major anatomic locations, such as the spine and femur. The validations and comparisons presented allow for accurate characterisation of future FEM studies evaluating fracture, failure, surgical outcomes, and

disease progression among other outcomes, modernizing shoulder FEMs. This not only improves our understanding of the shoulder but allows for comparative data that can be used to assess bone across all anatomic locations.

8.5 REFERENCES:

Austman, R.L., Milner, J.S., Holdsworth, D.W., Dunning, C.E., 2009. Development of a customized density–modulus relationship for use in subject-specific finite element models of the ulna. Proc. Inst. Mech. Eng. Part H J. Eng. Med. 223, 787–794. Doi:10.1243/09544119JEIM553

Bay, B.K., Smith, T.S., Fyhrie, D.P., Saad, M., 1999. Digital volume correlation: Three-dimensional strain mapping using X-ray tomography. Exp. Mech. 39, 217–226. Doi:10.1007/BF02323555

Bourne, B.C., Van Der Meulen, M.C.H., 2004. Finite element models predict cancellous apparent modulus when tissue modulus is scaled from specimen CT-attenuation. J. Biomech. 37, 613–621. Doi:10.1016/j.jbiomech.2003.10.002

Büchler, P., Ramaniraka, N.A., Rakotomanana, L.R., Iannotti, J.P., Farron, A., 2002. A finite element model of the shoulder: application to the coMParison of normal and osteoarthritic joints. Clin. Biomech. 17, 630–639. Doi:10.1016/S0268-0033(02)00106-7

Burr, D.B., Gallant, M.A., 2012. Bone remodelling in osteoarthritis. Nat. Rev. Rheumatol. 8, 665–673. Doi:10.1038/nrrheum.2012.130

Carter, D., Hayes, W., 1977. The compressive behavior of bone as a two-phase porous structure. J. Bone Jt. Surg. 59(7), 954-962

Chandran, V., Reyes, M., Zysset, P., 2017. A novel registration-based methodology for prediction of trabecular bone fabric from clinical QCT: A comprehensive analysis. PloS One 12, 1–23. Doi:10.1371/journal.pone.0187874

Chen, Y., Dall′Ara, E., Sales, E., Manda, K., Wallace, R., Pankaj, P., Viceconti, M., 2017. Micro-CT based finite element models of cancellous bone predict accurately displacement once the boundary condition is well replicated: A validation study. J. Mech. Behav. Biomed. Mater. 65, 644–651. Doi:10.1016/j.jmbbm.2016.09.014

Christiansen, B.A., 2016. Effect of micro-computed tomography voxel size and

segmentation method on trabecular bone microstructure measures in mice. Bone Reports 5, 136–140. Doi:10.1016/j.bonr.2016.05.006

Eberle, S., Göttlinger, M., Augat, P., 2013. An investigation to determine if a single validated density – elasticity relationship can be used for subject specific finite element analyses of human long bones. Med. Eng. Phys. 35, 875–883. Doi:10.1016/j.medengphy.2012.08.022

Enns-Bray, W.S., Ariza, O., Gilchrist, S., Widmer Soyka, R.P., Vogt, P.J., Palsson, H., Boyd, S.K., Guy, P., Cripton, P.A., Ferguson, S.J., Helgason, B., 2016. Morphology based anisotropic finite element models of the proximal femur validated with experimental data. Med. Eng. Phys. 38, 1339–1347. Doi:10.1016/j.medengphy.2016.08.010

Enns-Bray, W.S., Owoc, J.S., Nishiyama, K.K., Boyd, S.K., 2014. Mapping anisotropy of the proximal femur for enhanced image based finite element analysis. J. Biomech. 47, 3272–3278. Doi:10.1016/j.jbiomech.2014.08.020

Frich, H., Jensen, N.C., Odgaard, A., Pedersen, C.M., Sojbjerg, J.O., Dalstra, M., 1997. Bone strength of the glenoid and material properties. J. Shoulder Elb. Surg. 6, 1097–1104.

Harrison, N.M., McDonnell, P.F., O'Mahoney, D.C., Kennedy, O.D., O'Brien, F.J., McHugh, P.E., 2008. Heterogeneous linear elastic trabecular bone modelling using micro-CT attenuation data and experimentally measured heterogeneous tissue properties. J. Biomech. 41, 2589–2596. Doi:10.1016/j.jbiomech.2008.05.014

Helgason, B., Perilli, E., Schileo, E., Taddei, F., 2008. Mathematical relationships between bone density and mechanical properties: a literature review. Clin. Biomech. 23, 135–146. Doi:10.1016/j.clinbiomech.2007.08.024

Hermida, J., Flores-Hernandez, Hoenecke, H.R., D'Lima, D.D., 2014. Augmented wedge-shaped glenoid component for the correction of glenoid retroversion: a finite element analysis. J. Shoulder Elbow Surg. 23, 347–354.

Hussein, A.I., Louzeiro, D.T., Morgan, E.F., 2018. Differences in Trabecular Microarchitecture and Simplified Boundary Conditions Limit the Accuracy of Quantitative Computed Tomography-Based Finite Element Models of Vertebral Failure. J. Biomech. 140, 1–11. Doi:10.1115/1.4038609

Gupta, S., & Dan, P. 2004. Bone geometry and mechanical properties of the human scapula using computed tomography data. Trends Biomater. Artif. Organs, 17(2), 61-70.

Jackman, T.M., DelMonaco, A.M., Morgan, E.F., 2015. Accuracy of finite element analyses of CT scans in predictions of vertebral failure patterns under axial compression and anterior flexion. J. Biomech. 1–9. Doi:10.1016/j.jbiomech.2015.12.004

Knowles, N., Reeves, J.M., Ferreira, L.M., 2016. Quantitative Computed Tomography (QCT) derived Bone Mineral Density (BMD) in finite element studies: a review of the literature. J. Exp. Orthop. 3, 36. Doi:10.1186/s40634-016-0072-2

Lacroix, D., Murphy, L.A., Prendergast, P.J., 2014. Three-Dimensional Finite Element Analysis of Glenoid Replacement Prostheses : A CoMParison of Keeled and Pegged Anchorage Systems. J. Shou 122, 430–436.

Latypova, A., Maquer, G., Elankumaran, K., Pahr, D., Zysset, P., Pioletti, D.P., Terrier, A., 2016. Identification of elastic properties of human patellae using micro-finite element analysis. J. Biomech. 49, 3111–3115. Doi:10.1016/j.jbiomech.2016.07.031

Li, B., Aspden, R.M., 1997. Composition and Mechanical Properties of Cancellous Bone from the Femoral Head of Patients with Osteoporosis or Osteoarthritis. J. Bone Miner. Res. 12, 641–651. Doi:10.1359/jbmr.1997.12.4.641

Lievers, W.B., Petryshyn, A.C., Poljsak, A.S., Waldman, S.D., Pilkey, A.K., 2010. Specimen diameter and “side artifacts” in cancellous bone evaluated using end-constrained elastic tension. Bone 47, 371–377. Doi:10.1016/j.bone.2010.03.024

Liu, L., Ã, E.F.M., 2007. Accuracy and precision of digital volume correlation in quantifying displacements and strains in trabecular bone 40, 3516–3520. Doi:10.1016/j.jbiomech.2007.04.019

Madi, K., Tozzi, G., Zhang, Q., Tong, J., … A.C.-M. engineering &, 2013, undefined, n.d. Computation of full-field displacements in a scaffold implant using digital volume correlation and finite element analysis. Elsevier.

Maquer, G., Musy, S.N., Wandel, J., Gross, T., Zysset, P.K., 2015. Bone volume fraction and fabric anisotropy are better determinants of trabecular bone stiffness than other morphological variables. J. Bone Miner. Res. 30, 1000–1008. Doi:10.1002/jbmr.2437

Morgan, E., Bayraktar, H., Keaveny, T., 2003. Trabecular bone modulus–density

relationships depend on anatomic site. J. Biomech.

Nazemi, S.M., Amini, M., Kontulainen, S.A., Milner, J.S., Holdsworth, D.W., Masri, B.A., Wilson, D.R., Johnston, J.D., 2017. Optimizing finite element predictions of local subchondral bone structural stiffness using neural network-derived density-modulus relationships for proximal tibial subchondral cortical and trabecular bone. Clin. Biomech. 41, 1–8. Doi:10.1016/j.clinbiomech.2015.05.002

Nazemi, S.M., Cooper, D.M.L., Johnston, J.D., 2016. Quantifying trabecular bone material anisotropy and orientation using low resolution clinical CT images: A feasibility study. Med. Eng. Phys. 38, 978–987. Doi:10.1016/j.medengphy.2016.06.011

Oftadeh, R., Perez-Viloria, M., Villa-Camacho, J.C., Vaziri, A., Nazarian, A., 2015. Biomechanics and Mechanobiology of Trabecular Bone: A Review. J. Biomech. Eng. 137, 010802. Doi:10.1115/1.4029176

Renders, G.A.P., Mulder, L., Langenbach, G.E.J., van Ruijven, L.J., van Eijden, T.M.G.J., 2008. Biomechanical effect of mineral heterogeneity in trabecular bone. J. Biomech. 41, 2793–2798. Doi:10.1016/j.jbiomech.2008.07.009

Renders, G.A.P., Mulder, L., van Ruijven, L.J., Langenbach, G.E.J., van Eijden, T.M.G.J., 2011. Mineral heterogeneity affects predictions of intratrabecular stress and strain. J. Biomech. 44, 402–407. Doi:10.1016/j.jbiomech.2010.10.004

Rice, J., Cowin, S., Bowman, J., 1988. On the dependence of the elasticity and strength of cancellous bone on apparent density. J. Biomech. 21(2), 155-168

Ridzwan, M.I.Z., Sukjamsri, C., Pal, B., van Arkel, R.J., Bell, A., Khanna, M., Baskaradas, A., Abel, R., Boughton, O., Cobb, J., Hansen, U.N., 2018. Femoral fracture type can be predicted from femoral structure: A finite element study validated by digital volume correlation experiments. J. Orthop. Res. 36, 993–1001. Doi:10.1002/jor.23669

Schaffler, M., Burr, D., 1988. Stiffness of coMPact bone: effects of porosity and density. J. Biomech. 21(1), 13-16

Sukjamsri, C., Geraldes, D.M., Gregory, T., Ahmed, F., Hollis, D., Schenk, S., Amis, A., Emery, R., Hansen, U., 2015. Digital volume correlation and micro-CT: An in-vitro technique for measuring full-field interface micromotion around polyethylene implants. J. Biomech. 48, 3447–3454. Doi:10.1016/j.jbiomech.2015.05.024

Trabelsi, N., Yosibash, Z., 2011. Patient-specific finite-element analyses of the proximal femur with orthotropic material properties validated by experiments. J. Biomech. Eng. 133, 061001. Doi:10.1115/1.4004180

Ün, K., Bevill, G., Keaveny, T.M., 2006. The effects of side-artifacts on the elastic modulus of trabecular bone. J. Biomech. 39, 1955–1963. Doi:10.1016/j.jbiomech.2006.05.012

van Rietbergen, B., Weinans, H., Huiskes, R., Odgaard, A., 1995. A new method to determine trabecular bone elastic properties and loading using micromechanical finite-elements models. J. Biomech. 28, 69–81.

Wu, D., Isaksson, P., Ferguson, S.J., Persson, C., 2018. Young's modulus of trabecular bone at the tissue level: A review. Acta Biomater. 78, 1–12. Doi:10.1016/j.actbio.2018.08.001

Zauel, R., Yeni, Y.N., Bay, B.K., Dong, X.N., Fyhrie, D.P., Center, J., 2006. CoMParison of the Linear Finite Element Prediction of Deformation and Strain of Human Cancellous Bone to 3D Digital Volume Correlation Measurements. J. Biomech. Eng. 128(1), 1-6, doi:10.1115/1.2146001

APPENDIX A – GLOSSARY

Apparent Density:	Wet mass of tissue per total volume
Anisotropic:	Non-uniform in all directions
Arthroplasty:	A surgical procedure to restore joint function and reduce pain
Ash Density:	Ash mass of tissue per total volume
Attenuation:	Loss of intensity through a medium
Axial:	Plane separating the body into cranial and caudal regions. Also known as the transverse plane
Bone Density:	Mass of bone within a volume
Computed Tomography:	A medical imaging modality that uses ionizing radiation projected through a medium to collect a series of projections quantified by the object's attenuation along the x-ray beam's path
Coronal:	Plane separating the body into dorsal and ventral regions. Also known as the frontal plane
Distal:	Furthest from the body along a limb
Elastic Modulus	A mechanical property used to quantify the stiffness of a material, calculated as the stress divided by the strain
Excise:	to remove
Heterogeneous:	A non-uniform distribution of properties
Homogeneous:	A uniform distribution of properties
Homeostasis:	Regulation of the normal stability of a system

Hounsfield Unit:	A linear transformation of the linear attenuation coefficient used to calibrate radiodensity in computed tomography scanners
Lateral:	Furthest from the body's midline
Intensity:	The quantitative CT attenuation value per voxel
In-vitro:	Performed outside of the living body
In-vivo:	Performed or taking place within a living organism
Isotropic:	Uniform in dimensions
Medial:	Closest to the body's midline
Morphology:	Alteration to the native form or structure
Morphometric:	The quantitative analysis of form
Microarchitectural:	The architectural distribution of trabecular bone at the micro-level
Osteoarthritis:	Deficiency of a joint characterized by joint stiffness, inflammation, cartilage degradation, and bone adaptive changes
Osteoid:	New, unmineralized bone
Pathologic:	Involved, or caused by physical disease
Proximal:	Closest to the body along a limb
Radiodensity:	The inability of x-rays to pass through a medium
Resorption:	The breakdown of bone releasing minerals into the blood
Sclerosis:	Stiffening or hardening of a structure
Strain:	A measure of deformation, calculated as the change in length over the original length

Strain Energy Density:	A measure of the internal work or energy per unit volume when an object is deformed, calculated as the area under the stress-strain curve
Stress:	A measure of pressure, calculated as the force divided by the contact area
Subchondral:	The bone directly below the articular (chondral) surface
Tissue Density:	The density of individual trabecular. Also known as material or real density
Wolff's Law:	Bone adapts to mechanical stimuli by remodeling based on applied stresses

APPENDIX B – MATLAB® CODE TO GENERATE ABAQUS® INPUT FILES

OVERVIEW: *The following provides the Matlab® code to generate Abaqus® input files with hexahedral elements from QCT image data with nodal material properties, assign nodal material properties to QCT tetrahedral meshes and assign all pre-processing parameters for complete models (boundary conditions, field outputs, etc.). Matlab® code is also provided to that generates nodal material mapping with partial volume correction in whole-bone QCT FEMs. Finally, Matlab® code is provided that generates Abaqus® input files from hexahedral or tetrahedral microFEM data. A robust algorithm is used to generate homogeneous or heterogenous hexahedral microFEMs, due to the increase in model size.*[B]

[B]Hexahderal micro finite element code uses a robust algorithm described in: Faieghi M, Knowles NK, Tutunea-Fatan OR, Ferreira LM. Fast Generation of cartesian meshes from micro-computed tomography data. Computer-Aided Design Applications 2019; 16(1):161-171

B.1 Abaqus® Input File with Nodal Material Mapping & Hexahedral Mesh Generation from QCT Data

This script requires a pre-processed and segmented region exported as a grayvalue file, in a 4-D array of (x, y, z, I), where x, y, z is the centre of the voxels and I is the voxel CT-intensity. A DICOM stack is also required with the segmented region aligned to the CT coordinate system.

```
%%%%%%%%%%%%%%%%%%%%%%%%%%%%%%%%%%%%%%%%%%%%%%%%%%%%%%%%%%%%%%%%%%%%%%%%%%%%%%%%
%                                                                               %
%    This code creates C3D8 elements with element-wise materials and            %
%    the Abaqus input file from Mimics grayvalue text file for linear           %
%    compression analysis - including all BC's, and Constraints. The           %
%    code prompts for the voxel dimensions (isotropic), desired                 %
%    displacement, the sigma and beta values of the K2HPO4 calibration          %
%    and the a and b parameters of the desired density modulus equation         %
%                                                                               %
%    This script also assigns nodal material properties based on nodal          %
%   coordinates. Code uses functions ReadDicomStack and linear interp3          %
%        modified from Dr. Andrew Speirs, Carleton University.                  %
%        ©2016 Nikolas K Knowles, University of Western Ontario                 %
%                                                                               %
%%%%%%%%%%%%%%%%%%%%%%%%%%%%%%%%%%%%%%%%%%%%%%%%%%%%%%%%%%%%%%%%%%%%%%%%%%%%%%%%

%Load Text File of grayvalues output from Mimics

data = dlmread('16-05020L_Post-3_grayvalues.txt');

%Load the DICOM images using the ReadDicomStack Function

[I,info,A]=ReadDicomStack('H:\QCT Material Mapping\DICOMs\16-05020L');

I = I - 1024;

prompt = 'What are the voxel dimensions?';
vox = input(prompt);
vox_x = vox;
vox_y = vox;
vox_z = vox;

prompt1 = 'What is the file name?';
name = input(prompt1,'s');

prompt2 = 'What is the desired displacement value (0.5% strain)?';
disp = input(prompt2);

prompt3 = 'What is sigmaCT of the calibration equation?';
sigma = input(prompt3);
```

```
prompt4 = 'What is betaCT of the calibration equation?';
beta = input(prompt4);

prompt5 = 'What is alpha of the Modulus equation?';
a = input(prompt5);

prompt6 = 'What is beta of the Modulus equation?';
b = input(prompt6);

prompt7 = 'What density type is require (1=app, 2=ash, 3=cal)?';
dens = input(prompt7);

element_centre = data(:,1:3);%Position of the centre of the pixels (in-plane)

%Assigning Nodes to Each Pixel to Create 8-Node Elements

i=1;
for i=1:length(element_centre)
    %Front-plane
    N_1(i,:) = element_centre(i,:) + [-vox_x/2 -vox_y/2 vox_z/2];
    N_2(i,:) = element_centre(i,:) + [vox_x/2 -vox_y/2 vox_z/2];
    N_5(i,:) = element_centre(i,:) + [-vox_x/2 vox_y/2 vox_z/2];
    N_6(i,:) = element_centre(i,:) + [vox_x/2 vox_y/2 vox_z/2];
    %Back-plane
    N_3(i,:) = element_centre(i,:) + [vox_x/2 -vox_y/2 -vox_z/2];
    N_4(i,:) = element_centre(i,:) + [-vox_x/2 -vox_y/2 -vox_z/2];
    N_7(i,:) = element_centre(i,:) + [vox_x/2 vox_y/2 -vox_z/2];
    N_8(i,:) = element_centre(i,:) + [-vox_x/2 vox_y/2 -vox_z/2];
end

ele_nodes_all = [N_1 N_2 N_3 N_4 N_5 N_6 N_7 N_8];%The x,y,z coordinates for each of the
8 nodes in each element (Nodes 1 to 8)

%Remove Duplicate Nodes & eliminate extra row of Z nodes

nodes_all = [N_1; N_2; N_3; N_4; N_5; N_6; N_7; N_8];%All the nodes structured as Nx3
array
nodes_all = round(nodes_all,5);
nodes = unique(nodes_all,'rows');%Only the unique values of the nodes remain - non-
numbered, but indexed

%Structure Nodes & Elements

for j=1:length(N_1)
    ele_nodes_N_1 = dsearchn(nodes,N_1);
    ele_nodes_N_2  = dsearchn(nodes,N_2);
    ele_nodes_N_3  = dsearchn(nodes,N_3);
    ele_nodes_N_4  = dsearchn(nodes,N_4);
    ele_nodes_N_5  = dsearchn(nodes,N_5);
    ele_nodes_N_6  = dsearchn(nodes,N_6);
    ele_nodes_N_7  = dsearchn(nodes,N_7);
    ele_nodes_N_8  = dsearchn(nodes,N_8);
end
```

```
ele_nodes = [ele_nodes_N_1 ele_nodes_N_2 ele_nodes_N_3 ele_nodes_N_4 ele_nodes_N_5
ele_nodes_N_6 ele_nodes_N_7 ele_nodes_N_8];

i=1;
for i=1:length(nodes)
    node_form(i,:) = [i nodes(i,:)];%Structured nodes by number without duplicates
end

%Create Node sets for Top (max z) and Btm(min z)

btm_z = min(node_form(:,4));
top_z = max(node_form(:,4));

continuousIndex=(A\[nodes';ones(1,size(nodes,1))])' +1;

%Interpolate CT, giving intensity values at each node - X, Y index is
%intentionally transposed to account for orientation of DICOM's - viewable
%with imshow(I(:,:,1), []),impixelinfo

int=interp3(I,continuousIndex(:,2),continuousIndex(:,1),continuousIndex(:,3),'*linear');

int_min = min(I(:));%Check the minimum value of intensity

HU = int;

j=1;
n=1;
m=1;
for j=1:length(node_form)
    if node_form(j,4) == top_z
        top_set(n,:) = node_form(j,:);
        n=n+1;
    elseif node_form(j,4) == btm_z
        btm_set(m,:) = node_form(j,:);
        m=m+1;
    end
end

%Define the spacing for the nset
nset_top_spac = abs(top_set(2,1)-top_set(1,1));
nset_btm_spac = abs(btm_set(2,1)-btm_set(1,1));

%Define Reference Points for Centre of Top and Btm
centre_top = min(top_set(:,2:4))/2 + max(top_set(:,2:4))/2;%Top Reference Point
centre_btm = min(btm_set(:,2:4))/2 + max(btm_set(:,2:4))/2;%Btm Reference Point

k=1;
for k=1:length(ele_nodes)
    ele_node_form(k,:) = [k ele_nodes(k,:)];
end

%Calculate density using HU-betaCT/sigmaCT, calculated using linear
%regression
```

```
density_cal=((HU-(beta))/sigma)/1000; %{gK2HPO4/cc]

%Convert calibrated density to apparent or ash density (if required)

density_app = density_cal*2.1973 + 0.0115;%change to desired experimental relationship

density_ash = density_app*0.55; %As per Schileo et al. (2008)

%Define the density measure used

if dens == 1
    density = density_app;
elseif dens ==2
    density = density_ash;
elseif dens ==3
    density = density_cal;
end

%Set minimum density to 0.01
for k=1:size(density)
    if density(k) < 0.01
        density(k,:) = 0.01;
    else
        density(k,:) = density(k,:);
    end
end

%Update HU Field to E field
x=1;
for x = 1:length(density)
E(x,:) = a*((density(x))^b);
end

%Set minimum modulus to 1 MPa

for k=1:size(E)
    if E(k) < 1
        E(k,:) = 1;
    else
        E(k,:) = E(k,:);
    end
end

E_Field = [nodes(:,1:3) E];%Elements are built from gv file and each material is applied
to corresponding element

%Assign the Modulus values to the elements

%Plot Nodes &Element Centres
figure(1)
scatter3(node_form(:,2),node_form(:,3),node_form(:,4),'b');
xlabel('X-Axis')
ylabel('Y-Axis')
zlabel('Z-Axis')
```

```
hold on
scatter3(data(:,1),data(:,2),data(:,3),'r');

%Create Modulus.inp File for input

fid2 = fopen('Modulus.inp','w');
q=1;
for q=1:length(E_Field)%Repeat fprintf for all nodes in model
    fprintf(fid2,'Part-1.');
    fprintf(fid2,'%.f',q);
    fprintf(fid2,',');
    fprintf(fid2,'%.f',E(q));
    fprintf(fid2,'\n');
end
fclose(fid2);

%Format and print file as inp for Abaqus
name_run = strcat(name,'_RUN.inp');
fid = fopen(name_run,'w');
fprintf(fid,'*Part,name=PART');
%fprintf(fid,part);
fprintf(fid,'\n*Node\n');
formatNode = '%.f,%.4f,%.4f,%.4f\n';%format the output for index,x,y,z
fprintf(fid,formatNode, [node_form]');
fprintf(fid,'*Element,type=C3D8\n');
formatEle = '%.f,%.f,%.f,%.f,%.f,%.f,%.f,%.f,%.f\n';%format the output for index,elements
fprintf(fid,formatEle,[ele_node_form]');
fprintf(fid,'*Elset, elset=Section-1, generate\n');
fprintf(fid,'1,  1024,       1\n');
fprintf(fid,'*Nset,nset=TOP,generate\n');%nset is defined by first node in set, last node
in set, increment between node numbers and set
fprintf(fid,'%.f,%.f,%.f',top_set(1,1),top_set(length(top_set),1),nset_top_spac);
fprintf(fid,'\n*Nset,nset=BTM,generate\n');
fprintf(fid,'%.f,%.f,%.f',btm_set(1,1),btm_set(length(btm_set),1),nset_btm_spac);
fprintf(fid,'** Section: Section-1\n');
fprintf(fid,'*Solid Section, elset=Section-1, material=BONE\n');
fprintf(fid,'\n*End Part\n');
fprintf(fid,'**\n');
fprintf(fid,'**');
fprintf(fid,'\n**ASSEMBLY\n');
fprintf(fid,'**');
fprintf(fid,'\n*Assembly, name=Assembly\n');
fprintf(fid,'**');
fprintf(fid,'\n*Instance,name=PART-1,part=PART\n');
fprintf(fid,'*End Instance\n');
fprintf(fid,'**');
fprintf(fid,'\n*Node\n');%This defines the reference points
fprintf(fid,'%.f,%.4f,%.4f,%.4f\n',[1 centre_top]);%1st 'TOP' Reference Point Position
fprintf(fid,'%.f,%.4f,%.4f,%.4f\n',[2 centre_btm]);%2nd 'BTM' Reference Point Position
fprintf(fid,'*Nset, nset=_PickedSet6, internal\n');
fprintf(fid,' 1,\n');
fprintf(fid,'*Nset, nset=_PickedSet7, internal\n');
fprintf(fid,' 2,\n');
fprintf(fid,'*Nset, nset=_PickedSet8, internal\n');
```

```
fprintf(fid,' 2,\n');
fprintf(fid,'*Nset, nset=_PickedSet9, internal\n');
fprintf(fid,' 1,\n');
fprintf(fid,'** Constraint: BTM\n');
fprintf(fid,'*Rigid Body, ref node=_PickedSet7, tie nset=PART-1.BTM\n');
fprintf(fid,'** Constraint: TOP\n');
fprintf(fid,'*Rigid Body, ref node=_PickedSet6, tie nset=PART-1.TOP\n');
fprintf(fid,'*End Assembly\n');
fprintf(fid,'**MATERIALS\n');
fprintf(fid,'*Material, name=BONE');
fprintf(fid,'\n*Elastic, dependencies=1\n');
fprintf(fid,'1.,0.3, ,1.\n');%span the values of E
fprintf(fid,'6e5.,0.3, ,6e5.\n');
fprintf(fid,'**\n');
fprintf(fid,'** BOUNDARY CONDITIONS\n');
fprintf(fid,'**');
fprintf(fid,'\n** Name: BTM Type: Symmetry/Antisymmetry/Encastre\n');
fprintf(fid,'*Boundary\n');
fprintf(fid,'_PickedSet8, ENCASTRE\n');
fprintf(fid,'** ----------------------------------------------------------------\n');
fprintf(fid,'*INITIAL CONDITIONS, TYPE=FIELD, VARIABLE=1, INPUT=Modulus.inp\n');
fprintf(fid,'** ----------------------------------------------------------------\n');
fprintf(fid,'**\n ');
fprintf(fid,'** STEP: LOAD\n');
fprintf(fid,'**\n');
fprintf(fid,'*Step, name=LOAD, nlgeom=NO, inc=1000\n');
fprintf(fid,'*Static\n');
fprintf(fid,'0.1, 1., 1e-06, 1.\n');
fprintf(fid,'**\n');
fprintf(fid,'** BOUNDARY CONDITIONS\n');
fprintf(fid,'**\n');
fprintf(fid,'** Name: DISP Type: Displacement/Rotation\n');
fprintf(fid,'*Boundary\n');
fprintf(fid,'_PickedSet9, 1, 1\n');
fprintf(fid,'_PickedSet9, 2, 2\n');
fprintf(fid,'_PickedSet9, 3, 3,');
fprintf(fid,'%.4f\n',(-1)*disp);
fprintf(fid,'_PickedSet9, 4, 4\n');
fprintf(fid,'_PickedSet9, 5, 5\n');
fprintf(fid,'_PickedSet9, 6, 6\n');
fprintf(fid,'**\n');
fprintf(fid,'** OUTPUT REQUESTS\n');
fprintf(fid,'**\n');
fprintf(fid,'*Restart, write, frequency=0\n');
fprintf(fid,'**\n');
fprintf(fid,'** FIELD OUTPUT: F-Output-1\n');
fprintf(fid,'**\n');
fprintf(fid,'*Output, field, variable=PRESELECT\n');
fprintf(fid,'*Node Output\n');
fprintf(fid,'CF,RF,U\n');
fprintf(fid,'*Element Output, direction=YES\n');
fprintf(fid,'ELEDEN, ELEN, ENER, LE, PE, PEEQ, PEMAG, S\n');
fprintf(fid,'*Contact Output\n');
fprintf(fid,'CDISP, CSTRESS\n');
```

```
fprintf(fid,'**\n');
fprintf(fid,'** HISTORY OUTPUT: H-Output-1\n');
fprintf(fid,'**\n');
fprintf(fid,'*Output, history, variable=PRESELECT\n');
fprintf(fid,'*End Step');
fclose(fid);
```

B.2 Abaqus® Input File with Nodal Material Mapping to Tetrahedral Meshes from QCT Data

This script requires a tetrahedral mesh that has been separated into node and element .txt files. A DICOM stack is also required with the mesh aligned to the CT coordinate system.

```
%%%%%%%%%%%%%%%%%%%%%%%%%%%%%%%%%%%%%%%%%%%%%%%%%%%%%%%%%%%%%%%%%%%%%%%%%%%%%%%
%                                                                              %
%    This script assigns nodal material properties based on nodal              %
%   coordinates. Code uses functions ReadDicomStack and linear interp3         %
%        modified from Dr. Andrew Speirs, Carleton University.                 %
%     ©2016 Nikolas K Knowles, University of Western Ontario                   %
%                                                                              %
%%%%%%%%%%%%%%%%%%%%%%%%%%%%%%%%%%%%%%%%%%%%%%%%%%%%%%%%%%%%%%%%%%%%%%%%%%%%%%%


%Load Text Files

data = dlmread('14-02021L_625_10TET_NB_E_INT_Nodes.txt');
ele =  dlmread('14-02021L_625_10TET_NB_E_INT_Elements.txt');
nodes = data(:,2:4);

%Load the DICOM images using the ReadDicomStack Function
%I is the intensity array in 512x512xSlice# - IMPORTANT to note if indexed
%as GV (0) or HU (-1024) - Code automatically adjusts for this

[I,info,A]=ReadDicomStack('J:\OneDrive - The University of Western Ontario\QCT Material
Mapping\DICOMs\14-02021L');

I = I - 1024;

prompt1 = 'What is the file name?';
name = input(prompt1,'s');

prompt2 = 'What is the desired displacement value (0.5% strain)?';
disp = input(prompt2);

prompt3 = 'What is sigmaCT of the calibration equation?';
sigma = input(prompt3);

prompt4 = 'What is betaCT of the calibration equation?';
```

```
beta = input(prompt4);

prompt5 = 'What is alpha of the Modulus equation?';
a = input(prompt5);

prompt6 = 'What is beta of the Modulus equation?';
b = input(prompt6);

prompt7 = 'What density type is require (1=app, 2=ash, 3=cal)?';
dens = input(prompt7);


continuousIndex=(A\[nodes';ones(1,size(nodes,1))])' +1;

%Interpolate CT, giving intensity values at each node - X, Y index is
%intentionally transposed to account for orientation of DICOM's - viewable
%with imshow(I(:,:,1), []),impixelinfo

int=interp3(I,continuousIndex(:,2),continuousIndex(:,1),continuousIndex(:,3),'*linear');

int_min = min(I(:));%Check the minimum value of intensity

HU = int;

node_form = data;

btm_z = min(nodes(:,3));
top_z = max(nodes(:,3));

j=1;
n=1;
m=1;
for j=1:length(node_form)
    if node_form(j,4) == top_z
        top_set(n,:) = node_form(j,:);
        n=n+1;
    elseif node_form(j,4) == btm_z
        btm_set(m,:) = node_form(j,:);
        m=m+1;
    end
end

%Define the spacing for the nset
nset_top_spac = abs(top_set(2,1)-top_set(1,1));
nset_btm_spac = abs(btm_set(2,1)-btm_set(1,1));

%Define Reference Points for Centre of Top and Btm
centre_top = min(top_set(:,2:4))/2 + max(top_set(:,2:4))/2;%Top Reference Point
centre_btm = min(btm_set(:,2:4))/2 + max(btm_set(:,2:4))/2;%Btm Reference Point

%Calculate density using HU-betaCT/sigmaCT, calculated using linear
%regression

density_cal=((HU-(beta))/sigma)/1000; %[gK2HPO4/cc]
```

```
%Convert calibrated density to apparent or ash density (if required)

density_app = density_cal*2.1973 + 0.0115;%change to desired experimental relationship

density_ash = density_app*0.55; %As per Schileo et al. (2008)

%Define the density measure used

if dens == 1
    density = density_app;
elseif dens ==2
    density = density_ash;
elseif dens ==3
    density = density_cal;
end

%Set minimum density to 0.01
for k=1:size(density)
    if density(k) < 0.01
        density(k,:) = 0.01;
    else
        density(k,:) = density(k,:);
    end
end

%Update HU Field to E field
x=1;
for x = 1:length(density)
E(x,:) = a*((density(x))^b);
end

%Set minimum modulus to 1 MPa

for k=1:size(E)
    if E(k) < 1
        E(k,:) = 1;
    else
        E(k,:) = E(k,:);
    end
end

E_Field = [nodes(:,1:3) E];%Elements are built from gv file and each material is applied
to corresponding element

%Create Modulus.inp File for input

name_mod = strcat(name,'_Modulus.inp');
fid2 = fopen(name_mod,'w');
q=1;
for q=1:length(E_Field)%Repeat fprintf for all nodes in model
    fprintf(fid2,'Part-1.');
    fprintf(fid2,'%.f',q);
    fprintf(fid2,',');
```

```
    fprintf(fid2,'%.f',E(q));
    fprintf(fid2,'\n');
end
fclose(fid2);

%Format and print file as inp for Abaqus
name_run = strcat(name,'_RUN.inp');
fid = fopen(name_run,'w');
fprintf(fid,'*Part,name=PART');
%fprintf(fid,part);
fprintf(fid,'\n*Node,input=');
fprintf(fid,'%s',name);
fprintf(fid,'_Nodes.inp');
fprintf(fid,'\n*Element,type=C3D10,input=');
fprintf(fid,'%s',name);
fprintf(fid,'_Elements.inp\n');
fprintf(fid,'*Elset, elset=Section-1, generate\n');
fprintf(fid,'1,');
fprintf(fid,'%.f',length(ele));
fprintf(fid,',1\n');
fprintf(fid,'*Nset,nset=TOP\n');%nset is defined by first node in set, last node in set,
increment between node numbers and set
p=1;
o=1
for p=1:length(top_set)%Repeat fprintf for top_set for number of nodes in set
    fprintf(fid,'%.f,',top_set(p,1));
    o = o+1;
    if o == 16
        fprintf(fid,'\n');
        o=0;
    end
end
fprintf(fid,'\n*Nset,nset=BTM\n');
p=1;
o=1
for p=1:length(btm_set)%Repeat fprintf for top_set for number of nodes in set
    fprintf(fid,'%.f,',btm_set(p,1));
    o = o+1;
    if o == 16
        fprintf(fid,'\n');
        o=0;
    end
end
fprintf(fid,'\n**Section: Section-1\n');
fprintf(fid,'*Solid Section, elset=Section-1, material=BONE');
fprintf(fid,'\n*End Part\n');
fprintf(fid,'**\n');
fprintf(fid,'**');
fprintf(fid,'\n**ASSEMBLY\n');
fprintf(fid,'**');
fprintf(fid,'\n*Assembly, name=Assembly\n');
fprintf(fid,'**');
fprintf(fid,'\n*Instance,name=PART-1,part=PART\n');
fprintf(fid,'*End Instance\n');
```

```
fprintf(fid,'**');
fprintf(fid,'\n*Node\n');%This defines the reference points
fprintf(fid,'%.f,%.4f,%.4f,%.4f\n',[1 centre_top]);%1st 'TOP' Reference Point Position
fprintf(fid,'%.f,%.4f,%.4f,%.4f\n',[2 centre_btm]);%2nd 'BTM' Reference Point Position
fprintf(fid,'*Nset, nset=_PickedSet6, internal\n');
fprintf(fid,' 1,\n');
fprintf(fid,'*Nset, nset=_PickedSet7, internal\n');
fprintf(fid,' 2,\n');
fprintf(fid,'*Nset, nset=_PickedSet8, internal\n');
fprintf(fid,' 2,\n');
fprintf(fid,'*Nset, nset=_PickedSet9, internal\n');
fprintf(fid,' 1,\n');
fprintf(fid,'** Constraint: BTM\n');
fprintf(fid,'*Rigid Body, ref node=_PickedSet7, tie nset=PART-1.BTM\n');
fprintf(fid,'** Constraint: TOP\n');
fprintf(fid,'*Rigid Body, ref node=_PickedSet6, tie nset=PART-1.TOP\n');
fprintf(fid,'*End Assembly\n');
fprintf(fid,'**MATERIALS\n');
fprintf(fid,'*Material, name=BONE');
fprintf(fid,'\n*Elastic, dependencies=1\n');
fprintf(fid,'1.,0.3, ,1.\n');%span the values of E
fprintf(fid,'6e5.,0.3, ,6e5.\n');
fprintf(fid,'**\n');
fprintf(fid,'** BOUNDARY CONDITIONS\n');
fprintf(fid,'**');
fprintf(fid,'\n** Name: BTM Type: Symmetry/Antisymmetry/Encastre\n');
fprintf(fid,'*Boundary\n');
fprintf(fid,'_PickedSet8, ENCASTRE\n');
fprintf(fid,'** ----------------------------------------------------------------\n');
fprintf(fid,'*INITIAL CONDITIONS, TYPE=FIELD, VARIABLE=1, INPUT=');
fprintf(fid,'%s',name,'_Modulus.inp');
fprintf(fid,'\n** ----------------------------------------------------------------\n');
fprintf(fid,'**\n ');
fprintf(fid,'** STEP: LOAD\n');
fprintf(fid,'**\n');
fprintf(fid,'*Step, name=LOAD, nlgeom=NO, inc=1000\n');
fprintf(fid,'*Static\n');
fprintf(fid,'0.1, 1., 1e-06, 1.\n');
fprintf(fid,'**\n');
fprintf(fid,'** BOUNDARY CONDITIONS\n');
fprintf(fid,'**\n');
fprintf(fid,'** Name: DISP Type: Displacement/Rotation\n');
fprintf(fid,'*Boundary\n');
fprintf(fid,'_PickedSet9, 1, 1\n');
fprintf(fid,'_PickedSet9, 2, 2\n');
fprintf(fid,'_PickedSet9, 3, 3,');
fprintf(fid,'%.4f\n',(-1)*disp);
fprintf(fid,'_PickedSet9, 4, 4\n');
fprintf(fid,'_PickedSet9, 5, 5\n');
fprintf(fid,'_PickedSet9, 6, 6\n');
fprintf(fid,'**\n');
fprintf(fid,'** OUTPUT REQUESTS\n');
fprintf(fid,'**\n');
fprintf(fid,'*Restart, write, frequency=0\n');
```

```
fprintf(fid,'**\n');
fprintf(fid,'** FIELD OUTPUT: F-Output-1\n');
fprintf(fid,'**\n');
fprintf(fid,'*Output, field, variable=PRESELECT\n');
fprintf(fid,'*Node Output\n');
fprintf(fid,'CF,RF,U\n');
fprintf(fid,'*Element Output, direction=YES\n');
fprintf(fid,'ELEDEN, ELEN, ENER, LE, PE, PEEQ, PEMAG,FV1, S\n');
fprintf(fid,'*Contact Output\n');
fprintf(fid,'CDISP, CSTRESS\n');
fprintf(fid,'**\n');
fprintf(fid,'** HISTORY OUTPUT: H-Output-1\n');
fprintf(fid,'**\n');
fprintf(fid,'*Output, history, variable=PRESELECT\n');
fprintf(fid,'*End Step');
fclose(fid);
```

B.3 Abaqus® Input File with Nodal Material Mapping to Whole-Bone Tetrahedral Meshes from QCT Data

This script requires a tetrahedral mesh that has been separated into node and element .txt files. A DICOM stack is also required with the mesh aligned to the CT coordinate system. A .txt with the surface nodes listed is required to determine partial volume effects. This can be generated using a node set within Abaqus.

```
clear
clc
close all

%%%%%%%%%%%%%%%%%%%%%%%%%%%%%%%%%%%%%%%%%%%%%%%%%%%%%%%%%%%%%%%%%%%%%%%%%%%%%%%%
%                                                                               %
%    This script assigns nodal material properties based on nodal               %
%   coordinates. Partial Volume effects are reduced as per Helgason             %
%   et. al. (2008), using the nearest internal node method. Code                %
%   uses functions ReadDicomStack and linear interp3 modified from              %
%         from Dr. Andrew Speirs, Carleton University.                          %
%     ©2016 Nikolas K Knowles, University of Western Ontario                    %
%                                                                               %
%%%%%%%%%%%%%%%%%%%%%%%%%%%%%%%%%%%%%%%%%%%%%%%%%%%%%%%%%%%%%%%%%%%%%%%%%%%%%%%%


%Load Text File of nodes

data = dlmread('L180375_TET_DVC_DRIVEN_NODE-HU_Nodes.inp');
nodes = data(:,2:4);
ele =  dlmread('L180375_TET_DVC_DRIVEN_NODE-HU_Elements.inp');
name = ('L180375_TET_DVC_DRIVEN_NODE-HU');
```

```
%Import Surface Nodes
nodes_surf_temp = dlmread('L180375_Surf_Nodes.inp');%Export
nodes_surf = reshape(nodes_surf_temp,[],1);%Format as column
nodes_surf = nodes_surf(nodes_surf>0);%remove zero caused by column reshaping
nodes_surf_xyz = [nodes_surf data(nodes_surf,2:4)];%Create array with surface nodes
#,x,y,z

%Import Internal Nodes
nodes_int = setdiff(data(:,1),nodes_surf);%Collect all nodes that are not on the surface
nodes_int_xyz = [nodes_int data(nodes_int,2:4)];%Create array with internal nodes #,x,y,z

%Load the DICOM images using the ReadDicomStack Function
%I is the intensity array in 512x512xSlice#

[I,info,A]=ReadDicomStack('D:\OneDrive - The University of Western Ontario\DVC Material
Mapping\L180375 DICOMS');

I = I - 1024;

sigma = 1.525709776;
beta = -18.56463983;

%low thresh (in HU)
lowthresh=-5;
a1 = 1;
b1 = 0;

%Middle Equation - Trabecular bone
a2 = 32790;
b2 = 2.307;

%High Equation - Cortical Bone
highthresh=673;
a3 = 10200;
b3 = 2.01;

continuousIndex=(A\[nodes';ones(1,size(nodes,1))])' +1;

%Interpolate CT, giving intensity values at each node - X, Y index is
%intentionally transposed to account for orientation of DICOM's - viewable
%with imshow(I(:,:,1), []),impixelinfo

int=interp3(I,continuousIndex(:,2),continuousIndex(:,1),continuousIndex(:,3),'*linear');%
Trilinear interpolation of the Native HU Scaler Field

int_min = min(I(:));%Check the minimum value of intensity

HU = int;

%Collect the native HU Values for surface and internal nodes with x,y,z
nodes_surf_all = [nodes_surf_xyz HU(nodes_surf)];
nodes_int_all = [nodes_int_xyz HU(nodes_int)];
```

```
node_search = dsearchn(nodes_int_all(:,2:4),nodes_surf_all(:,2:4));%This function
determines the closest internal (volume) node from the list of surface nodes

% Apply new HU values
i=1;
for i=1:length(node_search)%Loop through each indexed node
         node_search_idx = node_search(i,1);
            if nodes_int_all(node_search_idx,5) > nodes_surf_all(i,5)
                new_surf_node_HU(i,:) = [nodes_surf_all(i,1:4)
nodes_int_all(node_search_idx,5)];%Collect the new HU value for each surface node with
node #,X,Y,Z,HU
            else
                new_surf_node_HU(i,:) = [nodes_surf_all(i,1:5)];
    end
end

% Combine PVE Corrected HU values and apply Density & Modulus

new_node_HU = [new_surf_node_HU;nodes_int_all];%Combine the updated surface node HU, and
keep all original internal node HU
structured_node_HU = sortrows(new_node_HU,1);
new_HU = structured_node_HU(:,5);

%Calculate density using HU-betaCT/sigmaCT, calculated using linear
%regression

density_cal=((new_HU-(beta))/sigma)/1000; %{gK2HPO4/cc]

%Convert calibrated density to apparent or ash density (if required)

density_app = density_cal*2.192 + 0.007;%change to desired experimental relationship

density_ash = density_app*0.6; %As per Schileo et al. (2008)

x=1;

for x = 1:length(density_cal)%Change density type to desired relationship (ash, app, cal)

    if (new_HU(x) < lowthresh)
        E(x,:) = a1*((density_cal(x))^b1);
        density(x,:) = density_cal(x);

    elseif (new_HU(x) > lowthresh) && (new_HU(x) < highthresh)
        E(x,:) = a2*((density_cal(x))^b2);
        density(x,:) = density_cal(x);

    elseif (new_HU(x) > highthresh)
        E(x,:) = a3*((density_ash(x))^b3);
        density(x,:) = density_ash(x);

    end

end
```

```
%Set minimum modulus to 1 MPa

E(E<1)=1;

E_Field = [nodes(:,1:3) E];%Elements are built from gv file and each material is applied
to corresponding element

%Create Modulus.inp File for input

name_mod = strcat(name,'_Modulus_EQ1.inp');
fid2 = fopen(name_mod,'w');
q=1;
for q=1:length(E_Field)%Repeat fprintf for all nodes in model
    fprintf(fid2,'PART-1-1.');
    fprintf(fid2,'%.f',q);
    fprintf(fid2,',');
    fprintf(fid2,'%.f',E(q));
    fprintf(fid2,'\n');
end
fclose(fid2);
%Format and print file as inp for Abaqus
name_run = strcat(name,'_RUN_EQ1.inp');
fid = fopen(name_run,'w');
fprintf(fid,'*Part,name=PART');
%fprintf(fid,part);
fprintf(fid,'\n*Node,input=');
fprintf(fid,'%s',name);
fprintf(fid,'_Nodes.inp');
fprintf(fid,'\n*Element,type=C3D10,input=');
fprintf(fid,'%s',name);
fprintf(fid,'_Elements.inp\n');
fprintf(fid,'*INCLUDE,input=');%Input the DVC NSET File
fprintf(fid,'%s',name);
fprintf(fid,'_NSET.inp');
fprintf(fid,'\n*Elset, elset=Section-1, generate\n');
fprintf(fid,'1,');
fprintf(fid,'%.f',length(ele)+1);
fprintf(fid,',1\n');
fprintf(fid,'**Section: Section-1\n');
fprintf(fid,'*Solid Section, elset=Section-1, material=BONE');
fprintf(fid,'\n*End Part\n');
fprintf(fid,'**\n');
fprintf(fid,'**');
fprintf(fid,'\n**ASSEMBLY\n');
fprintf(fid,'**');
fprintf(fid,'\n*Assembly, name=Assembly\n');
fprintf(fid,'**');
fprintf(fid,'\n*Instance,name=PART-1-1,part=PART\n');
fprintf(fid,'-42.003,    -122.7832,     153.0863\n');%CHANGE THIS FOR EACH SPECIMEN
fprintf(fid,'-42.003,    -122.7832,     153.0863, -42.6651050324232, -122.051162981904,
153.246733069347, 149.85316770895,');
fprintf(fid,'\n*End Instance\n');
fprintf(fid,'**');
fprintf(fid,'\n*End Assembly\n');
```

```
fprintf(fid,'**MATERIALS\n');
fprintf(fid,'*Material, name=BONE');
fprintf(fid,'\n*Elastic, dependencies=1\n');
fprintf(fid,'1.,0.3, ,1.\n');%span the values of E
fprintf(fid,'%.f',max(E));
fprintf(fid, ',0.3, ,');
fprintf(fid,'%.f',max(E));
fprintf(fid,'\n**\n');
fprintf(fid,'** ----------------------------------------------------------------\n');
fprintf(fid,'*INITIAL CONDITIONS, TYPE=FIELD, VARIABLE=1, INPUT=');%Include the material
file for FV nodal assignment
fprintf(fid,'%s',name,'_Modulus_EQ1.inp');
fprintf(fid,'\n** ----------------------------------------------------------------\n');
fprintf(fid,'**\n ');
fprintf(fid,'** STEP: LOAD\n');
fprintf(fid,'**\n');
fprintf(fid,'*Step, name=LOAD, nlgeom=NO, inc=1000\n');
fprintf(fid,'*Static\n');
fprintf(fid,'0.1, 1., 1e-06, 1.\n');
fprintf(fid,'**\n');
fprintf(fid,'** BOUNDARY CONDITIONS\n');
fprintf(fid,'**');
fprintf(fid,'\n*INCLUDE,input=');%Input the BCs File
fprintf(fid,'%s',name);
fprintf(fid,'_BCs.inp');
fprintf(fid,'\n** OUTPUT REQUESTS\n');
fprintf(fid,'**\n');
fprintf(fid,'*Restart, write, frequency=0\n');
fprintf(fid,'**\n');
fprintf(fid,'** FIELD OUTPUT: F-Output-1\n');
fprintf(fid,'**\n');
fprintf(fid,'*Output, field, variable=PRESELECT\n');
fprintf(fid,'*Node Output\n');
fprintf(fid,'CF,RF,U\n');
fprintf(fid,'*Element Output, direction=YES\n');
fprintf(fid,'ELEDEN, ELEN, ENER, LE, PE, PEEQ, PEMAG,FV1, S\n');
fprintf(fid,'*Contact Output\n');
fprintf(fid,'CDISP, CSTRESS\n');
fprintf(fid,'**\n');
fprintf(fid,'** HISTORY OUTPUT: H-Output-1\n');
fprintf(fid,'**\n');
fprintf(fid,'*Output, history, variable=PRESELECT\n');
fprintf(fid,'*End Step');
fclose(fid);
```

B.4 Abaqus® Input File with Homogeneous Material Properties from Hexahedral MicroCT Data

This code generates the Abaqus® input file with uniform boundary conditions, loads/displacements, steps, and outputs for microFEMs generated with homogeneous

tissue modulus. The inputs are node and element separated .inp files generated with the code described in Faieghi et al. 2019.

```
clear
clc

%%%%%%%%%%%%%%%%%%%%%%%%%%%%%%%%%%%%%%%%%%%%%%%%%%%%%%%%%%%%%%%%%%%%%%%%%%%%%%%
%                                                                              %
%    This code creates the BC's, Contraints, Load/Disp, Step(s),& RF's         %
%    generating the Abaqus input file for linear compression analysis          %
%       The code prompts for desired displacement and specimen ID              %
%        ©2017 Nikolas K Knowles, University of Western Ontario                %
%                                                                              %
%%%%%%%%%%%%%%%%%%%%%%%%%%%%%%%%%%%%%%%%%%%%%%%%%%%%%%%%%%%%%%%%%%%%%%%%%%%%%%%

%Load Text File of nodes from Hex Generator (Faieghi et al. 2019)

prompt2 = 'What is the file name?';
name = input(prompt2,'s');
name_nodes = strcat(name,'_Nodes.inp');
name_elements = strcat(name,'_Elements.inp');

data = dlmread(name_nodes);%read nodes
nodes = data(:,1:4);%x,y,z of nodes

elements = dlmread(name_elements);%read element. To be able to collect all nodes for
element set in material definition

prompt = 'What is the desired displacement value (0.5% strain)?';
disp = input(prompt,'s');

%Create Node sets for Top (max z) and Btm(min z)

btm_z = min(nodes(:,4));
top_z = max(nodes(:,4));

j=1;
n=1;
m=1;
for j=1:length(nodes)
    if nodes(j,4) == top_z
        top_set(n,:) = nodes(j,:);
        n=n+1;
    elseif nodes(j,4) == btm_z
        btm_set(m,:) = nodes(j,:);
        m=m+1;
    end
end

%Define the spacing for the nset. Reza's nodes are non-incrementally
%spaced, so format node sets for complete list of nodes in set
top_set_form = top_set(:,1);
```

```
btm_set_form = btm_set(:,1);

%Define Reference Points for Centre of Top and Btm
centre_top = min(top_set(:,2:4))/2 + max(top_set(:,2:4))/2;%Top Reference Point
centre_btm = min(btm_set(:,2:4))/2 + max(btm_set(:,2:4))/2;%Btm Reference Point

figure(1)
scatter3(top_set(:,2),top_set(:,3),top_set(:,4))
view([0 90])
pbaspect([1 1 1])

figure(2)
scatter3(btm_set(:,2),btm_set(:,3),btm_set(:,4))
view([0 90])
pbaspect([1 1 1])

%Format and print file as inp for Abaqus
name_run = strcat(name,'_RUN.inp');
fid = fopen(name_run,'w');
fprintf(fid,'*Part,name=PART');
%fprintf(fid,part);
fprintf(fid,'\n*Node,input=');
fprintf(fid,'%s',name);
fprintf(fid,'_Nodes.inp');
fprintf(fid,'\n*Element,type=C3D8,input=');
fprintf(fid,'%s',name);
fprintf(fid,'_Elements.inp');
fprintf(fid,'\n*Nset,nset=TOP\n');
fprintf(fid,'%.f,%.f,%.f,%.f,%.f,%.f,%.f,%.f,%.f,%.f\n',top_set_form);
%nset is defined by first node in set, last node in set, increment between node numbers
and set
fprintf(fid,'\n*Nset,nset=BTM\n');
fprintf(fid,'%.f,%.f,%.f,%.f,%.f,%.f,%.f,%.f,%.f,%.f\n',btm_set_form);
fprintf(fid,'\n*Elset, elset=_PickedSet4, internal, generate\n');%Create element set for
all elements, for material definition
fprintf(fid,'1,');
fprintf(fid,'%.f',length(elements));
fprintf(fid,',1');
fprintf(fid,'\n*Solid Section, elset=_PickedSet4, material=BONE');
fprintf('\n,');
fprintf(fid,'\n*End Part\n');
fprintf(fid,'**\n');
fprintf(fid,'**');
fprintf(fid,'\n**ASSEMBLY\n');
fprintf(fid,'**');
fprintf(fid,'\n*Assembly, name=Assembly\n');
fprintf(fid,'**');
fprintf(fid,'\n*Instance,name=PART-1,part=PART\n');
fprintf(fid,'*End Instance\n');
fprintf(fid,'**');
fprintf(fid,'\n*Node\n');%This defines the reference points
fprintf(fid,'%.f,%.4f,%.4f,%.4f\n',[1 centre_top]);%1st 'TOP' Reference Point Position
fprintf(fid,'%.f,%.4f,%.4f,%.4f\n',[2 centre_btm]);%2nd 'BTM' Reference Point Position
fprintf(fid,'*Nset, nset=_PickedSet6, internal\n');
```

```
fprintf(fid,' 1,\n');
fprintf(fid,'*Nset, nset=_PickedSet7, internal\n');
fprintf(fid,' 2,\n');
fprintf(fid,'*Nset, nset=_PickedSet8, internal\n');
fprintf(fid,' 2,\n');
fprintf(fid,'*Nset, nset=_PickedSet9, internal\n');
fprintf(fid,' 1,\n');
fprintf(fid,'** Constraint: BTM\n');
fprintf(fid,'*Rigid Body, ref node=_PickedSet7, tie nset=PART-1.BTM\n');
fprintf(fid,'** Constraint: TOP\n');
fprintf(fid,'*Rigid Body, ref node=_PickedSet6, tie nset=PART-1.TOP\n');
fprintf(fid,'*End Assembly\n');
fprintf(fid,'**\n');
fprintf(fid,'** MATERIALS');
fprintf(fid,'\n**\n');
fprintf(fid,'*Material, name=BONE');
fprintf(fid,'\n*Elastic');
fprintf(fid,'\n1000., 0.3');
fprintf(fid,'\n**\n');
fprintf(fid,'** BOUNDARY CONDITIONS\n');
fprintf(fid,'**');
fprintf(fid,'\n** Name: BTM Type: Symmetry/Antisymmetry/Encastre\n');
fprintf(fid,'*Boundary\n');
fprintf(fid,'_PickedSet8, ENCASTRE\n');
fprintf(fid,'** ----------------------------------------------------------------\n');
fprintf(fid,'**\n ');
fprintf(fid,'** STEP: LOAD\n');
fprintf(fid,'**\n');
fprintf(fid,'*Step, name=LOAD, nlgeom=NO, inc=1000\n');
fprintf(fid,'*Static\n');
fprintf(fid,'0.5, 1., 1e-06, 1.\n');
fprintf(fid,'**\n');
fprintf(fid,'** BOUNDARY CONDITIONS\n');
fprintf(fid,'**\n');
fprintf(fid,'** Name: DISP Type: Displacement/Rotation\n');
fprintf(fid,'*Boundary\n');
fprintf(fid,'_PickedSet9, 1, 1\n');
fprintf(fid,'_PickedSet9, 2, 2\n');
fprintf(fid,'_PickedSet9, 3, 3,');
fprintf(fid,'%.4f\n',(-1)*disp);
fprintf(fid,'_PickedSet9, 4, 4\n');
fprintf(fid,'_PickedSet9, 5, 5\n');
fprintf(fid,'_PickedSet9, 6, 6\n');
fprintf(fid,'**\n');
fprintf(fid,'** OUTPUT REQUESTS\n');
fprintf(fid,'**\n');
fprintf(fid,'*Restart, write, frequency=0\n');
fprintf(fid,'**\n');
fprintf(fid,'** FIELD OUTPUT: F-Output-1\n');
fprintf(fid,'**\n');
fprintf(fid,'*Output, field, variable=PRESELECT\n');
fprintf(fid,'*Node Output\n');
fprintf(fid,'CF,RF,U\n');
fprintf(fid,'*Element Output, direction=YES\n');
```

```
fprintf(fid,'ELEDEN, ELEN, ENER, LE, PE, PEEQ, PEMAG, S\n');
fprintf(fid,'*Contact Output\n');
fprintf(fid,'CDISP, CSTRESS\n');
fprintf(fid,'**\n');
fprintf(fid,'** HISTORY OUTPUT: H-Output-1\n');
fprintf(fid,'**\n');
fprintf(fid,'*Output, history, variable=PRESELECT\n');
fprintf(fid,'*End Step');
fclose(fid);
```

B.5 Abaqus® Input File with Heterogeneous Material Properties from Hexahedral MicroCT Data

This code generates the Abaqus® input file with uniform boundary conditions, loads/displacements, steps, and outputs for microFEMs generated with heterogeneous tissue modulus. The inputs are node, element, elsets, and materials separated .inp files generated with the code described in Faieghi et al. 2019.

```
clear
clc

%%%%%%%%%%%%%%%%%%%%%%%%%%%%%%%%%%%%%%%%%%%%%%%%%%%%%%%%%%%%%%%%%%%%%%%%%%%%%%%
%                                                                              %
%    This code creates the BC's, Contraints, Load/Disp, Step(s),& RF's         %
%    generating the Abaqus input file for linear compression analysis          %
%       The code prompts for desired displacement and specimen ID              %
%        ©2017 Nikolas K Knowles, University of Western Ontario                %
%                                                                              %
%%%%%%%%%%%%%%%%%%%%%%%%%%%%%%%%%%%%%%%%%%%%%%%%%%%%%%%%%%%%%%%%%%%%%%%%%%%%%%%

%Load Text File of nodes from Reza's Hex Generator

prompt2 = 'What is the file name?';
name = input(prompt2,'s');
name_nodes = strcat(name,'_Nodes_HETEROGENEOUS.inp');
name_elements = strcat(name,'_Elements_HETEROGENEOUS.inp');

data = dlmread(name_nodes);%read nodes
nodes = data(:,1:4);%x,y,z of nodes

elements = dlmread(name_elements);%read element. To be able to collect all nodes for
element set in material definition

prompt = 'What is the desired displacement value (0.5% strain)?';
disp = input(prompt,'s');

%Create Node sets for Top (max z) and Btm(min z)

btm_z = min(nodes(:,4));
```

```
top_z = max(nodes(:,4));

j=1;
n=1;
m=1;
for j=1:length(nodes)
    if nodes(j,4) == top_z
        top_set(n,:) = nodes(j,:);
        n=n+1;
    elseif nodes(j,4) == btm_z
        btm_set(m,:) = nodes(j,:);
        m=m+1;
    end
end

%Define the spacing for the nset. Reza's nodes are non-incrementally
%spaced, so format node sets for complete list of nodes in set
top_set_form = top_set(:,1);
btm_set_form = btm_set(:,1);

%Define Reference Points for Centre of Top and Btm
centre_top = min(top_set(:,2:4))/2 + max(top_set(:,2:4))/2;%Top Reference Point
centre_btm = min(btm_set(:,2:4))/2 + max(btm_set(:,2:4))/2;%Btm Reference Point

figure(1)
scatter3(top_set(:,2),top_set(:,3),top_set(:,4))
view([0 90])
pbaspect([1 1 1])

figure(2)
scatter3(btm_set(:,2),btm_set(:,3),btm_set(:,4))
view([0 90])
pbaspect([1 1 1])

%Format and print file as inp for Abaqus
name_run = strcat(name,'_RUN_HETEROGENEOUS.inp');
fid = fopen(name_run,'w');
fprintf(fid,'*Part,name=PART');
%fprintf(fid,part);
fprintf(fid,'\n*Node,input=');
fprintf(fid,'%s',name);
fprintf(fid,'_Nodes_HETEROGENEOUS.inp');
fprintf(fid,'\n*Element,type=C3D8,input=');
fprintf(fid,'%s',name);
fprintf(fid,'_Elements_HETEROGENEOUS.inp');
fprintf(fid,'\n*Nset,nset=TOP\n');
fprintf(fid,'%.f,%.f,%.f,%.f,%.f,%.f,%.f,%.f,%.f,%.f\n',top_set_form);
%nset is defined by first node in set, last node in set, increment between node numbers
and set
fprintf(fid,'\n\n*Nset,nset=BTM\n');
fprintf(fid,'%.f,%.f,%.f,%.f,%.f,%.f,%.f,%.f,%.f,%.f\n',btm_set_form);
fprintf(fid,'\n*Include,input=');
fprintf(fid,'%s',name);
fprintf(fid,'_Elsets_HETEROGENEOUS.inp');
```

```
fprintf('\n,');
fprintf(fid,'\n*End Part\n');
fprintf(fid,'**\n');
fprintf(fid,'**');
fprintf(fid,'\n**ASSEMBLY\n');
fprintf(fid,'**');
fprintf(fid,'\n*Assembly, name=Assembly\n');
fprintf(fid,'**');
fprintf(fid,'\n*Instance,name=PART-1,part=PART\n');
fprintf(fid,'*End Instance\n');
fprintf(fid,'**');
fprintf(fid,'\n*Node\n');%This defines the reference points
fprintf(fid,'%.f,%.4f,%.4f,%.4f\n',[1 centre_top]);%1st 'TOP' Reference Point Position
fprintf(fid,'%.f,%.4f,%.4f,%.4f\n',[2 centre_btm]);%2nd 'BTM' Reference Point Position
fprintf(fid,'*Nset, nset=_PickedSet6, internal\n');
fprintf(fid,' 1,\n');
fprintf(fid,'*Nset, nset=_PickedSet7, internal\n');
fprintf(fid,' 2,\n');
fprintf(fid,'*Nset, nset=_PickedSet8, internal\n');
fprintf(fid,' 2,\n');
fprintf(fid,'*Nset, nset=_PickedSet9, internal\n');
fprintf(fid,' 1,\n');
fprintf(fid,'** Constraint: BTM\n');
fprintf(fid,'*Rigid Body, ref node=_PickedSet7, tie nset=PART-1.BTM\n');
fprintf(fid,'** Constraint: TOP\n');
fprintf(fid,'*Rigid Body, ref node=_PickedSet6, tie nset=PART-1.TOP\n');
fprintf(fid,'*End Assembly\n');
fprintf(fid,'**\n');
fprintf(fid,'** MATERIALS');
fprintf(fid,'\n**\n');
fprintf(fid,'*Include,input=');
fprintf(fid,'%s',name);
fprintf(fid,'_Materials_HETEROGENEOUS.inp');
fprintf(fid,'\n**\n');
fprintf(fid,'** BOUNDARY CONDITIONS\n');
fprintf(fid,'**');
fprintf(fid,'\n** Name: BTM Type: Symmetry/Antisymmetry/Encastre\n');
fprintf(fid,'*Boundary\n');
fprintf(fid,'_PickedSet8, ENCASTRE\n');
fprintf(fid,'** ----------------------------------------------------------------\n');
fprintf(fid,'**\n ');
fprintf(fid,'** STEP: LOAD\n');
fprintf(fid,'**\n');
fprintf(fid,'*Step, name=LOAD, nlgeom=NO, inc=1000\n');
fprintf(fid,'*Static\n');
fprintf(fid,'0.5, 1., 1e-06, 1.\n');
fprintf(fid,'**\n');
fprintf(fid,'** BOUNDARY CONDITIONS\n');
fprintf(fid,'**\n');
fprintf(fid,'** Name: DISP Type: Displacement/Rotation\n');
fprintf(fid,'*Boundary\n');
fprintf(fid,'_PickedSet9, 1, 1\n');
fprintf(fid,'_PickedSet9, 2, 2\n');
fprintf(fid,'_PickedSet9, 3, 3,');
```

```
fprintf(fid,'%.4f\n',(-1)*disp);
fprintf(fid,'_PickedSet9, 4, 4\n');
fprintf(fid,'_PickedSet9, 5, 5\n');
fprintf(fid,'_PickedSet9, 6, 6\n');
fprintf(fid,'**\n');
fprintf(fid,'** OUTPUT REQUESTS\n');
fprintf(fid,'**\n');
fprintf(fid,'*Restart, write, frequency=0\n');
fprintf(fid,'**\n');
fprintf(fid,'** FIELD OUTPUT: F-Output-1\n');
fprintf(fid,'**\n');
fprintf(fid,'*Output, field, variable=PRESELECT\n');
fprintf(fid,'*Node Output\n');
fprintf(fid,'CF,RF,U\n');
fprintf(fid,'*Element Output, direction=YES\n');
fprintf(fid,'ELEDEN, ELEN, ENER, LE, PE, PEEQ, PEMAG, S\n');
fprintf(fid,'*Contact Output\n');
fprintf(fid,'CDISP, CSTRESS\n');
fprintf(fid,'**\n');
fprintf(fid,'** HISTORY OUTPUT: H-Output-1\n');
fprintf(fid,'**\n');
fprintf(fid,'*Output, history, variable=PRESELECT\n');
fprintf(fid,'*End Step');
fclose(fid);
```

APPENDIX C – COPYRIGHT RELEASES

SPRINGER NATURE LICENSE
TERMS AND CONDITIONS

Feb 21, 2019

This Agreement between ("You") and Springer Nature ("Springer Nature") consists of your license details and the terms and conditions provided by Springer Nature and Copyright Clearance Center.

License Number	4524300125262
License date	Feb 08, 2019
Licensed Content Publisher	Springer Nature
Licensed Content Publication	Springer eBook
Licensed Content Title	Micro-Computed Tomography: A Method for the Non-Destructive Evaluation of the Three-Dimensional Structure of Biological Specimens
Licensed Content Author	Martin Stauber, Ralph Müller
Licensed Content Date	Jan 1, 2008
Type of Use	Thesis/Dissertation
Requestor type	academic/university or research institute
Format	print and electronic
Portion	figures/tables/illustrations
Number of figures/tables/illustrations	1
Will you be translating?	no
Circulation/distribution	<501
Author of this Springer Nature content	no
Title	Improving Material Mapping in Glenohumeral Finite Element Models: A Multi-Level Evaluation
Institution name	The University of Western Ontario
Expected presentation date	Apr 2019
Portions	Figure 19.1
Requestor Location	
Billing Type	Invoice
Billing Address	
Total	0.00 CAD
Terms and Conditions	

JOHN WILEY AND SONS LICENSE
TERMS AND CONDITIONS

Feb 21, 2019

This Agreement between 650 Santa Monica Rd ("You") and John Wiley and Sons ("John Wiley and Sons") consists of your license details and the terms and conditions provided by John Wiley and Sons and Copyright Clearance Center.

License Number	4524300436457
License date	Feb 08, 2019
Licensed Content Publisher	John Wiley and Sons
Licensed Content Publication	Journal of Bone and Mineral Research
Licensed Content Title	Guidelines for assessment of bone microstructure in rodents using micro–computed tomography
Licensed Content Author	Mary L Bouxsein, Steven K Boyd, Blaine A Christiansen, et al
Licensed Content Date	Jun 30, 2010
Licensed Content Volume	25
Licensed Content Issue	7
Licensed Content Pages	19
Type of Use	Dissertation/Thesis
Requestor type	University/Academic
Format	Print and electronic
Portion	Figure/table
Number of figures/tables	1
Original Wiley figure/table number(s)	Fig. 6
Will you be translating?	No
Title of your thesis / dissertation	Improving Material Mapping in Glenohumeral Finite Element Models: A Multi-Level Evaluation
Expected completion date	Apr 2019
Expected size (number of pages)	1
Requestor Location	

Publisher Tax ID	EU826007151
Total	**0.00 CAD**

Terms and Conditions

SPRINGER NATURE LICENSE
TERMS AND CONDITIONS

Feb 21, 2019

This Agreement between 650 Santa Monica Rd ("You") and Springer Nature ("Springer Nature") consists of your license details and the terms and conditions provided by Springer Nature and Copyright Clearance Center.

License Number	4521290775072
License date	Feb 03, 2019
Licensed Content Publisher	Springer Nature
Licensed Content Publication	Annals of Biomedical Engineering
Licensed Content Title	The Effect of Material Heterogeneity, Element Type, and Down-Sampling on Trabecular Stiffness in Micro Finite Element Models
Licensed Content Author	Nikolas K. Knowles, Kenneth Ip, Louis M. Ferreira
Licensed Content Date	Jan 1, 2018
Licensed Content Volume	47
Licensed Content Issue	2
Type of Use	Thesis/Dissertation
Requestor type	academic/university or research institute
Format	print and electronic
Portion	full article/chapter
Will you be translating?	no
Circulation/distribution	<501
Author of this Springer Nature content	yes
Title	Improving Material Mapping in Glenohumeral Finite Element Models: A Multi-Level Evaluation
Institution name	The University of Western Ontario
Expected presentation date	Apr 2019
Requestor Location	
Billing Type	Invoice

Billing Address

Total 0.00 CAD

APPENDIX D – ETHICS APPROVALS

Western Research

Research Ethics

Western University Health Science Research Ethics Board
HSREB Annual Continuing Ethics Approval Notice

Date: February 01, 2016
Principal Investigator: Dr. George Athwal
Department & Institution: Schulich School of Medicine and Dentistry\Surgery,St. Joseph's Health Care London

Review Type: Expedited
HSREB File Number: 105912
Study Title: Morphological and finite element analysis of the normal and osteoarthritic glenohumeral joint.
Sponsor:

HSREB Renewal Due Date & HSREB Expiry Date:
Renewal Due -2017/01/31
Expiry Date -2017/02/12

The Western University Health Science Research Ethics Board (HSREB) has reviewed the Continuing Ethics Review (CER) Form and is re-issuing approval for the above noted study.

The Western University HSREB operates in compliance with the Tri-Council Policy Statement Ethical Conduct for Research Involving Humans (TCPS2), the International Conference on Harmonization of Technical Requirements for Registration of Pharmaceuticals for Human Use Guideline for Good Clinical Practice (ICH E6 R1), the Ontario Freedom of Information and Protection of Privacy Act (FIPPA, 1990), the Ontario Personal Health Information Protection Act (PHIPA, 2004), Part 4 of the Natural Health Product Regulations, Health Canada Medical Device Regulations and Part C, Division 5, of the Food and Drug Regulations of Health Canada.

Members of the HSREB who are named as Investigators in research studies do not participate in discussions related to, nor vote on such studies when they are presented to the REB.

The HSREB is registered with the U.S. Department of Health & Human Services under the IRB registration number IRB 00000940.

Ethics Officer, on behalf of Dr. Joseph Gilbert, HSREB Chair

Ethics Officer to Contact for Further Information: Erika Basile ___ Nicole Kaniki ___ Grace Kelly ___ Mina Mekhail ___ Vikki Tran ___

This is an official document. Please retain the original in your files

Western Research

Date: 27 February 2019

To: Dr. George Athwal

Project ID: 113023

Study Title: Mechanical Testing and Imaging of Osteotomized Humeral Bone

Application Type: HSREB Initial Application

Review Type: Delegate

Full Board Reporting Date: 12March2019

Date Approval Issued: 27/Feb/2019 10:55

REB Approval Expiry Date: 27/Feb/2020

Dear Dr. George Athwal

The Western University Health Science Research Ethics Board (HSREB) has reviewed and approved the above mentioned study as described in the WREM application form, as of the HSREB Initial Approval Date noted above. This research study is to be conducted by the investigator noted above. All other required institutional approvals must also be obtained prior to the conduct of the study.

Documents Approved:

Document Name	Document Type	Document Date	Document Version
general surgical consent	Written Consent/Assent	05/Jan/2017	Jan5/2017
Patient LOI and consent_Feb 22_CLEAN	Written Consent/Assent	22/Feb/2019	Feb22
Variable List_Jan 16	Other Data Collection Instruments	16/Jan/2019	Jan16

No deviations from, or changes to, the protocol or WREM application should be initiated without prior written approval of an appropriate amendment from Western HSREB , except when necessary to eliminate immediate hazard(s) to study participants or when the change(s) involves only administrative or logistical aspects of the trial.

REB members involved in the research project do not participate in the review, discussion or decision.

The Western University HSREB operates in compliance with, and is constituted in accordance with, the requirements of the TriCouncil Policy Statement: Ethical Conduct for Research Involving Humans (TCPS 2); the International Conference on Harmonisation Good Clinical Practice Consolidated Guideline (ICH GCP); Part C, Division 5 of the Food and Drug Regulations; Part 4 of the Natural Health Products Regulations; Part 3 of the Medical Devices Regulations and the provisions of the Ontario Personal Health Information Protection Act (PHIPA 2004) and its applicable regulations. The HSREB is registered with the U.S. Department of Health & Human Services under the IRB registration number IRB 00000940.

Please do not hesitate to contact us if you have any questions.

Sincerely,

Nicola Geoghegan-Morphet, Ethics Officer on behalf of Dr. Philip Jones, HSREB Vice-Chair

Note: This correspondence includes an electronic signature (validation and approval via an online system that is compliant with all regulations).

Curriculum Vitae

Nikolas Kelton Knowles, BEng, MESc, EIT

PhD Candidate

Biomedical Engineering Graduate Program – Biomechanics
Collaborative Training Program in Musculoskeletal Health Research
The University of Western Ontario

EDUCATION

Doctor of Philosophy (PhD), Biomedical Engineering – Biomechanics with Musculoskeletal Health Research 2015 – present
Biomedical Engineering Graduate Program, The University of Western Ontario, London, Ontario

- Awarded NSERC Alexander Graham Bell Canada Graduate Scholarship (CGS-D3), CMHR Transdisciplinary Bone & Joint Training Award & Ontario Graduate Scholarship (OGS)

Advanced Certificate in Curriculum, Teaching, and Learning in Science, Technology, Engineering, and Mathematics (STEM) Disciplines 2016 – 2017
Faculty of Education, The University of Western Ontario, London, Ontario

- Applied curriculum history and theory in the development of biomedical engineering course modules and generalized engineering curriculum

Master of Engineering Science (MESc), Mechanical Engineering with Musculoskeletal Health Research 2013 – 2015
Department of Mechanical and Materials Engineering, The University of Western Ontario, London, Ontario
Thesis Title: Osteoarthritis Induced Glenoid Morphology and Bone Quality: An Evaluation of Augmented Glenoid Components

- Awarded *CIHR JuMP Fellowship in Musculoskeletal Health Research*

Bachelor of Engineering (BEng), Biomedical and Mechanical Engineering 2009 – 2013
Department of Mechanical and Aerospace Engineering, Carleton University, Ottawa, Ontario

Ontario College Advanced Diploma, Mechanical Engineering Technology 2006 – 2009
School of Advanced Technology, Algonquin College, Ottawa, Ontario

Ontario College Certificate, General Arts and Science – General Studies 2005
Fanshawe College, Ottawa, Ontario

RELEVENT WORK EXPERIENCE

Research Assistant, Orthopaedic Research 2012 – present
Roth|McFarlane Hand and Upper Limb Centre, St. Josephs Health Care, London, ON

PROFESSIONAL DEVELOPMENT

Health Systems Structure and Trends 2017
Ivey Centre for Health Innovation, Richard Ivey School of Business, The University of Western Ontario, London, ON

Small & Medium Enterprises – Building the Case for Commercialization Venture Capitalism Investment 2017
Ivey Centre for Health Innovation, Richard Ivey School of Business, The University of Western Ontario, London, ON

Introduction to Venture Capital 2017
Ivey Centre for Health Innovation, Richard Ivey School of Business, The University of Western Ontario, London, ON

Health Economics and Design Logic 2017
Ivey Centre for Health Innovation, Richard Ivey School of Business, The University of Western Ontario, London, ON

Micro-Computed Tomography Scanner Training – Nikon XT H 225 ST 2016
The University of Western Ontario, London, ON

Simulia Abaqus Finite Element Software Training – Modeling Fracture & Failure 2016

MEMBERSHIPS

Orthopaedic Research Society (ORS) – Associate Member 2015 – present
Professional Engineers of Ontario (PEO) – Engineer in Training (EIT) 2013 – present
American Society of Mechanical Engineers (ASME) – Bioengineering Division 2011 – present

TEACHING EXPERIENCE

Western Biomedical Engineering Undergraduate Program
The University of Western Ontario, London, Ontario

- **Course Development** 2019
  - Co-developed curriculum for undergraduate course: Fundamentals of Biomedical Engineering Design (BME 3201)

Department of Mechanical and Materials Engineering
The University of Western Ontario, London, Ontario

- **Assistant Professor – Limited Duties Teaching Appointment** 2018
  Developed course material, developed and delivered lectures, developed assignments, quizzes, midterms and final exams for first year undergraduate class (ES 1021 – Properties of Materials; Course Enrollment: 263).

- **Teaching Assistant** 2013 – present
  - Courses: Advanced Research Translation for Biomedical Engineers (BIOMED 9650), Engineering Communications (ENGSCI 9670 & ENGSCI 2211), Materials Selection (MME 3379), Engineering Dynamics (MME 2213), Introductory Design and Innovation Studio (ES 1050), Robotics and Manufacturing Automation (MME 4452), and Product Design and Development (MME 2256)
- **Western Engineering Summer Academy Instructor** 2014 & 2015
  - Duties: developing course material in mechanical and biomedical engineering, structuring learning activities, facilitating student involvement

Collaborative Training Program in Musculoskeletal Health Research,
The University of Western Ontario, London, Ontario

- **Invited Lecturer** 2017
  - Developed course module (mechanical properties of MSK tissues and implants), instructed graduate students from multi-disciplinary backgrounds, moderated student debate presentations, and assessed students (MSK 9000 – Musculoskeletal Health Research A: Biomedical and Bioengineering Concepts (Course Enrollment: 27).

Biomedical Engineering Graduate Program
The University of Western Ontario, London, Ontario

- **Guest Judge** 2017
  - Evaluated biomedical engineering graduate students during e-poster presentations for Principles of Communications & Knowledge (BIOMED 9550)

Department of Mechanical and Aerospace Engineering
Carleton University, Ottawa, Ontario

- **Peer Assisted Study Session Facilitator** 2012
  - Duties: developing all course material for third year engineering study sessions, structured active learning modules for a variety of learning styles

ACADEMIC SERVICE

Academic Institutes

Bone and Joint Institute Strategic Planning, *The University of Western Ontario* 2017

Conferences

Novel Orthopaedic Devices Session Chair, *Canadian Bone and Joint Conference, London, ON* 2016

Committees

The University of Western Ontario

Faculty of Engineering First Year Operating Committee 2018
Bone and Joint Institute Trainee Leadership Committee – Chair 2017 – 2018
Bone and Joint Institute Governing Board – Trainee Representative 2017 – present
Bone and Joint Institute Teaching and Education Committee Trainee Representative 2015 – present
Society of Graduate Students Policy Committee – Member 2014 – 2017
Mechanical and Materials Engineering Graduate Student Society President 2014 – 2015

Mechanical and Materials Engineering Department Council Graduate Student Representative — 2014 – 2015

LEADERSHIP/MENTORSHIP EXPERIENCE

Advisory Committee

Emily West, MESc Candidate, Biomedical Engineering Graduate Program — 2015 – 2017
The University of Western Ontario, London, ON

Corey Smith, MESc Candidate, Biomedical Engineering Graduate Program — 2015 – 2017
The University of Western Ontario, London, ON

Informal Mentorship

- Five Masters students, and 2 undergraduate students
- Co-supervised 4 high-school cooperative education students
- Collaborated with 7 surgical fellows, and 1 surgical resident

PEER REVIEW ACTIVITIES

International Journal of Mechanical Engineering Education (n=1)	2019 – present
Medical Engineering & Physics (n=1)	2018 – present
Medical & Biological Engineering and Computing (n=1)	2017 – present
Journal of Orthopaedic Surgery and Research (n=10)	2016 – present
Simulation: Transactions of the Society for Modeling and Simulation International (n=1)	2016
Journal of Shoulder and Elbow Surgery (n=4)	2014 – present

SCHOLARSHIPS, AWARDS, & HONOURS

Ontario Graduate Scholarship (OGS) *Ontario Ministry of Advanced Education and Skills Development*	$15,000	2018 – 2019
CMHR Transdisciplinary Bone and Joint Training Award *The University of Western Ontario, London, ON*	$20,000	2015 – 2019
Collaborative Training Program in Musculoskeletal Health Research (CMHR)	$3,000	2015 – 2019
Western Graduate Research Scholarship *The University of Western Ontario, London, ON*	$35,000	2015 – 2019
Western Doctoral Excellence Research *The University of Western Ontario, London, ON*	$16,666	2015 – 2018
Alexander Graham Bell Canada Graduate Scholarship – Doctoral (CGS-D3) *Natural Sciences and Engineering Research Council*	$105,000	2015 – 2018
Ontario Graduate Scholarship (OGS) - (Declined) *Ontario Ministry of Advanced Education and Skills Development*	$15,000	2015 – 2016
Academic Achievement Award *PSAC610, The University of Western Ontario, London, ON*	$500	2015
Dr. Suzanne Bernier Memorial Award in Skeletal *The University of Western Ontario, London, ON*	$3,000	2015
1st Place Poster, Shoulder and Elbow Classification *American Academy of Orthopaedic Surgeons (AAOS) Annual Meeting, Las Vegas, NV*		2015

Featured Article, Quantification of the Position, Orientation and Surface Area of Posterior Bone Loss in Type B2 Glenoids The Journal of Shoulder and Elbow Surgery 24(4) issue		2015
Joint Motion Program (JuMP) CIHR Fellowship in Musculoskeletal Health Research and Leadership *The University of Western Ontario, London, ON*	$27,000	2013 – 2015
Western Graduate Research Scholarship *The University of Western Ontario, London, ON*	$11,500	2013 – 2015
Dean's Honour List *Carleton University, Ottawa, ON*		2013
Western Engineering Summer Research Award (WESRA) *The University of Western Ontario, London, ON*	$5,600	2012
Academic Scholarship *Carleton University, Ottawa, ON*	**$**2,000	2011
Dean's Honour List *Carleton University, Ottawa, ON*		2011
Sprott Scholarship *Carleton University, Ottawa, ON*	$2,500	2010
Academic Scholarship *Carleton University, Ottawa, ON*	**$**2,000	2009
Alstom Power Canada Inc. Award	$150	2009
Ontario International Education Opportunity Scholarship (OIEOS) *ICSAT, Faridabad, India & Algonquin College, Ottawa, ON*	$2,500	2008
Lanxess Higher Education Scholarship	$8,000	2008

RESEARCH GRANTS

Lawson Internal Research Fund – Pilot Study Dr. Louis Ferreira, Dr. George Athwal, Dr. Daniel Langohr, Nikolas Knowles *Development and Validation of Computational Models for Glenohumeral Joint Simulations*	$15,000	2015 – 2017
Western Bone and Joint Institute Catalyst Grant Dr. Louis Ferreira, Dr. George Athwal, Nikolas Knowles *Development and Validation of Patient-Specific 3D-Printed Bone Models with Heterogeneous Bone Density Distributions for Implant Design and Surgical Evaluation*	$15,000	2015 – 2016

PUBLICATIONS

Peer Reviewed Publications
Published/Accepted (n=23)

Knowles NK, Langohr GDG, Faieghi M, Nelson A, Ferreira LM. A Comparison of Density-Modulus Relationships Used in Finite Element Modeling of the Shoulder. Medical Engineering and Physics. 2019; 66:40-46

Raniga S, **Knowles NK**, Ferreira LF, Athwal GS. The Walch B Humerus: Glenoid Retroversion is Associated with Torsional Differences in the Humerus. Journal of Shoulder and Elbow Surgery. Accepted Feb. 2019

Knowles NK, Langohr GDG, Athwal GS, Ferreira LM. Polyethylene Glenoid Component Backside Fixation Geometry Influences Stability in Total Shoulder Arthroplasty. Computer Methods in Biomechanics and Biomedical Engineering. E-Pub Ahead of Print

Knowles NK, Langohr GDG, Faieghi M, Nelson A, Ferreira LM. Development of a Validated Glenoid Trabecular Density-Modulus Relationship. Journal of the Mechanical Behavior of Biomedical Materials. 2019; 90:140-145

Knowles NK, Ip K, Ferreira LM. The Effect of Material Heterogeneity, Element Type, and Down-Sampling on Trabecular Stiffness in Micro Finite Element Models. Annals of Biomedical Engineering. 2018. 2018; 47:615-23

Wegmann K, **Knowles NK**, Lalone EA, Hackl M, Müller LP, King GJW, Athwal GS. The Shape-Match of the Olecranon Tip for Reconstruction of the Coronoid Process: Influence of Side and Osteotomy Angle. Journal of Shoulder and Elbow Surgery 2019; 28(4):e117-e124

Wegmann K, **Knowles NK**, Lalone EA, Müller LP, Athwal GS, King GJW. Computed Tomography Analysis of the Radial Notch of the Ulna. Journal of Hand Surgery. 2018; In-Press

Knowles NK, Decoito I. Biomedical Engineering Undergraduate Education: A Canadian Perspective. International Journal of Mechanical Engineering Education. 2018. E-Pub Ahead of Print

Faieghi M, **Knowles NK**, Tutunea-Fatan OR, Ferreira LM. Fast Generation of Cartesian Meshes from Micro-Computed Tomography Data. Computer-Aided Design and Applications. 2019; 16(1):161-171

Paul RA, **Knowles NK**, Chaoui J, Gauci M, Ferreira LM, Walch G, Athwal GS. Characterization of the Dysplastic Walch Type C Glenoid. Bone and Joint Journal. 2018; 100(8): 1074-1079

Reeves JM, **Knowles NK**, Athwal GS, Johnson JA. Methods for Post-Hoc Quantitative CT Bone Mineral Density Calibration: Phantom-Only and Regression. Journal of Biomechanical Engineering. 2018; 140(9)

Chan K, **Knowles NK**, Chaoui J, Walch G, Ferreira LM, Athwal GS. Is the Walch B3 Glenoid Erosion Significantly Worse than the B2? Shoulder and Elbow. 2017

West E, **Knowles NK**, Ferreira LM, Athwal GS. A 3D Comparison of Humeral Head Retroversion by Sex and Measurement Technique. Shoulder and Elbow. 2017; 10(3):192-200

Chan K, **Knowles NK**, Chaoui J, Gauci M, Ferreira LM, Walch G, Athwal GS. Characterization of the Walch B3 Glenoid in Primary Osteoarthritis. Journal of Shoulder and Elbow Surgery. 2017; 26(5):909-914

Knowles NK, Reeves JM, Ferreira LF. Quantitative Computed Tomography (QCT) Derived Bone Mineral Density (BMD) in Finite Element Studies: A Review of the Literature. Journal of Experimental Orthopaedics. 2016; 3(1):36

Knowles NK, Ferreira LM, Athwal GS. The Arthritic Glenoid: Anatomy and Arthroplasty Designs. Current Reviews in Musculoskeletal Medicine. 2016; 9(1):23-29

Knowles NK, Ferreira LM, Athwal GS. Premorbid Retroversion is Significantly Greater in Type B2 Glenoids. Journal of Shoulder and Elbow Surgery. 2016; 25(7):1064-1068

Knowles NK, Gladwell M, Ferreira LM. An Intra-Bone Axial Load Transducer: Development and Validation in an In-Vitro Radius Model. Journal of Experimental Orthopaedics. 2015; 2:19

Knowles NK, Carroll MC, Keener JD, Ferreira LM, Athwal GS. A Comparison of Normal and Osteoarthritic Humeral Head Size and Morphology. Journal of Shoulder and Elbow Surgery. 2016; 25(3):502-509

Ferreira LM, **Knowles NK**, Richmond D, Athwal GS. Effectiveness of CT for the Detection of Glenoid Bone Graft Resorption Following Reverse Shoulder Arthroplasty. Orthopaedics and Traumatology: Surgery & Research 2015; 101(4):427-430

Knowles NK, Ferreira LM, Athwal GS. Augmented Glenoid Component Designs for Type B2 Erosions: A Computational Comparison by Volume of Bone Removal, and Quality of Remaining Bone. Journal of Shoulder and Elbow Surgery 2015; 24(8):1218-1226

Knowles NK, Keener JD, Ferreira LM, Athwal GS. Quantification of the Position, Orientation and Surface Area of Posterior Bone Loss in Type B2 Glenoids. Journal of Shoulder and Elbow Surgery 2015; 24(4):503-510

Knowles NK, Ferreira LM, Keener JD, Athwal GS. Regional Bone Density Variations in Osteoarthritic Glenoids: A Comparison of Symmetric to Asymmetric (Type B2) Erosion Patterns. Journal of Shoulder and Elbow Surgery 2015; 24(3):425-432

In-Revision (n=2)

Mahaffy M, **Knowles NK,** Athwal GS, Johnson JA. Bone Density Distribution in Type E Glenoids. Journal of Shoulder and Elbow Surgery (JSES-D-18-01153R1)

Kusins J, **Knowles NK,** Ryan M, Dall'Ara E, Ferreira LM. Performance of QCT-Derived Finite Element Models in Predicting Local Displacements Using Digital Volume Correlation. Journal of the Mechanical Behavior of Biomedical Materials (JMBBM-2019-265-R1)

Submitted (n=2)

Knowles NK, Kusins J, Faieghi M, Ryan M, Dall'Ara E, Ferreira LM. Material Mapping Strategies for QCT-Derived Scapular Models: A Comparison with Micro-CT Loaded Cadavers using Digital Volume Correlation. Annals of Biomedical Engineering (ABME-S-19-00191)

Knowles NK, Kusins J, Columbus MP, Athwal GS, Ferreira LM. Morphological and Apparent-Level Stiffness Variations Between Normal and Osteoarthritic Bone. Bone (BONE-D-19-00349)

In-Preparation (n=13)

Abdic S, **Knowles NK,** Johnson JA, Walch G, Athwal GS. Favard Type E2 Bone Loss Orientation.

Knowles NK, Kusins J, Pucchio AM, Ferreira LM. Micro-Level Trabecular Apparent Modulus can be Accurately Modeled by QCT Finite Element Models Based on Material Mapping Strategy and Element Type.

Ip K, **Knowles NK**, Ferreira LM. A Comparison of the Mechanical Properties of Trabecular Bone Between Micro Finite Element and Meshless Models

Larouche MR, **Knowles NK**, Ferreira LM, Athwal GS. A Computational Comparison of Distal Clavicle and Coracoid Process Autografts for Glenoid Deficiency. Journal of Shoulder and Elbow Surgery

Knowles NK, Columbus MP, Wegmann K, Athwal GS, Ferreira LM. Revision Shoulder Arthroplasty after Failed Shoulder Arthroplasty: A Systematic Review and Comparison of North American versus European Outcomes and Complications.

West E, **Knowles NK**, Gupta A, Ferreira LM, Athwal GS. Comparison of Humeral Head Osteotomy using Anatomic and Guide-Assisted Cuts.

Ting F, **Knowles NK**, Ferreira LF, Athwal GS. Proximal Humeral Morphological Variations in Type C, and Type B Pathologic Shoulders.

Ting F, **Knowles NK**, Ferreira LF, Athwal GS. Proximal Humeral Version Measurements are Independent of Distal Humeral Anatomy

Ting F, **Knowles NK**, Ferreira LF, Athwal GS. The Humeral Canal is Less Eccentric in Type C and Type B3 Pathologic Shoulders

Ting F, **Knowles NK**, Ferreira LF, Athwal GS. Rethinking Humeral Head Version

Haeni D, **Knowles NK**, Gupta A. Glenoid Bone Density Following Laterjet Procedures

Gupta A, **Knowles NK**, Athwal GS, Ferreira LF. Morphologic Analysis of the Three Columns of the Scapula: Surgical Implications in Reverse Shoulder Arthroplasty

Gupta A, **Knowles NK**, Ferreira LF, Athwal GS. Scapular Axis in the Setting of Severe Glenoid Bone Loss

Gupta A, **Knowles NK**, Athwal GS, Ferreira LF. Correlations Between the Scapular Body and Glenoid Anatomy

Published Book Chapters (n=1)

Aldebeyan W, **Knowles NK**, Ferreira LM, Athwal GS. Augmented Glenoid Replacement. Anatomic Shoulder Arthroplasty – Strategies for Clinical Management. Springer ISBN 978-3-319-29164-2

Published Abstracts (n=7)

Knowles NK, Langohr GDG, Athwal GS, Ferreira LM. Glenoid Component Fixation in Total Shoulder Arthroplasty. Bone and Joint Journal 2018;100(6);13

Faieghi M, **Knowles NK**, Ferreira LM, Tutunea-Fatan OR. Efficient Voxelization-Based Construction of Finite Element Meshes Originated from Micro-Computed Tomography Data. Proceedings of the 2018 CAD Conference

Skerratt G, **Knowles NK**, Wilson TD, Ferreira LF. Novel Methodology for Muscle Volumization: 3D Laser Surface Scanning Meets CT. The FASEB Journal 2017; 31:903.8

Gupta A, **Knowles NK**, Athwal GS, Ferreira LF. Morphologic Analysis of the Three Columns of the Scapula: Surgical Implications in Reverse Shoulder Arthroplasty. Bone and Joint Journal 2016; 99(4):3

West E, **Knowles NK**, Ferreira LM, Athwal GS. Comparison of Humeral Head Retroversion by Gender and Measurements Technique. Bone and Joint Journal 2016; 99(6):94

West E, **Knowles NK**, Ferreira LM, Athwal GS. Comparison of Humeral Head Osteotomy using Anatomic and Guide-Assisted Cuts. Bone and Joint Journal 2016; 98(21):10

Knowles NK, Langohr GDG, Athwal GS, Ferreira LM. A Finite Element Analysis of Augmented Glenoid Components. ASES 2015 Closed Meeting. Journal of Shoulder and Elbow Surgery 2016; 25(6):e166-e168

INVITED PRESENTATIONS

Knowles NK. Bone Quality in Two Osteoarthritic Glenoid Morphologies. (May 2015) 2015 Annual Dr. Suzanne Bernier Memorial Lecture in Skeletal Biology. The University of Western Ontario. London, ON. (Institutional) (Podium)

Knowles NK, Ferreira LM, Keener JD, Athwal GS. (March 2015) Quantification of the Position, Orientation and Surface Area of Posterior Bone Loss in Type B2 Glenoids. 2015 Annual Meeting of the American Academy of Orthopaedic Surgeons (AAOS). Las Vegas, NV. (International) (Guided Poster Tour Presentation)

Knowles NK, Ferreira LM, Keener JD, Athwal GS. (March 2015) Quantification of the Position, Orientation and Surface Area of Posterior Bone Loss in Type B2 Glenoids. 61st Annual Meeting of the Orthopaedic Research Society. Las Vegas, NV. (International) (Poster)

PRESENTATIONS AT CONFERENCES AND PROFESSIONAL MEETINGS

Podium (n=38); Poster (n=52)

Mahaffy M, **Knowles NK,** Athwal GS, Johnson JA. Bone Density Distribution in Type E Glenoids. International Combined Orthopaedic Research Society (ICORS) Meeting 2019. Montreal, Qc (National) (Podium)

Abdic S, **Knowles NK,** Johnson JA, Walch G, Athwal GS. Favard Type E2 Bone Loss Orientation. International Combined Orthopaedic Research Society (ICORS) Meeting 2019. Montreal, Qc (National) (Podium)

Kusins J, **Knowles NK,** Ryan M, Dall'Ara E, Ferreira LM. Quantitative Assessment of the Errors in Local Displacements of QCT-Derived Scapula Finite Element Models Using Digital Volume Correlation. International Combined Orthopaedic Research Society (ICORS) Meeting 2019. Montreal, Qc (National) (Poster)

Knowles NK, Kusins J, Pucchio AMR, Ferreira LM. (June 2019). Micro-Level Trabecular Apparent Modulus can be Accurately Modeled by QCT Finite Element Models Based on Material Mapping Strategy and Element Type. International Combined Orthopaedic Research Society (ICORS) Meeting 2019. Montreal, Qc (National) (Poster)

Knowles NK, Kusins J, Columbus MP, Athwal GS, Ferreira LM. (June 2019). Improving Computational Models of the Humerus by Comparing the Mechanical Properties of Normal and Pathologic Bone. International Combined Orthopaedic Research Society (ICORS) Meeting 2019. Montreal, Qc (National) (Poster)

Wegmann K, **Knowles NK**, Lalone EA, Hackl M, Müller LP, King GJW, Athwal GS. (March 2019) The Shape-Match of the Olecranon Tip for Reconstruction of the Coronoid Process: Influence of Side and Osteotomy Angle. The American Academy of Orthopaedic Surgeons (AAOS) General Meeting 2019. Las Vegas, NV (International) (Podium)

Raniga S, **Knowles NK**, Ferreira LF, Athwal GS. (March 2019). The Walch B Humerus: Glenoid Retroversion is Associated with Torsional Differences in the Humerus. The American Academy of Orthopaedic Surgeons General Meeting 2019. Las Vegas, NV (International) (Poster)

Knowles NK, Kusins J, Columbus MP, Athwal GS, Ferreira LM. (February 2019). Variations in the Mechanical Properties of Humeral Trabecular Bone: Towards Improving Computational Models of the Humerus. The 2019 Annual Meeting of the Orthopaedic Research Society. Austin, TX (International) (Podium)

Knowles NK, Kusins J, Pucchio AMR, Ferreira LM. (February 2019). Micro-Level Trabecular Apparent Modulus can be Accurately Modeled by QCT Finite Element Models Based on Material Mapping Strategy and Element Type. The 2019 Annual Meeting of the Orthopaedic Research Society. Austin, TX (International) (Poster)

Kusins J, **Knowles NK**, Ryan M, Dall'Ara E, Ferreira L. (February 2019). Quantitative Assessment of the Ability of QCT-Derived Scapula Finite Element Models in Predicting Local Displacements Using Digital Volume Correlation. The 2019 Annual Meeting of the Orthopaedic Research Society. Austin, TX (International) (Poster)

Mahaffy M, **Knowles NK,** Berkmortel C, Abdic Sejla, Johnson JA, Athwal GS. Density Distribution Analysis of the E2-Type Glenoid. The 2019 Annual Meeting of the Orthopaedic Research Society. Austin, TX (International) (Poster)

Raniga S, **Knowles NK**, Ferreira LF, Athwal GS. (October 2018). The Walch B Humerus: Glenoid Retroversion is Associated with Torsional Differences in the Humerus. Shoulder & Elbow Society of Australia 2018 Biennial Closed Conference, Perth, AU (International) (Podium)

Knowles NK, Kusins J, Columbus MP, Athwal GS, Ferreira LM. (October 2018). Variations in the Mechanical Properties of Humeral Trabecular Bone: Towards Improving Computational Models of the Humerus. The 31st Annual Congress of the International Society for Technology in Arthroplasty. London, UK (International) (E-Poster with Short Talk)

Knowles NK, Langohr GDG, Faieghi M, Nelson A, Ferreira LM. (October 2018). Accuracy of Density-Modulus Relationships Used in Finite Element Modeling of the Shoulder. The 31st Annual Congress of the International Society for Technology in Arthroplasty. London, UK (International) (Podium)

Knowles NK, Ip K, Ferreira LM. (October 2018). The Effect of Material Heterogeneity on Trabecular Stiffness in Micro Finite Element Models. The 31st Annual Congress of the International Society for Technology in Arthroplasty. London, UK (International) (E-Poster with Short Talk)

Raniga S, **Knowles NK**, Ferreira LM, Athwal GS. (October 2018). The Walch B Humerus: Glenoid Retroversion is Associated with Torsional Differences in the Humerus. The 31st Annual Congress of the International Society for Technology in Arthroplasty. London, UK (International) (Podium)

Knowles NK, Langohr GDG, Faieghi M, Nelson A, Ferreira LM. (August 2018). Accuracy of Density-Modulus Relationships Used in Finite Element Modeling of the Shoulder. American Society of Biomechanics Annual Meeting. Rochester, MN (International) (Poster)

Knowles NK, Ip K, Ferreira LM. (May 2018). (August 2018). The Effect of Material Heterogeneity on Trabecular Stiffness in Micro Finite Element Models. American Society of Biomechanics Annual Meeting. Rochester, MN (International) (Poster)

Ip K, **Knowles NK**, Ferreira LM. (August 2018). A Comparison of the Mechanical Properties of Trabecular Bone Between Micro-Finite Element and Meshless Models. American Society of Biomechanics Annual Meeting. Rochester, MN (International) (Poster)

Gupta A, **Knowles NK**, Athwal GS, Ferreira LM. (September 2018). Relationships of Scapular Coordinate Systems to Determine Glenoid Centre: Application to Glenoid Fixation in

Shoulder Arthroplasty. European Society for Surgery of the Shoulder and Elbow Congress (SECEC-ESSSE). Geneva, CH (International) (Poster)

Faieghi M, **Knowles NK**, Ferreira LM, Tutunea-Fatan OR. (July 2018) An Efficient Hexahedral Mesh Generation Algorithm for Micro-Level Trabecular Bone Modeling. 8th World Congress of Biomechanics. Dublin, IRL (International) (Poster)

Kusins JR, **Knowles NK**, Faieghi M, Nelson A, Ferreira LM. (July 2018). Development and Cross-Validation of a CT-Compatible Loading Device for Mechanical Testing of Trabecular Bone Specimens. 8th World Congress of Biomechanics. Dublin, IRL (International) (Podium)

Faieghi M, **Knowles NK**, Ferreira LM, Tutunea-Fatan OR. (July 2018) Efficient Voxelization-Based Construction of Finite Element Meshes Originated from Micro-Computed Tomography Data. CAD Conference 2018, Paris, FR (International) (Podium)

Knowles NK, Langohr GDG, Athwal GS, Ferreira LM. (June 2018). Glenoid Component Fixation in Total Shoulder Arthroplasty. The 2018 Annual of the Canadian Orthopaedic Association (COA) and Canadian Orthopaedic Research Society (CORS), Victoria, BC, (National) (Podium)

Knowles NK, Langohr GDG, Faieghi M, Nelson A, Ferreira LM. (June 2018). Development of a Validated Trabecular Density-Modulus Relationship. The 2018 Annual of the Canadian Orthopaedic Association (COA) and Canadian Orthopaedic Research Society (CORS), Victoria, BC, (National) (Podium)

Knowles NK, Ip K, Ferreira LM. (May 2018). The Effect of Material Heterogeneity on Trabecular Stiffness in Micro Finite Element Models. Canadian Bone and Joint Conference. London, ON (National) (Poster)

Ip K, **Knowles NK**, Ferreira LM. (May 2018).A Comparison of the Mechanical Properties of Trabecular Bone Between Micro-Finite Element and Meshless Models. Canadian Bone and Joint Conference. London, ON (National) (Poster)

Knowles NK, Columbus MP, Wegmann K, Athwal GS, Ferreira LM. (May 2018). Revision Shoulder Arthroplasty after Failed Shoulder Arthroplasty: A Systematic Review and Comparison of North American versus European Outcomes and Complications. Lawson Health Research Day. London, ON (Institutional) (Poster)

Knowles NK, Langohr GDG, Faieghi M, Nelson A, Ferreira LM. (March 2018). Development of a Validated Trabecular Density-Modulus Relationship. The 2018 Annual Meeting of the Orthopaedic Research Society (ORS), New Orleans, LA (International) (Poster)

Kusins JR, **Knowles NK**, Faieghi M, Nelson A, Ferreira LM. (March 2018). Development and Cross-Validation of a CT-Compatible Loading Device for Mechanical Testing of Trabecular Bone Specimens. The 2018 Annual Meeting of the Orthopaedic Research Society (ORS), New Orleans, LA (International) (Poster)

Knowles NK, Langohr GDG, Athwal GS, Ferreira LM. (March 2018). Polyethylene Glenoid Component Backside Geometry Influences Fixation in Total Shoulder Arthroplasty. 15th

International Symposium on Computer Methods in Biomechanics and Biomedical Engineering, Lisbon, PT (International) (Podium)

Knowles NK, Langohr GDG, Faieghi M, Nelson A, Ferreira LM. (March 2018). Development of a Validated Trabecular Density-Modulus Relationship. 15th International Symposium on Computer Methods in Biomechanics and Biomedical Engineering, Lisbon, PT (International) (Podium)

Kusins JR, **Knowles NK**, Faieghi M, Nelson A, Ferreira LM. (March 2018). Development and Cross-Validation of a CT-Compatible Loading Device for Mechanical Testing of Trabecular Bone Specimens. 15th International Symposium on Computer Methods in Biomechanics and Biomedical Engineering, Lisbon, PT (International) (Podium)

Ip K, Peng Y, **Knowles NK**, Moore C, Ferreira LM. (March 2018). Development of an In-Vitro Intrinsically Loaded Temporomandibular Force Simulator and Fast Computational Model Based on Method of External Approximations. 15th International Symposium on Computer Methods in Biomechanics and Biomedical Engineering, Lisbon, PT (International) (Podium)

Knowles NK, Langohr GDG, Athwal GS, Ferreira LM. (March 2018). Glenoid Component Fixation in Total Shoulder Arthroplasty. The 2018 Annual Meeting of the Orthopaedic Research Society (ORS), New Orleans, LA (International) (Poster)

Gupta A, **Knowles NK**, Athwal GS, Ferreira LM. (October 2017). Morphologic Analysis of the Three Columns of the Scapula: Surgical Implications in Reverse Shoulder Arthroplasty. 44th Japan Shoulder Society and 1st Asia-Pacific Shoulder and Elbow Symposium. Tokyo, JP (International) (E-Poster)

Gupta A, **Knowles NK**, Athwal GS, Ferreira LM. (October 2017). Relationships of Scapular Plane Definitions: Application to Glenoid Fixation in Total Shoulder Arthroplasty. 44th Japan Shoulder Society and 1st Asia-Pacific Shoulder and Elbow Symposium. Tokyo, JP (International) (Poster)

Knowles NK, Langohr GDG, Ferreira LM, Athwal GS. (September 2017). Glenoid Component Fixation in Total Shoulder Arthroplasty. International Society for Technology in Arthroplasty (ISTA) 2017. Seoul, Korea (International) (Podium)

Gupta A, **Knowles NK**, Athwal GS, Ferreira LM. (July 2017). Morphologic Analysis of the Three Columns of the Scapula: Surgical Implications in Reverse Shoulder Arthroplasty. The XXVI Congress of the International Society of Biomechanics. Brisbane, AU. (International) (Podium)

Gupta A, **Knowles NK**, Athwal GS, Ferreira LM. (July 2017). Relationships of Scapular Plane Definitions: Application to Glenoid Fixation in Total Shoulder Arthroplasty. The XXVI Congress of the International Society of Biomechanics. Brisbane, AU. (International) (Poster)

Gupta A, **Knowles NK**, Athwal GS, Ferreira LM. (June 2017). Morphologic Analysis of the Three Columns of the Scapula: Surgical Implications in Reverse Shoulder Arthroplasty. The 2017 COA/CORS Annual Meeting. Ottawa, ON. (National) (Poster)

Chan K, **Knowles NK**, Chaoui J, Walch G, Ferreira LM, Athwal GS. Characterization of the Walch B3 Glenoid in Primary Osteoarthritis. The 2017 COA/CORS Annual Meeting. Ottawa, ON. (National) (Podium)

Chan K, **Knowles NK**, Chaoui J, Walch G, Ferreira LM, Athwal GS. Is the Walch B3 Glenoid Erosion Significantly Worse than the B2? The 2017 COA/CORS Annual Meeting. Ottawa, ON. (National) (Poster)

Skerratt G, **Knowles NK**, Wilson TD, Ferreira LM. (April 2017). Novel Methodology for Muscle Volumization: 3D Laser Surface Scanning Meets CT. Experimental Biology 2017. Chicago, IL. (International) (Poster)

Knowles NK, Nelson A, Ferreira LM. (March 2017). Computational Evaluation of Glenoid Bone Loading using Micro-CT. 15 Annual Imaging Network Ontario Symposium. London, ON. (National) (Podium)

McGregor M, Banyan S, **Knowles NK**, Johnson JA, Lalone EA. (March 2017). The Effects of Transverse Bone Region on Cortical and Trabecular Bone Mineral Density at the Distal Radius. The 2017 Annual Meeting of the Orthopaedic Research Society (ORS), San Diego, CA (International) (Poster)

West E, **Knowles NK**, Ferreira LM, Athwal GS. (March 2017). Comparison of Humeral Head Retroversion by Sex and Measurement Technique. The 2017 Annual Meeting of the Orthopaedic Research Society (ORS), San Diego, CA (International) (Poster)

Reeves JM, **Knowles NK**, Ferreira LM, Athwal GS, Johnson JA. (March 2017). Methods for Post-Hoc Quantitative CT Bone Scan Calibration: Empty Chamber and Regression. The 2017 Annual Meeting of the Orthopaedic Research Society (ORS), San Diego, CA (International) (Poster)

Gupta A, **Knowles NK**, Athwal GS, Ferreira LM. (March 2017). Relationships of Scapular Plane Definitions: Application to Glenoid Fixation in Total Shoulder Arthroplasty. The 2017Annual Meeting of the Orthopaedic Research Society (ORS), San Diego, CA (International) (Poster)

Gupta A, **Knowles NK**, Athwal GS, Ferreira LM. (March 2017). Morphologic Analysis of the Three Columns of the Scapula: Surgical Implications in Reverse Shoulder Arthroplasty. The 2017Annual Meeting of the Orthopaedic Research Society (ORS), San Diego, CA (International) (Poster)

Skerratt G, **Knowles NK**, Wilson TD, Ferreira LM. (October 2016). 3D Laser Surface Scanned Musculature and Co-Registration with CT. Western Anatomy and Cell Biology Research Day. London, ON. (Institutional) (Poster)

West E, **Knowles NK**, Ferreira LM, Athwal GS. (October 2016). Comparison of Humeral Head Osteotomy using Anatomic and Guide-Assisted Cuts. International Society for Technology in Arthroplasty 2016 Meeting. Boston, MA. (International) (Poster with Talk)

West E, **Knowles NK**, Ferreira LM, Athwal GS. (October 2016). Comparison of Humeral Head Retroversion by Sex and Measurement Technique. International Society for Technology in Arthroplasty 2016 Meeting. Boston, MA. (International) (Podium)

Gupta A, **Knowles NK**, Ferreira LM, Athwal GS. (October 2016). Morphologic Analysis of the Three Columns of the Scapula: Surgical Implications in Reverse Shoulder Arthroplasty. International Society for Technology in Arthroplasty 2016 Meeting. Boston, MA. (International) (Podium)

Knowles NK, Ferreira LM, Athwal GS. (June 2016). Premorbid Retroversion is Significantly Greater in Type B2 Glenoids. 2016 Summer Biomechanics, Bioengineering and Biotransport Conference. National Harbor, MD. (International) (Podium)

Knowles NK, Langohr GDG, Athwal GS, Ferreira LM. (June 2016). A Finite Element Analysis of Augmented Glenoid Components. 2016 Summer Biomechanics, Bioengineering and Biotransport Conference. National Harbor, MD. (International) (Poster)

Knowles NK, Carroll MJ, Keener JD, Ferreira LM, Athwal GS. (June 2016). A Comparison of Normal and Osteoarthritic Humeral Head Size and Morphology. 2016 Summer Biomechanics, Bioengineering and Biotransport Conference. National Harbor, MD. (International) (Poster)

West E, **Knowles NK**, Ferreira LM, Athwal GS. (June 2016). Comparison of Humeral Head Osteotomy using Anatomic and Guide-Assisted Cuts. 2016 Summer Biomechanics, Bioengineering and Biotransport Conference. National Harbor, MD. (International) (Poster)

Knowles NK, Langohr GDG, Athwal GS, Ferreira LM. (June 2016) A Finite Element Analysis of Augmented Glenoid Components. The 2016 Annual Meeting of the Canadian Orthopaedic Association (COA). Quebec City, QC. (International) (Poster)

Knowles NK, Ferreira LM, Athwal GS. (June 2016). Premorbid Retroversion is Significantly Greater in Type B2 Glenoids. The 2016 Annual Meeting of the Canadian Orthopaedic Association (COA). Quebec City, QC. (International) (Poster)

West E, **Knowles NK**, Ferreira LM, Athwal GS. (June 2016). Comparison of Humeral Head Osteotomy using Anatomic and Guide-Assisted Cuts, The 2016 Annual Meeting of the Canadian Orthopaedic Association (COA). Quebec City, QC. (International) (Podium)

Knowles NK, Langohr GDG, Athwal GS, Ferreira LM. (May 2016) A Finite Element Analysis of Augmented Glenoid Components. The 13th International Congress of Shoulder and Elbow Surgery, Jeju, South Korea (International) (Podium)

Knowles NK, Langohr GDG, Athwal GS, Ferreira LM. (May 2016) A Custom Micro-CT Glenoid Loading Device for Cadaveric Glenoid Testing. Biomedical Engineering (BME) Research Day. London, ON (Institutional) (Poster)

West E, **Knowles NK**, Ferreira LM, Athwal GS. (June 2016). Comparison of Humeral Head Osteotomy using Anatomic and Guide-Assisted Cuts. The Canadian Bone and Joint Conference (National) (Poster)

Reeves JM, **Knowles NK**, Ferreira LM, Athwal GS, Johnson JA. (April 2016). Post-Hoc Calibration Methods in Quantitative Computed Tomography. The Canadian Bone and Joint Conference (National) (Poster)

Knowles NK, Langohr GDG, Athwal GS, Ferreira LM. (April 2016) A Finite Element Analysis of Augmented Glenoid Components. The Canadian Bone and Joint Conference (National) (Poster)

Knowles NK, Carroll MJ, Keener JD, Ferreira LM, Athwal GS. (March 2016) A Comparison of Normal and Osteoarthritic Humeral Head Size and Morphology. London Health Research Day. London, ON. (Institutional) (Poster)

West E, **Knowles NK**, Ferreira LM, Athwal GS. (June 2016). Comparison of Humeral Head Osteotomy using Anatomic and Guide-Assisted Cuts. London Health Research Day. London, ON. (Institutional) (Poster)

Knowles NK, Langohr GDG, Athwal GS, Ferreira LM. (March 2016) A Finite Element Analysis of Augmented Glenoid Components. The 2016 Annual Meeting of the Orthopaedic Research Society (ORS), Orlando, FL. (International) (Poster)

Knowles NK, Ferreira LM, Athwal GS. (March 2016). Premorbid Retroversion is Significantly Greater in Type B2 Glenoids. The 2016 Annual Meeting of the Orthopaedic Research Society (ORS), Orlando, FL. (International) (Poster)

Knowles NK, Carroll MJ, Keener JD, Ferreira LM, Athwal GS. (March 2016) A Comparison of Normal and Osteoarthritic Humeral Head Size and Morphology. The 2016 Annual Meeting of the Orthopaedic Research Society (ORS), Orlando, FL. (International) (Poster)

Knowles NK, Langohr GDG, Athwal GS, Ferreira LM. (March 2016) A Finite Element Analysis of Augmented Glenoid Components. American Shoulder and Elbow Surgeons Open Meeting. Orlando, FL. (International) (Podium)

Knowles NK, Langohr GDG, Athwal GS, Ferreira LM. (October 2015) A Finite Element Analysis of Augmented Glenoid Components. American Shoulder and Elbow Surgeons Closed Meeting. Asheville, NC. (International) (Podium)

Knowles NK, Ferreira LM, Athwal GS. (September 2015). Premorbid Retroversion is Significantly Greater in Type B2 Glenoids. Computer Methods in Biomechanics and Biomedical Engineering & Imaging and Visualization. Montreal, QC. (International) (Poster)

Knowles NK, Langohr GDG, Ferreira LM, Athwal GS**.** (September 2015) A Finite Element Analysis of Augmented Glenoid Components. Computer Methods in Biomechanics and Biomedical Engineering & Imaging and Visualization. Montreal, QC. (International) (Podium)

Knowles NK, Carroll MJ, Keener JD, Ferreira LM, Athwal GS. (September 2015) Osteoarthritic Humeral Heads are Morphologically Different Than Non-Arthritic Humeral Heads. Computer Methods in Biomechanics and Biomedical Engineering & Imaging and Visualization. Montreal, QC. (International) (Podium)

Knowles NK, Keener JD, Ferreira LM, Athwal GS. (September 2015) Regional Bone Density Variations in Osteoarthritic Glenoids: A Comparison of Symmetric to Asymmetric (Type B2) Erosion Patterns. Computer Methods in Biomechanics and Biomedical Engineering & Imaging and Visualization. Montreal, QC. (International) (Podium)

Knowles NK, Keener JD, Athwal GS, Ferreira LM. (September 2015) Quantification of the Position, Orientation and Surface Area of Posterior Bone Loss in Type B2 Glenoids. Computer Methods in Biomechanics and Biomedical Engineering & Imaging and Visualization. Montreal, QC. (International) (Podium)

Knowles NK, Ferreira LM, Athwal GS. (September 2015) A Comparison of Augmented Glenoid Component Designs for Type B2 Erosions: Evaluation by Volume of Bone Removal, and Quality of Remaining Bone. Computer Methods in Biomechanics and Biomedical Engineering & Imaging and Visualization. Montreal, QC. (International) (Podium)

Knowles NK, Ferreira LM, Keener JD, Athwal GS. (June 2015) Quantification of the Position, Orientation and Surface Area of Posterior Bone Loss in Type B2 Glenoids. 2015 Annual Meeting of the Canadian Orthopaedic Association (COA). Vancouver, BC. (International) (Podium)

Knowles NK, Ferreira LM, Athwal GS. (June 2015) A Comparison of Augmented Glenoid Component Designs for Type B2 Erosions: Evaluation by Volume of Bone Removal, and Quality of Remaining Bone. 2015 Annual Meeting of the Canadian Orthopaedic Association (COA). Vancouver, BC. (International) (Podium)

Knowles NK, Carroll MC, Ferreira LM, Keener JD, Athwal GS. (June 2015) An Anatomic Study of Normal and Osteoarthritic Humeral Head Size. 2015 Annual Meeting of the Canadian Orthopaedic Research Society (CORS). Vancouver, BC. (International) (Podium)

Knowles NK, Ferreira LM, Keener JD, Athwal GS. (June 2015) Regional Bone Density Variations in Osteoarthritic Glenoids: A Comparison of Symmetric to Asymmetric (Type B2) Erosion Patterns. 2015 Annual Meeting of the Canadian Orthopaedic Research Society (CORS). Vancouver, BC. (International) (Podium)

Knowles NK, Ferreira LM, Keener JD, Athwal GS. (March 2015) Quantification of the Position, Orientation and Surface Area of Posterior Bone Loss in Type B2 Glenoids. 2015 Annual Meeting of the American Academy of Orthopaedic Surgeons (AAOS). Las Vegas, NV. (International) (Poster)

Knowles NK, Athwal GS, Keener JD, Ferreira LM. (October 2014) Regional Bone Density Variations in Osteoarthritic Glenoids: A Comparison of Symmetric to Asymmetric (Type B2) Erosion Patterns. American Shoulder and Elbow Surgeons Closed Meeting. Pinehurst, NC (International) (Poster)

Knowles NK, Athwal GS, Keener JD, Ferreira LM. (July 2014) Morphology and Density Variations in Osteoarthritic Glenoids.7th World Congress of Biomechanics, Boston, MA (International) (Poster)

Knowles NK, Gladwell M, Ferreira LM. (June 2014) An Intra-Bone Axial Load Transducer: Development and Validation in an In-Vitro Radius Model. Combined Meeting of the AOA/COA - CORS 2014, Montreal, QC (International) (Poster)

Knowles NK, Richmond D, Athwal GS, Ferreira LM. (June 2014) Computed Tomography is Ineffective in Detecting Glenoid Bone Graft Resorption Following Reverse Shoulder Arthroplasty. Combined Meeting of the AOA/COA - CORS 2014. Montreal, QC (International) (Podium)

Knowles NK, Ferreira LM, Richmond D, Athwal GS. (Mar 2014) The Effectiveness of CT to Determine Bone Graft Resorption after BIO-RSA. 60th Annual Meeting of the Orthopaedic Research Society. New Orleans, LA (International) (Poster)

Knowles NK, Gladwell M, Ferreira LM. (Jan 2014) An Intra-Bone Axial Load Transducer: Development and Validation in an In-Vitro Radius Model. Bone and Joint Injury and Repair (BAJIR) Conference. London, ON (National) (Podium)